Volume 72A
Number 5
Sept.–Oct. 1968

Physics and Chemistry

U.S. DEPARTMENT OF COMMERCE

SECTION A
JOURNAL OF RESEARCH

NATIONAL BUREAU OF STANDARDS

Journal of Research

of the

National Bureau of Standards

A. Physics and Chemistry

Sept.–Oct. • 1968

VOLUME • 72A

NUMBER • 5

Editor: C. W. Beckett

Associate Editor: D. D. Wagman

Publication dates:
Feb. 1, Apr. 1, June 1, Aug. 1, Oct. 1, Dec. 1, 1968

JOURNAL OF RESEARCH

The National Bureau of Standards Journal of Research reports research and development in the fields of activity shown at right. Also included from time to time are survey articles on topics closely related to the Bureau's scientific and technical program.

The Journal is published in three separate sections as follows:

A. Physics and Chemistry

Contains papers of interest primarily to scientists working in these fields. Issued six times a year. Annual subscription: domestic, $6.00; foreign, $7.25. Single copy, $1.00.

B. Mathematical Sciences

Presents studies and compilations designed mainly for the mathematician and the theoretical physicist. Issued quarterly. Annual subscription: domestic, $2.25; foreign, $2.75. Single copy, 75c.

C. Engineering and Instrumentation

Reports research and development results of interest chiefly to the engineer and the applied scientist. Issued quarterly. Annual subscription: domestic, $2.75; foreign, $3.50. Single copy, 75c.

NATIONAL BUREAU OF STANDARDS

The National Bureau of Standards[1] was established by an act of Congress March 3, 1901. Today, in addition to serving as the Nation's central measurement laboratory, the Bureau is a principal focal point in the Federal Government for assuring maximum application of the physical and engineering sciences to the advancement of technology in industry and commerce. To this end the Bureau conducts research and provides central national services in three broad program areas and provides central national services in a fourth. These are: (1) basic measurements and standards, (2) materials measurements and standards, (3) technological measurements and standards, and (4) transfer of technology.

The Bureau comprises the Institute for Basic Standards, the Institute for Materials Research, the Institute for Applied Technology, and the Center for Radiation Research.

THE INSTITUTE FOR BASIC STANDARDS provides the central basis within the United States of a complete and consistent system of physical measurement, coordinates that system with the measurement systems of other nations, and furnishes essential services leading to accurate and uniform physical measurements throughout the Nation's scientific community, industry, and commerce. The Institute consists of an Office of Standard Reference Data and a group of divisions organized by the following areas of science and engineering:

Applied Mathematics—Electricity—Metrology—Mechanics—Heat—Atomic Physics—Cryogenics[2]—Radio Physics[2]—Radio Engineering[2]—Astrophysics[2]—Time and Frequency.[3]

THE INSTITUTE FOR MATERIALS RESEARCH conducts materials research leading to methods, standards of measurement, and data needed by industry, commerce, educational institutions, and government. The Institute also provides advisory and research services to other government agencies. The Institute consists of an Office of Standard Reference Materials and a group of divisions organized by the following areas of materials research:

Analytical Chemistry—Polymers—Metallurgy—Inorganic Materials—Physical Chemistry.

THE INSTITUTE FOR APPLIED TECHNOLOGY provides for the creation of appropriate opportunities for the use and application of technology within the Federal Government and within the civilian sector of American industry. The primary functions of the Institute may be broadly classified as programs relating to technological measurements and standards and techniques for the transfer of technology. The Institute consists of a Clearinghouse for Scientific and Technical Information,[3] a Center for Computer Sciences and Technology, and a group of technical divisions and offices organized by the following fields of technology:

Building Research—Electronic Instrumentation—Technical Analysis—Product Evaluation—Invention and Innovation—Weights and Measures—Engineering Standards—Vehicle Systems Research.

THE CENTER FOR RADIATION RESEARCH engages in research, measurement, and application of radiation to the solution of Bureau mission problems and the problems of other agencies and institutions. The Center for Radiation Research consists of the following divisions:

Reactor Radiation—Linac Radiation—Applied Radiation—Nuclear Radiation.

[1] Headquarters and Laboratories at Gaithersburg, Maryland, unless otherwise noted; mailing address Washington, D.C. 20234.
[2] Located at Boulder, Colorado 80302.
[3] Located at 5285 Port Royal Road, Springfield, Virginia 22151.

U.S. DEPARTMENT OF COMMERCE
C. R. Smith, Secretary
NATIONAL BUREAU OF STANDARDS
A. V. Astin, Director

Order all publications from the Superintendent of Documents
U.S. Government Printing Office, Washington, D.C. 20402.
Use of funds for printing this publication approved by the Director of the Bureau of the Budget (June 22, 1966).

JOURNAL OF RESEARCH of the National Bureau of Standards—A. Physics and Chemistry
Vol. 72A, No. 5, September–October 1968

Studies in Bomb Calorimetry. A New Determination of the Energy of Combustion of Benzoic Acid in Terms of Electrical Units

K. L. Churney and G. T. Armstrong

Institute for Basic Standards, National Bureau of Standards, Washington, D.C. 20234

(July 20, 1968)

The heat of combustion of NBS Standard Sample 39i of benzoic acid under standard bomb conditions has been determined in terms of electrical units. A value of $-26{,}434.0$ J g^{-1} was obtained. The total uncertainty in our determination is estimated to be ± 3.3 J g^{-1}. The uncertainty due to random errors was 1.7 J g^{-1} and is based on the appropriate factors for the Student t distribution at the 95 percent confidence limits for eleven determinations of the energy equivalent of the calorimeter and six determinations of the heat of combustion of benzoic acid. The principal systematic error, neglect of surface temperature correction for our calorimeter, has been assigned a value of ± 2.6 J g^{-1} until more reliable estimates of the correction can be made. Particular emphasis was placed on improving the precision of a calorimetric measurement over those previously obtained in this laboratory by the use of more sensitive auxiliary measuring equipment and more accurate procedures to evaluate the corrected temperature rise.

Key Words: Benzoic acid, heat of combustion; bomb calorimetry, procedures and errors; heat of combustion; bomb-calorimeter, electrical calibration; Dickinson calorimeter.

1. Introduction

Benzoic acid has served for many years as a reference material of known energy of combustion for calibrating bomb calorimeters. At the National Bureau of Standards (NBS), the Heat Division of the Institute for Basic Standards, or its predecessors, has certified the energy of combustion of various batches of benzoic acid in terms of electrical units for this purpose. Maintenance of a capability of a high degree of accuracy and precision in bomb calorimetry is a prerequisite for this certification activity.

The calorimetric measurements on which the certifications at NBS have been based have been made in most instances with a calorimeter of the same design, except for slight modifications, as that used by Dickinson [1].[1] In July of 1964, we started a study whose goal was to design a new bomb calorimeter capable of higher accuracy and precision than existing calorimeters. The first step in this project was a study of the performance of an existing Dickinson calorimeter (NBS 57662). The study was made in the hope that it would lead to a better understanding of the limitations inherent in the Dickinson calorimeter.

A second reason for making the study is that the last certification of benzoic acid in terms of electrical units at NBS was made in 1942 [2]. More recent certifications have been based upon intercomparison of benzoic acid samples. It appeared likely that a certification in terms of electrical units could now be made with greater accuracy than had been possible heretofore, because of the substantial improvement in the precision and accuracy of the auxiliary measuring instruments of the calorimetric station since 1942. Although there was no reason to suspect that the intercomparisons of samples had introduced undetected systematic errors in the certification of batches of benzoic acid, we wished to confirm the absence of such errors.

The general features of the calorimeter and its method of operation have been adequately described elsewhere [3, 4, 5]. A summary of pertinent details is given in sections 2 and 4.

The basis for the correction of the observed temperature rise of the calorimeter for the effects of heat transfer from its environment, Newton's cooling law, and of stirring energy is found in the discussion of Coops, Jessup, and Van Nes [4]. The particular method of calculation used in this work is described in section 5 in some detail because of the higher accuracy obtained by the use of fewer approximations.

[1] Figures in brackets indicate the literature references at the end of this paper.

Previous analysis of extensive calorimetric data from this laboratory had suggested that the uncertainty in our calorimetric measurements might be due mainly to the uncertainties in temperature measurements during the drift periods. Increasing the precision of the measurements of the resistance of the platinum thermometer led to a substantial improvement in the precision of measurement of the calorimeter temperatures but revealed the presence of small systematic deviations from Newton's cooling law. Modification of the calorimeter and our method of operating it suggested some possible explanations for these systematic deviations and reduced but did not entirely eliminate them as is discussed in sections 3, 5.1a, and 6.2.

A series of electrical calibrations to determine the energy equivalent of the calorimeter and a series of benzoic acid combustions to determine the energy equivalent, in terms of electrical standards, of the combustion of benzoic acid are described in sections 4 and 5. Presentation of the results is completed in section 6 by an analysis of random and systematic errors.

2. Experimental Apparatus

The calorimetric apparatus consists of a stirred-water calorimeter surrounded by an isothermal jacket. The calorimeter consists of a closed can which contains a stirrer, a platinum resistance thermometer placed near the can wall, a combustion bomb with fuse leads and handle, an electrical heater that fits snugly around the lower half of the bomb, and a weighed, fixed, quantity of water sufficient to be in contact with the calorimeter lid after the calorimeter has been assembled. The calorimeter temperature is always kept below that of the jacket.

2.1. Calorimeter and Jacket

The calorimeter and jacket are essentially the same as described previously by Jessup [6], except for the following modifications.

The calorimeter jacket has been enclosed by an air bath, kept near 27.5 °C with a regulation of ±0.2 °C by an on-off controller. The air bath was required to make sure the average jacket temperature did not change with time. Thermocouple measurements had shown the lid (i.e., top) of the jacket was about 0.006 °C colder than the rest of the jacket, presumably due to poor water circulation in the lid, when the room temperature was 3 °C below that of the jacket. The jacket temperature regulator was replaced by a commercially available proportional controller having reset action and a nickel resistance thermometer for a sensor.

To insure a constant stirring rate, the calorimeter stirrer was turned by a synchronous motor.

The oxygen combustion bomb and its internal fittings are those described previously [7], except for two changes. The fuses were made of 2 cm of 0.002-in-diam platinum wire rather than a combustible metal to eliminate any energy contribution due to fuse combustion as described by Prosen [5]. The stem of the bomb needle valve was modified so that the inside of the bomb could be directly connected to the pressure gage of the oxygen manifold during filling, for a more accurate pressure measurement.

The calorimeter heater is an improved version of a type described previously [8]. It consists of a 32-Ω heater element of glass-insulated, 0.010-in-diam Advance wire which was soft soldered at both ends to 18-gage, Formvar-covered, copper, current leads. The element was inserted in a 3/16-in-diam 0.030-in-wall, soft copper tube. The tube was flattened against the element after the space between the tube and element was filled with epoxy-resin cement. The tube (sheath) length was selected so that, after the heater was coiled to fit the bomb, at least 20 cm of each current lead of the heater element was inside the calorimeter. The length of each current lead between the calorimeter and jacket was 5 cm. Of the two 26-gage copper potential leads, one was attached to a current lead at the calorimeter boundary, the other to the remaining current lead at the jacket boundary.

Four jacket terminals pass through the jacket to "temper" thermally the heater leads (or fuse leads in the case of a benzoic acid combustion). They are the same as those described previously [9], except the electrical insulation was changed to a 0.008-in-thick layer of Teflon tape and epoxy-resin cement. The insulation resistance both from the heater element to its tube sheath and from the jacket terminals to the jacket wall is greater than 100 MΩ at 100 V.

2.2. Calorimeter Temperature Measurement Equipment

The platinum resistance thermometer is of the Meyers type of construction [10], having a 20-cm-long, 7-mm-diam Pyrex sheath, and an ice-point resistance of about 25.5 Ω. The resistance element is wound in a single coil very close to the glass sheath to provide fast response and to minimize self-heating. For these experiments the thermometer head was protected from thermal drafts by a cylindrical aluminum shield covered with asbestos and aluminum. The thermometer leads are connected to the bridge via a selector box. The thermometer was reproduceably inserted to a depth of 21 cm in the calorimeter can (height, 23 cm).

The sensitivity of the measurement of the change in resistance of the platinum resistance thermometer was increased from 10^{-5} Ω (10^{-4} °C) to 10^{-6} Ω (10^{-5} °C). This was accomplished by replacing the G–2 Mueller bridge (smallest dial unit 10^{-4} Ω) by a G–3 Mueller bridge (smallest dial unit 10^{-5} Ω) and using a more sensitive detector of the bridge imbalance.

The main features of the G–3 Mueller bridge are discussed briefly elsewhere [10]. Special shielding of the bridge and alteration of the heater supply for the bridge thermostat have been described previously [11].

Two galvanometer systems were used with the bridge. The new and more sensitive system consists of a photoelectric amplifier, having a taunt suspension galvanometer, and secondary galvanometer. A ½-mm deflection of the secondary galvanometer corresponded to a change in thermometer resistance of 1 $\mu\Omega$ (1×10^{-5} °C), with bridge current reversal and a thermometer current of 2 mA. The less sensitive galvanometer system, essentially the same as that described previously [12], but with a somewhat more sensitive galvanometer, was used to measure the thermometer resistance only during the rapid temperature rise of the main period of an electrical calibration experiment.

2.3. Ignition Energy Circuit

The electrical energy required for ignition of the benzoic acid pellet was determined by measuring the voltage before (about 25 V) and after (about 24 V) the discharge of a capacitor having a measured capacitance of $(40.6 \pm 0.5) \times 10^3$ μF. The circuit is similar to that described by Boyd [13].

The fraction of the energy released by the capacitor that is dissipated in the part of the circuit external to the calorimeter was 0.25 ± 0.10. The first step in determining this number was to measure the corrected temperature rise caused by 50 complete discharges of the capacitor, when a short was connected across the fuse electrodes in the bomb interior. The fraction of energy dissipated external to the calorimeter for this particular experiment was calculated using the known capacitance, voltages, etc. The fraction dissipated in actual combustion experiment was calculated by combining this data with the measured lead resistances and the resistances between the bomb fuse terminals in the actual combustion experiments. The main source of the estimated uncertainty in the fraction is the assumption that the combustion fuse resistance does not change before it melts.

2.4. Electrical Calibration Circuits

The basic circuit for supplying electrical power to the heater has been described elsewhere [4].

Two separate, commercially available, Zener-diode-stabilized, d-c power supplies were used to supply electrical energy to the heater. One unit, with a range of 0–2 A and 0–60 V and operated in the constant-voltage mode, was used to supply power at levels of 60 and 110 W to the heater. The other unit, having a range of 0–5 A and 0–105 V and operated either in the constant-current or constant-voltage mode, was used to supply power at 270 W. The stabilities of these power supplies in the constant voltage mode was 2 to 10 ppm as inferred from measurements of heater voltage.

The time interval during which power is supplied to the heater was measured with a time counter accurate to within ± 0.0001 s.

The heater current is determined by measuring the voltage across a Reichsanstalt-type, 0.01-Ω standard resistor.

The potential drop across the heater is determined with a 1:1000 nominal voltage divider or volt-box connected to the heater potential leads.

The resistive elements of the volt-box are: (a) a commercially available unit consisting of ten[2] equal 10,000-Ω resistors and two 1,000-Ω resistors hermetically sealed in an oil-filled box, and (b) a 100-Ω standard resistor. Permanent copper links connect the 10,000-Ω resistors in series with the parallel combination of one[3] 1,000-Ω resistor and the standard resistor. Movable shorting bars are used to connect the 10,000-Ω resistors in parallel with this combination. The bars are made from copper, have a 1-cm-square cross section, and mercury-wetted surfaces to make electrical connections.

The volt-box is calibrated by measuring the resistance of the 100–1,000-Ω parallel combination and then the resistance of all the resistors connected in parallel. In calculating the volt-box ratio, use is made of the fact that, because of the close matching of the 10,000-Ω resistors, the ratio of series to parallel resistance of the 10,000-Ω resistor set is equal to 100 : 1 within 1 ppm [14].

The imprecision of the volt-box ratio in 9 determinations made during the course of the electrical calibrations was 0.6 ppm (standard deviation of a single determination). This is approximately the a priori estimated precision of a measurement. The inaccuracy was estimated to be between 2 and 10 ppm.

Potential measurements were made to 0.03 μV with a six-dial double potentiometer using the more sensitive of the two galvanometer systems described in section 2.2. The range of the potentiometer extends to 0.111111 V in steps of 0.1 μV. The potentiometer voltage reference consisted of three saturated, Weston standard cells mounted in an improved version of a constant temperature box similar to one described previously [15]. Since both short- and long- (3 months) term temperature regulation of the box, as indicated by a platinum resistance thermometer in the cell compartment, was within ± 0.001 °C, the standard cell voltage could be assumed to be constant to better than 1 ppm during the course of the electrical calibrations (see sec. 5.3). The potentiometer interdial corrections were determined in the laboratory before and after the set of electrical calibration experiments. The potentiometer ratio was checked more frequently using an auxiliary circuit similar to that described elsewhere [16]. Its constancy, based on eleven determinations during the course of the electrical calibrations, was 1 ppm (standard deviation of a determination).

The resistors of the auxiliary circuit and the volt-box as well as the standard current resistor were kept in a stirred-oil bath whose temperature was kept within 0.01° of 33.16 °C. At this temperature, the rate of

[2] The relative equality and stability (1 yr) of the resistors are ± 0.0015 percent and ± 0.0005 percent, respectively.

[3] The other 1,000-Ω resistor is used only when a volt-box ratio of 1:100 is required.

change of the resistances with temperature is extremely small. Because of the constancy of the bath temperature, the resistance of the resistors could be assumed to be constant to better than 1 ppm during the electrical calibration experiments.

The resistance ratios required in the calibration of the volt-box and potentiometer were measured with the Mueller bridge described in section 2.2.

2.5. Oxygen Handling Equipment

The oxygen manifold and associated purification equipment are essentially as described by Jessup [3]. A high-purity grade of commercially available oxygen [4] was further purified for use in the benzoic acid combustions. The final oxygen pressure is measured to 0.01 atm on a calibrated Bourdon pressure gage. The temperature of the oxygen in the bomb is measured to the nearest 0.1 °C with a calibrated mercury thermometer inserted in a brass cup that fits snugly around the bomb while the bomb is being filled.

3. Tests of the Apparatus

Numerous measurements of the variation of the thermometer resistance with time during drift periods not associated with the principal calorimetric measurements showed that the imprecision of the measurements, as indicated by the average deviation of the observations from the best smooth curve drawn through the data, could be reduced to a few microohms. This was done by making resistance measurements at 1 min intervals with the bridge commutator set in alternately the N and then (i.e., next minute) in the R positions. Bridge current reversal and interpolation to 10^{-6} Ω were made in the usual manner [17]. The effect of the time variation in the lead resistance was eliminated by calculating the resistance $R(t)$, at any time t, from the observed readings, adjusted for interdial corrections, $R'(t)$, $R'(t-1)$, $R'(t+1)$ according to eq (1).

$$R(t)=\frac{R'(t-1)}{4}+\frac{R'(t)}{2}+\frac{R'(t+1)}{4}. \qquad (1)$$

Proper operation of the bridge commutator was critical in making these more precise measurements. This required replacing the mercury in the switch every three to six experiments and periodic reamalgamation of switch contacts.

Small systematic deviations of the best smooth curves drawn through the values of $R(t)$ from the resistance-time curves predicted by Newton's cooling law were observed. The shape of these deviation curves differed. A study of possible causes of the deviations was inconclusive. The changes in the calorimeter jacket, calorimeter stirrer motor, and the thermal shielding of the thermometer head, mentioned in section 2, reduced but did not completely eliminate the deviations.

The stirring of the calorimeter was varied in order to test the possible effect of variation of the heat generated by stirring as a source of deviations. Although the study of this factor was incomplete, we found no clear evidence to indicate that random fluctuations of the energy of stirring of the water might cause deviations either when the stirrer was operated intermittently or when the stirrer was turning at a constant rate. The installation of a synchronous motor to turn the calorimeter stirrer was made to insure a constant rate. We did obtain some results suggesting that actual misalinement or flutter in the stirrer shaft might be a source of deviations.

To test the applicability of Newton's cooling law over a wider range of temperature than usually occurs in a drift period (0.01 °C or less), the average rate of change of the resistance of the thermometer was measured at six calorimeter temperatures below that of the jacket, 12 to 19 resistance measurements were made at each calorimeter temperature by the procedure given above. Resistances were averaged according to eq (1). The drift rate, $\Delta R(t)/\Delta t$, corresponding to a selected thermometer resistance, $R_S(t)$, was determined from the best straight line passing through the first order differences plotted as a function of time. The number of values of $R(t)$ at each calorimeter temperature, the value of $R_S(t)$, $\Delta R(t)/\Delta t$ for the selected values of $R(t)$, and the estimated average deviation of the first order differences from the straight line are given in columns 1, 2, 3, and 4 of table 1.

TABLE 1. *Calorimeter drift rate as a function of calorimeter temperature*

No. of values of $R(t)$	$R_S(t)$	$\Delta R(t)/\Delta t$, Ω × 10^6 min^{-1}		
		"Obs"	Av. dev.	"Obs"–"Calc." [a]
10	28.00717	568.7	0.5	−0.8
17	28.06315	460.7	0.7	+0.7
13	28.11692	355.0	0.6	+0.2
11	28.16559	260.0	0.7	+0.4
15	28.21188	169.0	0.4	0.0
13	28.25985	74.7	0.5	−0.5

[a] $\left(\frac{\Delta R(t)}{\Delta t}\right)_{calc} = 1956.35\ (28.29828 - R(t))$.

It may be shown that, if Newton's cooling law holds, $\Delta R(t)/\Delta t$ should be a linear function of $R(t)$ with an error of less than 3×10^{-8} Ω min^{-1} in $\Delta R(t)/\Delta t$ for our calorimeter and resistance thermometer. The differences between the "observed" values and those calculated from a least squares fit of the data, assuming that $R(t)$ has negligible error in comparison to $\Delta R(t)/\Delta t$, are given in column 5 of table 1. The root mean square deviation, 0.5×10^{-6} Ω min^{-1}, is substantially smaller than the value of 3.3×10^{-6} Ω min^{-1} obtained previously by Jessup [18]. Some of the differences is due to the lower sensitivity of Jessup's resistance measure-

[4] Supplier's impurity analyses were 10.0, 84.0, 0.18, and 15.9 molar ppm for argon, nitrogen, water, and methane, respectively.

ment (10^{-5} Ω) and some is due to the averaging effect of eq (1).[5] In any event, the random deviations from Newton's cooling law appear to be substantially less than those obtained previously. This is consistent with an improvement in the calorimetric measurements which is discussed further in section 6.1.

A summary of the magnitudes and types of deviations from Newton's cooling law during drift periods of the calorimetric measurements themselves is given in section 5.1.

4. Experimental Procedures

4.1. Benzoic Acid Combustions

The general experimental procedure involved in a benzoic acid experiment closely follows that given by Jessup [19]. Significant differences are given below.

The benzoic acid received no special treatment prior to the experiment but was used as it came from the bottle of NBS standard sample 39i. Pellets of 1.51 ± 0.015 g were prepared and accurately weighed after ½-hr temperature equilibration in a platinum crucible in a balance having a readability of 1 μg.

After the bomb was filled to a pressure of 30 atm of oxygen, 15 to 20 min were allowed to elapse, to ensure temperature equilibration of the bomb and oxygen, before the final pressure and temperature were read.

The temperature of the calorimeter jacket was determined by measuring the resistance of the platinum resistance thermometer to ± 10 μΩ as originally described in section 3 using bridge-current reversal.

Fifteen to 20 min after the calorimeter had been heated to a temperature about 3 °C below that of the jacket, measurements of calorimeter temperature were started. The preliminary calorimeter-temperature measurements with lower sensitivity were essential to establish the values of the drift rate and the differences between the readings with the commutator in the N and R positions as a preliminary step to the much more difficult measurements to follow. After 5 to 10 min of these readings, the galvanometer sensitivity was increased to permit measurements to ± 1 μΩ, and these more precise measurements were carried out for an initial period of at least 12 min.

One minute after the final resistance measurement of the initial period, the fuse was ignited by discharging the capacitor and initial and final capacitor voltages were noted. Time-temperature measurements during the rapid temperature rise of the main period were made with the thermometer current reduced from 2 mA to 0.6 mA.

After the change in thermometer resistance was less than 0.002 Ω min^{-1}, resistance measurements at one minute intervals were resumed with alternate N and R commutator positions at a sensitivity of ± 10 μΩ. Measurements to ± 1 μΩ sensitivity were started after the drift decreased to 0.000200 Ω min^{-1} and continued through the remainder of the main period (defined to end 20 min after ignition) and a final period of at least 12 min. The jacket temperature was then remeasured as before.

Table 2 illustrates a typical set of resistance and time measurements made during a combustion experiment. The letters N and R refer to the bridge commutator settings. Columns labeled average resistance are values of $R(t)$ calculated by eq (1) using uncorrected rather than corrected dial readings. The course of the experiment with time can be readily followed by reference to table 2 while reading the foregoing text.

TABLE 2. *Observations of time and thermometer resistance during a combustion experiment*

Time	Resistance minus 28.0		Average resistance minus 28.0	Drift
	N	*R*		
Min	*Ohms*	*Ohms*	*Ohms*	*Ohms min⁻¹ × 10⁶*
0	0.18169			
1		0.18241		
2	.18296			
3		.18368		
4	.18422			
5		.18494		
6	.185487			
7		.186196		
8	.186747		0.186785	
9		.187451	.187412	627
10	.188000		.188037	625
11		.188698	.188661	624
12	.189246		.189283	622
13		.189943	.189906	623
14	.190492		.190527	621
15		.191183	.191148	621
16	.191733		.191769	621
17		.192427	.192389	620
18	.192967		.193005	616
19		.193660	.193622	617
20	.194199		.194235	613
21		.194882	.194849	614
22	.195434		.195465	616
23		.196110	.196076	611
24	.196659		.196686	609
25		.197330		
26	Ignition			
26.2892	.20			
26.4802	.21			
26.5710	.24			
26.6511	.26			
26.7207	.28			
26.7993	.30			
26.8762	.32			
26.9740	.34			
27.0828	.36			
27.2201	.38			
27.3731	.40			
27.4658	.41			
27.5742	.42			
27.7227	.43			
27.8993	.44			
28.1146	.45			
28.2697	.455			
28.4495	.460			
28.6790	.465			
29.0040	.470			
29.1801	.472			
29.3914	.474			
29.6697	.476			
29.8461	.477			
30.0682	.478			
30.2112	.4785			
30.3543	.4790			
30.4885	.4795			
30.7058	.4800			
30.9726	.4805			
31.1630	.4808			
31.4654	.4812			
32	.48175			
33		0.46220		
34	.48241			
35		.482614		

[5] See section 5.1a.

TABLE 2. *Observations of time and thermometer resistance during a combustion experiment*—Continued

Time	Resistance minus 28.0		Average resistance minus 28.0	Drift
	N	*R*		
Min	*Ohms*	*Ohms*	*Ohms*	*Ohms min*$^{-1}$ × 10^6
36	.48258+			
37				
38	.482684			
39		.482830		
40	.482769			
41		.482915	0.482863	
42	.482854		.482906	43
43		.483000	.482948	42
44	.482938		.482989	41
45		.483080	.483031	42
46	.483024		.483074	43
47		.483166	.483116	42
48	.483107		.483158	42
49		.483250	.483200	42
50	.483192		.483241	41
51		.483331	.483282	41
52	.483274		.483323	41
53		.483413	.483364	41
54	.483355		.483405	41
55		.483496	.483446	41
56	.483437		.483488	42
57		.483580	.483530	42
58	.483522		.483572	42
59		.483664	.483613	41
60	.483603		.483654	41
61		.483746	.483695	41
62	.483684		.483736	41
63		.483830	.483778	42
64	.483769		.483819	41
65		.483908	.483859	40
66	.483852		.483900	41
67		.483989	.483941	41
68	.483934		.483983	42
69		.484076	.484025	42
70	.484013			

4.2. Electrical Energy Measurements

Much of the experimental procedure was similar to that outlined for the chemical heat measurements in the previous section. The procedure for making the electrical calibration measurements is essentially that outlined previously [4, 2].

The combustion bomb was prepared without a pellet or platinum fuse but contained the usual platinum crucible and the usual amounts of oxygen and water.

Just prior to a run, the temperature of the standard cell enclosure was measured. The emfs at the output leads of the volt-box and the 0.01-Ω standard current resistor were measured before and after a run when no power was supplied to the heater to obtain values of the residual (thermal) emf of the circuit.

Thermometer-resistance measurements during the rapid temperature rise (i.e., while the electrical power was on) of the main period were made in the same manner as in the benzoic acid experiments. Measurements of the potentials at the output of the volt-box and across the current resistor which were 0.054 and 0.018 V, respectively, for the 110 W calibration experiments were made between temperature measurements. (The time of each potential measurement was differentiated from those of the main period temperatures by actuating the timer-printer with the standard second signal to record two times, exactly 1 s apart, which bracketed the time of the corresponding measurement.) In this way it was possible to obtain up to eight measurements of both the heater current and voltage during a 5 min heating period.

At frequent intervals during the course of the calibration experiments, the volt-box was calibrated, the potentiometer ratio was determined, and the constancy of the resistance of the 0.01-Ω standard resistor was checked.

5. Calculation of Results of Calorimetric Experiments

A series of 6 benzoic acid combustion experiments and then a series of 16 electrical calibration experiments were carried out. The electrical calibration experiments are separated into three groups depending upon whether the amount of power supplied to the calorimeter heater was approximately 110, 60, or 270 W.

5.1. Calculations of the Corrected Temperature Rise

Values of corrected temperature rises are listed for the appropriate experiments in tables 3 and 4. Observed temperature rises were of the order of 2.82 °C, and the correction due to heat transfer between the calorimeter and jacket was about 1.5 percent of this value.

a. Treatment of Initial and Final Period Data

The observed readings of the bridge during the initial and final periods, illustrated in table 2, were converted to ohms by applying the various bridge corrections and then averaging according to eq (1). Temperatures corresponding to each $R(t)$ were calculated by the Callendar equation [10]. The parameters in this equation that are characteristic of our thermometer were determined by the Temperature Section of the Heat Division, NBS.

The calorimeter temperatures, $\theta(I, J)$, for the initial ($I=0$) and the final ($I=1$) drift periods were fitted to the integral form of Newton's cooling law, eqs (2).

$$\theta(I, J) = C(I) + D(I) \cdot P(J) \tag{2a}$$

$$P(J) = (1 - e^{-KJ})K. \tag{2b}$$

In eq (2), $C(I)$ and $D(I)$ are different constants for each drift period, J is the time of occurrence of the temperature relative to the start of the appropriate drift period, and K, the cooling constant of the calorimeter, is defined by eq (3).

$$K = [D(0) - D(1)]/[C(1) - C(0)]. \tag{3}$$

A consistent fit of the temperature-time data by eqs (2) and (3) was started by estimating values of $C(I)$, $D(I)$, and K from the first and last datum points of each drift period. Calculation of "improved" values

TABLE 3. *Benzoic acid combustion calculations*

Expt. No.	Mass	$F \times 10^6$	$\Delta\theta$	$m_s(1+F)/\Delta\theta$	E^1 (cont)	ΔE_{IGN}	$-\Delta E$ (HNO_3)	A*	$\frac{E \text{ (cal)}}{(-\Delta E_B)}$
	g		°C	g °C^{-1}	J °C^{-1}	J	J	(g °C^{-1}) $\times 10^6$	g °C^{-1}
1	1.523394	−189.8	2.849658	0.5344869	+1.43	+1.49	+0.49	−27.8	0.5344591
2	1.507283	−166.7	2.819376	0.5345267	+1.79	+1.60	+0.52	−39.3	0.5344874
3	1.492242	−166.9	2.791449	0.5344869	+1.80	+0.93	+0.70	−46.0	0.5344409
4	1.493978	−160.8	2.794708	0.5344880	+1.88	+1.23	+0.58	−46.6	0.5344414
5	1.525560	−157.2	2.853627	0.5345198	+1.93	+1.21	+0.58	−46.3	0.5344705
6	1.501083	−180.8	2.807857	0.5345043	+1.57	+1.38	+0.52	−33.8	0.5344705

Average..... 0.5344616
Std. dev. of experiment..... 0.0000183(0.0034%)
Std. dev. of mean..... 0.0000075(0.0014%)

* $A = \left[\frac{\Delta E_{IGN} - \Delta E\ (HNO_3)}{(+\Delta\theta)} - E^1\ (\text{cont})\right] \frac{1}{(-\Delta E_B)}$

TABLE 4. *Calculation of the energy equivalent of the calorimeter*

Expt. No.	$\int_0^T E_T E_T dt$ (p^2 s) $\times 10^{+3}$	$(F_2/F_1)\int_0^T E_c^2 dt$ (p^2 s) $\times 10^{+3}$	Q_T/F_1 (p^2 s) $\times 10^{+3}$	Q_r J	$\Delta\theta$ °C	$-E^1$ (cont) J °C^{-1}	E (cal) J °C^{-1}
Heater power 110 W							
7	3550.0634	1.1258	0.0377	38,955.397	2.757342	0.30	14,128.18
8	3559.4812	1.1288	.0377	39,058.739	2.764372	0.32	14,129.66
9	3615.7432	1.1467	.0378	39,676.104	2.808623	0.39	14,126.92
10	3605.5325	1.1434	.0378	39,564.063	2.800523	0.02	14,127.40
11	3585.7557	1.1372	.0378	39,347.050	2.785424	0.20	14,126.25
12	3591.6315	1.1390	.0378	39,411.526	2.789739	0.16	14,127.48
13	3578.4748	1.1348	.0378	39,267.158	2.779515	0.16	14,127.50
14	3591.6153	1.1390	.0378	39,411.348	2.789528	0.14	14,128.46
15	3588.6870	1.1381	.0378	39,379.216	2.787293	0.14	14,128.26
Heater power 60 W							
16	3575.0618	1.1342	0.0069	39,229.362	2.776922	0.07	14,126.99
17	3573.4132	1.1337	.0070	39,211.273	2.775357	0.07	14,128.44
Heater power 270 W							
18*	3582.3243	1.1348	7.3177	39,389.320	2.788869	0.13	14,123.89
19*	3548.3917	1.1240	7.3241	39,017.047	2.762050	0.13	14,126.25
20*	3506.1535	1.1107	7.2380	38,552.619	2.729664	0.16	14,123.74
21*	3588.2289	1.1368	7.2382	39,453.237	2.792813	0.16	14,126.86
22	3612.1828	1.1440	0.0208	39,636.866	2.805518	0.19	14,128.36

*Constant current mode of power supply; all others constant voltage mode.

of these constants proceeded by computing the deviations, $F(I, J)$, of the "observed" temperatures from those calculated by eq (2) using the initial estimates of $C(I)$, $D(I)$, and K. These deviations were fitted by least squares with deviation equations linear in $P(J)$ according to eq (4).

$$F(I, J) = B(0, I) + B(1, I)P(J). \tag{4}$$

The values of $B(0, I)$ and $B(1, I)$ were used to correct the initial estimates of $C(I)$, $D(I)$, and K. The cycle of calculations, performed by a high speed digital computer, was repeated until either the sum of the squares of the deviations of the initial and final drift periods increased or the values of K calculated on two successive cycles differed less[6] than 1×10^{-7} min^{-1}.

[6] The latter "stop" was inserted because there is no assurance of a distinct minimum in the sum of the squares of the deviations. It was, in fact, the terminating step of all the calculations after two or three iterations. The value of 1×10^{-7} min^{-1} is based on the fact that the jacket temperature was constant to only about 1×10^{-4} °C, and K is approximately 2×10^{-3} min^{-1}.

The observed temperature rise was computed from the calculated values of initial and final temperatures using eqs (2) and the final values of $C(I)$, $D(I)$, and K.

This method of curve fitting assumes the values of $\theta(I, J)$ of each drift period are independent which cannot be so since the temperatures are calculated from observed resistances which were averaged according to eq (1).

It can be shown that, because of the use of eq (1), runs or deviations of the same sign should occur when the difference between "observed" and calculated temperatures are plotted as a function of time even though the errors are random. Usually, runs of three to five deviations of the same sign were observed. This indicates that in the case of random errors, those in the resistance measurements predominate. The systematic errors in the values of "observed" temperature and the calculated temperatures caused by using eq (1) are negligible.

Although the deviation plots sometimes showed systematic deviations from Newton's cooling law, they

were small. The average root mean square deviation of "observed" from calculated values of $\theta(I, J)$ was slightly less than 2×10^{-5} °C.

b. Treatment of Main Period Data

The correction to be added to the observed temperature rise due to heat transfer from the jacket and stirring energy is calculated according to a method discussed by Dickinson (see [20, 4]). In this method, the main period data is used to evaluate the parameter t_x, defined by eq (5), and the remaining parameters are determined from the values of $C(I)$, $D(I)$, and K determined from the drift period data in section 5.1a.

$$t_x = t_f - \frac{1}{(\theta_f - \theta_i)} \int_{t_i}^{t_f} (\theta - \theta_i) dt. \tag{5}$$

In eq (5), θ_i and θ_j are the temperatures at the beginning, t_i, and end, t_f, of the main period, respectively.

To keep the error in the calculation of the correction to the observed temperature rise to 1×10^{-5} °C in our experiments, t_x must be calculated to 0.1 s and the integral in eq (5) must be calculated with an accuracy of 1 part in 10,000. The following two procedures were adopted to minimize the calculation error.

First, the temperature-time data were graphed to eliminate gross errors and fill in gaps where data was sparse by superimposing corresponding portions of the main period of similar experiments.

Second, because eq (5) may be rewritten with an integral whose integrand is independent of temperature, temperatures of the main period were calculated in the same manner. Since virtually all the resistance measurements during the rapid temperature rise were made with fixed commutator position, the formula for the estimated correction for thermometer lead resistance applied to these readings was used throughout the main period. Thus, although the method of calculation of temperatures was in other respects the same as that for the initial and final periods, θ_i and θ_f in eq (5) are not quite the same as those used in calculating the observed temperature rise. We assumed the thermometer lead resistance correction varied linearly with the thermometer resistance in the main period from the average initial to the average final drift correction. Since the difference between these corrections was about 15 $\mu\Omega$ for all the experiments, the net effect of an error in the assumption is negligible in comparison to other errors in the treatment of the data of the main period.

The integral in eq (5) was evaluated using the spline numerical integration procedure whose characteristics are described in detail elsewhere [21]. Essentially, the method fits a piecewise cubic with continuous first and second derivatives to the data. Calculations were carried out with a high speed computer using a program written in the Dartmouth BASIC language [22]. This program was based on a subroutine originally written in FORTRAN [23].

5.2 Benzoic Acid Combustion Calculations

Since benzoic acid is certified as a secondary heat standard for use in determining the energy equivalent of bomb calorimeters, it is convenient to express its energy of combustion per unit mass of benzoic acid under so-called standard bomb-conditions [4]. Determination of the energy of combustion of benzoic acid under standard bomb conditions, ΔE_B, is carried out in two steps, the first of which is summarized in this section.

In order to compare the benzoic acid combustion data with the electrical calibration data, we defined the standard calorimeter to be the calorimeter can containing sufficient water so that their combined weight is 3750 g, the calorimeter lid, the electrical heater, and the combustion bomb with its standard contents, its external fuse leads and its handle. The standard bomb contents were defined to be 1 g of water, the platinum crucible, platinum fuse, and 0.441 moles of oxygen (30 atm at 25 °C).

By selecting the temperature to which the isothermal bomb process is referred to be the final temperature the calorimeter would have if the heat transfer from the calorimeter environment and stirring energy were zero, the ratio of the energy equivalent of the standard calorimeter, E(cal), in joules per degree, to ΔE_B, in joules per gram, can be calculated from the experimental results by eq (6) (see [20], [5]).

$$\frac{E\,(\text{cal})}{-\Delta E_B} = \frac{(1+F)m_s}{\Delta\theta} + \left[\frac{\Delta E_{\text{IGN}} - \Delta E_{\text{HNO}_3}}{(\Delta\theta)} - E^i\,(\text{cont})\right] \frac{1}{(-\Delta E_B)}. \tag{6}$$

In eq (6), $\Delta\theta$ is the corrected temperature rise, m_s is the mass (i.e., weight in vacuo) of benzoic acid in grams, ΔE_{IGN} is the electrical energy supplied to the calorimeter to ignite the benzoic acid, ΔE_{HNO_3} is the energy of formation of nitric acid produced in the actual combustion reaction, and E^i (cont) is the correction added to E(cal) to give the energy equivalent of the actual calorimeter prior to sample combustion. The quantity F is related to the energy of combustion, $\Delta E_B'$, per gram of benzoic acid under actual bomb conditions by eq (7).

$$\Delta E_B' = (1+F)\Delta E_B \tag{7}$$

Numerical values of F were calculated from the approximate formula given by Coops, Jessup, and Van Nes [4].

Since the second term on the right-hand side of eq (6) constitutes only a small contribution to the total, an approximate value of ΔE_B may be used in this term. For this we used $-26{,}434$ J g^{-1}. An error of 10 J g^{-1} in this value of ΔE_B would produce an error of only 1 ppm in $-E(\text{cal})/\Delta E_B$.

A summary of the calculations is given in table 3. In calculating F (col. 3), the pressure of oxygen at θ_h was calculated from observed pressures using the equation of state for oxygen given by Coops, Jessup, and Van Nes [4]. E^i(cont), listed in column 5, was evaluated using 1.21 J g^{-1} $°C^{-1}$ [4] for the heat capacity of benzoic acid and a value of 21.17 J mol^{-1} [20] for the constant volume heat capacity of oxygen at 30 atm. Measurement of ΔE_{IGN} is summarized in section 2.3 and the determination of $\Delta E(HNO_3)$ was made in the usual manner [4].

More accurate values of F were calculated by evaluation of the Washburn correction by the procedure described by Hubbard, Scott, and Waddington [20] using the computer program developed by Shomate [24]. A very slight difference was observed in the F values, for which a correction is made in the calculation of $(-\Delta E_B)$ at the bottom of table 5. (The dispersion of the values of $E(\text{cal})/(-\Delta E_B)$ was not altered significantly.)

5.3. Electrical Calibration Calculations

The energy equivalent of the calorimeter, E(cal), is related to the total electrical energy, Q_e, supplied to the calorimeter during a calibration experiment, by eq (8)

$$Q_e = [E(\text{cal}) + E^i(\text{cont})]\Delta\theta. \tag{8}$$

In eq (8), $\Delta\theta$ is the corresponding corrected temperature rise and E^i(cont) was defined in section 5. Q_e was evaluated by eq (9)

$$Q_e = F_1 \int_0^T E_V E_I dt - F_2 \int_0^T E_I^2 dt + Q_T. \tag{9}$$

In eq (9) the various terms on the right are, respectively, the energy calculated from the potentiometer measurements, the correction for current passing through the volt-box, and correction for transients (i.e., any voltages not measured with the potentiometer). E_V and E_I are the observed dial readings of the potentiometer at the output of the volt-box and across the current resistor, respectively after applying interdial and "zero" corrections. T is the length of time power is supplied to the heater. F_1 and F_2 are constants which depend upon the volt-box ratio, resistance of the current resistor, the standard cell voltage, and the calibration of the potentiometer.

The numerical values of the terms on the right of eq (9) divided by F_1 are given in the first three columns of table 4. The unit p in these tables stands for a "potentiometer unit" and is nominally 1 V. The values of Q_e, $\Delta\theta$, E^i(cont), and E(cal) are listed in the remaining columns of table 4.

Because of the constancy of the volt-box and potentiometer ratios and the inferred constancy of the standard current resistor and standard cell voltage to 1 ppm or better, F_1 and F_2 were assumed to be constants. This assumption causes negligible imprecision in E(cal) as compared to that from other sources. The numerical values of F_1 and F_2 are 1.09765196 $V^2\Omega^{-1}p^2$ and 1.099975×10^{-4}, respectively.

The standard cell voltage was determined by the NBS Electrochemistry Section of the Electricity Division by comparison with the NBS voltage standard. A correction of 1.4 microvolts [25] was added to this calibrated value since the average temperature of the cells during our measurements was 0.024 °C less than at the time the cells were calibrated.

The resistance of the standard current resistor was based on its certified resistance at 25 °C and the temperature coefficient of its resistance as determined by the supplier. The maximum error in this calculated value of resistance at the oil bath temperature (33.16 °C), as determined by ten potentiometric comparisons during the electrical calibration experiments of its resistance with that of a standard 0.1 Ω resistor calibrated by the NBS Resistance and Reactance Section, was found to be 0.002 percent or less. After our measurements were completed, a more accurate value for the resistance was determined by the NBS Resistance and Reactance Section. The corresponding correction to the data was made in the final calculation of $(-\Delta E_B)$ in table 5.

The first potentiometer measurements were made some 10 to 25 s after power was applied to the calorimeter heater. A total of 6, 13, and 2 measurements of E_V or E_I were made for the 110, 60, and 270 W experiments, respectively. Smoothed values of E_V and E_I were obtained from separate plots of the observed values as a function of time; the time dependence, more or less unknown, of the 270 W measurements had to be inferred from other considerations [26]. Values of the integrals in eq (9) were computed with the spline integration subroutine of the computer program used in the calculation of the integral in eq (5).

After the electrical calibrations were completed it was found that large voltage transients occur when the power source supplying 270 W to the calorimeter heater in the constant current mode is switched from the dummy heater to the calibration circuit. These transients had disappeared well before the first measurements of E_V and E_I were made with the potentiometer. Subsequent examination of the voltage-time characteristics of this power source in the constant voltage mode and of the power source used to supply 110 and 60 W to the calorimeter heater in the constant voltage mode also indicated the presence of transients, but these were much smaller.

Numerical values of the energy supplied to the calorimeter by these transients are based on separate determinations of the transient voltage-time curves, as observed on an oscilloscope, for the power supplies operated in the appropriate mode of operation. Corrections to account for the slightly different average values of power supplied to the heater in the actual electrical calibrations were made assuming the length of time required to switch the power supply from the dummy to the calorimeter heater was constant.

TABLE 5. *Summary of calculation of* $(-\Delta E_B)$

Expt. No.	Number of expts.	Heater power	Average E(cal), J °C^{-1}	Standard deviation of an experiment, J °C^{-1}	Standard deviation of average, J °C^{-1}	95% confidence limits J °C^{-1}
7–15	9	110 W (constant voltage	14,127.79	0.99 (0.007%)	0.33	0.76
16–17	2	60 W (constant voltage)	14,127.72	0.99	0.73	1.60
18–21	4	270 W (constant current)	14,125.19	1.6	0.80	2.55
22	1	300 W (constant voltage)	14,128.36	.....	.....	.....
Adopted value			14,127.79	0.99 (0.007%)	0.30	0.68

Summary of benzoic acid combustions

Expt. No.	Number of expts.	Average	E(cal)/$(-\Delta E_B)$, g °C^{-1}	Standard deviation of an experiment, g °C^{-1}	Standard deviation of average, g °C^{-1}	95% confidence limits g °C^{-1}
1–6	6	.....	0.534461.6	(0.0034%)	0.0000075	0.0000193

Calculation of $-\Delta E_B$

Nominal $(-\Delta E_B)$	26,433.69 J g^{-1}
Correction for $R_{0.01}$	+0.21 J g^{-1}
Correction for F	+.15 J g^{-1}
Corrected $(-\Delta E_B)$ =	26,434.05 J g^{-1}
with an uncertainty interval (random) of	1.7 J g^{-1}

5.4. Summary of results

The calculations of the energy equivalent of the calorimeter are summarized at the top of table 5. Ninety-five percent confidence limits are calculated by multiplying the standard deviation of the mean by the appropriate factor of the Student t-distribution. Assuming equal precision, standard deviations computed for experiments 7–15 and for 16–17 are pooled together. Comparison of the average values of E(cal) listed in table 5 for the three heater powers used in experiments 7 through 21 show they lie within their combined uncertainty (random) intervals. However, the results of experiments 18–22 were not used in computing a weighted average for E(cal) for the following two reasons.

First, it will be noted from columns 2 and 4 of table 4 that the contribution of Q_T to E(cal) is 0.2 percent in the case of experiments 18–21. For the other experiments, the power supplies were operated in the constant voltage mode and the contribution of Q_T to E(cal) is less than 0.0012 percent. Since we feel that a systematic error in the estimate of Q_T of 20 percent is not unreasonable, the difference between the average E(cal) of experiments 18–21 and the remainder is probably caused by a systematic error due at least in part to the error in Q_T.

Second, it will be noted that experiments 18–22 were carried out with the highest heater power and, thus, the shortest time necessary to warm the calorimeter 3 °C. This resulted in the unfortunate situation that we were able to make only a few measurements of heater current or voltage when the change in voltage, or current, was the most rapid. We feel the uncertainty introduced in E(cal) by the uncertainty in our estimates of the time dependence of the voltage, or current may be appreciable. Thus, the agreement of experiment 22 with 7–17 is regarded as being somewhat fortuitous. Experiment 22 was given zero weight on the basis that we suspect its uncertainty is considerable larger than experiments 7–17.

The results of the benzoic acid combustions and the value determined for ΔE_B for benzoic acid are summarized at the bottom of the table 5. The precision of ΔE_B was calculated as suggested by Rossini [27]; the contribution of the imprecision due to the various factors taken as constants in determining E (cal) was neglected since it was estimated to be 10 ppm.

6. Appraisal of Experimental Results

6.1. Random Errors

The standard deviation of a single combustion experiment with this particular calorimeter had never before been lower than 0.012 percent, for an extended series of measurements. It is clear from table 5 that the precision of the present measurements is substantially better than the previous work.

We were particularly interested to see whether or not we could account for the standard deviation of a measurement of either $-E$(cal)/ΔE_B or E(cal) in terms of the various factors we might expect to vary from experiment to experiment.

Common to both sets of measurements were the uncertainty in the corrected temperature rise and the absence of a buoyancy correction to the weight of the water placed in the calorimeter can.

The uncertainty in the corrected temperature rise was evaluated from the variances of the estimates of the various parameters appearing in eqs (2) and (3), using the usual propagation of error formulas [27] and assuming that the "average" root mean square deviation of $\theta(t)$ for the initial and final drift periods

may be treated as a random error. These "averages" were arbitrarily multiplied by $\sqrt{2}$ since they are probably too small due to the use of eq (1) (see sec. 5.1a). The error in the integral in eq (5) was based on the approximations that the main error is contributed by the errors in the times recorded during the rapid temperature rise of the main period and that the integral may be computed by the trapezoidal rule.

The uncertainty due to the absence of the buoyancy correction in the calorimeter weight was estimated from the known variation in air density during the benzoic and experiments (12 mg/l [7]) and the approximate volume of the calorimeter can plus water (2.59 l). The resulting percentage error was arbitrarily multiplied by two because it is quite evident from the method used to adjust the weight of water in the can (see [3]) that the aforementioned variation in air density is a minimum estimate. Other factors, such as convection currents, may also make a substantial contribution to the weighing error.

The random error in $E(\text{cal})/\Delta E_B$ due to the uncertainty of the mass of the benzoic acid sample is based on a conservative estimate of ± 10 μg for a sample weight of 1.5 g.

The estimates of the varous errors contributed by the parameters which make up F_1 are based on the deviations of their measurements. The standard current resistor, $R_{0.01}$, was assumed to have a stability of 2 ppm.

The estimate of the random error in E(cal) due to the random error in the integrals in eq (9) was based on the approximation that 13 smoothed pairs of values of E_V and E_I separated by 30 s time intervals were numerically integrated by the trapezoidal rule. The errors in the smoothed values of E_V and E_I were taken as $\pm 2 \times 10^{-7}$ potentiometer units.

The estimate of the random error due to the heater leads is based on the analysis given by Ginnings and West [28]. The dimensionless parameters L_s and L_c of that analysis were calculated to be 0.34 and 0.28, respectively. The variation in the heater lead resistance was estimated to be ± 0.002 Ω; the heater resistance is 32 Ω.

A summary of the errors and a comparison with the observed standard deviation of an experiment is given in table 6. The discrepancy between the observed and estimated values for the electrical calibrations is probably greater than the uncertainty of our estimates.

6.2. Systematic Errors

One of the main assumptions customarily made in using a stirred-water "isoperibol" calorimeter is that the correction to the temperature rise due to heat transfer from the calorimeter jacket and heat delivered by the stirrer can be computed from Newton's cooling law and temperatures measured inside the calorimeter.

It is generally understood that this assumption would be valid if the calorimeter temperature were strictly uniform throughout the calorimeter.[8] Real calorimeters have, of course, temperature gradients or, equivalently, temperature differences due to the effects of lags. Thus, the surface temperature of the calorimeter, which determines the rate of heat transfer between the calorimeter and jacket, is in general different from that measured by the thermometer, even though it is placed as close to the calorimeter wall as is practical.

The effect of a temperature gradient on calorimetric measurements has been analyzed to some extent for "isoperibol" calorimeters [29, 30, 31], and in detail for aneroid adiabatic calorimeters [32]. Harper [29] has shown that if the lag of the temperature measurement system (i.e., including both thermometer and electrical detecting system) is the same throughout a calorimeter experiment then the lag causes no error in the corrected temperature rise. White [30], in effect, considers the temperature gradient to be the superposition of those due to (1) heat transfer from the jacket and stirring, and (2) heat released in the calorimeter during the main period. By an argument identical to that used by Harper, he showed that the lag due to the first of these sources causes no error in the corrected temperature rise, while the lag due to the second source will cause an error. However, if the latter lag is a constant which is independent of the source of heat (i.e., electrical heater or combustion bomb), then it will cause no error in the heat of combustion of benzoic acid. White felt that the constancy of the lag due to different heat sources could be verified by appropriate experiments.

[7] Square root of the sum of squares of the deviations divided by the number of measurements minus one.

[8] Convective heat transfer between the calorimeter and jacket must also be negligible. For this discussion, we assume this is so.

TABLE 6. *Estimated random errors in* $-\text{E}(cal)/(-\Delta\text{E}_\text{B})$ *and* $\overline{\text{E}(cal)}$

	Benzoic acid ($-E$ (cal)/ΔE_B)	Electrical calibrations ($-E$ (cal))
	%	%
Corrected temperature rise	0.0022	0.0019
Bouyancy correction	0.0018	0.0018
Mass of benzoic acid	0.0007	.....
$\int_0^T E_V E_I dt$	.....	0.0003
k/E'_{sc}	.....	0.0001
E_{sc}	.....	0.0001
$R_{0.01}$	.....	0.0002
Volt box ratio	.....	0.0001
Heater leads	.....	0.0005
Estimated standard deviation of a measurement	0.0030	0.0027
Observed standard deviation of a measurement	0.0034	0.0070

TABLE 7. *Summary of values of* $(-\Delta E_B)$ *for benzoic acid*

Author	Sample	Value	Uncertainty
		$J\,g^{-1}$	$J\,g^{-1}$
Jessup and Green [2, 18, 33] (1934)	39d, 39e	26,432.0	±2.6
Prosen and Rossini [35] (1939–41)	39e	26,434.7	±2.2
Jessup [2, 33] (1942)	39e, 39f, B	26,433.8	±2.6
Coops et al. [31] (1946–8)	39b, 39f, VUS	26,438.0	±4
Coops et al. [31] (1954)	39b, VUS	26,435.0	±4
Challoner et al. [34] (1954)	C	26,436.0	±4
This work (1966)	39i	26,434.0	±3.3

Coops et al. [31], have suggested one method of making the lag due to different heat sources the same and have incorporated this in the design of their calorimeter.

An experimental test that has frequently been applied is that the lag is a constant if it can be shown that the energy equivalent of the calorimeter is invariant with the power supplied to the electrical heater. This criterion has been shown to be incorrect by West [32] for a calorimeter in which heat flow equations are linear. It is interesting to note that part of this argument depends upon showing that the contributions to the correction on the observed temperature rise of the temperature transients due to turning the electrical heater on and off exactly cancel. Indirect evidence that this cancellation is the case for our calorimeter is given in section 7. This conformity of our calorimeter with West's analysis of behavior of transients suggests that the remainder of West's argument may be applicable to the Dickinson calorimeter. The invariance of the energy equivalent found in the electrical experiments with varying electrical power (see table 5), thus, does not provide information about possible systematic errors.

A series of tests was carried out to see whether or not measurements based on the average surface temperature of the calorimeter in place of that registered by the platinum thermometer would give a different value of ΔE_B for benzoic acid. On the basis of these tests, which must be considered to be preliminary in nature, it was found that there is a difference between the temperatures of the calorimater surface and the water in the vicinity of the resistance thermometer and that this difference varies with time in the electrical calibrations in a different way than in the benzoic acid experiments. Because of certain experimental difficulties, we assigned an uncertainty to the difference in values of ΔE_B calculated from these observations that was about the same as the magnitude of the difference. Until a more reliable estimate based on more accurate tests is obtained, we have somewhat arbitrarily assigned an uncertainty of ± 0.01 percent of ΔE_B to take into account the possible correction for the effect of surface temperature.

The net contribution of other sources of systematic errors in the electrical calibrations is estimated to be at most ± 0.004 percent of ΔE_B.

6.3. Discussion of Results

In table 7, we have listed the more recent determinations of $(-\Delta E_B)$ for benzoic acid in joules per gram of sample.[9] Samples indicated by the number 39 followed by a letter refer to batches of the benzoic acid standard sample issued by NBS. B refers to a sample of 39e purified by fractional crystallization from benzene. VUS and C refer to benzoic acid samples from sources other than NBS and are described in the corresponding references.

Uncertainty intervals listed in table 7 are those cited by the authors except for the work of Jessup and Green [2, 18, 33] which we assumed to be equal to the later work of Jessup [2]. The bounds for the uncertainty interval for our own work was computed by the procedure recommended by Rossini [27] as

$$\sqrt{(1.7)^2+(1.1)^2+(2.6)^2}.$$

Aside from our own work, only that of Challoner, Gundry, and Meetham [34] incorporates an uncertainty due to the effect of surface temperature. In the latter, a correction of -0.046 ± 0.0057 percent had to be applied to the energy equivalent of the calorimeter to correct for the difference in surface temperature effects during the main period of an electrical calibration and a benzoic acid combustion experiment. Our preliminary experiments suggest that the magnitude of the surface temperature correction is not insignificant for our results although it is smaller than that of Challoner et al. A substantial contribution to the uncertainty of our results has been allowed because of the unknown magnitude of our surface temperature correction. It would be preferable, in spite of the difficulty of measuring it, to evaluate the correction experimentally in absolute calorimetric measurements unless the calorimeter has been specifically designed to eliminate the error.

[9] We have been informed by private communication from Mosselman and Dekker [36], and from Head [37], of very recent electrical determinations of the energy of combustion of benzoic acid in their respective laboratories. These determinations are both based on measurements made in calorimeters containing water flow channels of the type devised by Coops et al. [31], and both are reported to be in excellent agreement with the value we list for this work in table 7. The work of Mosselman and Dekker includes some measurements on NBS Standard Sample 39i.

7. Appendix. Analysis of Main Period of the Electrical Calibration Experiments

If the temperature transients due to turning the electrical heater on and off make no net contribution to the corrected temperature rise, the two areas between the main period curves of the electrical calibrations and the straight lines given by eqs (10a), (10b), and (10c) should be equal since the heater power does not vary with time.

$$\theta(t) = \theta_i + (d\theta/dt)_i(t - t_i); \qquad t_i \leq t \leq t_1 \qquad (10a)$$

$$\theta(t) = \theta_3 + (d\theta/dt)_3(t - t_3); \qquad t_1 \leq t \leq t_2 + t_b \qquad (10b)$$

$$\theta(t) = \theta_f + (d\theta/dt)_f(t_f - t); \qquad t_2 + t_b \leq t \leq t_f. \qquad (10c)$$

Equations (10a) and (10c) are linear extrapolations of the initial and final drift period curves into the main period, and the constants θ_3, t_3 and $\left(\frac{d\theta}{dt}\right)_3$ of eq (10b) are determined from a linear least squares fit of the main period data during the rapid temperature rise. The times t_1 and $t_2 + t_b$ are the times of intersections of eq (10b) with eq (10a) and (10c).

To test whether or not the areas are equal, we noted that if they are, then the time t_1 should be approximately equal to time[10] t_b and both should be independent of the power supplied to the heater or $(d\theta/dt)_3$. Comparison of columns 3 through 5 of table 8 shows this is very nearly true. Further, the equality of the areas means that the integral in eq (5) for t_x is the area enclosed by the lines of eqs (10a) through (10c) and θ_i. Corrected temperature rises computed using values $t_f - t_x$ determined in this manner differed by less than one part in 10^5 from those listed in section 5. The latter are based on values of $t_f - t_x$ determined by the more accurate spline integration procedure.

TABLE 8. *Average main period characteristics, electrical calibration*

Heater power watts	No. of Expts.	t_1 min	t_b min	$(d\theta/dt)_3$ °C min^{-1}	t_2 min	t_{max} min
60	2	0.238	0.224	0.252	11.2	12.5–13
110	9	0.242	0.235	0.480	5.8	8.5
270	5	0.230	0.254	1.15	2.5	4–5.5

8. References

[1] Dickinson, H. C., Bull. BS **11,** 189 (1914).
[2] Jessup, R. S., J. Res. NBS **29,** 247 (1942) RP1490.
[3] Jessup, R. S., NBS Monograph 7, February 26, 1960.
[4] Coops, J., Jessup, R. S., and Van Nes, K., Calibrations of Calorimeters for Reactions in a Bomb at Constant Volume, ch. 3, Experimental Thermochemistry, Vol. **1,** F. D. Rossini, Editor (Interscience Publishers, Inc., New York, N.Y., 1956).
[5] Prosen, E. J. Compounds Containing Carbon, Hydrogen, Oxygen, and Nitrogen, ch. 6, Experimental Thermochemistry, Vol. **I,** F. D. Rossini, Editor (Interscience Publishers, Inc., New York, N.Y., 1956).
[6] Jessup, R. S., ibid, figures 1a, 1b, and Appendix 7.1e.
[7] Jessup, R. S., ibid., Appendix 7.1d.
[8] Domalski, E. S., and Armstrong, G. T., J. Res. NBS **69A** (Phys. and Chem.), No. 2, 137 (1965).
[9] Jessup, R. S., ibid., p. 20, figure 1c.
[10] Stimson, H. F., Precision Resistance Thermometry and Fixed Points, ch. 9, Temperature, Its Measurement and Control in Science and Industry, Vol. **II,** H. C. Wolfe, Editor, American Institute of Physics (Reinhold Publishing Corp., New York, 1955).
[11] Armstrong, G. T., Wong, P. K., and Kreiger, L. A., Rev. Sci. Instr. **30,** 339–343 (1959).
[12] Jessup, R. S., ibid., Appendix 7.1c.
[13] Boyd, R. H., Rev. Sci. Instr. **35,** 1086, 1964.
[14] Pailthrope, R. M., and Riley, J. C., An Improved Technique for Establishing Resistance Ratios, ESI Bulletin No. 35 (Electro Scientific Industries, Portland, Oreg., November 1962).
[15] Mueller, E. F. and Stimson, H. F., J. Res. NBS **13,** 699 (1934), RP739.
[16] Osborne, N. S., Stimson, H. F., Ginnings, D. C., J. Res. NBS **23,** 197, 261 (1939), RP1228.
[17] Jessup, R. S., ibid, p. 7.
[18] Jessup, R. S. and Green, C. B., J. Res. NBS **13,** 469 (1934), RP721.
[19] Jessup, R. S., NBS Monograph 7, Sec. 3.2 and 4.
[20] Hubbard, W. N., Scott, D. W., and Waddington, G., Standard States and Corrections for Combustions in a Bomb at Constant Volume, ch. 5, Experimental Thermochemistry, Vol. **I,** F. D. Rossini, Editor (Interscience Publishers, Inc., New York, N.Y., 1956).
[21] Walsh, J. H., Ahlberg, J. H., and Nilson, E. H., J. Math. and Mech. **11,** (No. 2), 225 (1962).
[22] Darmouth Basic Library, Code: Spline, Converted to Basic Language by Messina, C., NBS, September (1965).
[23] Katsanis, T., NASA Technical Note, D–2546, December (1964).
[24] Shomate, C. H., Fortran IV Computer Program for Reduction of Heat of Combustion Calorimetric Data, Code 5052 (U.S. Naval Ordnance Test Station, China Lake, California, January 1967).
[25] Hamer, W. J., NBS Monograph 84, January 15, 1965.
[26] Ginnings, D. C., West, E. D., Principles of Calorimetric Design, ch. 4, Experimental Thermodynamics, Vol. **I,** Calorimetry of Non Reacting Systems, J. P. McCullough, Editor (Butterworth and Co., Ltd., In press).
[27] Rossini, F. D., Assignment of Uncertainties to Thermochemical Data, ch. 14, Experimental Thermochemistry, Vol. **I,** F. D. Rossini, Editor (Interscience Publishers, Inc., New York, N.Y., 1956).
[28] Ginnings, D. C., West, E. D., Rev. Sci. Instr. **35,** 965 (1964).
[29] Harper, D. R., J. Res. NBS **8,** 659 (1912).
[30] White, W. P., The Modern Calorimeter (Reinhold Publishing Corp., New York, 1928), p. 89, p. 36. See also J. Am. Chem. Soc. **40,** 1861–1863, 1918 and Phys. Rev. **31,** 568–570, 1910.
[31] Coops, J., Adriaanse, N., Van Nes, K., Rec. Trav. Chim. **75,** 237 (1956).
[32] West, E. D., J. Res. NBS **67A** (Phys. and Chem.), No. 4, 331 (1963).
[33] Jessup, R. S., J. Res. NBS **36,** 421 (1946), RP1711.
[34] Challoner, A. R., Gundry, H. A., Meetham, A. R., Phil. Trans. Roy. Soc. (London), **A247,** 553 (1955).
[35] Prosen, E. J. and Rossini, F. D., J. Res. NBS **33,** 439 (1944), RP1619.
[36] Mosselman, C., and Dekker, H., The Free University, Amsterdam, Private Communication.
[37] Head, A. J., Natl. Physical Laboratory, Teddington, private communication.

[10] We assume the transient can be represented by a single exponential.

(Paper 72A5–511)

JOURNAL OF RESEARCH of the National Bureau of Standards—A. Physics and Chemistry
Vol. 72A, No. 5, September–October 1968

Effect of Low Pressures on the Room Temperature Transitions of Polytetrafluoroethylene

G. M. Martin and R. K. Eby

Institute for Materials Research, National Bureau of Standards, Washington, D.C. 20234

(May 24, 1968)

Between approximately 20 and 30 °C at atmospheric pressure, polytetrafluoroethylene exhibits a phase (denoted as IV), which has not been observed in P–V–T measurements at pressures above 10^8 Nm^{-2} (1 Kilobar). Data are presented to resolve this phase in the temperature range 0 to 50 °C and the pressure range 0 to 0.686×10^8 Nm^{-2}. The II–IV (20 °C) transition pressure increases with temperature according to the equation $P = (-820 + 26.9t + 0.68t^2) \times 10^5$ and the IV–I (30 °C) transition according to the equation $P = (-91 - 57.8t + 1.99t^2) \times 10^5$ suggesting a possible triple point near 2.6×10^8 Nm^{-2} and 54 °C. However, the IV–I transition probably cannot be resolved by volume measurements at pressures above 2×10^8 Nm^{-2} because its volume of transition is small and the two transitions overlap. The enthalpies of the transitions are calculated for different pressures and some thermodynamic properties of phase IV are determined indirectly. It is shown that, if the effect of volume change is subtracted, random reversals of the hand of the helical conformation of the molecule can account for appreciable fractions of the enthalpy and corresponding entropy change for the combined transitions at atmospheric pressure.

Key Words: Dilatometry; enthalpy; entropy; helical molecule; low pressure; phase diagram; polytetrafluoroethylene; transitions; triple point.

Volume measurements over a wide range of temperature and pressure have established a phase diagram for polytetrafluoroethylene with three solid phases and the melt [1, 2, 3, 4].[1] Most of the data were obtained by the piston displacement method and had a low pressure limit of about 10^8 Nm^{-2} (1 Kilobar) imposed by friction. They show a transition line which extrapolates to the "20 °C" transition observed in measurements at atmospheric pressure but do not show a separate line extrapolating to the smaller "30 °C" transition which is also observed at atmospherical pressure [5, 6, 7]. This may be due to a lack of sensitivity in the method, but it is also possible that the "30 °C" transition line terminates in a triple point with the "20 °C" transition line at some pressure below 10^8 Nm^{-2}. Low pressure data of sufficient accuracy to determine this have not been available. This note reports measurements obtained with a dilatometer at temperatures between 0 and 50 °C and pressures up to 0.686×10^8 Nm^{-2}.

The polytetrafluoroethylene was similar to a sample used in other measurements [8] (sample number 3). At the start of the present work, the density determined at 25 °C by hydrostatic weighing was 2.253 g/cm^3 which corresponds to a crystallinity of about 90 percent. The data given here are based on the sample as a whole and have not been subjected to the small correction for crystallinity.

The polymer was evacuated for 16 hr at a pressure of 1.3×10^{-3} Nm^{-2} (10^{-5} torr) in a glass dilatometer, which was then filled with mercury. The dilatometer was placed inside a pressure vessel which was immersed in a temperature bath regulated within ± 0.05 °C. Windows in the bath and in the pressure vessel permitted measurement of the mercury level with a cathetometer. An estimated uncertainty of $\pm 5 \times 10^{-3}$ cm in this reading corresponds to an uncertainty of less than $\pm 2 \times 10^{-5}$ cm^3/g in the calculated specific volume. Pressure was measured with a calibrated Bourdon type gage (uncertainty less than $\pm 10^5$ Nm^{-2}). Observed volume changes were corrected for changes in the volume of the glass and mercury. Details of the apparatus have been described previously [9].

Volume measurements were made as a function of temperature at each pressure. The pressure was applied at 50 °C and the temperature lowered in steps at the rate of about one degree per hour, which was decreased to 1/4 to 1/24 degree per hour near the "20 °C" transition. After the lowest temperature was reached, the sample was heated in the same manner to 50 °C and the pressure released.

[1] Figures in brackets indicate the literature references at the end of this paper.

Figure 1 shows the specific volume as a function of temperature for each pressure in the range of the transitions. Equilibrium volumes are given except at the 20 °C transition, where the volume at a given temperature changes slowly over a long period of time and in some cases was still varying linearly with the logarithm of time after 24 hr. The 20 °C transition takes place about 1.6 °C lower on cooling than on heating [6] and this difference is approximately independent of pressure. The 30 °C transition did not exhibit hysteresis and the data show that it can be observed even at the highest pressure, 0.686×10^8 Nm^{-2}.

Figure 2 shows the phase diagram at low pressure. Transition temperatures are taken to be the temperatures of the maximum slopes in the specific volume-temperature curves since these values could be determined more precisely than the points at which the last trace of the low temperature phase disappears. The intermediate phase is called IV to distinguish it from those already numbered [1]. The temperature difference between the two transitions decreases with increasing pressure and extrapolations based on the second degree curves shown in figure 2 indicate a possible triple point at approximately 2.6×10^8 Nm^{-2} and 54 °C. Such a triple point is out of the range of the present apparatus and in the range of the usual high pressure techniques. However, as discussed later, there is some doubt whether volume measurements will be able to resolve the IV–I transition at higher pressures.

Straight lines were fitted to the specific volume-temperature data below the II–IV and above the IV–I transitions and the total volume change for both transitions was found by taking the difference between these lines (see fig. 1). This technique was not as satisfactory for determining the volume changes of each transition separately, because the two transitions overlap. Therefore, plots of the slopes of the specific volume-temperature curves against temperature (fig. 3) were used for the analysis. The shaded areas were measured to obtain the IV–I transition volumes and these values could then be subtracted from the total volume changes to find the II–IV transition volumes. This method is based on the approximation that the cutoff "tails" of each transition have equal areas. Although other assumptions could be made, they could not be shown to yield more accurate results.

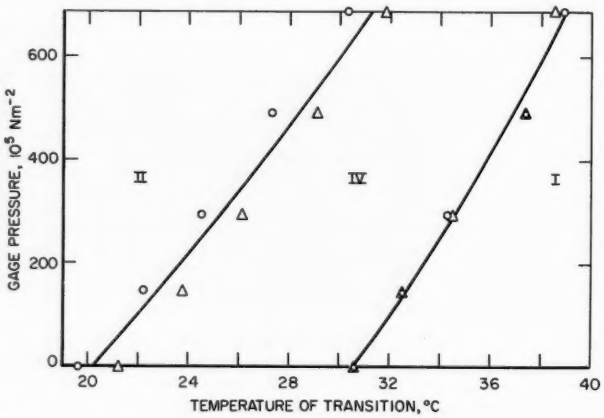

FIGURE 2. *Relations between pressure and transition temperatures for polytetrafluoroethylene.*

The lines represent the second degree curves $P = (-820 + 26.9t + 0.68t^2) \times 10^5$ (II–IV) and $P = (-91 - 57.8t + 1.99t^2) \times 10^5$ (IV–I) which were fitted to the data, ○ = cooling; Δ = heating.

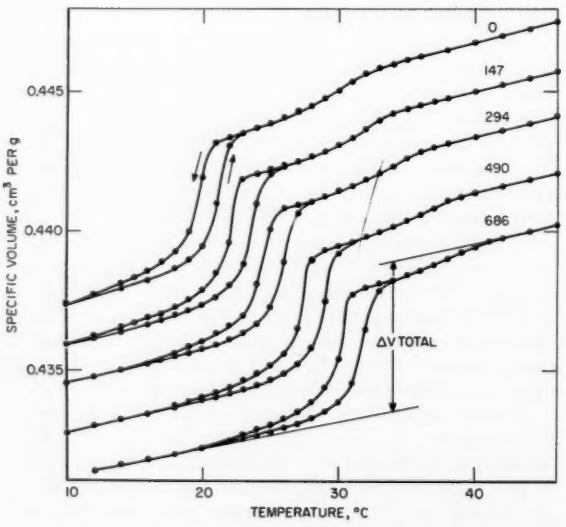

FIGURE 1. *Specific volume versus temperature for polytetrafluoroethylene in the region near the room temperature transitions.*

The numbers on the curves give the gage pressures in 10^5 Nm^{-2}.

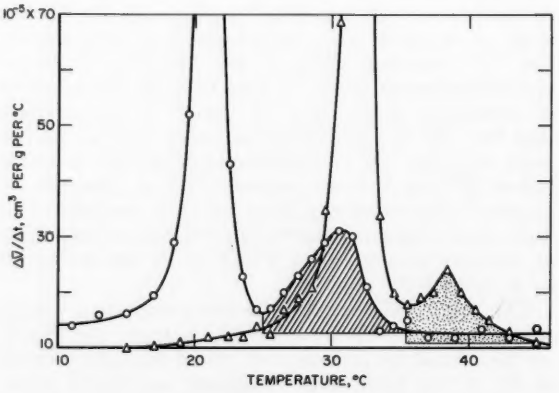

FIGURE 3. *Slopes of specific volume versus temperature curves plotted against temperature for polytetrafluoroethylene.*

Heating cycle. ○ = 0×10^5 Nm^{-2} pressure; Δ = 686×10^5 Nm^{-2} pressure.

Figure 4 shows that, while the total transition volume and the IV–I transition volume decrease, the II–IV transition volume does not vary significantly with increasing pressure. Less accurate measurements made directly on the specific volume-temperature curves in the same way that the total transition volumes were determined yielded slightly smaller II–IV transition volumes, but did confirm the lack of variation with pressure. Because of the small transition volume at 0.686×10^8 Nm^{-2}, the decreasing trend in this quantity, and the decreasing temperature separation of the two transitions, the IV–I transition would be difficult to resolve by volume measurements at pressures above 2×10^8 Nm^{-2}. Probably a technique such as x-ray diffraction would be required.

The Clapeyron equation may be written

$$\Delta H = T\Delta V dP/dT. \tag{1}$$

In it, ΔH, T, ΔV, and P represent the heat, absolute temperature, volume, and pressure of transition, respectively. Values of ΔH for the II–IV and IV–I transitions at one atmosphere calculated by eq (1) are in reasonable agreement with data in the literature [4, 7, 10, 11] and with results obtained by differential scanning calorimetry on the present sample. (The D.S.C. results were obtained at much greater rates of heating and cooling and varied appreciably from measurement to measurement.) The transition heats were also calculated for other pressures and are given in figure 5. For the II–IV transition, ΔH increases with pressure while for the IV–I it is almost unchanged.

The following equations also apply to the transitions:

$$d\Delta V/dP = (dT/dP)\Delta\alpha + \Delta\beta \tag{2}$$

and

$$d\Delta H/dP = (dT/dP)\Delta C_P + \Delta V - T\Delta\alpha. \tag{3}$$

In these, $\alpha \equiv (\partial V/\partial T)_P$, $\beta \equiv (\partial V/\partial P)_T$, and $C_P \equiv (\partial H/\partial T)_P$. Now, the modulus for ultrasonic longitudinal waves is the same in phases IV and II [8]. This suggests that β_{IV} might be approximately equal to β_{II}. If it is assumed that this is correct, the data in figures 1, 2, 4, and 5, together with eqs (2) and (3), yield the following approximate values for phase IV at one atmosphere: $\alpha_{II} = \alpha_{IV}$ and $C_{PI} = C_{PII}$. In this way, the properties of phase IV can be determined even though they cannot be measured directly because of the overlap of the transitions.

Experimental support has been presented for the occurrence in the crystals of randomly located reversals of the pitch of the molecular helix, i.e., a change from a left to a right handed or from a right to a left handed helix [12]. Experimental data yield an energy of reversal of 0.053 eV in Phase I and calculations based on three models of molecular interaction give an average ratio of the energy of reversal in phase II to that in phase I of 1.16 [12]. On this basis, the energy of reversal in phase II can be taken as 0.062 eV. These numbers may be used to calculate the concentration

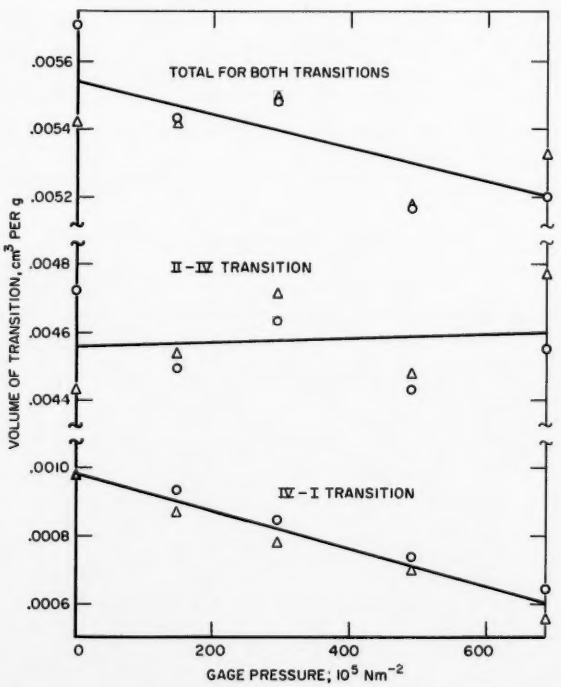

FIGURE 4. *Change in volumes of transition with pressure for polytetrafluoroethylene.*

○ = cooling; Δ = heating. The straight lines are fitted to the data by least squares.

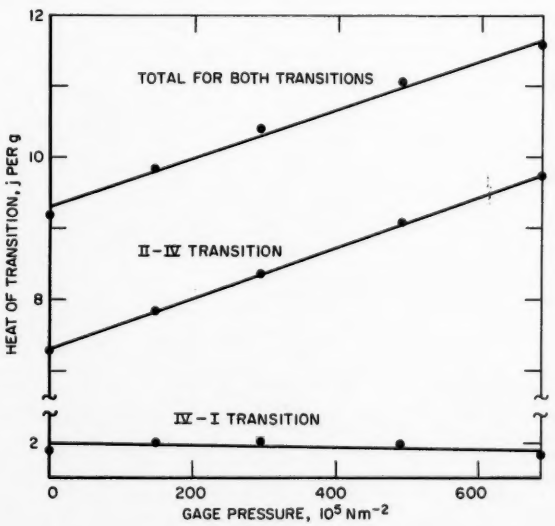

FIGURE 5. *Variation of heat of transition with pressure for polytetrafluoroethylene.*

The straight lines are fitted to the data by least squares.

312-248 O-68—2

of random reversals present in phase II at the II–IV transition temperature and in phase I at the IV–I transition temperature and from these the associated changes in entropy and enthalpy.[2] This can be accomplished by first using the equation for the Boltzmann distribution: $n_1/n_2 = \exp(-E/kT)$ where n_1 is the number of reversals, n_2 is the number of bonds not reversed, E the energy of reversal, and k the Boltzmann constant. The entropy of mixing is then given by $s = k \ln(n!/n_1!n_2!)$ where n is the total number of bonds. The resulting changes in enthalpy and entropy are 2.2 J/g and 0.013 J/gK, respectively. If we assume that these changes occur only at the transitions (neglecting any change within the small temperature range of phase IV), the above values can be compared with the total enthalpy change given in figure 5 and the corresponding entropy change. After correction for the effects of volume change [4, 14], the latter values are 7.6 J/g and 0.026 j/gK. Thus, randomly located reversals of the hand of the helix can account for about 30 percent of the enthalpy change at constant volume and about 50 percent of the entropy change at constant volume that occurs at the transitions. Of the quantities in the calculations above, the value of E in phase II is probably the least accurate. For example, it corresponds to eight reversals of pitch per 100 bonds, a number not consistent with the x-ray data [4]. If E_{II} were 0.080 eV, the calculated enthalpy and entropy would be 5.7 J/g and 0.032 J/gK, respectively. These values give the best fit to the experimental data and correspond to the more reasonable concentration of four reversals per 100 bonds.

In summary, *PVT* measurements indicate that phase IV of polytetrafluoroethylene probably exists at pressures up to 2.6×10^8 Nm^{-2}. The diffuse IV–I transition and the triple point will be difficult to detect with high pressure techniques because of the small transition volume and the small temperature separation from the diffuse II–IV transition. Enthalpies and entropies of transition have been calculated from the *PVT* data and compared with those calculated for changes in the number of randomly located reversals of the hand of the helical molecule. The results show that such reversals can account for appreciable fractions of the enthalpy and entropy of the combined II–IV and IV–I transitions at atmospheric pressure. The values of $(\delta V/\delta T)_p$ and $(\delta V/\delta P)_T$ in phase IV are estimated to be approximately the same as in phase II while the value of $(\delta H/\delta T)_p$ in phase IV is estimated to be close to that in phase I.

[2] A similar calculation has been presented recently, but it assumed that there were no reversals in phase II [13].

References

[1] Weir, C. E., J. Res. NBS **50,** 95 (1953) RP2395.
[2] Beecroft, R. I., and Swenson, C. A., J. Appl. Phys. **30,** 1793 (1959).
[3] Pistorius, C. W. F. T., Polymer **5,** 315 (1964).
[4] Sperati, C. A., and Starkweather, H. W., Jr., Fortschr. Hoch Polym.-Forsch. **2,** 465 (1961). (In English.)
[5] Rigby, H. A., and Bunn, C. W., Nature **164,** 583 (1949).
[6] Quinn, F. A., Jr., Roberts, D. E., and Work, R. N., J. Appl. Phys. **22,** 1085 (1951).
[7] Yasuda, T., and Araki, Y., J. Polymer Sci. **5,** 331 (1961).
[8] Eby, R. K., and Sinnott, K. M., J. Appl. Phys. **32,** 1765 (1961).
[9] Martin, G. M., and Mandelkern, L., J. Appl. Phys. **34,** 2312 (1963).
[10] Furukawa, G. T., McCoskey, R. E., and King, G. J., J. Res. NBS **49,** 273 (1962) RP2364.
[11] Marx, P., and Dole, M., J. Am. Chem. Soc. **77,** 4771 (1955).
[12] Brown, R. G., J. Chem. Phys. **40,** 2900 (1964).
[13] Bates, T. W., and Stockmayer, W. H., Macromolecules 1, 17 (1968).
[14] Starkweather, H. W., Jr., and Boyd, R. H., J. Phys. Chem. **64,** 410 (1960).

(Paper 72A5–512)

JOURNAL OF RESEARCH of the National Bureau of Standards—A. Physics and Chemistry
Vol. 72A, No. 5, September–October 1968

Electrostatic Potentials and Their Spatial Derivatives About Point Defects in Ionic Crystals

Herbert S. Bennett

Institute for Materials Research, National Bureau of Standards, Washington, D.C. 20234

(June 10, 1968)

The electrostatic potential which arises from a lattice array of point ions is computed in terms of a Taylor's series expansion for small distances from a lattice site. This expansion gives the change in electrostatic energy when an ion moves in the background of a perfect point ion lattice potential. The Taylor's series coefficients for terms up to fourth order in the ion displacement are evaluated for the NaCl and CaF_2 lattice structures.

Key Words: CaF_2; classical ionic lattice theory; electrostatic potential; lattice distortion; NaCl; point defect.

1. Introduction

Most theoretical studies of defects in ionic solids require a knowledge of the manner in which the lattice distorts to accommodate the defect. Classical ionic lattice theory gives the interaction energy $U_{\mu\nu}$ between two ions μ and ν at a separation $r_{\mu\nu}=|\mathbf{r}_\mu-\mathbf{r}_\nu|$; namely,

$$U_{\mu\nu}=(Z_\mu Z_\nu/r_{\mu\nu})-(C^{(6)}_{\mu\nu}/r^6_{\mu\nu})-(C^{(8)}_{\mu\nu}/r^8_{\mu\nu})+\varphi_{\text{rep}}(r_{\mu\nu}), \quad (1)$$

where the four terms are respectively the coulomb electrostatic, dipole–dipole, dipole–quadrupole, and repulsive contributions to the lattice energy. The charge on the ion ν is Z_ν, $C^{(6)}_{\mu\nu}$ and $C^{(8)}_{\mu\nu}$ are the van der Waals constants for ions μ and ν, and the repulsive energy $\varphi_{\text{rep}}(r_{\mu\nu})$ takes the Pauli exclusion principle between the μth and the νth ion cores into account. The repulsive energy φ_{rep} is a short-range function of $r_{\mu\nu}$. The cohesive energy $\Phi(r_0)$ for the crystal becomes,

$$\Phi(r_0)=\frac{1}{2}\sum_{\mu\neq\nu}U_{\mu\nu}+U_0, \quad (2)$$

where r_0 is the nearest neighbor distance for the perfect lattice and where U_0 is the lattice energy.

The presence of a defect causes the neighboring ions to move from their perfect lattice sites. This motion will modify the energy of the lattice and this change in the lattice energy is most important in a study of the properties of defects in ionic solids. Among the many terms which occur in the change in the lattice energy due to a defect is the one which represents the change in electrostatic energy when a neighboring ion moves in the background of a perfect point ion lattice potential.

As an example, let us consider the F center, which is an electron localized about an anion vacancy. The ions neighboring the F center defect move in a self consistent manner to accommodate the F electron. The many terms in the change in lattice energy are grouped in some convenient manner. One of these terms is the change in electrostatic energy ΔV_ν which occurs when a neighboring cation moves in the background of a perfect point ion lattice potential [1];[1]

$$\Delta V_\nu(\mathbf{r}'_\nu-\mathbf{r}_\nu)=Z_\nu\sum_{\mu\neq\nu}z_\mu\{|\mathbf{r}'_\nu-\mathbf{r}_\mu|^{-1}-|\mathbf{r}_\nu-\mathbf{r}_\mu|^{-1}\}. \quad (3)$$

The quantity $\Delta V_\nu(\mathbf{r}'_\nu-\mathbf{r}_\nu)$ is the change in electrostatic coulombic energy when ion ν moves from the perfect lattice site $\mathbf{r}_\nu$ to the position $\mathbf{r}'_\nu$, which is not a perfect lattice site, in the background of a perfect lattice point ion potential. Denoting the distortion (ion displacement) by $\mathbf{r}=\mathbf{r}'_\nu-\mathbf{r}_\nu$ we write the energy of the νth ion at the position $\mathbf{r}'_\nu=\mathbf{r}_\nu+\mathbf{r}$ in the form,

$$V_\nu(\mathbf{r})=Z_\nu\sum_{\mu\neq\nu}Z_\mu|\mathbf{r}_\nu-\mathbf{r}_\mu+\mathbf{r}|^{-1}. \quad (4)$$

[1] Figures in brackets indicate the literature references at the end of this paper.

Hence, the change in the electrostatic coulomb energy when only the νth ion moves in the background of a perfect lattice is

$$\Delta V_\nu(\mathbf{r}) = V_\nu(\mathbf{r}) - V_\nu(\mathbf{r}=0). \tag{5}$$

The few researchers [2, 3, 4], who have considered local lattice distortions near the F center in a manner self consistent with the F electron state, consider only the alkali halides and neglect this term ΔV_ν. This may be reasonable in the alkali halides for optical absorption discussions in which the lattice distortions are small. But one may question their neglecting the term ΔV_ν for optical emission studies in the alkali halides and for other optical discussions in the alkaline earth fluorides and oxides. The lattice distortion may be as large as twelve percent of the nearest neighbor distance r_0 for the relaxed excited state in the alkali halides and in the alkaline earth halides and for all states in the alkaline earth oxides. In this paper we shall express the term ΔV_ν as a series expansion in the distortion $\mathbf{r}=\mathbf{r}'_\nu - \mathbf{r}_\nu$ and evaluate by Ewald's method [5] the lattice summations which give the series coefficients. We shall compute explicitly these coefficients for the NaCl and CaF_2 lattice structures.

2. Formulation

When $(r/r_0) < 1$, we may expand the electrostatic energy given by eq (4) in a Taylor's series about the point $\mathbf{r}=\mathbf{0}$;

$$V_\nu(\mathbf{r}) \approx V_\nu(\mathbf{r}=0) + \mathbf{r}\cdot\nabla V_\nu(\mathbf{r}) + \frac{1}{2}(\mathbf{r}\cdot\nabla)^2 V_\nu(\mathbf{r})$$

$$+\frac{1}{6}(\mathbf{r}\cdot\nabla)^3 V_\nu(\mathbf{r}) + \frac{1}{24}(\mathbf{r}\cdot\nabla)^4 V_\nu(\mathbf{r}) + \ldots . \tag{6}$$

The various derivatives of $V_\nu(\mathbf{r})$ with respect to the Cartesian components of $\mathbf{r}$ are evaluated at $\mathbf{r}=\mathbf{0}$. Many of the derivatives in eq (6) will be zero by symmetry arguments, but which ones are zero will depend upon the specific lattice structure and upon whether an anion or a cation moves.

Let us first consider the point lattices and the reciprocal lattices for the NaCl and CaF_2 structures. The primitive translational vectors for these two lattices are

$$\mathbf{a}_1 = (a/2)(0,1,1), \qquad \mathbf{a}_2 = (a/2)(1,0,1)$$

and $\mathbf{a}_3 = (a/2)(1,1,0)$

and the volume of the unit cell v_c is

$$v_c = \mathbf{a}_1\cdot(\mathbf{a}_2\times\mathbf{a}_3) = (a^3/4).$$

The lattice constant a is the Na–Na distance or the Ca–Ca distance. When a cation is at the origin, the position vector $\mathbf{r}_l^+$ for the other cations (Na^+ or Ca^{++}) is

$$\mathbf{r}_l^+ = (a/2)[(l_2+l_3)\hat{x} + (l_3+l_1)\hat{y} + (l_1+l_2)\hat{z}]$$

where the l_i's are $0, \pm1, \pm2, \pm3$, etc. The anions for NaCl structures are located at the sites

$$\mathbf{r}_l^- = \mathbf{r}_l^+ + \mathbf{x}_a,$$

where $\mathbf{x}_a = (a/2)(\hat{x}+\hat{y}+\hat{z})$ and the anions for the CaF_2 structures are located at the sites

$$\mathbf{r}_l^-(1) = \mathbf{r}_l^+ + \mathbf{x}_a(1) \text{ and } \mathbf{r}_l^-(2) = \mathbf{r}_l^+ + \mathbf{x}_a(2),$$

where

$$\mathbf{x}_a(1) = (a/4)(\hat{x}+\hat{y}+\hat{z}) \text{ and } \mathbf{x}_a(2) = (3a/4)(\hat{x}+\hat{y}+\hat{z}).$$

We also choose the distortion $\mathbf{r}$ to be given by

$$\mathbf{r} = (a/4)(\sigma_1\hat{x} + \sigma_2\hat{y} + \sigma_3\hat{z}). \tag{7}$$

The position of a nearest neighbor cation when an anion is the reference ion is $\mathbf{r}_c = (a/2)(0,0,1)$ for NaCl structures and $\mathbf{r}_c = (a/4)(1,1,1)$ for CaF_2 structures. The nearest neighbor distance r_0 for the perfect lattice is then $r_0 = (a/2)$ for NaCl structures and $r_0 = (\sqrt{3}a/4)$ for CaF_2 structures. Thus,

$$v_c(\text{NaCl}) = 2r_0^3 \text{ and } v_c(CaF_2) = (16/3\sqrt{3})r_0^3.$$

The first term of eq (6) is directly proportional to the Madelung constant for the νth ion, $\alpha_\nu = [V_\nu(\mathbf{r}=\mathbf{0})r_0/Z_\nu]$. Throughout this paper, we will use the nearest neighbor distance as the reference distance.

The vectors $\mathbf{b}_1 = (1/a)(-1,1,1)$, $\mathbf{b}_2 = (1/a)(1,-1,1)$ and $\mathbf{b}_3 = (1/a)(1,1,-1)$ are the reciprocal triad of the primitive translational vectors $\mathbf{a}_1$, $\mathbf{a}_2$, and $\mathbf{a}_3$. The wave vector in the reciprocal lattice is

$$\mathbf{g} = 2\pi(n_1\mathbf{b}_1 + n_2\mathbf{b}_2 + n_3\mathbf{b}_3)$$

where the n_i's are $0, \pm1, \pm2, \pm3$, etc.

The series given in eq (4) is conditionally convergent. Hence, straightforward evaluations for such series will be most tedious and usually unsatisfactory. The Ewald's method [5, 6] is an elegant procedure by which one converts the series (4) into the sum of two series—each one of which converges rapidly. Referring the reader to references five and six for the details of Ewald's method, we have the following representation for the lattice summations appearing in eq (4):

$$\varphi(\mathbf{x};\mathbf{r}) = \sum_{\mathbf{l}} |\mathbf{r}_l^+ + \mathbf{x} + \mathbf{r}|^{-1}$$

$$= \frac{\pi}{v_c}\frac{1}{G^2}\sum_{\mathbf{g}} \frac{\exp(-g^2/4G^2)}{(g^2/4G^2)} \cos\mathbf{g}\cdot(\mathbf{x}+\mathbf{r})$$

$$+ \sum_{\mathbf{l}} |\mathbf{r}_l^+ + \mathbf{x} + \mathbf{r}|^{-1} \operatorname{erfc}\{G|\mathbf{r}_l^+ + \mathbf{x} + \mathbf{r}|\}, \tag{8}$$

when

$$\mathbf{x}+\mathbf{r}\neq 0$$

and

$$\varphi(\mathbf{x}=0;\ \mathbf{r}=0)=\sum_{\mathbf{l}\neq 0}|\mathbf{r}_l^+|^{-1}$$

$$=\frac{\pi}{v_c}\frac{1}{G^2}\sum\frac{\exp(-g^2/4G^2)}{(g^2/4G^2)}$$

$$+\sum_{\mathbf{l}\neq 0}|\mathbf{r}_l^+|^{-1}\ \mathrm{erfc}\ \{G|\mathbf{r}_l^+|\}-\frac{2G}{\sqrt{\pi}}. \qquad (9)$$

We choose the quantity G so that the series in $\mathbf{g}$ and the series in $\mathbf{l}$ are both rapidly convergent. The complementary error function erfc (z) is defined by

$$\mathrm{erfc}\ (z)=(2/\sqrt{\pi})\int_z^\infty \exp(-y^2)dy$$

and is normalized so that erfc $(0)=1$. Hence, the potential energy for a cation displaced a distance $\mathbf{r}$ from its perfect lattice site is

$$V_c(\mathrm{NaCl};\ \mathbf{r})=Z_c[Z_c\varphi(\mathbf{x}=0;\ \mathbf{r})+Z_a\varphi(\mathbf{x}_a;\ \mathbf{r})], \qquad (10)$$

and

$$V_c(\mathrm{CaF_2};\mathbf{r})=Z_c[Z_c\varphi(\mathbf{x}=0;\mathbf{r})+Z_a\{\varphi(\mathbf{x}_a(1);\mathbf{r})+\varphi(\mathbf{x}_a(2);\mathbf{r})\}]; \qquad (11)$$

and the potential energy for an anion displaced a distance $\mathbf{r}$ from its perfect lattice site is

$$V_a(\mathrm{NaCl};\mathbf{r})=Z_a[Z_c\varphi(\mathbf{x}=\mathbf{0};\mathbf{r}-\mathbf{x}_a)+Z_a\varphi(\mathbf{x}_a;\mathbf{r}-\mathbf{x}_a)], \qquad (12)$$

and

$$V_a(\mathrm{CaF_2};\mathbf{r})=Z_a[Z_c\varphi(\mathbf{x}=\mathbf{0};\mathbf{r}-\mathbf{x}_a(1))+Z_a\{\varphi(\mathbf{x}_a(1);\mathbf{r}-\mathbf{x}_a(1))+\varphi(\mathbf{x}_a(2);\mathbf{r}-\mathbf{x}_a(2))\}]. \qquad (13)$$

The ionicity of the cations is Z_c and the ionicity of the anions is Z_a.

We then see from expansion (6) that the term $V_\nu(\mathbf{r}=\mathbf{0})$ and the following types of derivatives

$$(\partial^n V_\nu(\mathbf{r})/\partial x^s\partial y^t\partial z^u)|_{\mathbf{r}=0}$$

must be evaluated, where n, s, t, and u are zero and positive integers and where $n=s+t+u$. We shall use the Ewald representation to compute the term $V_\nu(\mathbf{r}=\mathbf{0})$ in expansion (6). Because the spatial derivatives of the lattice summation (4) for $V_\nu(\mathbf{r})$ lead to expressions which converge more rapidly than the lattice summation (4) itself converges, we find that Ewald's method is not necessary whenever we evaluate $(\partial^n V_\nu(\mathbf{r})/\partial x^s\partial y^t\partial z^u)$ for $n\geq 4$. The evaluation of such derivatives is straight forward but is very tedious. We tabulate in appendix A these derivatives up to order four; i.e., $n\leq 4$.

3. Results

Combining eqs (6), (7) and the equations in appendix A, we write the electrostatic energy in the form,

$$V_\nu(\mathbf{r})=\frac{\alpha_\nu}{r_0}+\frac{1}{r_0}\Big\{(\sigma_1+\sigma_2+\sigma_3)V_{\nu x}+\frac{1}{2}(\sigma_1^2+\sigma_2^2+\sigma_3)V_{\nu 2x}+(\sigma_1\sigma_2+\sigma_2\sigma_3+\sigma_3\sigma_1)V_{\nu xy}+\frac{1}{6}(\sigma_1^3+\sigma_2^3+\sigma_3^3)V_{\nu 3x}+\frac{1}{2}(\sigma_1^2\sigma_2+\sigma_2^2\sigma_3+\sigma_3^2\sigma_1+\sigma_1\sigma_2^2+\sigma_2\sigma_3^2+\sigma_3\sigma_1^2)V_{\nu 2xy}+\sigma_1\sigma_2\sigma_3V_{\nu xyz}+\frac{1}{24}(\sigma_1^4+\sigma_2^4+\sigma_3^4)V_{\nu 4x}+\frac{1}{6}(\sigma_1\sigma_2^3+\sigma_1^3\sigma_2+\sigma_2\sigma_3^3+\sigma_2^3\sigma_3+\sigma_3\sigma_1^3+\sigma_3^1\sigma_1)V_{\nu 3xy}+\frac{1}{4}(\sigma_1^2\sigma_2^2+\sigma_2^2\sigma_3^2+\sigma_3^2\sigma_1^2)V_{\nu 2x2y}+\frac{1}{2}(\sigma_1^2\sigma_2\sigma_3+\sigma_1\sigma_2^2\sigma_3+\sigma_1\sigma_2\sigma_3^2)V_{\nu 2xyz}+\cdots\Big\}. \qquad (14)$$

The series coefficients $V_{\nu sxtyuz}$ are the derivatives $(\partial^n V_\nu/\partial x^s\partial y^t\partial z^u)$ evaluated at $\mathbf{r}=\mathbf{0}$. We list in table 1 the Madelung constants α_ν and the series coefficients $V_{\nu sxtyuz}$ for the NaCl and CaF_2 structures.

TABLE 1. *The Madelung constant α_ν and the series coefficients $V_{\nu sxtyuz}$ which appear in eq (14) for* NaCl *and* CaF_2 *structures*

The reference ion moves a distance r given by eq (7) from its perfect lattice site. The reference distance is the nearest neighbor distance r_0; $r_0=(a/2)$ for NaCl structures and $r_0=(\sqrt{3}a/4)$ for CaF_2 structures. The number $N\times 10^{+n}$ is denoted by $N+0n$.

Reference ion	NaCl structures		CaF_2 structures	
	Cation	Anion	Cation	Anion
α_ν	−1.7476	+1.7476	−7.565	+4.070
$V_{\nu x}$	0.0	0.0	0.0	0.0
$V_{\nu 2x}$	0.0	0.0	0.0	0.0
$V_{\nu xy}$	0.0	0.0	0.0	0.0
$V_{\nu 3x}$	0.0	0.0	0.0	0.0
$V_{\nu 2xy}$	0.0	0.0	0.0	0.0
$V_{\nu xyz}$	0.0	0.0	0.0	.1664+02
$V_{\nu 4x}$	−.2148+02	+.2148+02	+.2983+02	−.4843+02
$V_{\nu 3xy}$	0.0	0.0	0.0	0.0
$V_{\nu 2x2y}$	+.1074+02	−.1074+02	−.1491+02	+.2423+02
$V_{\nu 2xyz}$	0.0	0.0	0.0	0.0

The author acknowledges several helpful conversations with A. D. Franklin.

4. Appendix A: Derivatives of the Electrostatic Potential

The $\mathbf{r}\cdot\nabla$ operator which appears in eq (6) is

$$\mathbf{r}\cdot\nabla=\left(\sigma_1'\frac{\partial}{\partial x}+\sigma_2'\frac{\partial}{\partial y}+\sigma_3'\frac{\partial}{\partial z}\right), \tag{A1}$$

where $\sigma_i'=(a/4)\sigma_1$. Let us denote a given term in the series (4) by $T=(x^2+y^2+z^2)^{-1/2}=r^{-1}$. We then list the spatial derivatives up to order four:

$$\frac{\partial T}{\partial x}=-\frac{x}{r^3};$$

$$\frac{\partial^2 T}{\partial x\partial y}=\frac{3xy}{r^5},\ \frac{\partial^2 T}{\partial x^2}=\frac{3x^2}{r^5}-\frac{1}{r^3};$$

$$\frac{\partial^3 T}{\partial x\partial y\partial z}=\frac{-15xyz}{r^7},\ \frac{\partial^3 T}{\partial x^2\partial y}=\frac{-15x^2y}{r^7}+\frac{3y}{r^5},$$

$$\frac{\partial^3 T}{\partial x^3}=-\frac{15x^3}{r^6}+\frac{9x}{r^5};$$

$$\frac{\partial^4 T}{\partial x^2\partial y\partial z}=\frac{105x^2yz}{r^9}-\frac{15yz}{r^7},$$

$$\frac{\partial^4 T}{\partial x^3 y}=\frac{105x^3y}{r^9}-\frac{45xy}{r^7},$$

$$\frac{\partial^4 T}{\partial x^2\partial y^2}=\frac{105x^2y^2}{r^9}-\frac{15(x^2+y^2)}{r^7}+\frac{3}{r^5},$$

$$\frac{\partial^4 T}{\partial x^4}=\frac{105x^4}{r^9}-\frac{90x^2}{r^7}+\frac{9}{r^5}.$$

5. References

[1] Bennett, H. S., Phys. Rev. **169,** 729 (1968).
[2] Gourary, B. S., and Adiran, F. J., Phys. Rev. **105,** 1180 (1957).
[3] Kojima, T., J. Phys. Soc. Japan **12,** 918 (1957).
[4] Wood, R. F., and Joy, H. W., Phys. Rev. **136,** A451 (1964).
[5] Ziman, J. M., Principles of the Theory of Solids, p. 37. (Cambridge University Press, Cambridge, England, 1964).
[6] Tosi, M. P., Solid State Physics **16,** 1, edited by F. Seitz and D. Turnbull (Academic Press Inc., New York, 1964).

(Paper 72A5–513)

JOURNAL OF RESEARCH of the National Bureau of Standards—A. Physics and Chemistry
Vol. 72A, No. 5, September–October 1968

Electric Fields Produced by a Charge Density in Ionic Crystals

Herbert S. Bennett

Institute for Materials Research, National Bureau of Standards, Washington, D.C. 20234

(June 12, 1968)

Spatially extended defects such as the F center give rise to an effective defect charge density which may produce important polarizations in the crystal. The electric field in the crystal depends upon these induced dipoles. Lattice summations for the contribution to the electric field which arises from ionic shells centered about the defect are evaluated for the NaCl and CaF_2 lattice structures.

Key Words: CaF_2; dipole shell coefficient; electric fields; NaCl; polarization; spatially extended defects.

1. Introduction

We shall evaluate in this paper the ionic and electronic polarizations which defects induce in ionic crystals. Such polarizations play a major role in the energy of formation, the mobility, the self energy, and the electronic structure of defects.

We shall consider an ionic crystal which contains one molecule $M_{n_+}X_{n_-}$ per volume v_c of the crystal. The volume v_c is the volume of a unit cell and is given by

$$v_c = \mathbf{a}_1 \cdot (\mathbf{a}_2 \times \mathbf{a}_3), \tag{1}$$

where $\mathbf{a}_1$, $\mathbf{a}_2$, and $\mathbf{a}_3$ are the primitive translational vectors. For NaCl and CaF_2 structures, the primitive translational vectors are $\mathbf{a}_1 = (a/2)(0, 1, 1)$, $\mathbf{a}_2 = (a/2)(1, 0, 1)$ and $\mathbf{a}_3 = (a/2)(1, 1, 0)$, and the volume of the unit cell is $v_c = a^3/4$. The lattice constant a is the cation-cation distance. The nearest neighbor distance (cation-anion) is $r_0 = (a/2)$ for NaCl structures and $r_0 = (\sqrt{3}/4)a$ for CaF_2 structures. The cations are at

$$\mathbf{r}^+ = (a/2)[(l_2+l_3)\hat{x} + (l_3+l_1)\hat{y} + (l_1+l_2)\hat{z}].$$

The anions for NaCl structures are at

$$\mathbf{r}^- = \mathbf{r}^+ + (a/4)(\hat{x}+\hat{y}+\hat{z}),$$

and the anions for CaF_2 structures are at

$$\mathbf{r}_1^- = \mathbf{r}^+ + (a/4)(\hat{x}+\hat{y}+\hat{z}),$$

and at

$$\mathbf{r}_2^- = \mathbf{r}^+ + (a/4)(-\hat{x}-\hat{y}-\hat{z}).$$

The integers l_i have the values $0, \pm 1, \pm 2$, etc. The above discussion places a cation at the origin. We shall treat also the case for which an anion is at the origin. For this latter case we have the reference vectors $\mathbf{r}_a = (a/2)(0, 0, 1)$ for NaCl structures and $\mathbf{r}_a = (a/4)(-1, -1, -1)$ for CaF_2 structures.

We view the anions X and the cations M as polarizable point charges occupying the lattice sites. The anion ionicity is Z_a and the cation ionicity is Z_c. The unit cell is electrically neutral, $n_+Z_c + n_-Z_a = 0$. We also associate an ionic polarizability α_a^d or α_c^d and an electronic polarizability α_a^e or α_c^e with each ion in the lattice. These polarizabilities determine the response of the crystal to weak static and high frequency electric fields. We represent an ion which is located at the lattice site $\mathbf{r}_\nu$ and which experiences a static electric field $\mathbf{E}(\mathbf{r}_\nu)$ as a point charge $Z_a e$ or $Z_c e$ located at $\mathbf{r}_\nu$ and upon which we superpose a point dipole moment

$$\boldsymbol{\mu}(\mathbf{r}_\nu) = (\alpha^e + \alpha^d)\mathbf{E}(x_\nu). \tag{2}$$

When the period of the electric field is much shorter than the characteristic period for ionic motion but also longer than the orbital period for the electrons about the ion, the point dipole moment is

$$\boldsymbol{\mu}(\mathbf{r}_\nu) = \alpha^e \mathbf{E}(\mathbf{r}_\nu). \tag{3}$$

We assume that the response is linear in the electric

field. In general, the polarizability is a tensor. However, we choose here for convenience that it be diagonal and isotropic. This is a very reasonable assumption for cubic crystals. When we view an ionic crystal as a dielectric continuum, the static dielectric constant ϵ_0 and the high frequency (optical) dielectric constant ϵ_∞ give us information about the ionic and electronic dipoles which are induced by weak electric fields.

For our purposes here, we may represent the defect by a spatially dependent charge density $\rho(r)$ [1].[1] For example, the F center in an ionic crystal consists of an electron (the F electron) localized about an anion vacancy. We choose the anion vacancy to be at the lattice site $\mathbf{r}=\mathbf{0}$. We characterize quantum mechanically the F electron by its stationary wave function $\psi_n(\mathbf{r})$ with energy eigenvalue ϵ_n where n represents all the quantum numbers of the given state. The F electron gives rise to the spatial charge density

$$\rho_r(\mathbf{r}) = -e\psi_n^*(\mathbf{r})\psi_n(\mathbf{r}).$$

Also, we view the anion vacancy as the addition of a positive point charge $Z_v e = -Z_a e$ at the site $r=0$ $\rho_v(\mathbf{r}) = Z_v e\delta^3(\mathbf{r})$. The total charge density $\rho_d(\mathbf{r})$ of the F center at $\mathbf{r}=\mathbf{0}$ then becomes.

$$\rho_d(\mathbf{r}) = e[Z_v\delta^3(\mathbf{r}) - \psi_n^*(\mathbf{r})\psi_n(\mathbf{r})]. \tag{4}$$

The total electric field which a polarizable ion experiences is the sum of the electric field due to the defect charge density $\rho_d(\mathbf{r})$ and the electric field due to the electronic dipoles and the ionic dipoles which the defect charge density induces on all the other ions of the crystal. A. D. Franklin and D. J. Sparks [2] have computed the electric fields produced by a point charge $\rho_p(\mathbf{r}) = Z_{\text{eff}} e\delta^3(\mathbf{r})$ in ionic crystals. We will compute in this paper the electric fields produced by extended charge distributions in the NaCl and CaF_2 lattice structures.

Our intended research on the electronic structure of the F center motivates us to carry out the present computations. The F electron and the lattice, particularly the nearest neighbors to the defect, form a very strongly interacting system which we must treat self-consistently. The polarizations which accompany the F center are most important when we use the polarizable ion theory for the F center [1].

2. Formulation

In order to make the present computations feasible, we shall consider only the spherically symmetric part $\rho_s(r)$ of the charge density $\rho_d(\mathbf{r})$; i.e., we average $\rho_d(\mathbf{r})$ over the unit sphere.

$$\rho_s(r) = (4\pi)^{-1}\int_0^{2\pi} d\phi \int_0^{\pi} \sin\phi d\phi \rho(\mathbf{r}), \tag{5}$$

where $r=|\mathbf{r}|$. For convenience, we will suppress the subscript s.

The electrostatic potential $\phi(r_1)$ at the point $\mathbf{r}_1$ due to the spherically symmetric part $\rho(r)$ of the defect charge density $\rho_d(\mathbf{r})$ is given by the expression,

$$\phi(r_1) = \frac{\int_0^{r_1} \rho(r) r^2 dr}{r_1} + \int_{r_1}^{\infty} \frac{\rho(r) r^2 dr}{r}. \tag{6}$$

We do not allow the dielectric response of the system to enter in eq (6). The negative gradient of the electrostatic potential then prescribes the electric field $\mathbf{E}_d(\mathbf{r}_1)$ at $\mathbf{r}_1$ due to the charge density $\rho(r)$;

$$\mathbf{E}_d(\mathbf{r}_1) = E_d(\mathbf{r}_1)\hat{r}_1 = -\frac{\partial\phi(r_1)}{\partial r_1}\hat{r}_1 = \frac{\int_0^{r_1}\rho(r)r^2dr}{r_1^2}\hat{r}_1, \tag{7}$$

where $\hat{r}_1 = \mathbf{r}_1/|\mathbf{r}_1|$ is the unit vector in the direction $\mathbf{r}_1$. We also define the average amount of charge $Q(r)$ contained within a sphere of radius r centered about $r=0$,

$$Q(r) = \int_0^r \rho(r_1) r_1^2 dr_1. \tag{8}$$

Combining eqs (7) and (8) gives us

$$E_d(r) = r^{-2}Q(r). \tag{9}$$

The electric field $\mathbf{E}_d(\mathbf{r}_\nu)$ at $\mathbf{r}_\nu$ due to the defect charge density induces a dipole moment $\boldsymbol{\mu}(\mathbf{r}_\nu)$ on the ion at site $\mathbf{r}_\nu$. The electric field at the site $\mathbf{r}_{\nu_1}$ due to the dipole moment $\boldsymbol{\mu}(\mathbf{r}_\nu)$ at the site $\mathbf{r}_\nu$ is

$$\mathbf{E}_{\text{dip}}(\mathbf{r}_{\nu_1};\mathbf{r}_\nu) = \frac{3(\mathbf{r}_{\nu_1}-\mathbf{r}_\nu)[\boldsymbol{\mu}(\mathbf{r}_\nu)\cdot(\mathbf{r}_{\nu_1}-\mathbf{r}_\nu)]}{|\mathbf{r}_{\nu_1}-\mathbf{r}_\nu|^5} - \frac{\boldsymbol{\mu}(\mathbf{r}_\nu)}{|\mathbf{r}_{\nu_1}-\mathbf{r}_\nu|^3}. \tag{10}$$

The total electric field which the polarizable ion at $\mathbf{r}_\nu$ experiences is the sum of the electric field due to the defect and the electric field due to the dipoles induced on all the other ions except the ion at $\mathbf{r}_\nu$,

$$E_{\text{tot}}(\mathbf{r}_\nu) = \mathbf{E}_d(\mathbf{r}_\nu) + \sum_{\nu_1\neq\nu}{}' \mathbf{E}_{\text{dip}}(\mathbf{r}_\nu;\mathbf{r}_{\nu_1}), \tag{11}$$

where the prime denotes a sum over all lattices sites except the site $\mathbf{r}_{\nu_1}=\mathbf{r}_\nu$. Multiplying the left and right hand sides of eq (11) by the appropriate polarizability for the ion at $\mathbf{r}_\nu$ converts eq (11) to a system of $3N$ equations having $3N$ unknown variables—the three components of the dipole moments $\boldsymbol{\mu}(\mathbf{r}_\nu)$ at each of the N sites in the lattice. Because N has the same order of magnitude as Avogadro's number, we cannot solve the system of equations given by eq (11). Hence, we must make further approximations. The approxima-

[1] Figures in brackets indicate the literature references at the end of this paper.

tions which we will employ to overcome the above formidable task are known as the Mott-Littleton procedure [3].

We divide the crystal into two regions. Region I contains all the ions on shells centered about the defect and having a radius less than or equal to r_s. The radius r_s is the radius of the sth shell of ions centered about the defect. Region II contains all the remaining ions. The Mott-Littleton procedure solves the system of equations given by eq (11) for only region I and employs a continuum model to approximate the solutions for the dipole moments of region II.

We first outline the prescription for the dipole moments in region II. We view region II as a dielectric continuum. The electric field $\mathbf{E}$ and the displacement vector $\mathbf{D}$ are related in region II by the constituitive equation for a dielectric continuum,

$$\mathbf{D}(\mathbf{r})=\epsilon\mathbf{E}(\mathbf{r})=\mathbf{E}(\mathbf{r})+4\pi\mathbf{P}(\mathbf{r}), \tag{12}$$

where ϵ is the appropriate dielectric constant and the polarization $\mathbf{P}(\mathbf{r})$ is the dipole moment per unit volume,

$$\mathbf{P}(\mathbf{r})=[(\epsilon-1)/4\pi]\mathbf{E}(\mathbf{r}). \tag{13}$$

The dipole moment per unit cell at $\mathbf{r}_l$ is,

$$\mathbf{P}_c(\mathbf{r}_l)=v_c\mathbf{P}(\mathbf{r})=v_c[(\epsilon-1)/4\pi]\mathbf{E}(\mathbf{r}) \tag{14}$$

The Mott-Littleton presecription asserts that all dipole moments point in a radial direction from the defect and divides the dipole moment per unit cell among the $n_+ + n_-$ ions contained in the unit cell in proportion to their individual polarizabilities;

$$\boldsymbol{\mu}_{\mathrm{II}}(\mathbf{r}_\nu)=\frac{\alpha_\nu}{(n_+\alpha_c+n_-\alpha_a}\, v_c\, \frac{(\epsilon-1)}{4\pi}\, \frac{\mathbf{E}_d(\mathbf{r}_\nu)}{\epsilon_1}\, \hat{r}_\nu \tag{15}$$

When treating the F center problem one must distinguish between the electronic polarizations and the ionic polarizations. The electronic polarizations respond to the rapid changes in $\rho_d(\mathbf{r})$ which occur whenever the F electron undergoes a transition from one state to another state. However, the ionic polarizations may not respond to such rapid changes in $\rho_d(\mathbf{r})$. Hence, when $\epsilon_1=\epsilon_\infty$, then ϵ must be ϵ_∞. But when $\epsilon_1=\epsilon_0$, $\epsilon=\epsilon_\infty$ when we compute only the electronic polarizations and $\epsilon=\epsilon_0$ when we compute both the electronic and ionic polarizations. When both ionic and electronic polarizations occur $\alpha_\nu=\alpha_\nu^e+\alpha_\nu^d$ and when only electronic polarizations occur $\alpha_\nu=\alpha_\nu^e$. Referring to eq (15) we define the polarizability of an ion in region II by the quantity,

$$M_{\mathrm{II}}(\nu)=\frac{\alpha_\nu v_c(\epsilon-1)}{4\pi\epsilon_1(n_+\alpha_c+n_-\alpha_a)}. \tag{16}$$

The electric field at a site $\mathbf{r}_1$ in region I due to all the dipoles [eq (15)] in region II is

$$\mathbf{E}_{\mathrm{out}}(\mathbf{r}_1)=\sum_{\substack{\nu\\ r_\nu>r_s}}\frac{Q(r_\nu)M_{\mathrm{II}}(\nu)}{r_\nu^3|\mathbf{r}_1-\mathbf{r}_\nu|^3}\left[\frac{3(\mathbf{r}_1-\mathbf{r}_\nu)\{\mathbf{r}_\nu\cdot(\mathbf{r}_1-\mathbf{r}_\nu)\}}{|\mathbf{r}_1-\mathbf{r}_\nu|^2}-\mathbf{r}_\nu\right]. \tag{17}$$

The summation is over all the sites in region II. The radial part of $\mathbf{E}_{\mathrm{out}}(\mathbf{r}_1)$, $E_{\mathrm{out}}(\mathbf{r}_1)=\mathbf{E}_{\mathrm{out}}(\mathbf{r}_1)\cdot(\mathbf{r}_1/|\mathbf{r}_1|)$, is given by,

$$E_{\mathrm{out}}(\mathbf{r}_1)=\sum_{\substack{\nu\\ r_\nu>r_\nu}}\frac{Q(r_\nu)M_{\mathrm{II}}(\nu)}{r_1r_\nu^3|\mathbf{r}_1-\mathbf{r}_\nu|^5}\times[2(\mathbf{r}_\nu\cdot\mathbf{r}_1)r_1^2-3r_\nu^2r_1^2-(\mathbf{r}_\nu\cdot\mathbf{r}_1)^2+2\mathbf{r}_\nu^2(\mathbf{r}_\nu\cdot\mathbf{r}_1)]. \tag{18}$$

When we express the summation which appears in eq (18) in terms of a summation over the shells, we may evaluate more easily the radial part of $\mathbf{E}_{\mathrm{out}}(\mathbf{r}_1)$. Each shell of ions centered about the defect has ions of the same type and each ion of shell s exhibits the same polarizability $M_{\mathrm{II}}(\nu)=M_{\mathrm{II}}(s)$. Hence, we may write an alternate expression, which is computationally more practical, for the radial field $E_{\mathrm{out}}(\mathbf{r}_1)$; namely,

$$E_{\mathrm{out}}(\mathbf{r}_1)=r_0^{-5}\sum_{s'>s}Q(\mathbf{r}_{s'})M_{\mathrm{II}}(s')D(s',\mathbf{r}_1). \tag{19}$$

The dipole coefficients for each shell s, which is outside region I, $D(s;\mathbf{r}_1)$ is a summation over the $n(s)$ ions on the sth shell;

$$D(s;\mathbf{r}_1)=\sum_{m=1}^{n(s)}\frac{r_0^5}{r_1r_s^3|\mathbf{r}_1-\mathbf{r}_m|^5}\times[2(\mathbf{r}_m\cdot\mathbf{r}_1)r_1^2-3r_m^2r_1^2-(\mathbf{r}_m\cdot\mathbf{r}_1)^2+2r_m^2(\mathbf{r}_m\cdot\mathbf{r}_1)]. \tag{20}$$

where the site $\mathbf{r}_m$ is the position of the mth ion of shell s and $|\mathbf{r}_m|=r_s$.

We may show from cubic symmetry arguments and from the assumption of radial dipoles that the dipole coefficient $D(s,\mathbf{r}_1)$ evaluated for the lattice site $\mathbf{r}_1$ on shell t in region I is the same for all the other lattice sites $\mathbf{r}_m$ on the same shell t in region I.

The system of equations for the dipole moments, eq (11), is tractable only when region I contains a small number of shells; e.g., u shells. Incorporating eqs (19) and (20) into eq (11) and assuming that the dipole moments in region I also are radially directed, we may reduce the system of equations given by eq (11) to u equations containing the u dipole moments on the ions in region I. The magnitude of each dipole moment at the lattice sites on a given shell will be the same.

3. Results

The experience which we have gained from our study of the F center in the alkaline earth oxide CaO [4] indicates that reasonable agreement with experiment obtains when we use the first order Mott-Littleton pro-

cedure to evaluate the polarizations associated with the F center. We shall present therefore the first order Mott-Littleton prescription in order to demonstrate a specific example of how one might use the preceding discussion.

The first order Mott-Littleton approximation states that region I contains only the first shell and that region II contains all the remaining shells. The first shell about an anion defect contains n_c cations at a distance $r_1 = r_0$ from the defect center. Again, we assume that the induced dipole moment on an ion in the first shell points in a radial direction and has a magnitude μ_1. The radial electric field at the site $\mathbf{r}_1$ due to the dipole moments $\mu_1 \hat{r}_m$ on the $(n_c - 1)$ other ions on the first shell is

$$E_1 \hat{r}_1 = \frac{\mu_1 C_1 \hat{r}_1}{r_1^3}, \tag{21}$$

where the same shell dipole coefficient C_1 is a constant for a given lattice structure. The system of equations represented by eq (11) reduces in the first order Mott-Littleton approximation to one equation for the one unknown dipole moment μ_1; namely,

$$\mu_1 = \alpha_1 \left[\frac{Q(r_1)}{r_1^2} + E_{\text{out}}(r_1) + \frac{\mu_1 C_1}{r_1^3} \right]. \tag{22}$$

Equation (22) then predicts that the dipole moment $\mu_1 \hat{r}_1$ on the ions in the first shell about the defect is

$$\mu_1 \hat{r}_1 = \frac{\alpha_1 \left[\frac{Q(r_1)}{r_1^2} + E_{\text{out}}(r_1) \right]}{\left[1 - \frac{C_1 \alpha_1}{r_1^3} \right]} \hat{r}_1, \tag{23}$$

TABLE 1. *The dipole coefficients* D(s, $\mathbf{r}_1$) *for* NaCl *structures*

The defect site is an anion site and the evaluation site $\mathbf{r}_1$ is a cation site on the first nearest neighbor shell centered about the anion defect site. Region I contains only the first nearest neighbor shell. Region II contains all the remaining shells. The number of cations in the first shell is $n_c = 6$ and the same shell dipole coefficient C_1 for the $(n_c - 1) = 5$ other ions on the first shell is $C_1 = -2.3713$. The radius of shell s is r_s in units of $(a/4)$ and the dipole coefficients $D(s, r_1)$ for the shells outside the first shell are given by eq (20). The lattice constant is a and the nearest neighbor distance is $r_0 = (a/2)$. The dipole coefficients are expressed in the form $N \times 10^n$.

Shell	Radius squared	Dipole coefficient $D(s, r_1)$				Number of ions in shell
		Cation shell		Anion shell		
	r_s^2	N	n	N	n	
2	8			−0.2287	+1	12
3	12	−0.4293	−0			8
4	16			+.3742	−0	6
5	20	+.4580	−1			24
6	24			−.5176	−1	24
7	32			−.1073	−1	12
8	36	−.7591	−2			30
9	40			+.1535	−1	24
10	44	+.3931	−2			24
11	48			−.2678	−2	8
12	52	−.1040	−2			24
13	56			−.3719	−2	48
14	64			+.1112	−2	6
15	68	+.8232	−3			48
16	72			+.9372	−3	36
17	76	−.8172	−3			24
18	80			+.3199	−3	24
19	84	+.1159	−3			48
20	88			−.6631	−3	24
21	96			−.2046	−3	24
$\sum_s D(s, r_1)$		−.3881		−1.965		

where $E_{\text{out}}(r_1)$ is given by eq (19) in terms of the dipole coefficients $D(s, \mathbf{r}_1)$.

We list in tables 1 and 2 the dipole coefficients $D(s, \mathbf{r}_1)$ for the NaCl and CaF_2 structures. The computer program used to evaluate the dipole coefficients may be easily modified to treat defects centered about cations and to treat any number of shells in region I. The results given in tables 1 and 2 are applicable directly to the F center problem.

The author thanks A. D. Franklin for many informative discussions.

TABLE 2. *The dipole coefficients* D(s, $\mathbf{r}_1$) *for* CaF_2 *structures*

The defect site is an anion site and the evaluation site $\mathbf{r}_1$ is a cation site on the first nearest neighbor shell centered about the anion defect site. Region I contains only the first nearest neighbor shell. Region II contains all the remaining shells. The number of cations in the first shell is $n_c = 4$ and the same shell dipole coefficient C_1 for the $(n_c - 1) = 3$ other ions on the first shell is $C_1 = -1.1482$. The radius of shell s is r_s in units of $(a/4)$ and the dipole coefficients $D(s, r_1)$ for the shells outside the first shell are given by eq (20). The lattice constant is a and the nearest neighbor distance is $r_0 = (3^{1/2}a/4)$. The same shell coefficient C_1 given in ref. 2 is expressed in terms of the anion-anion distance and the above value is in terms of the anion-cation distance. The dipole coefficients are expressed in the form $N \times 10^n$.

Shell	Radius squared	Dipole coefficient $D(s, r_1)$				Number of ions in shell
		Cation shell		Anion shell		
	r_s^2	N	n	N	n	
2	4			−0.3170	+1	6
3	8			−.5616	−0	12
4	11	−.3580	−0			12
5	12			+.3263	−0	8
6	16			−.4316	−1	6
7	19	+.8516	−1			12
8	20			−.3001	−1	24
9	24			+.1424	−1	24
10	27	−.1084	−1			16
11	32			+.5379	−3	12
12	35	−.1090	−1			24
13	36			+.2722	−2	30
14	40			−.3217	−2	24
15	43	+.7107	−2			12
16	44			−.8402	−3	24
17	48			+.7626	−3	8
18	51	+.4131	−3			24
19	52			−.4039	−4	24
20	56			+.7445	−3	48
21	59	−.9259	−3			36
22	64			−.2120	−3	6
23	67	−.8697	−3			12
24	68			−.8123	−4	48
25	72			−.2217	−3	36
26	75	−.1190	−3			28
27	76			+.1574	−3	24
28	80			−.8521	−4	24
29	83	+.1069	−2			36
30	84			−.3467	−4	48
31	88			+.1588	−3	24
32	91	−.2775	−3			24
33	96			+.4782	−4	24
$\sum_s D(s, r_1)$		−.2882		−3.464		

4. References

[1] Bennett, H. S., Phys. Rev. **169**, 729 (1968).
[2] Franklin, A. D., and Sparks, D. J., J. Res. NBS **71A** (Phys. and Chem.). No. 1, 1 (1967).
[3] Mott, N. F., and Littleton, M. J., Trans. Far. Soc. **34**, 485 (1938).
[4] Bennett, H. S., Bull. Am. Phys. Soc. Ser. II, **13**, 420 (1968); and to be published.

(Paper 72A5–514)

JOURNAL OF RESEARCH of the National Bureau of Standards—A. Physics and Chemistry
Vol. 72A, No. 5, September–October 1968

Mass Spectrometric Study of the Photoionization of Some Fluorocarbons and Trifluoromethyl Halides*

Clemente Juan Noutary**

(June 16, 1968)

The photoionization curves and the threshold energies for the molecule and several abundant fragment ions of CF_4, C_2F_6, C_3F_8, C_4F_{10}, CF_3H, CF_3Cl, CF_3Br, and CF_3I have been measured. The threshold energies are correlated and the ionic heats of formation and some bond dissociation energies are calculated. It is apparent that the values obtained for the CF_3^+ ions are not the adiabatic ones, but include large amounts of excess energy. This excess is the lowest for the CF_3^+ from CF_3I for which an explanation is suggested. Assuming that the excess is not zero for the last compound we obtain the following upper limits: $\Delta Hf_0^\circ(CF_3)^+ \leq +365.3$ kJ mol^{-1} $= +87.3$ kcal mol^{-1}; $I(CF_3)^+ \leq 8.62$ eV; $I(C_2F_5)^+ \leq 8.72$ eV; $I(C_3F_7)^+ \leq 8.70$ eV; $I(C_4F_9)^+ \leq 8.68$ eV. From the mean value $D(C_p - C_p) = 402 \pm 2$ kJ mol^{-1} $= 96.0 \pm 0.5$ kcal mol^{-1} the bond dissociation energies $D(C_p - C_s) = 363 \pm 3$ kJ mol^{-1} $= 86.8 \pm 0.8$ kcal mol^{-1} and $D(C_s - C_s) = 337 \pm 4$ kJ mol^{-1} $= 80.6 \pm 1.0$ kcal mol^{-1} and $D(C_p - F) = 525$ kJ mol^{-1} $= 125.7$ kcal mol^{-1} are calculated.

Key Words: CF_4; C_2F_6; C_3F_8; C_4F_{10}; CF_3H; CF_3Cl; CF_3Br; CF_3I; heats of formation; ionization energies; mass spectrometric; photoionization; vacuum ultraviolet.

1. Introduction

The spectra, ionization and dissociation energies of various ions from fluorocarbons and trifluoromethyl halides have been measured by electron impact [1–11][1] or spectroscopically [12] by several authors. The heat of formation and the bond dissociation energies have also been measured or calculated by various methods [13–26]. Many of those values are not in good agreement. However, recent measurements have given improved values for some fundamental data—from which most bond energies are derived—such as the heat of formation of HF in aqueous solution by Johnson et al. [30] and the heat of formation of CF_4 by Domalski and Armstrong [31]. General and critical reviews have been made by Benson [27], Kerr [28], and Lacher and Skinner [29].

The photoionization of the (CF_3) free radical has also been measured recently by Lifshitz and Chupka [32]. Thus it has seemed worthwhile to remeasure by photon impact the ionization energies of selected positive ions from several fluorocarbons. To assist in the interpretation of the results we include measurements of trifluoromethyl halides and fluoroform. All of these results are reported and discussed in this paper.

2. Experimental Procedure

Measurements were made by means of an instrument previously described [33]. It consists of a single focusing, 15 cm radius, 60 degree deflection mass spectrometer with a Seya-Namioka vacuum ultraviolet monochromator of a focal length of 1 m and a resolution of 1 Å with both slits of the monochromator fixed at 0.1 mm. The gold-coated 1200 groove/mm grating could be manually rotated with a resetability better than 0.5 Å.

The wavelengths were measured with an accuracy better than 1 Å. The photon sources used were as follows:

1. From 1400 to 1050 Å the continuum discharge in argon at a pressure of 400 mm excited by means of a 800 W 2450 MHz microwave generator.
2. From approximately 1100 to 900 Å the many-lined spectrum produced by microwave discharge in hydrogen.
3. From 950 to 600 Å the Hopfield continuum excited by a d-c discharge in helium at a pressure of 250 mm.

The relative photon intensity was measured by the photoelectric effect on a piece of chemically clean tungsten intercepting the beam of light when it leaves

*Work performed under the auspices of the International Atomic Energy Agency (Vienna, Austria) through the National Academy of Sciences (Washington, D.C.) and supported in part by the U.S. Atomic Energy Commission.

**Guest worker, Institute for Materials Research, National Bureau of Standards, Washington, D.C. 20234. Permanent address: Comisión Nacional de Energía Atómica, Buenos Aires, Argentina.

[1] Figures in brackets indicate the literature references at the end of this paper.

the ion source. A correction for the sensitivity of photon detection as a function of the wavelength was introduced according to Wheaton [34]. The ion current was measured with a 20 stage electron multiplier, a preamplifier, an amplifier, and scaler.

An empirical formula was established to correct for the decrease in the sample reservoir pressure, the molecular weight and the viscous flow of the gas through the leak. A program to permit all the above processing of the data by computer was written and used in most of this work.

A smoothing computational procedure using Chebyshev polynomials was also applied to some curves using a program developed at the NBS by R. B. Parlin, but all the ionization thresholds were determined before introducing any smoothing.

The gases used were obtained from commercial sources and purities, as stated by the suppliers, were generally better than 99.5 mole percent. Mass spectra indicated no interfering impurities significant to these measurements.

3. Results

Some typical photoionization yield curves for fluorocarbons and perfluoromethyl halides are shown in figures 1 to 5. The wavelength is plotted in the abscissa and the ion yield (ion current per photon transmitted through the ion source) is plotted in arbitrary units on the ordinate.

Molecular ions were not observed in any of the fluorocarbons but they appeared in all the perfluoromethyl halides and in fluoroform. The CF_3^+ ions were the most abundant in all the molecules examined at a wavelength of 584 Å. The observed ionization thresholds of all ions are summarized in table 1.

CF_3^+ ion from CF_4. The onset was located at 799 ± 1 Å in good agreement with that of 796.7 Å found by Cook et al. [12]. It was gradual and smooth with no hot bands or autoionization peaks observed. The principal feature is a very definite increase in slope at approximately 725 Å suggesting that at higher energies two ionization mechanisms are superimposed.

$C_2F_5^+$ ion from C_2F_6. The onset is at 805 Å and the curve is smooth and gradual until 720 Å. Then to 685 Å a partially resolved structure probably due to autoionization is observed and also another one near 650 Å.

CF_3^+ ion from C_2F_6. The threshold at 910 Å is followed by a very long and continuous slope until 600 Å with some structure superimposed near 730 Å – 690 and 640 Å probably due to some autoionization.

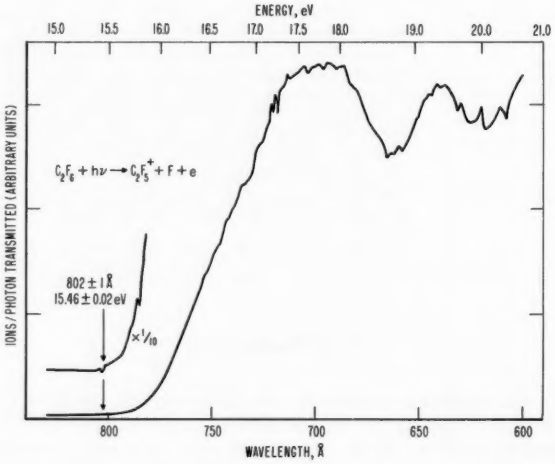

FIGURE 2. *Ionization curve for* $C_2F_5^+$ *ion from* C_2F_6.

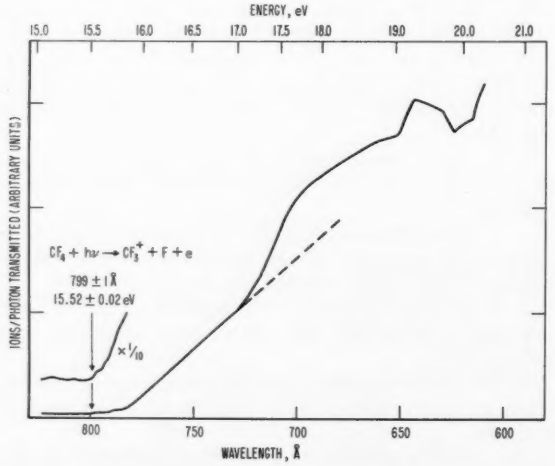

FIGURE 1. *Ionization curve for* CF_3^+ *ion from* CF_4.

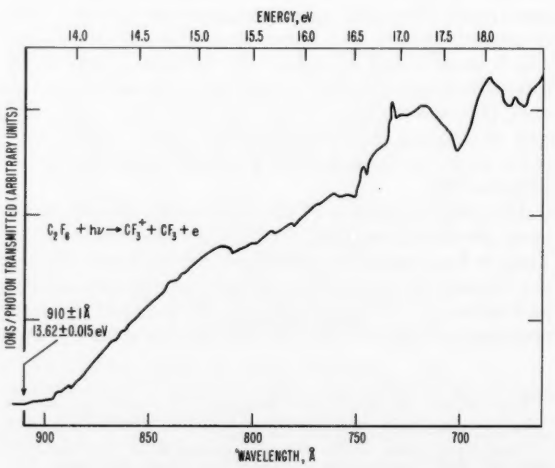

FIGURE 3. *Ionization curve for* CF_3^+ *ion from* C_2F_6.

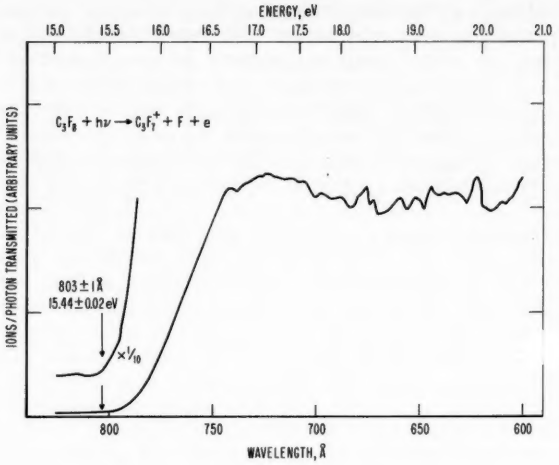

FIGURE 4. *Ionization curve for* $C_3F_7^+$ *ion from* C_3F_8.

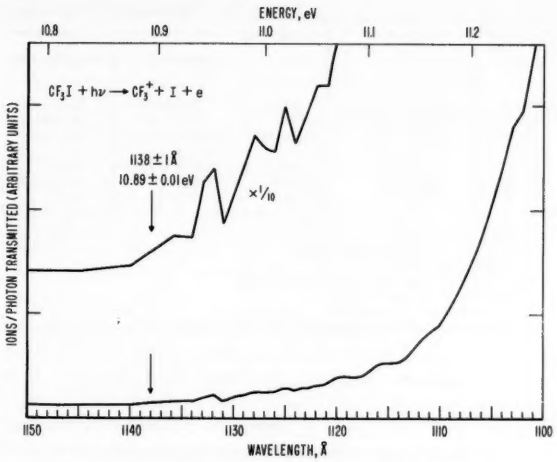

FIGURE 5. *Ionization curve for* CF_3^+ *ion from* CF_3I.

TABLE 1. *Summary of experimental ionization thresholds*

Substance	Ion	Å	eV	kJ mol^{-1}	kcal mol^{-1}	Observations
CF_4	$(CF_4)^+$					No ions.
	$CF_3)^+$	799	15.52	1498	357.9	
C_2F_6	$(C_2F_6)^+$					No ions.
	$(C_2F_5)^+$	802	15.46	1492	356.5	
	$(CF_3)^+$	910	13.62	1314	314.1	
	$(CF)^+$	740	16.75	1616	386.3	
C_3F_8	$(C_3F_8)^+$					No ions.
	$(C_3F_7)^+$	803	15.44	1490	356.1	
	$(C_2F_5)^+$	931	13.32	1285	307.2	
	$(CF_3)^+$	938	13.22	1276	304.9	
C_4F_{10}	$(C_4F_{10})^+$					No ions.
	$(C_3F_9)^+$	804	15.42	1488	355.6	
	$(C_3F_7)^+$	932	13.30	1283	306.7	
	$(C_3F_5)^+$	792	15.65	1510	360.9	
	$(C_2F_5)^+$	950	13.05	1259	300.9	
	$(C_2F_3)^+$	792	15.65	1510	360.9	
	$(CF_3)^+$	938	13.22	1276	304.9	
CF_3Cl	$(CF_3Cl)^+$	1001	12.43	1199	286.8	
	$(CF_3)^+$	982	12.57	1213	290.0	
CF_3Br	$(CF_3Br)^+$	Detected but not measured.				Small peak.
	$(CF_3)^+$	1059	11.84	1142	273.0	
CF_3I	$(CF_3I)^+$	1212	10.23	987	236.0	
	$(CF_3)^+$	1138	10.89	1051	251.0	
CF_3H	$(CF_3H)^+$	Detected but not measured.				Small peak.
	$(CF_3)^+$	877	14.14	1364	326.1	

In this and subsequent tables and text, the following equivalences are used: 1 eV molecule^{-1} = 96.4870 kJ mol^{-1}; 1 kcal mol^{-1} = 4.1840 kJ mol^{-1}; 1 cm^{-1} = 12398.1 × 10^{-8} eV.

$C_3F_7^+$ ion from C_3F_8. The curve begins at 803 Å and increases gradually until nearly 745 Å (the onset of the CF^+ ion) where it reaches a flat top.

CF_3^+ from CF_3I. The onset is very gradual and difficult to locate exactly, but definitely at an energy not higher than 10.89 eV. Some structure in the curve (probably due to vibrations in the ion) could be clearly seen when a correction for the scattered light was introduced.

The curves of the remaining ions also exhibit smooth thresholds followed by more or less gradual increases. Occasionally a rapid increase is observed which is interpreted as the beginning of a new dissociation process. No other special characteristics were observed of consequence for this work. It is noteworthy that in these molecules as in the case of hydrocarbon ions [35] little evidence is obtained for autoionization except as noted above.

4. Discussion

The values at room temperature of the heat of formation $\Delta Hf^\circ_{298}(CF_3X)$ and the heat of dissociation $D_{298}(CF_3-X)$ for X = F, Cl, Br, I, H and CF_3 are known. Thus it is possible to derive in each case a value for the heat of formation $\Delta Hf^\circ_{298}(CF_3)$ of the free radical by the relation

$$\Delta Hf^\circ_{298}(CF_3) = \Delta Hf^\circ_{298}(CF_3-X) + D_{298}(CF_3-X) - \Delta Hf^\circ_{298}(X).$$

The values of $\Delta Hf^\circ_0(CF_3X)$ were calculated using the values of $H_{298}-H_0$ given in NBS Technical Note 270–3 [14]. Calling $(CF_3^*)^+$ the ions, excited or not, in the state and with all the excess energy with which they are obtained by photoionization at the threshold, we have calculated:

$$\Delta Hf^\circ_0(CF_3^*)^+ = \Delta Hf^\circ_0(CF_3X) + A(CF_3^*) - \Delta Hf^\circ_0(X)$$

In the case of the free radical CF_3 the value[2] $\Delta Hf^\circ_{298}(CF_3) = -112.5$ kcal mol^{-1} has been obtained by averaging the other six numbers in that column in table 2; it coincides with the value -112.5 ± 1.2 kcal mol^{-1} measured by Coomber and Whittle [21]. The

[2] The use of units of kcal mol^{-1} in portions of this paper is for the purpose of comparing present results with previously published data.

TABLE 2a. *Thermodynamic values (in kcal mol^{-1}) of several fluorocarbons* [a]

ΔHf°_{298}	(CF_3X)	Ref.[b]	$\Delta Hf^\circ_0(CF_3X)$[c]	$D_{298}(CF_3-X)$	Ref.[b]	$A(CF_3^+)$	$\Delta Hf^\circ_{298}(CF_3)$	$\Delta Hf^\circ_0(CF_3^+)^+$	E.E.	$I(CF_3^+)^+$ [f]
CF_3-F	-222.87 ± 0.38	[31]	-221.5 ± 0.4	129.3 ± 2	21	357.9	-112.45	118.0	>30.7	229.5
CF_3-H	$-165.1\ \pm0.5$	[24]	-163.4 ± 0.5	106.2 ± 0.5	25	326.1	-111.0	109.6	>21.8	220.6
CF_3-CF_3	$-321.0\ \pm0.1$	[22]	-319.0 ± 0.1	$93\ \pm4$	18	314.1	-114.0	106.6	>19.3	218.1
CF_3			-111.5				[d] -112.5	101.8	>14.5	[g] 213.3
CF_3-Cl	$-165.8\ \pm0.5$	[23]	-164.6 ± 0.5	82.9	(e)	290.0	-112.0	96.7	>9.4	208.2
CF_3-Br	$-155.5\ \pm0.2$	[19–20]	-152.6 ± 0.2	69.4 ± 0.8	20	273.0	-112.8	92.2	>4.9	203.7
CF_3-I	-139.4	[24]	-138.0	53.7	24	251.0	-111.3	87.3	>0.0	198.8

[a] Estimated uncertainties.
[b] Refers to numbers in the bibliography.
[c] Calculated from ΔHf°_{298}.
[d] Average of the other six values in this column.
[e] Calculated from CF_3Br and CF_3I.
[f] Calculated from E.E. $+\Delta Hf^\circ_0(CF_3^+)^+$ from CF_3I.
[g] Obtained by Lifschitz and Chupka [32] by photoionization of CF_3 free radical.

TABLE 2b. *Thermodynamical values in kJ mol^{-1} for the same compounds*

ΔHf°_{298}	(CF_3X)	$\Delta Hf^\circ_0(CF_3X)$	$D_{298}(CF_3-X)$	$A(CF_3^+)$	$\Delta Hf^\circ_{298}(CF_3)$	$\Delta Hf^\circ_0(CF_3^+)$	E.E.	$I(CF_3^+)^+$
CF_3-F	-956.9	-926.8	541.0	1497.5	-470.5	493.7	>128.4	960.2
CF_3-H	-697.0	-683.7	444.0	1364.4	-464.4	458.6	>91.2	923.0
CF_3-CF_3	-1343.0	-1334.0	389.0	1314.2	-477.0	446.0	>80.8	912.5
CF_3		-466.5			-470.7	425.9	>60.7	892.5
CF_3-Cl	-693.7	-688.7	346.8	1213.4	-468.6	404.6	>39.3	871.1
CF_3-Br	-650.6	-638.5	290.4	1142.2	-472.0	385.8	>20.5	852.3
CF_3-I	-583.7	-577.8	224.7	1050.2	-465.7	365.3	>0.0	831.8

corresponding $\Delta Hf^\circ_0(CF_3^*)^+$ was obtained by correcting to 0 K and adding the threshold photoionization energy of 9.5 eV = 213.3 kcal mol^{-1} measured by Lifschitz and Chupka [32].

From the comparison of the $\Delta Hf^\circ_{298}(CF_3)$ values so obtained it is easy to see that the thermochemical values agree quite well; their differences are not larger than ±1.5 kcal mol^{-1}. On the contrary the differences in $\Delta Hf^\circ_0(CF_3^*)^+$ are much larger, some 30 kcal mol^{-1} from CF_4 to CF_3I. The disagreement is too large to be attributed to the errors in either the photoionization or the thermochemical measurements. It is apparent that for some reason we have not measured the adiabatic potential and some excess energy is included (perhaps very small for CF_3I).

The substances in table 2 have been listed according to their decreasing values of $\Delta Hf^\circ_0(CF_3^*)^+$. We observe that the order is one of increasing atomic weight of X and of increasing C–X distances [36] for the halides. This suggests the following explanation. In all the listed CF_3X molecules the orbitals of the valence electrons of the carbon are sp^3. It has been demonstrated [26] that the CF_3 free radical is not planar. That suggests that the orbitals retain at least some sp^3 character. However, the CF_3^+ ion is planar, and the three valence electrons are in sp^2 orbitals lying in a plane with the vacant p orbital perpendicular to it [37]. It seems reasonable then to assume that, like the isoelectronic BF_3 molecule, an electron from one of the nonbonding pairs of an F jumps to the $p-C$ orbital forming a π bonding. There are three similar possible configurations in resonance with the empty p orbital structure and with some partially ionic structures [38]. In the case of BF_3 a resonance energy of 48 kcal mol^{-1} has been calculated [39]. It is likely that in the CF_3^+ ion due to more favorable charge distribution conditions that value will be still higher.

The following consequences can be deduced:

If we accept the approximate value of 10.8 eV suggested by Lifschitz and Chupka as the vertical ionization potential of the CF_3 free radical, an adiabatic threshold energy lower than 8.62 eV (as our measurements from CF_3I suggest) does not seem unreasonable but very probable. This would require that both the FCF angles and the FC distances in the free radical be approximately the same as those in the CF_3X molecules; in other words that the C orbitals be still nearly pure sp^3.

If the B–F distances change from 1.43 Å in the BF_4^- to 1.295 Å in BF_3 because of the resonance of the π bonding and especially because of that of the partially ionic forms [38, 41], similar and perhaps larger changes can be expected from CF_3 radical to CF_3^+ ion. Thus some appreciable amount of energy must be associated with the symmetrical stretching vibrations. Of course large out-of-plane bending vibrations are also expected.

It is likely that in the case of the CF_3X molecules, at least part of the resonance energy is not lost as excess energy but transferred by radiationless mechanisms to the dissociation coordinate in accordance with the fundamental postulate of the quasiequilibrium theory of mass spectra [40]. In that case the changes in orbital configurations, the π bonding and the res-

onance, occur at least partially before the dissociation is completed. Palko and Drury have suggested that the formation of the π orbitals in BF_3 is due to the high repulsion between the nonbonding electron pairs crowded in the small valence shell of the F atoms. Thus it can be expected that the process will be rather difficult to complete in CF_3X before dissociation when the X atom is F, easier when it is Cl and Br, and still easier with I.

Despite the fact that CF_3I^+ has a longer residence time in the ion source than CF_3Br^+, the molecular ion peak is relatively larger. No molecular or corresponding metastable peak is observed with CF_4. This indicates that the dissociation process is the longest with CF_3I, shorter in CF_3Br and CF_3Cl, and so short in CF_4 that it is not improbable that some appreciable kinetic energy could be lost in the fragmentation.

Thus in the CF_3I the dissociation process gives more time and far less difficulty to the transfer of the resonance energy to the dissociation coordinate; this is enough for the transfer to be total or nearly so. In the rapid dissociation of the CF_4 only a small amount can be transferred, the other part being lost as excess energy. Similar reasoning would explain the intermediate situation in the dissociation of CF_3-Cl, CF_3-Br, and also with the nonhalogens like CF_3-H and CF_3-CF_3, etc. The decisive influence of the crowding of electrons in the valence shell of F and X could explain why the nontransferred excess energy is so definitely dependent on the nature of the atoms related to the bond broken in those molecules, as we will see later.

In the case of the CF_3 free radical there is no fragmentation and thus below the vertical ionization potential the transfer of excess energy to the ionization process must be reached through a completely different mechanism. Thus only in this case vibrational peaks appear clearly superimposed on the threshold of the ionization yield curve. Apparently only the out-of-plane bending frequencies are observed on the curves obtained by Lifshitz and Chupka.

This does not need to be interpreted in the sense that there are not other vibrations in the ion but only as an evidence that this is the only one which has a transfer mechanism rapid enough or efficient enough to be detected.

This could explain the inability to observe the true adiabatic threshold energy. The difference between the adiabatic and the observed value would correspond at least to some energy of the completely symmetrical stretching vibrations.

The smallest excess of energy is that of $D(CF_3-I)$, but we have not found any indication that it is zero or very small, so we can calculate only lower limits of the excesses of energy (table 3).

It has been suggested above that the excess energy would only depend on the bond broken. We can effectively observe from table 1 that for the CF_3^+ ions obtained from C_3F_8 and C_4F_{10}, in both of which we obtain the same ion by breaking similar bonds, where the only probable difference is a difference in excess energy, this difference is exactly zero. However, in the case of the $C_2F_5^+$ ions obtained from C_2F_6 and C_3F_7, in which different bonds are broken, the difference is 2.14 eV. Further, in the case of the $C_3F_7^+$ ions obtained from C_3F_8 and C_4F_{10}, in which the same two kinds of bonds are broken, the difference is also 2.14 eV.

TABLE 3. *Lower limits of excess energy calculated from threshold energies*

Bond dissociation	Excess energy		
	kcal mol^{-1}	kJ mol^{-1}	eV
$D(CF_3-F)$	> 30.7	> 128	> 1.32
$D(CF_3-H)$	> 22.3	> 93	> 0.96
$D(CF_3-CF_3)$	> 19.3	> 81	> 0.83
$I(CF_3)$	> 14.5	> 61	> 0.63
$D(CF_3-Cl)$	> 9.4	> 39	> 0.41
$D(CF_3-Br)$	> 4.9	> 20	> 0.21
$D(CF_3-I)$	> 0.0	> 0	> 0.00

Comparing the threshold energies of CF_3^+ and $C_2F_5^+$ from C_3F_8, and assuming the same excess energy because the same bond is broken, we get

$$I(C_2F_5)^+ = I(CF_3)^+ + 0.10 \text{ eV};$$

from CF_3^+ and $C_3F_7^+$ (from C_4F_{10})

$$I(C_3F_7)^+ = I(CF_3)^+ + 0.08 \text{ eV};$$

by difference: $I(C_2F_5^+) - I(C_3F_7)^+ = 0.02$ eV.

This is exactly the difference between the threshold energies of the $(C_2F_5)^+$ from C_2F_6 and $(C_3F_7)^+$ from C_3F_8.

The difference of 0.40 eV between threshold energies of CF_3^+ from C_2F_6 and from C_3F_8 is easily explained by the fact that in the first case a bond between two primary carbons is broken whereas in the second one it is a bond between a primary and a secondary carbon. The difference of 0.27 eV between the threshold energy of $(C_2F_5)^+$ from C_3F_8 and C_4F_{10} would likewise be due to the fact that one bond is between a primary and a secondary carbon and the other between two secondary carbons.

There probably are small differences in the excess energy related to each kind of bond and so the differences observed do not necessarily measure accurately the differences in bond energies. As a rule, the internal consistency of the values obtained by photoionization is not a proof in itself that the differences in threshold energies can give accurately the differences in bond dissociation energies. Nevertheless in this case if we note that the difference in the appearance potentials of the $(CF_3)^+$ ions from CF_4 and C_2F_6 is 43.8 kcal mol^{-1} but the calculated difference in excess energy is only 8.4 kcal mol^{-1} (less than one fifth) it seems probable that the differences in excess energy are small between bonds connecting the same kinds of atoms (all C—C or all C—F) but differing only in the fact that the carbons are primary or secondary. When the total differences are small themselves, they can

be taken to good approximation as differences in bond dissociation energies, perhaps with not less accuracy than direct thermochemical measurements.

In our case we can write approximately $D(C_1-C_1)-0.4$ eV $\simeq D(C_1-C_2)\simeq D(C_2-C_2)+0.3$ eV and consider that to a good approximation all the m-19 ions measured had the same excess energy A and all the others an excess $B\simeq A-8.4$ kcal mol^{-1}, despite the fact that the values obtained from CF_3I indicate that $B\geqslant 19.3$ kcal mol^{-1} which is a rather large value.
If we accept the values

$$I(CF_3)^+\leqslant 8.62 \text{ eV}\simeq 198.8 \text{ kcal mol}^{-1} \text{ and}$$
$$\Delta Hf^\circ(CF_3)^+\leqslant +87.3 \text{ kcal mol}^{-1} \text{ we get}$$
$$I(C_2F_5)^+=I(CF_3)^++0.10 \text{ eV}\leqslant 8.72 \text{ eV}$$
$$I(C_3F_7)^+=I(CF_3)^++0.08 \text{ eV}\leqslant 8.70 \text{ eV}$$
$$I(C_4F_9)^+=I(C_3F_7)^+-0.02 \text{ eV}\leqslant 8.68 \text{ eV}.$$

Accepting the mean value

$$\Delta Hf^\circ_{298}(CF_3)=-112.5\pm 0.4 \text{ kcal mol}^{-1} \text{ we get}$$
$$D_{298}(CF_3-CF_3)=96.0\pm 0.5 \text{ kcal mol}^{-1} \text{ and}$$
$$D_{298}(CF_3-F)-D_{298}(CF_3-CF_3)=33.3 \text{ kcal mol}^{-1}=1.44 \text{ eV}.$$

Thus this CF bond is approximately 1.44 eV stronger than the C–C bonds between primary carbons.

Less accurately we can write:

$$D_{298}(C_1-C_2)\simeq D_{298}(C_1-C_1)-0.40 \text{ eV}=86.8 \text{ kcal mol}^{-1}$$
$$D_{298}(C_2-C_2)\simeq D_{298}(C_1-C_1)-0.67 \text{ eV}=80.6 \text{ kcal mol}^{-1}.$$

It is thus possible to predict the following values for the appearance potentials from C_5F_{12}.

$A(C_5F_{11})^+=15.4$ eV $A(C_2F_5)^+=13.0$ eV
$A(C_4F_9)^+=13.3$ eV $A(CF_3)^+=13.2$ eV
$A(C_3F_7)^+=13.0$ eV $I(C_5F_{11})^+\leqslant 8.68$ eV.

Assuming for all the C_1-F dissociations the same excess energy of 30.7 kcal mol^{-1} found for $D(CF_3-F)$ we can obtain

$$D(C_2F_5-F)=125.8 \text{ kcal mol}^{-1}$$
$$D(C_3F_7-F)=125.6 \text{ kcal mol}^{-1}.$$

This coincidence suggests that in the second case the lost F was also bonded to a primary carbon and we can accept a mean value

$$D(C_1-F)=125.7 \text{ kcal mol}^{-1},$$

slightly lower than $D(F_3C-F)$. This result can be compared with

$$D(CF_3-Br)=69.4\pm 0.8 \text{ kcal mol}^{-1}$$
$$D(C_2F_5-Br)=D(C_3F_7-Br)=67.0\pm 2.5 \text{ kcal mol}^{-1}$$

obtained by Coomber and Whittle [2]. If in the second case F were bonded to the secondary carbon, that would have meant $D(C_1-F)=D(C_2-F)$. This does not seem likely. The value obtained for $\Delta Hf^\circ_{298}(CF_3)$ from C_2F_6 appears to be too high, and that from CF_3I too low. It is likely that:

$$D(CF_3-CF_3)=96.0\pm 0.5 \text{ kcal mol}^{-1}$$
$$D(CF_3-Br)=69.7\pm 1 \text{ kcal mol}^{-1}$$
$$D(CF_3-I)=52.5\pm 1 \text{ kcal mol}^{-1}.$$

Table 4 has been obtained using these values.

We can also mention that except for CF_3-F, the C_1-F bonds are $D_{298}(C_1-F)-D_{298}(C_1-C_1)=29.7$ kcal mol$^{-1}=1.28$ eV stronger than the C_1-C_1 bonds.

5. Conclusion

Very precise values of the threshold energies for the molecular and fragment ions can be obtained by photoionization, but there is no reason to assume a priori that those values correspond to the adiabatic transition.

It is shown in this paper that in some cases the total excess energy with which the ions are obtained at threshold can be different from zero by amounts that cannot be neglected. Nevertheless, in the present state of the art, when this excess energy can be determined, photoionization can give dissociation energy values as good or better than direct thermochemical methods.

I am indebted to H. M. Rosenstock, V. H. Dibeler, G. T. Armstrong, and W. H. Evans for very helpful suggestions and discussions and to the International

TABLE 4.

Dissociation	Adiabatic dissociation			Excess energy			Photoionization dissociation		
	kcal mol^{-1}	kJ mol^{-1}	eV	kcal mol^{-1}	kJ mol^{-1}	eV	kcal mol^{-1}	kJ mol^{-1}	eV
F_3C-F	129.3	541	5.61	> 30.7	> 128	> 1.32	> 160.0	> 669	> 6.93
C_1-F	125.7	525	5.45	> 30.7	> 128	> 1.32	> 156.4	> 653	> 6.77
F_3C-H	106.2	444	4.61	> 22.3	> 93	> 0.96	> 128.5	> 537	> 5.57
C_1-C_1	96.0	402	4.16	> 19.3	> 81	> 0.83	> 115.3	> 482	> 4.99
C_1-C_2	86.8	363	3.76	> 19.3	> 81	> 0.83	> 106.1	> 444	> 4.59
C_2-C_2	80.6	337	3.49	> 19.3	> 81	> 0.83	> 99.9	> 418	> 4.32
F_3C-Cl	81.7	342	3.54	> 9.4	> 39	> 0.41	> 91.1	> 381	> 3.95
F_3C-Br	69.7	292	3.02	> 4.9	> 20	> 0.21	> 74.6	> 312	> 3.23
F_3C-I	52.5	220	2.28	> 0	> 0	> 0	> 52.5	> 0	> 2.28

Atomic Energy Agency (Vienna, Austria), The National Academy of Sciences (Washington, D.C.), and the Comisión Nacional de Energía Atómica (Buenos Aires, Argentina) for their financial support.

It's a pleasure for me to acknowledge the valuable assistance of Miss Susan Kay Liston and Miss Rosemary Suckow, who obtained some of the photoionization yield curves, and of J. A. Walker for maintenance of the instrument.

6. References

[1] Mohler, F. L., Dibeler, V. H., and Reese, R. M., J. Res. NBS **49,** 343 (1952) RP2370.
[2] Dibeler, V. H., Reese, R. M., and Mohler, F. L., J. Res. NBS **57,** 113 (1956) RP2700.
[3] Marriott, J., and Craggs, J. D., J. Electronics **1,** 405 (1956).
[4] Bibby, M. M., and Carter, G., Trans. Faraday Soc. **59,** 2455 (1963).
[5] Dorman, F. H., J. Chem. Phys. **41,** 2857 (1954).
[6] Pottie, R. F., J. Chem. Phys. **42,** 2607 (1965).
[7] Bibby, M. M., Toubelis, B. J., and Carter, F., Electronic Letters **1,** 51 (1965).
[8] Lifschitz, C., and Long, F. A., J. Phys. Chem. **69,** 3746 (1965).
[9] Fisher, I. P., Homer, J. B., and Lossing, F. P., J. Am. Chem. Soc, **87,** 957 (1965).
[10] Kiser, R. W., and Hobrock, D. L., J. Am. Chem. Soc. **87,** 922 (1965).
[11] Forman, F. H., J. Chem. Phys. **44,** 35 (1966).
[12] Cook, G. R., and Ching, B. K., J. Chem. Phys. **43,** 1794 (1963).
[13] NBS Circular 500.
[14] NBS Technical Note 270–3, Wagman, D. D., Evans, W. H., Halow, I., Parker, V. B., Bailey, S. M., and Schumm, R. H. (January 1968).
[15] JANAF TABLES—The Dow Chemical Co.
[16] Sinke, G. C., J. Chem. Eng. Data **10,** 295 (1965).
[17] Tschuikow-Roux, E., J. Phys. Chem. **69,** 1075–1077 (1965).
[18] Tschuikow-Roux, E., J. Chem. Phys. **43,** 2251 (1965).
[19] Coomber, J. W., and Whittle, E., Trans. Faraday Soc. **62,** 2183 (1966).
[20] Coomber, J. W., and Whittle, E., Trans. Faraday Soc. **63,** 608 (1967).
[21] Coomber, J. W., and Whittle, E., Trans. Faraday Soc. **63,** 1394 (1967).
[22] Sinke, G. A., J. Phys. Chem. **70,** 1326 (1966).
[23] Lord, A., Goy, C. A., and Pritchard, H. D., mentioned by Lacher and Skinner [29] to be published.
[24] Goy, C. A., Lord, A., and Pritchard, H. D., J. Phys. Chem. **71,** 1086–9 (1967).
[25] Ampheett, J. C., Coomber, J. W., and Whittle, E., J. Phys. Chem. **70,** 593–4 (1966).
[26] Fessenden, R. W., and Schuler, R. H., J. Chem. Phys. **43,** 2704 (1965).
[27] Benson, S. W., Chem. Educ. **42,** 502 (1965).
[28] Kerr, J. A., Chem. Reviews **66,** 465 (1966).
[29] Lacher, J. R., and Skinner, H. A., (private communication).
[30] Johnson, G. K., Feder, H. M., and Hubbard, W. N., J. Phys. Chem. **70,** 1 (1966).
[31] Domalski, E. S., and Armstrong, G. T., J. Res. NBS **71A** (Phys. and Chem.), No. 2, 105 (1967).
[32] Lifshitz, C., and Chupka, W. A., J. Chem. Phys. **47,** 3439 (1967).
[33] Dibeler, V. H., and Reese, R. M., J. Res. NBS **A68** (Phys. and Chem.), No. 4, 409 (1964).
[34] Wheaton, J. E. G., J. Opt. Soc. Am. **54,** 1287 (1964).
[35] Chupka, W. A., and Berkowitz, J., J. Chem. Phys. **47,** 2921 (1967), Steiner, B., Giese, C. F., and Inghram, M. G., J. Chem. Phys. **34,** 189 (1961), Dibeler, V. H., Krauss, M., Reese, R. M., and Harlee, F. N., J. Chem. Phys. **42,** 3791 (1965).
[36] Interatomic Distances, Special Publ. No. 18 and Suppl., The Chemical Society (London, 1965).
[37a] Walsh, A. D., J. Chem. Soc., p. 2260–2330 (1953).
[37b] Jahn, H. A., and Teller, E., Proc. Roy. Soc. (London) **A161,** 220 (1937).
[38] Pauling, L., The Nature of the Chemical Bond, p. 237 (Cornell University Press, Ithaca, N.Y., 1945).
[39] Cotton, F. A., and Letto, J. R., J. Chem. Phys. **30,** 993 (1959).
[40] Rosenstock, H. M., Doctoral Thesis, University of Utah (1954).
[41] Palko, A. A., and Drury, S., J. Chem. Phys. **47,** 2561 (1967).

(Paper 72A5–515)

JOURNAL OF RESEARCH of the National Bureau of Standards—A. Physics and Chemistry
Vol. 72A, No. 5, September–October 1968

Infrared Matrix Spectra of Lithium Fluoride

Stanley Abramowitz and Nicolo Acquista

Institute for Basic Standards, National Bureau of Standards, Washington, D.C. 20234

and

Ira W. Levin

National Institute of Arthritis and Metabolic Diseases, National Institutes of Health, Bethesda, Maryland 20014

(June 19, 1968)

Evidence for a linear dimer Li_2F_2 has been obtained by extending the spectral measurements for matrix isolated lithium fluoride into the far infrared region. The vapors from solid ^6LiF, ^7LiF, and $^6LiF/^7LiF$ mixtures were deposited in argon matrices at liquid hydrogen temperatures. Vibrational assignments were made on the basis of the following linear species: $^6Li_2F_2$, $^7Li_2F_2$, $^{6,7}Li_2F_2$ and $^{7,6}Li_2F_2$. Although the specific geometry of the dimer could not be determined, a normal coordinate analysis supported the spectral interpretation of a linear structure ($C_{\infty v}$).

Key Words: Force field; infrared; lithium fluoride dimer; low temperature; matrix; vibrational assignment.

1. Introduction

Infrared spectra of matrix isolated lithium fluoride species indicate the formation of a rhomboid dimer of D_{2h} symmetry in addition to the monomeric form [1–5].[1] Several prominent spectral features, however, are not satisfactorily assigned to a specific LiF system, in particular, the sets of relatively strong bands that occur in argon matrices at 722 and 495 cm^{-1} and at 769 and 522 cm^{-1} for the isolated vapors of ^7LiF and ^6LiF, respectively. Since the matrix absorption bands for the two isotopic forms of the monomer appear at 842 and 888 cm^{-1}, some workers attribute the additional bands to monomeric LiF absorptions arising from supplementary matrix trapping sites [1, 2]. Alternatively, other investigators believe that the unassigned bands may be due to the formation of either a trimer or higher polymeric species [3, 6]. Reddington, however, suggests that the controversial features possibly reflect the two high frequency stretching modes of a matrix stabilized linear dimer [5].

In the present study the infrared measurements on matrix isolated lithium fluoride are extended into the far infrared region. Since the spectrum exhibits absorption features from several species, carefully controlled matrix diffusion experiments in conjunction with double boiler techniques for producing the gaseous molecules allowed the absorption bands of a given molecular type to be grouped together. Spectra from isotopic molecules, as well as mixtures of varying isotopic compositions, aided both the grouping and assignment of the vibrational features. One group of bands which occur in the 700 cm^{-1}, 500 cm^{-1}, and far infrared regions are interpreted as absorptions of a linear dimer with two nonequivalent lithium atoms. Other simple interpretations for these features, such as supplementary trapping sites or a cyclic trimer, are considered and found to be inconsistent with the sum of data observed.

2. Experimental

The methods used to isolate high temperature species in rare gas matrices have been described in detail elsewhere [7]. Depending upon the spectral region studied, the infrared spectra were obtained either with a Perkin-Elmer model 99G monochromator or a Perkin-Elmer model 301 spectrophotometer [8]. An Air Products Cryotip supplied the refrigeration at liquid hydrogen temperatures and provided the

[1] Figures in brackets indicate the literature references at the end of this paper.

necessary controlled temperature regulation from 20 to 33 K, while an electron bombardment furnace vaporized the LiF samples.'^{6}LiF and ^{7}LiF samples; supplied by the Stable Isotopes Division, Oak Ridge National Laboratory, were evaporated in double oven crucibles and were deposited in an argon matrix on thin CsI windows. These samples, as well as isotopic mixtures, were investigated in the region from 1000 to 150 cm^{-1}.

The narrow absorption bands of the same species will either increase or lose intensity at the same rate upon controlled diffusion at temperatures above 20 K, thus providing a convenient method of identifying groups of bands with a particular molecular species. Mole ratios of the species in the vapor are altered by raising the temperature of the gas effusing from the Knudsen cell; therefore, one can assign bands to the same species by their relative decrease in intensity relative to the LiF monomer. Enriched samples of ^{6}LiF containing 95 percent ^{6}LiF and 5 percent ^{7}LiF were utilized in addition to ^{n}LiF which has about 95 percent ^{7}LiF and 5 percent ^{6}LiF. Additional information was obtained by examining the spectrum of thick deposits of ^{7}LiF in the region of the ^{6}LiF absorptions and vice versa. The difficulties in estimating both the temperature of the effusing gas and the ratio of the matrix diluent to the sample (M/S) have been discussed [1, 2, 5, 7]. M/S ratios of 500:1 to 1000:1, and temperatures from 850 °C to 1200 °C are representative of the conditions used in these experiments.

Internal and external absorption standards were used to calibrate the observed spectra. Spectral slit widths of about 0.5 cm^{-1} and 1.0 cm^{-1} were employed in the region from 1000 to 400 cm^{-1} and from 400–150 cm^{-1}, respectively.

3. Experimental Results

Classifying the sets of bands of the various species by controlled diffusion experiments and double boiler observations yields the following groups: (1) monomeric bands of LiF at 835 cm^{-1} for ^{7}LiF and 888 cm^{-1} for ^{6}LiF; (2) bands due to the cyclic dimer of $^7Li_2F_2$, $^6Li_2F_2$ and $^6Li^7LiF_2$; (3) bands at 767.8, 518.6, 270.2, 261.0 and 157.1 cm^{-1} for ^{6}LiF and at 720.5, 497.5, 255.2, 245.7, and 152.8 cm^{-1} for ^{7}LiF; (4) all other bands in the spectrum which increased in intensity relative to the monomer during diffusion experiments at temperatures above 20 K (and also are significantly lower in intensity relative to the monomeric species when the temperature of the effusing gas is raised). The behavior of the fourth group of bands indicate that they originate from polymeric species containing more lithium atoms than the species responsible for the other absorption bands in the spectrum.

Upon controlled diffusion at temperatures up to 33 K, the group 2 bands decreased in intensity relative to the monomer at a significantly more rapid rate than the group 3 bands. The group 3 bands decreased in intensity at a somewhat greater rate than the monomeric bands, while the group 4 bands all increased in intensity. At elevated temperatures of effusion both group 2 and 3 bands were reduced in intensity relative to the monomer with the diminution in group 2 greater than that in group 3. As we already indicated, the group 4 bands were decreased in relative intensity to a greater extent than both groups 2 and 3.

The relative intensity of all features compared to the monomeric species was only a function of the temperature of the effusing vapor. Flow rates were varied over the range of 0.05 to 0.20 mmol/min of argon without observing any change in the spectrum. This precludes any explanation of the five bands in group 2 based upon supplementary trapping sites in the matrix for the monomeric species. Also, it is unlikely that an argon matrix could perturb the vibrational frequency of a monomeric lithium fluoride to cause the large observed matrix shifts. The details of the five absorption bands belonging to group 3 which, again, because of their behavior and isotopic splitting patterns, belong to the same molecular species, will now be discussed in detail with particular emphasis directed towards assigning these bands to a linear dimer with two nonequivalent lithium atoms. In a later section a discussion of other possibilities will be included.

3.1. The 400–150 cm^{-1} Region

The observed infrared spectra of matrix isolated ^{7}LiF, ^{6}LiF, and a 1:1 mixture of ^{7}LiF/^{6}LiF appear in figure 1a for the 240–300 cm^{-1} region. The strong features at 293.8 and 276.4 cm^{-1} in ^{6}LiF and ^{7}LiF are assigned to the lowest infrared active vibration ν_4 of the planar rhomboid dimer of LiF. Confirmation is given by the triad at 293.8, 284.7, and 276.4 cm^{-1} for the 1:1 mixture of ^{7}LiF/^{6}LiF, since the observed relative intensities of 1:2:1 are those expected for a dimer with equivalent lithium atoms. (A sample containing equal part of ^{6}LiF and ^{7}LiF would be expected to exhibit bands of relative intensity of 1:2:1 and 1:1:1:1 for the cases of a dimer containing equivalent and nonequivalent lithium atoms.) The observed ratio of 1.0630 for $\nu_4(^6Li)/\nu_4(^7Li)$ agrees quite well with the calculated ratio of 1.0594 from the product rule for this mode. The behavior of this absorption area upon warming the matrix and allowing diffusion to occur is identical to the bands at 626, 646, and 661 cm^{-1} and 537, 550, and 569 cm^{-1} which were previously assigned to the ν_5 and ν_6 species of the rhomboid dimer of $^7Li_2F_2$, $^6Li^7LiF_2$, and $^6Li_2F_2$ [2]. The three sets of features also exhibit the same relative intensity diminution relative to the monomeric species when spectra are observed in samples deposited from higher effusing temperatures.

The other set of bands in this region exhibit a different rate of disappearance on warming the matrix than those demonstrated by the features ascribed to the ring-shaped dimer. Also, the diminution in intensity of these bands, upon deposition from a higher

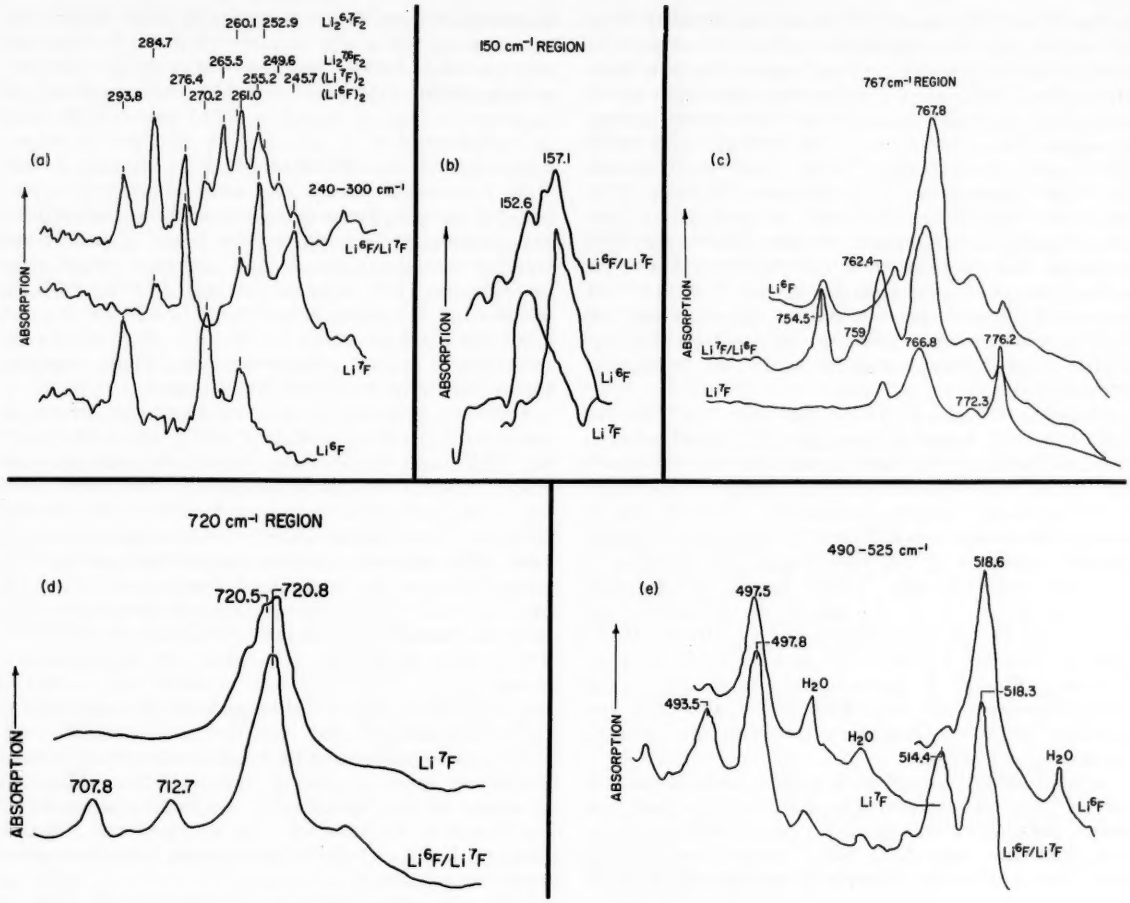

FIGURE 1. *Infrared spectra of matrix isolated* ^{7}LiF, ^{6}LiF, *and a 1:1 mixture of* ^{6}LiF/^{7}LiF.

(a) 240–300 cm^{-1} region
(b) 150 cm^{-1} region
(c) 767 cm^{-1} region
(d) 720 cm^{-1} region
(e) 490–525 cm^{-1} region

effusing temperature relative to the change in intensity of the monomeric species, is distinctly less than that observed for the ring-shaped dimer. These features occur at 270.2 and 261.0 cm^{-1} for ^{6}LiF and at 255.2 and 245.7 cm^{-1} for ^{7}LiF. The spectrum of the isotopic mixture gives additional bands at 265.5, 260.1, 252.9 and 249.6 cm^{-1}. These absorptions are assigned to the linear dimer species. Since the frequencies for the pure isotopic molecules are less than 10 cm^{-1} apart, the vibrations probably correspond to different symmetry representations; namely, the stretching (Σ) and bending (Π) modes of the dimer. Thus, we assign the bands at 255.2, 270.2, 265.5, and 260.1 to the ν_3 vibrations, the lowest stretching mode, of F–^{7}Li–F–^{7}Li, F–^{6}Li–F–^{6}Li, F–^{7}Li–F–^{6}Li, and F–^{6}Li–F–^{7}Li, respectively. The bands at 245.7, 261.0, 252.9, and 249.6 cm^{-1} then correspond to the ν_4 bending modes of F–^{7}Li–F–^{7}Li, F–^{6}Li–F–^{6}Li, F–^{7}Li–F–^{6}Li, F–^{6}Li–F–^{7}Li, respectively. The measurements reported were obtained under higher resolution conditions than those shown. In addition to trapping the species from the isotopic mixtures, thick deposits of the nearly pure isotopic samples, as well as 1:1 to 1:3 mixtures, were observed.

Arguments concerning the assignment based upon intensity considerations in this region are quite difficult. Particularly, there are bands in this region which are due to the polymeric or aggregate species containing more than two lithium atoms. Evidence for these bands is obtained from temperature cycling experiments in which the dimeric bands disappear and the polymeric bands increase in intensity. Also, for the pure ^{6}Li and ^{7}Li spectra, one notices absorptions in the wings of the bands (between 270.2 and 261.0 cm^{-1} in ^{6}LiF and 255.2 and 245.7 in ^{7}LiF) that is due

to the polymeric species. Therefore, a detailed intensity match with the expected 1:1:1:1 ratio for the mixed isotope is not possible in this region. Despite these difficulties, however, one observes qualitative agreement for the pairs of lines in the mixed isotope. Consider 265.5, 249.6 cm^{-1} for $^{7,6}Li_2F_2$ and 260.1, 252.9 cm^{-1} for $^{6,7}Li_2F_2$. These lines have roughly the same intensity ratio as the pairs of lines 270.2, 261.0 cm^{-1} and 255.2, 245.7 cm^{-1} for the pure species. (The buildup in intensity of the 261.0 and 260.1 peaks is due to their near coincidence.) Since the natural and enriched samples of the ^{7}LiF and ^{6}LiF contained about 5 percent of the other isotope, the thick deposits of the individual species gave features of the mixed isotope spectra with the appropriate intensity ratios.

Absorption bands at 152.8 and 157.1 cm^{-1} for the ^{7}LiF and ^{6}LiF samples presented the same behavior upon diffusion in the matrix and the same intensity diminution upon deposition from a higher temperature as the previous features assigned to the linear dimer. The spectrum appears in figure 1b. The mixed isotopic sample indicates a superposition of the spectra of the two pure samples. These bands are assigned to ν_5 of the F–^{7}Li–F–^{7}Li and F–^{6}Li–F–^{6}Li species. It was not possible to resolve the spectrum for the mixture into the F–^{6}Li–F–^{7}Li and F–^{7}Li–F–^{6}Li components, although it appears clear from the normal coordinate analysis described below that the frequencies for ν_5 of these mixed species are between about 152 and 157 cm^{-1}.

Several other absorption features, both broad and narrow, were observed in the spectra of the pure and mixed isotopes. Their behavior upon diffusion, however, indicates that these bands arose from systems other than either the dimeric or monomeric species.

3.2. The 900–400 cm^{-1} Region

The absorption bands arising from the two stretching modes of a linear Li_2F_2 molecule are expected in this region. The higher frequency stretching mode of Li_2F_2 occurs at 767.8 and 720.5 cm^{-1} in $^6Li_2F_2$ and $^7Li_2F_2$. Spectra of these regions are given in figures 1c and 1d. In addition to these features, one observes the two stretching modes ν_5 and ν_6 (B_{2u} and B_{3u}) of the rhomboid dimer, as well as the bands for the monomer. Although these features are not presented in the figures, the species occur at substantially the same frequencies as reported previously [1–5].

Features also appear which are attributed to species other than the monomer or either dimer. These bands increase in intensity upon diffusion which indicates that they are possibly due to a polymer of three or more LiF aggregates. No further discussion concerning the species responsible for these absorptions will be given here.

High resolution spectra of 1:1 mixtures of ^{6}LiF/^{7}LiF show the 767.8 cm^{-1} band split into two components of equal intensity. These correspond to ν_1 of F–^{6}Li–F–^{6}Li and F–^{6}Li–F–^{7}Li at 767.8 and 766.8 cm^{-1}. The approximate equality of intensities of these two components (in a 1:1 isotopic mixture) is expected and provides further evidence for a dimer with two nonequivalent lithium atoms. The corresponding absorption in ^{7}LiF is found at 720.5 cm^{-1}. This band is complicated by a shoulder to the low frequency side which is more prominent in a 1:1 mixture of ^{6}LiF/^{7}LiF. Two weaker bands also were found in the mixed isotopic sample. These features, as shown by diffusion experiments, are not due to the linear dimeric form. Careful measurements of ^{7}LiF and various mixtures of ^{6}LiF and ^{7}LiF indicate that ν_1 of F–^{7}Li–F–^{7}Li is at 720.5 cm^{-1} while ν_1 of F–^{7}Li–F–^{6}Li is at 720.8 cm^{-1}. The small isotope shifts for the ν_1 and ν_2 modes, as seen in the normal coordinate calculations, supports the existence of the linear dimer model.

Features attributed to the ν_2 symmetric stretching mode of F–Li–F–Li occur at 497.5 and 518.6 cm^{-1} in $^7Li_2F_2$ and $^6Li_2F_2$. The mixed isotopic spectra, given in figure 1e, show features at 493.5 and 514.4 cm^{-1} that are not due to any dimeric or monomeric species. These bands increase markedly in intensity upon diffusion and may be due to the same species responsible for the unassigned absorptions in the 768 and 721 cm^{-1} regions. Measurements of various mixed isotopic samples of ^{7}LiF and ^{6}LiF show ν_2 of F–^{6}Li–F–^{7}Li to be at 497.8 cm^{-1}, while the corresponding frequency of F–^{7}Li–F–^{6}Li is at 518.3 cm^{-1}. In this region it was again useful to measure the spectrum of ^{7}LiF at 768 and 518 cm^{-1} and ^{6}LiF at 721 and 497 cm^{-1} with thick samples in order to obtain the mixed isotope spectrum in a 5 percent concentration. The sets of observed frequencies for the final assignment of the linear Li_2F_2 molecule appear in tables 3 and 4, along with the calculated frequencies from the normal coordinate analysis.

The absorption spectrum of monomeric ^{7}LiF in the argon matrix is shown in figure 2. The doublets ascribed to the fundamental modes of the diatomic LiF species are the only absorption bands in the spectrum which exhibit reversible temperature dependent behavior. As the temperature is raised from 20–33 K, the doublet is smeared out with an apparent blue shift of about 1 cm^{-1} for the low frequency

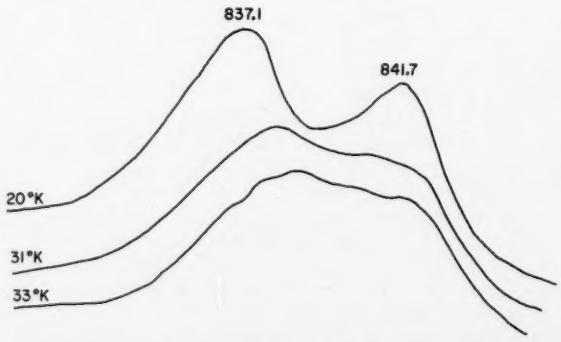

FIGURE 2. *Monomeric* ^{7}LiF *in* Ar *at various temperatures.*

component. No conclusion regarding the cause of this behavior will be given here, except to note that only the absorption bands attributed to monomeric ^6LiF and ^7LiF at 842 and 888 cm^{-1} exhibit such a phenomenon.

4. Discussion

In order to support the interpretation of a linear Li_2F_2 dimeric species, we performed a normal coordinate analysis for the four isotopic systems. Several models for the linear structure were considered; namely, a F–Li–F–Li dimer in which all bonds were equivalent, a F–Li–F · · · Li dimer with a bifluoride structure, and a species F–Li · · · F–Li containing an elongated central bond. For the normal LiF bonds of the model structures, a length of 1.51 Å from the gas phase was assumed, while a value of 2.01 Å from crystalline LiF was taken for the long bonds [9]. The force field for a chosen model was first refined about the ^6Li and ^7Li isotopic species. Interaction force constants were systematically varied until close fits to the observed frequencies were attained. This force field was then used to calculate the frequencies for the mixed isotopic species, namely, the F–^{6}Li–F–^{7}Li and F–^{7}Li–F–^{6}Li molecules. In view of the assumptions concerning the bond lengths and interactions in the force constant matrix, the significance of the force field is limited. Consequently, rather than stressing the values of the individual force constants, recognizing that the force field is not unique, we prefer to emphasize the closeness of the frequency fit for the four isotopic molecules as evidence favoring the linear dimeric structure.

For a linear dimer, F–Li–F–Li of $C_{\infty v}$ symmetry, the vibrational representation is $\Gamma_v = 3\Sigma^+ + 2\Pi$, with the stretching vibrations occurring in the Σ^+ species and the bending modes conforming to Π symmetry. The vibrational problem was cast in terms of the internal coordinates and force constant matrix that appear in table 1. Familiar *GF* matrix methods were used in solving the vibrational secular equation.

TABLE 1. *Internal coordinates and force constant matrix for the linear* Li_2F_2 *dimer.*

a) Internal coordinates

F–Li–F–Li
r s t
α = < F Li F
β = < Li F Li

b) Force constant matrix

f	r	s	t	α	β
r	f_r	f_{rs}	f_{rt}		
s		f_s	f_{st}		
t			f_t		
α				f_α	$f_{\alpha\beta}$
β					f_β

Since the elements of the *G* matrix for the stretching vibrations are independent of bond length, the frequency fits for the Σ^+ species of the three linear dimers are equivalent. The force constants for the various stretching force constants and the comparison between the observed and calculated frequencies appear in tables 2 and 3, respectively. Again, the force constants were refined about only the $^6Li_2F_2$ and $^7Li_2F_2$ isotopes. The frequencies for the mixed isotopes are determined from this potential function. Since a unique potential function probably cannot be determined from the frequency data alone in this manner, it is not worthwhile to refine the force field over all isotopes. The results of the normal coordinate calculation for the Π species appear in table 4. For these vibrations, the change in geometry affects the calculated frequencies. Table 4 indicates, however, that a distinction in geometry cannot be made decisively for the Π species since the frequency fits are quite reasonable for the three models.

TABLE 2. *Summary of force constants for the linear dimer models of* Li_2F_2. *The stretching force constants are in units of millidynes per angstrom, while the bending force constants are in units of millidynes · angstroms*

Model	Species	Force constant
F–Li–F–Li	Σ^+	$f_r + f_s = 3.71$
		$f_{rs} = 0.96$
		$f_t = 0.59$
		$f_{rt} + f_{st} = 1.41$
	Π	$f_\alpha + f_\beta = 0.26$
		$f_{\alpha\beta} = 0.05$
F–Li–F · · · Li[a]	Π	$f_\alpha + f_\beta = 0.36$
		$f_{\alpha\beta} = 0.10$
F–Li · · · F–Li[a]	Π	$f_\alpha + f_\beta = 0.46$
		$f_{\alpha\beta} = 0.18$

[a] A dotted line represents a longer bond distance.

TABLE 3. *Comparison between the observed and calculated frequencies, in* cm^{-1}, *for the* Σ^+ *symmetry species of the linear* Li_2F_2 *dimer.*

	Obs	Calc	$\Delta\nu$	Obs	Calc	$\Delta\nu$
	F^6LiF^6Li			F^7LiF^7Li		
ν_1	767.8	768.0	+0.2	720.5	720.3	−0.2
ν_2	518.6	518.8	+0.2	497.5	498.2	+0.7
ν_3	270.2	266.5	−3.7	255.2	258.7	+3.5
	F^6LiF^7Li			F^7LiF^6Li		
ν_1	766.8	767.7	+0.9	720.8	720.8	0
ν_2	497.8	499.5	+1.7	518.3	517.2	−1.1
ν_3	260.1	258.9	−1.2	265.5	266.3	−0.8

Although rather drastic approximations enter the force field calculation, we can make several observations concerning the various possibilities for a linear model. The plausibility of the bifluoride structure suggests that $f_r = f_s$ and $f_{rt} = 0$. The results of this computation yield values of $f_r = 1.8$ mdyn/Å, $f_t = 0.24$ mdyn/Å, and $f_{rr} = 0.91$ mdyn/Å. Although the interaction force constant is rather large, the values are

TABLE 4. *Comparison between the observed and calculated frequencies, in cm^{-1}, for the* Π *symmetry species of three models for the* Li_2F_2 *linear dimer.*

	Obs	Calc	$\Delta\nu$	Obs	Calc	$\Delta\nu$
a) F–Li–F–Li						
	$^6Li_2F_2$			$^7Li_2F_2$		
ν_4	261.0	261.1	+0.1	245.7	245.5	−0.2
ν_5	157.1	158.5	+0.6	152.8	151.3	−1.5
	$^{6-7}Li_2F_2$			$^{7-6}Li_2F_2$		
ν_4	252.9	260.7	+7.8	249.6	247.6	−2.0
ν_5		152.3			154.6	
b) F–Li–F · · · Li						
	$^6Li_2F_2$			$^7Li_2F_2$		
ν_4	261.0	261.7	+0.7	245.7	244.9	−0.8
ν_5	157.1	157.8	+0.7	152.8	152.0	−0.8
	$^{6-7}Li_2F_2$			$^{7-6}Li_2F_2$		
ν_4	252.9	261.7	+8.8	249.6	245.0	−4.6
ν_5		152.1			157.8	
c) F–Li · · · F–Li						
	$^6Li_2F_2$			$^7Li_2F_2$		
ν_4	261.0	261.0	0	245.7	245.7	0
ν_5	157.1	158.8	+1.7	152.8	151.0	−1.8
	$^{6-7}Li_2F_2$			$^{7-6}Li_2F_2$		
ν_4	252.9	252.0	−0.9	249.6	255.4	+5.8
ν_5		153.9			155.3	

not unreasonable. The frequency fits for the $^6Li_2F_2$ and $^7Li_2F_2$ are approximately 1 cm^{-1}, except for ν_2 which is about 11 cm^{-1}. Including another interaction force constant, however, in the combinational form of $f_{st}+f_{rt}$, we reduce the error in the frequency fit to well within 1 cm^{-1} for the pure 6 and 7 species, except for ν_3, which is about 3.5 cm^{-1} from the observed value. This frequency fit is tabulated in table 3 for all the isotopic species. The values for the diagonal force constants in this case are $f_r=f_s=1.85$ mdyn/Å and $f_t=0.6$ mdyn/Å. Again, the interaction force constants are relatively large; namely, $f_{rs}=0.96$ mdyn/Å and the linear combination of $f_{st}+f_{rt}=1.41$ mdyn/Å. The refinement of the force constants about the observed frequencies depends upon a least squares method; however, the number of known data is not great enough to make a statistical analysis of the force constants profitable. Since additional molecular information, as for example, rotational distortion data or mean-square amplitude data for the gas phase species, is required to further characterize the force field, other sets of force constants may exist which fit the data. Summarizing, we wish to stress that the probable nonuniqueness of the force field precludes a choice of structures on the basis of individual values of the force constants. The close frequency fit determined from the modified potential function, however, strongly indicates the linear nature of the trapped species.

Approximate descriptions of the stretching Σ^+ modes for the ^{7}LiF and ^{6}LiF species are defined by the calculated normal coordinate vectors. The highest frequency ν_1 appears to be mainly a F–Li–F out-of-phase stretching mode, while the ν_3 vibration is composed primarily of the Li–F–Li out-of-phase motion. The ν_2 vibration is approximately a F–Li, F–Li symmetric stretching motion. Since it is not clear which linear dimer model is preferred, detailed descriptions of the bending modes are not given.

A further problem arises in the assignment of the ν_3 and ν_4 vibrations to the Σ^+ and Π species, respectively, since the assignment may reasonably be reversed. A choice cannot be made on the basis of the product rule. For example, the assignment presented in table 3 for $^6Li_2F_2$ and $^7Li_2F_2$ gives an isotopic frequency ratio of 1.176 for $\nu_1\nu_2\nu_3/\nu_1'\nu_2'\nu_3'$, which is compared to a calculated value of 1.144 from the product rule. Reversing the assignments for the stretching and bending modes, ν_3 and ν_4, respectively, gives an isotopic frequency value of 1.180. Table 5 presents the frequency fit for the bifluoride model, as an example, for an assignment with the two frequencies reversed. As before, the force field that was refined about the $^6Li_2F_2$ and $^7Li_2F_2$ isotopic frequencies was used to calculate the frequencies for the mixed species. The fit for the reversed frequency assignment is only slightly worse than the fit in tables 3 and 4. Although it is difficult to resolve the choice definitely, we prefer the assignment with the stretching motion at the higher frequency.

TABLE 5. *Comparison between the observed and calculated frequencies, in cm^{-1}, for the bifluoride structure of the* Li_2F_2 *linear dimer. The* ν_3 *and* ν_4 *frequencies are reversed from the assignment presented in tables 3 and 4.*

	Obs	Calc	$\Delta\nu$	Obs	Calc	$\Delta\nu$
	$^6Li_2F_2$			$^7Li_2F_2$		
ν_1	767.8	768.0	0.2	720.5	720.3	−0.2
ν_2	518.6	518.1	−.5	497.5	498.5	1.0
ν_3	261.0	257.3	−3.7	245.7	249.3	4.6
ν_4	270.2	271.3	1.1	255.2	254.1	−1.1
ν_5	157.1	157.9	0.8	152.8	151.9	−0.9
	$^{6-7}Li_2F_2$			$^{7-6}Li_2F_2$		
ν_1	766.8	767.7	0.9	720.8	720.7	−0.1
ν_2	497.8	499.8	2.8	518.3	516.6	−1.7
ν_3	252.9	249.5	−3.4	265.5	257.1	−8.5
ν_4	260.1	271.2	11.1	249.6	254.0	4.4
ν_5		152.1			157.7	

The observed product rule for the pure species is also consistent with a D_{3h} cyclic structure for the trimer. If one assigns 767.8, 518.6, and 261.0 cm^{-1} to $^7Li_3F_3$ and 720.8, 497.5, and 245.7 cm^{-1} to $^6Li_3F_3$, the product rule predicts a value of 1.158 for the E' modes as compared to an observed value of 1.180. The infrared active bending modes (A_2'') could then be satisfactorily assigned to 270.2, 265.5, 260.1, and 255.2 for $^6Li_3F_3$, $^6Li_2{}^7LiF_3$, $^6Li^7Li_2F_3$, and $^7Li_3F_3$, respectively. This assignment leaves the far infrared bands at 152–157 cm^{-1} unassigned. It also does not explain the intensity results obtained for the 767.8 and 766.8 cm^{-1} bands nor the intensity ratios obtained by

running ^{6}LiF in the region of ^{7}LiF and vice versa. It is, perhaps, interesting to note that any breakdown in symmetry due to site group splitting to D_3 or C_3 symmetry will not affect the number of expected bands, since E' of D_{3h} maps onto E in both D_3 and C_3 groups, while A_2'' maps onto A_2 and A, respectively. Assignment of these features to a cyclic trimer of lithium fluoride is also inconsistent with the vibrational data in the 770 and 500 cm^{-1} regions for the mixed species. In particular, it is hard to envision a molecule of this symmetry experiencing such small isotope shifts for stretching modes; that is, the cyclic model would require an isotope shift for the E' stretching modes of $^7Li_3F_3$ and $^7Li_2{}^6LiF_3$ to be of the order of one cm^{-1}.

The evidence then for a linear dimer of lithium fluoride can be briefly summarized as follows. Using double boiler and diffusion experiments, five absorption bands are shown to belong to the same molecular species. The expected intensity is found in the 767.8 and 766.8 cm^{-1} bands of $^6Li_2F_2$ and the $^6Li^7LiF_2$ isotopic variants of the proposed dimers. The Teller-Redlich product rule for the proposed assignment is 1.176 for the Σ modes. If one reverses the assignment for ν_3 and ν_4, the product rule calculation yields 1.180. Both of these product rule values are consistent with the calculated value of 1.144. (While this agreement is a necessary prerequisite for the proposed structure, product rule calculations are not sufficient proofs.) Examining the spectrum of ^{n}LiF and ^{6}LiF (95 percent enriched) in regions of ^{6}LiF and ^{7}LiF, respectively, in rather heavy deposits, one observes the spectrum of the mixed isotope (in a 5 percent concentration) that is consistent with a linear dimer model. Finally, an empirical force field determined from $^6Li_2F_2$ and $^7Li_2F_2$ predicts quite well the observed vibrational spectrum for the two mixed isotopic linear species.

Some of us (S. A. and N. A.) wish to acknowledge the support of the Propulsion Division of the Air Force Office of Scientific Research, U.S. Department of Defense.

5. References

[1] Linevsky, M. J., J. Chem. Phys. **34,** 587 (1961).
[2] Linevsky, M. J., J. Chem. Phys. **38,** 658 (1963).
[3] Snelson, A., and Pitzer, K. S., J. Phys. Chem. **67,** 882 (1963).
[4] Schlick, S., and Schnepp, O., J. Chem. Phys. **41,** 463 (1964).
[5] Reddington, R. L., J. Chem. Phys. **44,** 1238 (1966).
[6] Snelson, A., J. Chem. Phys. **46,** 3652 (1967).
[7] Mann, D. E., Calder, G. V., Seshadri, K. S., White, D., and Linevsky, M. J., J. Chem. Phys. **46,** 1138 (1967).
[8] Certain commercial instruments are identified in this paper to specify completely the experimental procedure. In no case does such identification imply a recommendation or endorsement by the National Bureau of Standards or the National Institutes of Health.
[9] Tables of Interatomic Distances and Configuration in Molecules and Ions, Sutton, L. E., Ed. (The Chemical Society, London, 1958).
[10] Wilson, E. B., Decius, J. C., and Cross, P. C., Molecular Vibrations (McGraw-Hill Book Co., Inc., New York, 1955).

(Paper 72A5–516)

JOURNAL OF RESEARCH of the National Bureau of Standards—A. Physics and Chemistry
Vol. 72A, No. 5, September–October 1968

Electronic Transition Moment Integrals for First Ionization of CO and the A—X Transition in CO^+. Some Limitations on the use of the *r*-Centroid Approximation*

Paul H. Krupenie

Institute for Basic Standards, National Bureau of Standards, Washington, D.C. 20234

and

William Benesch

Institute for Molecular Physics, University of Maryland, College Park, Maryland 20742

(May 25, 1968)

Integrals necessary for the determination of transition moment matrix elements from experimental data have been evaluated numerically by use of vibrational wave functions derived from RKR potentials. A power series expansion for the electronic transition moment has been assumed. The significant quantities which can be related to an arbitrary center of expansion are vibrational overlap integrals and quantities of the form $\int \psi_{v'} r^n \psi_{v''} dr$. Experimental band intensities and relative populations for vibrational levels of the initial electronic state are needed to determine the expansion coefficients. Transition moment integrals have been calculated for first ionization from the ground electronic state of CO and for the $A^2\Pi_i - X^2\Sigma^+$ transition of CO^+. Comparison of these integrals with previous calculations based on Morse functions has shown them to be rather sensitive to the wave-functions [potentials] used. Characteristics generally attributed to the *r*-centroid and related integrals are examined, and some limitations on the use of the *r*-centroid approximation are discussed, following a review of assumptions made in the use of that approximation.

Key Words: Electronic transition moment integrals; Franck-Condon factors; Franck-Condon principle; transition probabilities; CO; CO^+.

1. Introduction

Quantitative determination of transition probabilities for diatomic molecules is generally based on the "dipole approximation", the bases and limitations of which have been stated by Bethe and Salpeter [1]. The length form for the transition moment matrix element is commonly used for simplicity. Herzberg [2] has given the basis for the approximate separation of nuclear and electronic multipole moments so that only the electronic contribution need be considered. The Born-Oppenheimer approximation is assumed valid, i.e.,

$$\psi_{\text{total}}(x, r) \simeq \psi_e(x, r)\psi_v(r) \tag{1}$$

where r is the internuclear distance and x refers to the electronic coordinates. Vibration-rotation interaction and isotope effects are not considered here.

Intensities of electronic-vibrational bands or radiative lifetimes of vibrational energy levels are most often used to provide the measures of transition probabilities. This discussion emphasizes the use of intensities.

The integrated intensity of an electronic-vibrational band (electric dipole transition) is given by [2]

$$I_{v'v''} = N_{v'} A_{v'v''} hc\sigma_{v'v''} = \text{const.}\, N_{v'} \sigma_{v'v''}^4 |R_{v'v''}|^2 \tag{2}$$

for emission, and by

$$I_{v'v''} = \text{const.}\, N_{v''} \sigma_{v'v''} |R_{v'v''}|^2 \tag{3}$$

for absorption. $N_{v'}$ and $N_{v''}$ are the populations of levels v' and v'', $A_{v'v''}$ is the transition probability for spontaneous emission, $\sigma_{v'v''}$ is the wave number of the

*A preliminary version of these results was presented at the Molecular Spectroscopy Symposium, Ohio State University, Columbus, Ohio, 8 September 1966. This research sponsored in part by the U.S. Army Research Office—Durham.

transition, and $R_{v'v''}$ is the multipole moment matrix element whose square is the band strength, $S_{v'v''}$. The transition probability is proportional to the square of the matrix element [2] which is given by

$$R_{v'v''}=\int \psi_{v'}(r)R_e(r)\psi_{v''}(r)dr \tag{4}$$

where the electronic transition moment is given by

$$R_e(r)=\int \psi_{e'}(x, r)M(x)\psi_{e''}(x, r)dx. \tag{5}$$

$\psi_{v'}$ and $\psi_{v''}$ are the vibrational wave functions for levels v' and v'', $\psi_{e'}$ and $\psi_{e''}$ are the corresponding electronic wave functions, and $M(x)$ is the electric multipole moment, a function only of electronic coordinates (e.g., electronic dipole moment is $e\Sigma x_i$). For an electric quadrupole or magnetic multipole transition, the more complicated expressions analogous to (5) still reduce to some function of internuclear distance, $R_e(r)$.

There exists ambiguity about some quantities which appear in (2) and (3). A characteristic wave number for the band is not clearly defined. If absolute intensities are considered then the constants include statistical weights of the upper and lower electronic states. Transition moment and band strength have been defined in the literature in several different ways. A critical discussion of these and related topics has recently been given by Tatum [3].

$R_e(r)$ usually cannot be calculated from first principles because of insufficient knowledge about electronic wave functions, so we assume that R_e can be approximated by

$$R_e(r)=R_0+R_1(r-r_0)+R_2(r-r_0)^2+\ldots \tag{6}$$

where r_0 is some meaningful center of expansion for the electronic transition. A possible choice for r_0 is $(r'_e+r''_e)/2$ which will generally lie within a region where both $\psi_{v'}$ and $\psi_{v''}$ are nonvanishing; however, this choice is arbitrary. An r_0 "characteristic" of the 0–0 transition has been suggested in the literature, but this is not always a useful choice when $|r'_e-r''_e|$ is large, since the 0–0 transition may not be easily observable.

It is tempting to consider (6) a Taylor series and to relate the expansion coefficients, R_i, to derivatives of $R_e(r)$; however, the use of generally imprecise data on intensities and vibrational populations, together with the inclusion of only a few terms in the expansion, makes this procedure uncertain. The transition moment can be simply approximated as

$$R_e(r)=R_0+R_1r+R_2r^2+\ldots \tag{6a}$$

and the empirical coefficients R_i obtained by using the observed values of I, σ, and N in (2) or (3), and employing the method of least squares.

Substitution of (6a) into (4) gives the matrix element

$$R_{v'v''}=R_0(v', v'')+R_1(v', rv'')+R_2(v', r^2v'')+\ldots \tag{7}$$

the square of which is the band strength. In (7) integrals of the form $\int \psi_{v'}r^n\psi_{v''}dr$ are indicated by (v', r^nv''). In the r-centroid approximation [4], the square of (7) is approximated as

$$S_{v'v''}=-|R_{v'v''}|^2\simeq R_e^2(\bar{r}_{v'v''})q_{v'v''}. \tag{8}$$

The band strength is written as the Franck-Condon factor [square of the vibration overlap integral] times the square of the transition moment as a function of r-centroid which is

$$\bar{r}_{v'v''}=\frac{(v', rv'')}{(v', v'')}. \tag{9}$$

Separability of the total wave functions in the Born-Oppenheimer approximation does not necessarily imply the factorability of the band strength into an electronic part times a vibrational part. That factorization is based on an assumed form [r-dependence] for the intermediate parameter, the transition moment.

For constant $R_e(r)$, $S_{v'v''}$ includes only a single term, $R_0^2q_{v'v''}$, and the Franck-Condon factor contains all the relative band-to-band variation. For linear $R_e(r)$, (7) becomes

$$R_{v'v''}=R_0(v', v'')+R_1(v', rv'') \tag{7a}$$

or

$$R_{v'v''}=(v', v'')(R_0+R_1\bar{r}_{v'v''}) \tag{7b}$$

and $S_{v'v''}$ has the form of (8) [5, 4]. In the r-centroid approximation the assumption is made that the band strength is also factorable as in (8) for [slowly varying] nonlinear $R_e(r)$. This is based on the assumed near equality of ratios [4]

$$\bar{r}_{v'v''}=\frac{(v', rv'')}{(v', v'')}\simeq\frac{(v', r^2v'')}{(v', rv'')}\simeq\frac{(v', r^nv'')}{(v', r^{n-1}v'')} \tag{10}$$

up to perhaps $n\simeq 10$. A consequence of this assumption is [4] that, for any reasonable function, $f(r)$,

$$(v', f(r)v'')=f(\bar{r}_{v'v''})(v', v'') \tag{11}$$

which, in particular, always implies (8). Our numerical calculations on the ratios of (10) for the ionization transition $(X^2\Sigma^+)$ $CO^+-(X^1\Sigma^+)$ CO and the A–X transition in CO^+ suggest that for nonlinear R_e, the band strength may not always be factored according to (8) [6].

An implicit assumption made in this type of calculation is that R_e must be a slowly varying function of r [2]. How slowly varying this should be is not clear. Nevertheless, in several cases [7], significant variation has been deduced from use of experimental intensities and (2) and (8). It is, of course, possible for an appreciable apparent variation in R_e over a small range of r to arise from inaccurate intensity measurements, inaccurate values of $q_{v'v''}$, or the possibly invalid approximation (8).

Tyte [8] has cautioned against the casual use of experimental intensities in determining the form of the transition moment, for the relative intensity distribution may depend on experimental conditions. There are also built-in complications in the use of intensities because of blended rotational structure and partial overlap of bands.

The use of radiative lifetimes for determining $R_e(r)$ is even more complicated than use of intensities as can be seen from the following equation

$$\tau_{v'} = \frac{1}{\sum\limits_{v''} A_{v'v''}} = \frac{1}{\text{const.} \sum\limits_{v''} \sigma^3_{v'v''} |R_{v'v''}|^2} \qquad (12)$$

2. Transition Moment Integrals for $X^2\Sigma^+(CO^+) - X^1\Sigma^+(CO)$ and $A^2\Pi_i(CO^+) - X^2\Sigma^+(CO^+)$

Our original objective was the tabulation of Franck-Condon factors and r-centroids for ionization transitions of CO and electronic transitions of CO^+. Our results for $X(CO^+)-X(CO)$ and $A(CO^+)-X(CO^+)$ showed numerous instances where, within a given v' or v'' progression, the r-centroids did not vary monotonically (tables 1–2). Later we became aware of a number of cases where this nonmonotonic behavior had occurred [9, 7b] for calculations based on both Morse and RKR potentials. Meanwhile, there had appeared a theoretical deduction by Nicholls [10] that $\bar{r}_{v'v''}$ must vary monotonically with respect to wavenumber within a progression.

Nicholls used the Morse function with the Fraser-Jarmain approximation of mean exponential coefficient [11]. His conclusion, however, does not depend on the potential used, but only on the assumption that (10) and (11) are valid. In this case $f(r)$ is the potential function, and (11) leads to the graphical method for determining $\bar{r}_{v'v''}$ [4, 12]

$$G(v') - G(v'') = U'(\bar{r}_{v'v''}) - U''(\bar{r}_{v'v''}) \qquad (13)$$

where G is the vibrational term value and U is the potential energy. Since (13) always gives monotonic values within a progression, it may be necessary to revise r-centroids and transition moments determined in this manner.

The transition moment integrals in (7) were evaluated by use of vibrational wave functions based on RKR potentials [13]. These wave functions have been obtained by a method previously discussed by Benesch et al. [14a].

Since the raw wave function is generated as a combination of two unnormalized segments propagated toward each other from either end of the range of interest, an accommodation must be made at the meeting point. The possible methods of arranging for such an accommodation have been discussed elsewhere at length [14]. In the present work, special care has been taken to insure that the location of the meeting point be such as (a) to prevent either segment from slipping into instability and (b) to provide a relatively large value of the wave function ordinate as a basis for the rescaling of the separate segments prior to joining. Experience has shown that in order to cover all cases of mating, with slopes and ordinates large and small, it is helpful to introduce a monitoring routine for the immediate detection and rectification of pathological cases.

TABLE 1. *Transition moment integrals for the* $X^2\Sigma^+(CO^+) - X^1\Sigma^+(CO)$ *transition*

Entries have been arbitrarily terminated beyond $v'' = 10$. The last two columns are in Å. The values of $q_{v'v''}$ tabulated here are to be compared with those based on Morse functions [M. Halmann and I. Laulicht, J. Chem. Phys. **43**, 1503–9 (1965)]. The integrals in (7) are obtained by multiplying the ratios of integrals listed and using $(v', v'') = q_{v'v''}^{1/2}$.

v'	v''	$q_{v'v''}$	$\frac{(v', rv'')}{(v', v'')}$	$\frac{(v', r^2v'')}{(v', rv'')}$	v'	v''	$q_{v'v''}$	$\frac{(v', rv'')}{(v', v'')}$	$\frac{(v', r^2v'')}{(v', rv'')}$
0	0	0.9644E−00	1.126	1.127					
1	0	.3566E−01	1.304	1.281	1	6	0.1921E−05	0.666	0.572
2	0	.9802E−04	1.839	1.654	2	6	.7703E−04	0.770	0.735
8	0	.7982E−06	1.177	1.176	3	6	.1414E−02	0.812	0.772
					4	6	.1776E−01	0.884	0.852
0	1	.3383E−01	0.950	0.918	5	6	.1339E−00	0.964	0.929
1	1	.8967E−00	1.135	1.138	6	6	.6424E−00	1.184	1.198
2	1	.6923E−01	1.312	1.290	7	6	.2038E−00	1.356	1.338
3	1	.2435E−03	1.908	1.691	8	6	.6476E−03	2.480	1.926
4	1	.2566E−05	1.078	0.739	9	6	.1555E−03	1.299	1.149
8	1	.1476E−05	1.171	1.170	10	6	.8092E−06	2.343	1.986
10	1	.6424E−06	1.184	1.184	11	6	.1117E−05	1.288	1.236
11	1	.1251E−05	1.186	1.186	12	6	.1308E−05	1.138	1.156
12	1	.5070E−06	1.197	1.197					
					2	7	.7916E−05	0.728	0.689
0	2	.1586E−02	0.865	0.829	3	7	.1560E−03	0.760	0.717
1	2	.6286E−01	0.954	0.922	4	7	.2254E−02	0.813	0.772
2	2	.8341E−00	1.144	1.149	5	7	.2319E−01	0.889	0.860
3	2	.1006E−00	1.320	1.299	6	7	.1412E−00	0.964	0.927
4	2	.4286E−03	1.958	1.718	7	7	.6098E−00	1.195	1.211
5	2	.6665E−05	1.135	0.830	8	7	.2179E−00	1.369	1.350
6	2	.5311E−06	1.456	1.471	9	7	.6308E−03	2.643	1.979
					10	7	.2262E−03	1.350	1.206
0	3	.8571E−04	0.797	0.754	11	7	.1448E−05	2.420	2.008
1	3	.4451E−02	0.869	0.834	13	7	.1127E−05	1.089	1.120
2	3	.8769E−01	0.958	0.926					
3	3	.7772E−00	1.153	1.160	1	8	.5427E−06	1.066	1.101
4	3	.1301E−00	1.329	1.308	3	8	.1620E−04	0.693	0.622
5	3	.5757E−03	2.042	1.758	4	8	.3081E−03	0.781	0.751
6	3	.2249E−04	1.181	0.958	5	8	.3286E−02	0.817	0.777
7	3	.6232E−06	1.600	1.591	6	8	.2738E−01	0.891	0.862
8	3	.2231E−05	1.166	1.172	7	8	.1445E−00	0.962	0.923
9	3	.5205E−06	1.159	1.161	8	8	.5837E−00	1.205	1.225
11	3	.5928E−06	1.216	1.212	9	8	.2392E−00	1.379	1.361
					10	8	.4082E−03	3.138	2.095
0	4	.5492E−05	0.746	0.699	11	8	.5033E−03	1.350	1.242
1	4	.3297E−03	0.807	0.768					
2	4	.8268E−02	0.874	0.840	3	9	.2779E−05	0.741	0.734
3	4	.1073E−00	0.961	0.928	4	9	.3635E−04	0.721	0.675
4	4	.7262E−00	1.163	1.173	5	9	.4595E−03	0.764	0.720
5	4	.1570E−00	1.337	1.318	6	9	.4433E−02	0.817	0.775
6	4	.7474E−03	2.103	1.788	7	9	.3314E−01	0.898	0.872
7	4	.4340E−04	1.226	1.025	8	9	.1505E−00	0.962	0.920
10	4	.5835E−06	1.146	1.152	9	9	.5651E−00	1.218	1.239
11	4	.9991E−06	1.146	1.147	10	9	.2468E−00	1.392	1.374
					11	9	.2017E−03	4.116	2.246
0	5	.5930E−06	0.785	0.785	12	9	.5838E−03	1.420	1.306
1	5	.2570E−04	0.752	0.707	13	9	.1432E−05	0.601	6.320
2	5	.7541E−03	0.806	0.764					
3	5	.1301E−01	0.880	0.848	4	10	.6832E−05	0.770	0.780
4	5	.1228E−00	0.963	0.930	5	10	.6254E−04	0.716	0.666
5	5	.6811E−00	1.173	1.185	6	10	.6689E−03	0.761	0.714
6	5	.1823E−00	1.346	1.328	7	10	.5730E−02	0.818	0.774
7	5	.7760E−03	2.235	1.842	8	10	.3944E−01	0.906	0.884
8	5	.5198E−04	1.304	1.086	9	10	.1463E−00	0.956	0.908
9	5	.1238E−05	1.870	1.768	10	10	.5538E−00	1.229	1.253
10	5	.5950E−06	1.115	1.153	11	10	.2578E−00	1.406	1.388
11	5	.1120E−05	1.181	1.192	13	10	.8231E−03	1.466	1.359

TABLE 2. *Transition moment integrals for the* $A^2\Pi_i - X^2\Sigma^+$ *transition of* CO^+

The last three columns are in Å. The integrals in (7) are obtained by multiplying the ratios of integrals listed and using $(v', v'') = q_{v'v''}^{1/2}$. The only deletion in this Deslandres array is 0–13 ($q < 0.5 \times 10^{-6}$).

v'	v''	$q_{v'v''}$	$\frac{(v', r^1v'')}{(v', v'')}$	$\frac{(v', r^2v'')}{(v', r^1v'')}$	$\frac{(v', r^3v'')}{(v', r^2v'')}$
0	0	0.4237E−01	1.178	1.179	1.181
1	0	.1131E−00	1.161	1.162	1.163
2	0	.1666E−00	1.145	1.146	1.146
3	0	.1797E−00	1.130	1.130	1.130
4	0	.1585E−00	1.115	1.115	1.115
5	0	.1221E−00	1.101	1.101	1.101
6	0	.8519E−01	1.088	1.087	1.087
7	0	.5496E−01	1.075	1.074	1.073
8	0	.3358E−01	1.063	1.062	1.061
9	0	.1959E−01	1.051	1.050	1.048
10	0	.1114E−01	1.040	1.038	1.036
11	0	.6158E−02	1.029	1.027	1.025
0	1	.1518E−00	1.202	1.203	1.204
1	1	.1926E−00	1.184	1.184	1.184
2	1	.9885E−01	1.167	1.166	1.165
3	1	.1422E−01	1.147	1.143	1.139
4	1	.4447E−02	1.146	1.153	1.161
5	1	.4119E−01	1.125	1.127	1.129
6	1	.7890E−01	1.110	1.111	1.112
7	1	.9512E−01	1.096	1.097	1.097
8	1	.9066E−01	1.084	1.083	1.083
9	1	.7431E−01	1.071	1.071	1.070
10	1	.5541E−01	1.059	1.059	1.058
11	1	.3833E−01	1.048	1.047	1.046
0	2	.2505E−00	1.227	1.228	1.228
1	2	.8117E−01	1.207	1.206	1.204
2	2	.2743E−02	1.205	1.216	1.227
3	2	.7248E−01	1.177	1.178	1.179
4	2	.9599E−01	1.159	1.159	1.159
5	2	.4992E−01	1.143	1.141	1.139
6	2	.6767E−02	1.123	1.116	1.109
7	2	.3288E−02	1.127	1.136	1.146
8	2	.2723E−01	1.107	1.109	1.112
9	2	.5362E−01	1.093	1.094	1.095
10	2	.6855E−01	1.080	1.080	1.081
11	2	.6956E−01	1.068	1.068	1.068
0	3	.2522E−00	1.253	1.253	1.253
1	3	.5236E−03	1.270	1.296	1.318
2	3	.1074E−00	1.217	1.218	1.219
3	3	.7054E−01	1.197	1.196	1.194
4	3	.1025E−02	1.158	1.137	1.113
5	3	.3040E−01	1.170	1.173	1.176
6	3	.7028E−01	1.153	1.153	1.154
7	3	.5856E−01	1.137	1.136	1.135
8	3	.2218E−01	1.121	1.118	1.114
9	3	.1022E−02	1.093	1.074	1.054
10	3	.5758E−02	1.106	1.113	1.120
11	3	.2496E−01	1.090	1.093	1.095
0	4	.1736E−00	1.280	1.280	1.280
1	4	.9207E−01	1.263	1.265	1.266
2	4	.8573E−01	1.240	1.239	1.237
3	4	.3553E−02	1.239	1.250	1.261
4	4	.7630E−01	1.207	1.208	1.209
5	4	.5820E−01	1.188	1.187	1.185
6	4	.4001E−02	1.162	1.151	1.139
7	4	.1388E−01	1.166	1.171	1.176
8	4	.4927E−01	1.147	1.148	1.150
9	4	.5485E−01	1.132	1.131	1.131
10	4	.3186E−01	1.117	1.115	1.113
11	4	.7620E−02	1.101	1.095	1.088
0	5	.8628E−01	1.309	1.308	1.307
1	5	.1917E−00	1.289	1.289	1.290
2	5	.4351E−03	1.218	1.179	1.133
3	5	.9682E−01	1.250	1.251	1.252
4	5	.3713E−01	1.227	1.224	1.221
5	5	.7790E−02	1.224	1.232	1.240
6	5	.6208E−01	1.199	1.200	1.201
7	5	.4859E−01	1.180	1.179	1.177
8	5	.5927E−02	1.157	1.148	1.139
9	5	.6402E−02	1.163	1.171	1.179
10	5	.3430E−01	1.142	1.144	1.146
11	5	.4762E−01	1.128	1.128	1.128
0	6	.3206E−01	1.339	1.337	1.336
1	6	.1766E−00	1.317	1.317	1.316
2	6	.7181E−01	1.299	1.301	1.304
3	6	.6324E−01	1.273	1.271	1.269
4	6	.1862E−01	1.264	1.269	1.274
5	6	.7878E−01	1.238	1.238	1.238
6	6	.1521E−01	1.214	1.209	1.203
7	6	.1157E−01	1.212	1.219	1.225
8	6	.5276E−01	1.191	1.192	1.193
9	6	.4151E−01	1.173	1.171	1.170
10	6	.7227E−02	1.151	1.144	1.135
11	6	.2664E−02	1.163	1.176	1.188
0	7	.9157E−02	1.370	1.368	1.366
1	7	.1001E−00	1.347	1.346	1.345
2	7	.1736E−00	1.325	1.326	1.327
3	7	.8726E−03	1.347	1.373	1.395
4	7	.9872E−01	1.283	1.283	1.284
5	7	.6614E−02	1.250	1.240	1.229
6	7	.4152E−01	1.249	1.252	1.255
7	7	.5698E−01	1.227	1.226	1.225
8	7	.5268E−02	1.200	1.190	1.179
9	7	.1402E−01	1.203	1.209	1.215
10	7	.4586E−01	1.184	1.185	1.186
11	7	.3641E−01	1.166	1.165	1.163
0	8	.2012E−02	1.402	1.400	1.398
1	8	.3885E−01	1.378	1.377	1.375
2	8	.1628E−00	1.355	1.354	1.354
3	8	.9119E−01	1.336	1.338	1.340
4	8	.3093E−01	1.304	1.300	1.296
5	8	.5219E−01	1.294	1.297	1.300
6	8	.5274E−01	1.268	1.266	1.265
7	8	.1508E−02	1.283	1.304	1.323
8	8	.5031E−01	1.238	1.240	1.241
9	8	.3841E−01	1.218	1.215	1.213
10	8	.1301E−02	1.182	1.159	1.133
11	8	.1551E−01	1.196	1.202	1.207
0	9	.3258E−03	1.443	1.439	1.436
1	9	.1104E−01	1.411	1.409	1.407
2	9	.8872E−01	1.387	1.385	1.384
3	9	.1743E−00	1.363	1.364	1.364
4	9	.1598E−01	1.352	1.359	1.365
5	9	.8310E−01	1.316	1.315	1.314
6	9	.4099E−02	1.319	1.333	1.346
7	9	.6895E−01	1.279	1.280	1.280
8	9	.1547E−01	1.252	1.246	1.240
9	9	.1258E−01	1.253	1.260	1.267
10	9	.4873E−01	1.229	1.229	1.230
11	9	.2553E−01	1.209	1.206	1.203
0	10	.3799E−04	1.497	1.489	1.483
1	10	.2314E−02	1.445	1.442	1.440
2	10	.3206E−01	1.421	1.419	1.417
3	10	.1410E−00	1.395	1.394	1.394
4	10	.1289E−00	1.373	1.375	1.376
5	10	.3217E−02	1.317	1.299	1.280
6	10	.8506E−01	1.327	1.328	1.329
7	10	.1063E−01	1.292	1.284	1.275
8	10	.3627E−01	1.291	1.295	1.298
9	10	.4829E−01	1.267	1.265	1.264
10	10	.1165E−02	1.218	1.191	1.160
11	10	.2329E−01	1.241	1.245	1.249
0	11	.2098E−05	1.650	1.609	1.581
1	11	.3642E−03	1.479	1.477	1.475
2	11	.8085E−02	1.457	1.454	1.452
3	11	.6676E−01	1.429	1.428	1.426
4	11	.1717E−00	1.404	1.404	1.404
5	11	.5958E−01	1.385	1.389	1.392
6	11	.4027E−01	1.348	1.344	1.341
7	11	.4330E−01	1.339	1.343	1.346
8	11	.4729E−01	1.310	1.307	1.305
9	11	.3530E−02	1.318	1.333	1.347
10	11	.5099E−01	1.278	1.279	1.280
11	11	.2368E−01	1.255	1.250	1.246
0	12	.9359E−06	1.398	1.421	1.441
1	12	.2899E−04	1.575	1.560	1.548
2	12	.1464E−02	1.494	1.491	1.488
3	12	.2066E−01	1.466	1.463	1.461
4	12	.1093E−00	1.438	1.437	1.436
5	12	.1651E−00	1.413	1.414	1.415
6	12	.1034E−01	1.408	1.418	1.428
7	12	.7871E−01	1.360	1.359	1.358
8	12	.5876E−02	1.364	1.376	1.388
9	12	.6467E−01	1.321	1.321	1.321
10	12	.6190E−02	1.284	1.272	1.260
11	12	.2388E−01	1.291	1.296	1.300
0	13	.....			
1	13	.1413E−05	1.721	1.675	1.643
2	13	.1713E−03	1.546	1.541	1.536
3	13	.4279E−02	1.506	1.503	1.500
4	13	.4146E−01	1.476	1.474	1.472
5	13	.1489E−00	1.447	1.447	1.446
6	13	.1264E−00	1.424	1.426	1.428
7	13	.1659E−02	1.332	1.300	1.263
8	13	.8401E−01	1.371	1.372	1.373
9	13	.3539E−02	1.318	1.300	1.279
10	13	.4699E−01	1.332	1.335	1.337
11	13	.3228E−01	1.305	1.301	1.298

A number of other checking and diagnostic procedures were instituted in order to seek out computing artifacts and to determine the level of reliability of the results. The effects of changes in integration grid size were examined. Tables were generated for the point-by-point comparison of the function $(d^2\psi/dr^2)/\psi$ with $(U-E)$ as a measure of compliance with the Schroedinger equation, while a macroscopic test consisted of computing self-overlap integrals and overlaps for wave functions of differing vibrational quantum number within the same electronic state. In other words, tables of $\int \psi_{v'}\psi_{v''}dr$ have been computed for all the values of v' and v'' of interest within a single electronic state. The self overlap integrals [squared] were found to be good to 5×10^{-6} and the overlap integrals [squared] of orthogonal functions were no larger than 0.5×10^{-6}. Finally, it was determined that calculated B_v values (i.e., const. $(v, 1/r^2\ v)$) agreed with the corresponding input data values to within 0.0007 to 0.0028 cm^{-1}. Accordingly, we rounded the calculated table entries to four digits, deleting those for transitions having $q_{v'v''} < 0.5\times10^{-6}$.

The significant features of tables 1 and 2 are these: (a) For numerous vibrational transitions the ratios of integrals in (10) are not equal. (b) Within a number of v' or v'' progressions the $\bar{r}_{v'v''}$ do not vary monotonically. In other progressions the $\bar{r}_{v'v''}$ are monotonic, but are noticeably not a smooth function of v' (or v''). (c) The onset of nonsmooth behavior correlates with minima in the $q_{v'v''}$, whether or not q is small in an absolute sense. (Fig. 1, table 3.)

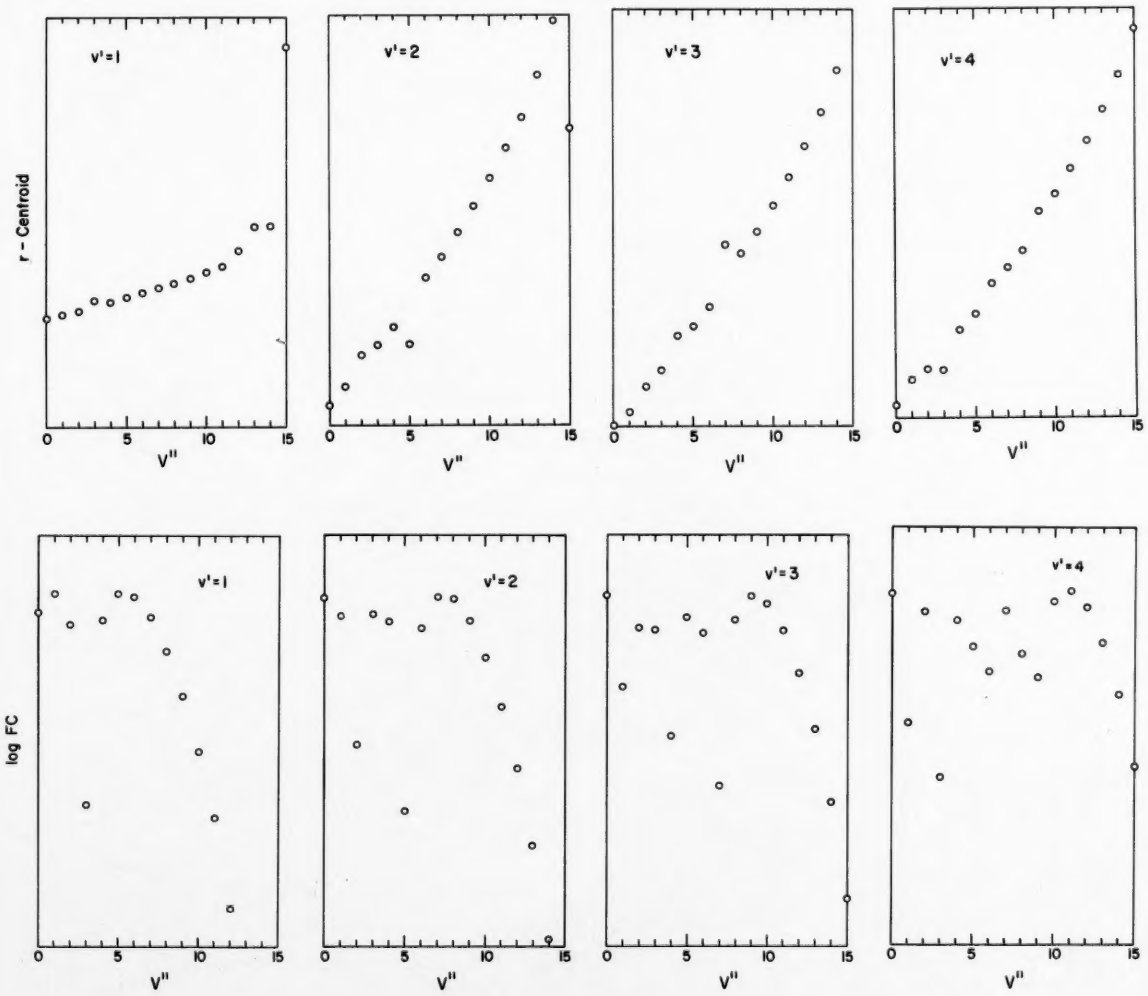

FIGURE 1. $r_{v'v''}$ *and* log $q_{v'v''}$ *for* $A^2\Pi_i - X^2\Sigma^+$, CO^+, $v' = 1, 2, 3, 4$ *progressions.*
Calculated values for $v'' = 14, 15$ are based on extrapolation of the potential function for the X state and are not considered reliable.

Fraser [4] has stated conditions for the assumed validity of the r-centroid approximation:

(a) $\mu_A\omega_e \simeq 10^4$; μ_A is the reduced mass of the molecule in atomic weight units, ω_e is in cm^{-1};

(b) $0.01\ \text{Å} < |r_{e'} - r_{e''}| < 0.25\ \text{Å}$;

(c) n_{max} is $\simeq 10$ in (10);

(d) $q_{v'v''}$ is not small (though small is not specified).

Condition (b) is fulfilled for the CO^+ transition but not for the ionization transition, so that in the latter case, the r-centroid approximation must be assumed to fail under Fraser's criteria. Qualitatively, the nonsmooth features are more prominent for the ionization transition.

It has been suggested [15] that the functional form of the electronic transition moment is more important than the choice of wave function in evaluating (4). However. the choice of wave function (or, more properly, the potential function from which the wave function is generated) can also be significant. RKR-based $q_{v'v''}$ and $\bar{r}_{v'v''}$ are compared in table 4 with previous values based on Morse functions [16]. This comparison does not confirm a statement by Nicholls [17] that the parameters (integrals) are insensitive to the exact potential used. Flinn [18] and Spindler [19] have also shown large differences between RKR and Morse integrals, even for small quantum numbers. From all these results we conclude that wave functions based on RKR potentials should be used where possible so that attention can be centered on the form of the transition moment.

Halevi [20] has assumed, as have others before him, that most of the contribution to the integrals in (7)

	0	1	2	3	4	5	6	7	8	9	10	11	12	13
0	.424-1	.152	.251	.252	.174	.863-1	.321-1	.916-2	.201-2	.326-3	.380-4	.210-5	.936-6	.259-6
1	.113	.193	.812-1	.524-3	.921-1	.192	.177	.100	.389-1	.110-1	.231-2	.364-3	.290-4	.141-5
2	.167	.989-1	.274-2	.107	.857-1	.435-3	.718-1	.174	.163	.887-1	.321-1	.809-2	.146-2	.171-3
3	.180	.142-1	.725-1	.705-1	.355-2	.968-1	.632-1	.873-3	.912-1	.174	.141	.668-1	.207-1	.428-2
4	.158	.445-2	.960-1	.102-2	.763-1	.371-1	.186-1	.987-1	.309-1	.160-1	.129	.172	.109	.415-1
5	.122	.412-1	.499-1	.304-1	.582-1	.779-2	.788-1	.661-2	.522-1	.831-1	.322-2	.596-1	.165	.149
6	.852-1	.789-1	.677-2	.703-1	.400-2	.621-1	.152-1	.415-1	.527-1	.410-2	.851-1	.403-1	.103-1	.126
7	.550-1	.951-1	.329-2	.586-1	.139-1	.486-1	.116-1	.570-1	.151-2	.690-1	.106-1	.433-1	.787-1	.166-2
8	.336-1	.907-1	.272-1	.222-1	.493-1	.593-2	.528-1	.527-2	.503-1	.155-1	.363-1	.473-1	.588-2	.840-1
9	.196-1	.743-1	.536-1	.102-2	.548-1	.640-2	.415-1	.140-1	.384-1	.126-1	.483-1	.353-2	.647-1	.354-2
10	.111-1	.554-1	.685-1	.576-2	.319-1	.343-1	.723-2	.459-1	.130-2	.487-1	.116-2	.510-1	.619-2	.470-1
11	.616-2	.383-1	.696-1	.250-1	.762-2	.476-1	.266-2	.364-1	.155-1	.255-1	.233-1	.237-1	.239-1	.323-1

TABLE 3. *Franck-Condon factors for the* $A^2\Pi_i - X^2\Sigma^+$ *system of* CO^+

Nonmonotonic r-centroids were found, generally, where the q's of neighboring bands in a progression differed by a factor of some 10^2. The transition with the smaller q, then, may have an r-centroid which breaks the monotonic series, while the band itself, falling in a hole between Condon loci, will be extremely weak or unobserved. Bands which have been observed are underlined. For a compendium of experimental data see P. H. Krupenie, "The Band Spectrum of Carbon Monoxide," National Standard Reference Data Series, National Bureau of Standards NSRDS–NBS No. 5 (1966).

TABLE 4. $q_{v'v''}$ *and* $\bar{r}_{v'v''}$ *for the* $A^2\Pi_1 - X^2\Sigma^+$, CO^+ *system*

Each entry for $q_{v'v''}$ includes the power of 10 (e.g., $-3 = 10^{-3}$) by which it is multiplied. Most differences between RKR and Morse data taken from ref. 16 are small. Only the values showing large differences are compared.

$v'-v''$	$q_{v'v''}$		$\bar{r}_{v'v''}$ (Å)	
	RKR	Morse	RKR	Morse
4–1	4.447–3	5.796–3	1.146	1.136
2–2	2.743–3	3.228–3	1.205	1.191
6–2	6.767–3	4.973–3	1.123	1.130
7–2	3.288–3	5.155–3	1.127	1.116
1–3	5.236–4	5.677–4	1.270	1.234
4–3	1.025–3	5.787–4	1.158	1.182
5–3	3.040–2	3.336–2	1.170	1.166
9–3	1.022–3	2.345–4	1.093	1.110
10–3	5.758–3	8.830–3	1.106	1.098
3–4	3.553–3	4.186–3	1.239	1.223
6–4	4.001–3	2.730–3	1.162	1.174
2–5	4.351–4	3.505–4	1.218	1.268
9–5	6.402–3	9.005–3	1.163	1.153
10–6	7.227–3	4.869–3	1.151	1.161
3–7	8.726–3	1.054–3	1.347	1.303
8–7	5.268–3	3.702–3	1.200	1.212
7–8	1.508–3	2.289–3	1.283	1.253
10–8	1.301–3	4.986–4	1.182	1.205
5–10	3.217–3	2.976–3	1.317	1.347
10–10	1.165–3	5.736–4	1.218	1.252
1–12	2.899–5	4.088–5	1.575	1.539
7–13	1.659–3	3.046–3	1.332	1.393

comes from a narrow region around $\bar{r}_{v'v''}$. This need not be so. $\int \psi_{v'}\psi_{v''} r dr$ is evaluated numerically as $\sum_r \psi_{v'}\psi_{v''} r \Delta r$. Plots of such cumulative sums as a function of r (fig. 2) may show regions having large slope which indicate large contribution to the integral in that r interval. Three general effects occur. Figure 2(a) describes an integral where there is no contribution except very near the average value of r. If the wave functions were delta functions then such sums would be step functions, and only at a single value of r would there be a contribution to the integral. In such instances the ratios of integrals in (10) would be equal. For functions whose product $\psi_{v'}\psi_{v''}$ is sharply peaked, whether for small or large overlap integral, a plot closely similar to figure 2(a) would be expected. Figure 2(b) shows smaller oscillations with the most significant contribution to the integral coming at large r. Figure 2(c)–(g) shows several regions with significant slope; the sums show large oscillations about the final value of (v', rv'').

Figure 2(c)–(g) describes what is likely true of many integrals, even for q as large as 0.1 (no integral for larger q has been checked, except 0–0, X–X). In

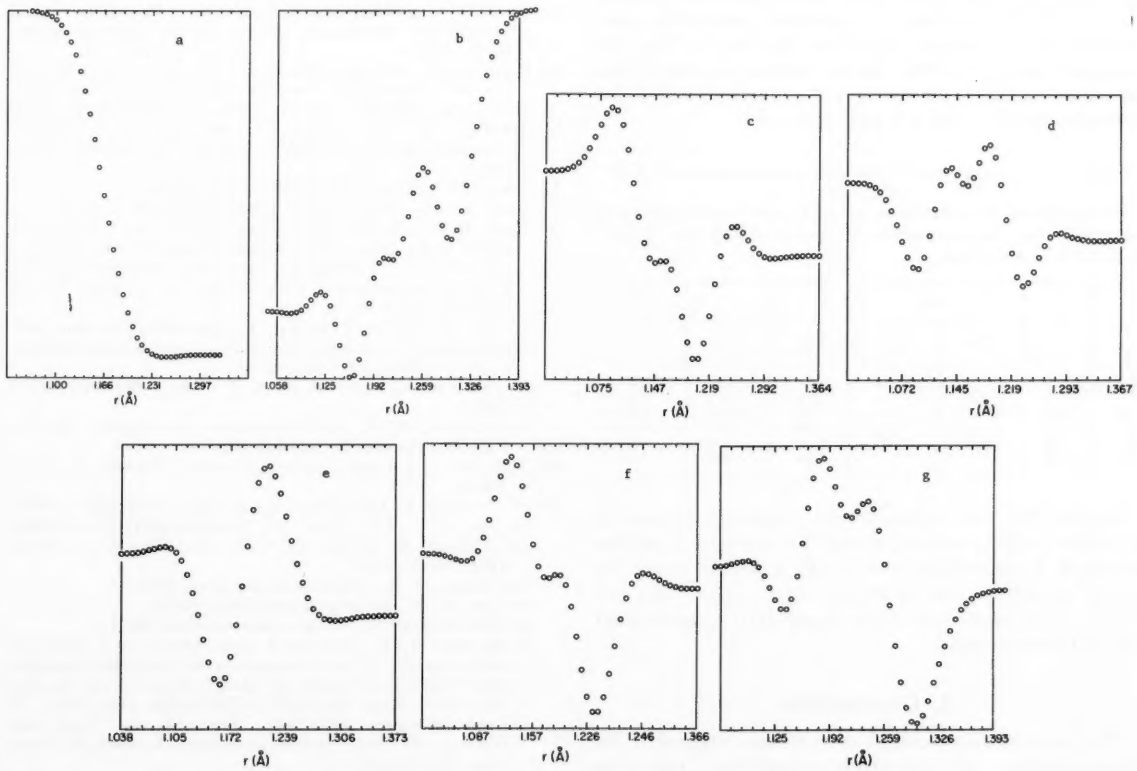

FIGURE 2. $\sum_r \psi_{v'}\psi_{v''} r \Delta r$ *for* A–X, CO^+ *transitions.*

(a) 1–0, (b) 2–6, (c) 6–2, (d) 7–2, (e) 2–2, (f) 4–3, (g) 2–5. The ordinate is 0 for smallest r; the ordinate is (v', rv'') for largest r. $q_{v'v''}$ decreases from (a) ≃ 0.1 to (g) ≃ 0.0004.

312-248 O-68—4

table 2 and the ratios (10) are not closely the same for $q \leq 2 \times 10^{-2}$. In table 1 the results are erratic. Only a detailed examination of all integrals would reveal whether the wave functions show delta-function like behavior as in figure 2(a).

Nicholls and Jarmain [12] state: "Comparison between the calculated values of $\bar{r}_{v'v''}$ of a band system and the ranges of r between the classical turning points for each of the levels v' and v'' has shown that $\bar{r}_{v'v''}$ lies within, or close to the region which is common to both ranges." This is generally true, but James [21] has already pointed out examples where $\bar{r}_{v'v''}$ lie outside the range of turning points and do not represent a meaningful average r. Since products of the wave functions do not become insignificantly small till 0.06 Å beyond the turning points, it is not surprising if an r-centroid lies beyond the turning points, providing tails of both wave functions are involved. Table 5 shows some of the extreme examples we have obtained. The A–X, 0–0 and 1–0 transitions illustrate the influence of wave function tails. For 0–0 the turning points do not overlap by 0.026 Å; for 1–0 they overlap slightly. In both instances, $\bar{r}_{v'v''} \simeq \dfrac{r''_{\max} + r'_{\min}}{2}$.

Since the ground states of CO and CO^+ have nearly the same r_e and nearly the same potential shapes, almost all the ionization transition probability gets dumped into a single transition for low v. The 0–0 transition has $q = 0.964$. Large values of q are found for other members of the $\Delta v = 0$ sequence, where, for example, the 7–7 entry is still above 0.6.

TABLE 5. *$\bar{r}_{v'v''}$ lying outside turning points for some* $A-X$, CO^+ *transitions*

Turning points are taken from ref. 13. $\bar{r}_{v'v''}$ and turning points are in Å. Each entry for $q_{v'v''}$ includes the power of 10 (e.g., $-3 = 10^{-3}$) by which it is multiplied.

$v'-v''$	$\bar{r}_{v'v''}$	$A^2\Pi_i$		$X^2\Sigma^+$		$q_{v'v''}$
		$r_{\min}$	$r_{\max}$	$r_{\min}$	$r_{\max}$	
0–0	1.178	1.191	1.304	1.071	1.165	4.237–2
11–0	1.029	1.046	1.634	1.071	1.165	6.158–3
0–6	1.339			0.977	1.330	3.206–2
0–7	1.370	1.191	1.304	0.968	1.350	9.157–3
0–8	1.402			0.961	1.370	2.012–3
0–9	1.443			0.954	1.390	3.258–4

Halevi [20] has expanded the transition moment in a Taylor series centered about the r-centroid and has obtained a correction term to $R_e^2(\bar{r}_{v'v''})q_{v'v''}$ which depends on the second derivative of $R_e(\bar{r}_{v'v''})$. This correction term may have little quantitative significance when (10) is not valid.

3. Conclusions

We have drawn several conclusions regarding the determination of electronic-vibrational transition probabilities from a study of two electronic transitions:

(1) The r-centroid approximation for obtaining electronic transition moments and band strengths may prove to be not continuously valid along the significant portion of a vibrational progression. The band strength may not always be factored as $R_e^2(\bar{r}_{v'v''})q_{v'v''}$ for nonlinear R_e.

(2) Interpretation of the r-centroid as an average r is not always meaningful.

(3) The transition moment integrals are sensitive to the potential used; they should be calculated from RKR potentials where possible.

(4) The Fraser criteria are not sufficient to insure the validity of the r-centroid approximation.

(5) The series expansion for the transition moment may be used when the r-centroid approximation fails.

We thank Roger Main for bringing to our attention the work by Tatum prior to its publication. The computer time for this project was supported by National Aeronautics and Space Administration Grant NsG–398 to the Computer Science Center of the University of Maryland.

4. References

[1] Bethe, H. A., and Salpeter, E. E., Quantum Mechanics of One- Two-Electron Atoms, pp. 248–52, 278–84 (Springer-Verlag, Berlin, 1957).

[2] Herzberg, G., Spectra of Diatomic Molecules, Second Edition, Seventh Printing (D. Van Nostrand Co., Inc., New York, 1961); pp. 199–204. See the references cited by Herzberg.

[3] Tatum, J. B., The interpretation of intensities in diatomic molecular spectra, Astrophys. J. Suppl. **14,** No. 124, 21–56 (1967).

[4] Fraser, P. A., Can. J. Phys. **32,** 515–21 (1954).

[5] Poots, G., Proc. Phys. Soc. (London). **A66,** 1181–4 (1953).

[6] Bates, D. R., Monthly Notices Roy. Astron. Soc. **112,** 614–36 (1952). Bates coined the expression Franck-Condon factor to represent $(v', v'')^2$ which is a factor of the band strength when a series or polynomial approximation is assumed for the transition moment.

[7] (a) Tyte, D. C., Proc. Phys. Soc. (London) **A80,** 1354–63 (1962).
(b) Wallace, L. V., and Nicholls, R. W., J. Atm. Terrestrial Phys. **7,** 101–5 (1955); **24,** 749 (1962).
(c) Turner, R. G., and Nicholls, R. W., Can. J. Phys. **32,** 475–9 (1954).
(d) Carleton, N. P., and Papaliolios, C., J. Quant. Spectry. Radiative Transfer **2,** 241–4 (1962).

[8] Tyte, D. C., J. Quant. Spectry. Radiative Transfer **5,** 545–7 (1965).

[9] (a) Felenbok, P., Proc. Phys. Soc. (London) **A86,** 676–7 (1965).
(b) Jain, D. C., Proc. Phys. Soc. (London) **A81,** 171–4 (1963).
(c) Tawde, N. R., and Korwar, V. M., Proc. Phys. Soc. (London) **A80,** 794–5 (1962).
(d) Gilmore, F. R., private communication (RKR).
(e) Zare, R. N., private communication (RKR).
(f) Schmeltekopf, A., private communication (RKR).
(g) Wentink, T., Jr., Isaacson, L., and Spindler, R. J., Research on the Opacity of Low Temperature Air: Oscillator Strengths and Transition Moments of Band Systems of N_2, O_2, and NO, Tech. Rept. No. AFWL–TR–65–139, Dec. 1965, Air Force Weapons Laboratory, Research and Technology Division, Air Force Systems Command, Kirtland Air Force Base, New Mexico.
(h) Jain, D. C., J. Quant. Spectry. Radiative Transfer **4,** 427–40 (1964).
(i) Murthy, N. S., and Nagaraj, S., Proc. Phys. Soc. (London) **A84,** 827–8 (1964).

(j) Geiger, J., and Topschowsky, M., Z. Naturforsch. **21a,** No. 5, 626–34 (1966).
(k) Prasad, S. S., Proc. Phys. Soc. (London) **A82,** 419–21 (1963).
[10] Nicholls, R. W., Proc. Phys. Soc. (London) **A85,** 159–62 (1965).
[11] Fraser, P. A., and Jarmain, W. R., Proc. Phys. Soc. (London) **A66,** 1145–52 (1953).
[12] Nicholls, R. W., and Jarmain, W. R., Proc. Phys. Soc. (London) **A69,** 253–64 (1956).
[13] Krupenie, P. H., and Weissman, S., J. Chem. Phys. **43,** 1529–34 (1965).
[14] (a) Benesch, W., Vanderslice, J. T., Tilford, S. G., and Wilkinson, P. G., Astrophys. J. **143,** 236–52 (1966).
(b) Benesch, W., Vanderslice, J. T., Tilford, S. G., and Wilkinson, P. G., Astrophys. J. **144,** 408–18 (1966).
[15] (a) Shuler, K., Proc. Phys. Soc. (London) **A65,** 70 (1952).
(b) Cashion, J. K., J. Chem. Phys. **41,** 3988–94 (1964).
[16] Nicholls, R. W., Can. J. Phys. **40,** 1772–83 (1962).
[17] Nicholls, R. W., J. Res. NBS **69A** (Phys. and Chem.) No. 4, 369–73 (1965).
[18] Flinn, D. J., Spindler, R. J., Fifer, S., and Kelly, M., J. Quant. Spectry. Radiative Transfer **4,** 271–82 (1964).
[19] Spindler, R. J., J. Quant. Spectry. Radiative Transfer **5,** 165–204 (1965); see especially p. 194. Spindler infers from Morse-RKR comparison on the calculated integrals that 1% error in turning points causes $\simeq 10\%$ error in q.
[20] Halevi, P., Proc. Phys. Soc. **86,** 1051–4 (1965).
[21] James, T. C., J. Mol. Spectry. **20,** 77–87 (1966).

(Paper 72A5–517)

312-248 O–68—5

JOURNAL OF RESEARCH of the National Bureau of Standards—A. Physics and Chemistry
Vol. 72A, No. 5, September–October 1968

The Configurations $3d^n4p$ in Doubly Ionized Atoms of the Iron Group*

C. Roth

McGill University, Montreal, Canada

(June 18, 1968)

Experimental levels of the configurations $3d^n4p$ in the third spectra of the iron group were compared with corresponding calculated values. Besides the electrostatic and spin-orbit interactions the $\alpha L(L+1)$, βQ and T corrections were considered in the individual and general treatments. The insertion of the parameters β and T improved the results by about 25 percent. The root-mean-square (rms) error on fitting 581 experimental levels by means of 21 free interaction parameters was 138 cm^{-1}. Altogether 912 energy levels were predicted.

Key Words: βQ and T corrections; configurations $3d^n4p$; energy levels; iron group; interaction parameters; third spectra.

1. Introduction

Individual and general treatments of the configurations $3d^n+3d^{n-1}4s$ in the third spectra of the iron group were considered by Y. Shadmi [1]. Preliminary investigations of some configurations $3d^n4p$ in the third spectra of the iron group were performed by Shimoni, Hollander and Abraham [2–4].

Racah and Trees [5–7] have shown that second order effects caused by perturbations on the configuration ln by configurations differing from ln by two electrons can be described by a model interaction of the form

$$2\alpha(\mathbf{l}_1\cdot\mathbf{l}_2)+\beta q_{12},$$

where q_{12} is the seniority operator [8]. For the configuration d^n this becomes

$$\alpha[L(L+1)-6n]+\beta Q,$$

where Q is the total seniority operator [8]. If the constant $-6n\alpha$ is incorporated into the height of the configuration the above correction reduces to

$$\alpha L(L+1)+\beta Q.$$

The $\alpha L(L+1)$ correction was first introduced by Trees [5]. The effect of the βQ correction was studied by Racah and Shadmi [9] in the even configurations $(3d+4s)^n$ of the second spectra of V, Cr, and Fe.

Trees and Jorgenson [10] have shown that the main perturbing configuration on $3s^23p^63d^n$ is the configuration $3s^23p^43d^{n+2}$. Trees [11] also remarked that the configuration $3s3p^63d^{n+1}$ should give a perturbation of the same magnitude as $3s^23p^43d^{n+2}$. This perturbation is not included in $2\alpha(\mathbf{l}_1\cdot\mathbf{l}_2)+\beta q_{12}$, since now the configurations differ by only one electron. By second-order perturbation theory this effect depends upon the ratio $\frac{H^2}{\Delta E}$, where H is the interaction parameter that appears in the nondiagonal term,

$$H=\frac{R^2(3d\,3d,\ 3d\,3s)}{35},$$

and ΔE is the energy difference between the two configurations. The parameter $\frac{H^2}{\Delta E}$ is denoted by T. When calculating the model interaction one uses second-order perturbation theory of degenerate configurations which permits the introduction of these interactions before diagonalizing the energy matrices of the separate configurations. Hence the algebraic matrices of T are not diagonal. It should be noted that T represents a three-body interaction whereas α and β represent two-body interactions.

Rajnak and Wybourne [12], by using second-order perturbation theory obtained expressions for the matrix elements of the electrostatic interaction between the ℓ^n configuration and the different species

*An invited paper. The major part of this paper is based on a chapter of the author's doctoral dissertation, the Hebrew University of Jerusalem, Israel.

of perturbing configurations differing from ℓ^n by one or two electrons or electron-holes. Effective three-body interactions were considered to account for the perturbation due to one-electron excitations. Racah and Stein [13] developed an elegant method which considerably simplified the calculations of Rajnak and Wybourne.

The electrostatic and spin-orbit interaction matrices for the configurations d^np were available from the matrix library at the Hebrew University. To these matrices the author added the algebraic matrices of the parameters β and T using the program ADDCONF of Racah.

In the first part (the individual treatment, ILS), the algebraic matrices multiplied by radial parameters are diagonalized using the program of Racah [14]. Besides the eigenvalues, the diagonalization routine also yields the derivatives of the eigenvalues with respect to the parameters, the squares of the eigenvectors (percentage compositions) and the calculated Lande g values. The appropriate experimental levels are then fitted to the eigenvalues and using the derivatives obtained in the diagonalization, a least squares optimization of the parameters is performed. In these calculations the improved values of the theoretical energy levels, the corrected values of the parameters including their statistical deviations and the sum of the squares of the differences between the observed and calculated levels are obtained.

Where the Δ_i are the differences between the observed and calculated levels, n is the number of known levels, and m is the number of free parameters, the rms error Δ defined as

$$\Delta=\sqrt{\frac{\sum_{i=1}^{n}\Delta_i^2}{n-m}}$$

is also given by the least squares routine. The same derivatives can be used for several variations in the least squares either imposing different conditions on the parameters or inserting the experimental levels with different assignments. These latter variations are particularly important since they help to determine whether certain experimental levels may be inserted with changed assignments, or in some cases even rejected. The parameters of that variation which yields the best results are used to perform a new diagonalization. This iterative process is continued until mathematical convergence is attained.

If the parameters obtained from the individual treatments can be expressed in terms of simple interpolation formulas a general diagonalization is performed. Then in the general least squares (GLS) all the configurations $3d^n4p$ are considered as one problem by forcing the interaction parameter to vary linearly, or perhaps linearly with small quadratic corrections.

2. Parameters

For the $d-d$ interaction the Slater parameters F^2 and F^4 were replaced by

$$B=\frac{1}{441}\left[9F^2(dd)-5F^4(dd)\right]=F_2(dd)-5F_4(dd)$$

$$C=\frac{5}{63}F^4(dd)=35F_4(dd).$$

For the $d-p$ interaction the parameters F_2, G_1, and G_3 are given by

$$F_2=\frac{1}{35}F^2(dp),\ G_1=\frac{1}{15}G^1(dp)\ \text{and}\ G_3=\frac{3}{245}G^3(dp)$$

The parameters of the spin-orbit interactions for the electrons d and the electron p are denoted by ζ_d and ζ_p, respectively. The three correction parameters mentioned previously are denoted by α, β, and T. Finally, the additive parameter chosen to normalize to zero the lowest energy value for a particular configuration, is denoted by A.

3. Discussion and Results

By extrapolating and intrapolating the results of Shimoni, Hollander and Abraham [2–4], approximate initial values for the parameters of the individual treatment were obtained. Since the effects of the parameters β and T had not been considered previously for the third spectra, they were inserted initially here with a value of zero. However, since derivatives with respect to these two parameters were obtained it was possible to study the effects of β and T by letting them vary freely in the least-squares. After two iterations in the individual treatments of all the configurations mathematical convergence was attained for all the parameters. Then on the basis of the results from the individual treatments a general diagonalization was performed in which the parameters B, C, F_2, G_1, G_3, α, and ζ_p varied linearly, whereas ζ_d had in addition a small quadratic correction. The parameters β and T again had an initial value of zero.

The configurations d^np consist of 372 theoretical terms splitting into 912 levels. In the general least-squares 225 experimental terms splitting into 581 levels were inserted. The rms error with β and T eliminated was 180.3 cm^{-1} (28 free parameters) whereas when β and T were allowed to vary linearly the rms error was reduced to 138.4 cm^{-1} (32 free parameters). The values of β and T in the latter variation were

$$\beta(d^np)=-285\pm22-(45\pm20)(n-5)$$

$$T(d^np)=-3.2\pm0.2-(0.6\pm0.2)(n-5)$$

the uncertainties in these parameters and those following in the text and tables are the rms deviations obtained in the least squares optimization of their values.

Since α and β take into account second order effects by two-body interactions we would expect that if β be allowed to vary the value of α should drop. That is indeed the case as in the variation with β and T eliminated α had values (in units of cm^{-1})

$$\alpha_1 = 82 \pm 1 + (1.2 \pm 0.9)(n-5),$$

whereas by letting β and T vary linearly in the GLS we obtained

$$\alpha_2 = 56 \pm 1.8 - (2.5 \pm 1.4)(n-5).$$

In addition C increases when β is inserted. With β and T eliminated the value of C in the GLS was

$$C(d^n p) = 3920.8 \pm 6.3 + (287.1 \pm 5.5)(n-5)$$

whereas by letting β and T vary linearly in the GLS we had

$$C(d^n p) = 4062.2 \pm 9.9 + (327.8 \pm 8.6)(n-5).$$

This result also is as expected since if we consider the basis configuration d^2 the only term affected by β is ^1S, which contains $7C$.

In figures (1–8) we give values of the parameters versus atomic number obtained from the individual least squares (the vertical lines indicate the rms errors in the values of the parameters). The straight lines (and the parabola for ζ_d) give the values of the parameters from the general least squares. From the graphs it is apparent that the assumption of linearity (with a small quadratic correction for ζ_d) is valid here.

Unless specified otherwise the source of the experimental data is "Atomic Energy Levels," Vols. **I** and **II** by C. E. Moore [15], henceforth referred to as AEL.

The numerical values of all levels and parameters are in cm^{-1}.

We now wish to discuss briefly the results for each configuration.

Sc III – $4p$. This configuration consists of only 1 term splitting into 2 levels. It is useful in providing a value for the parameter ζ_p.

Ti III – $3d4p$. In the configuration dp there are 6 terms splitting into 12 levels, all of which are known experimentally for Ti III.

In the individual least squares we fitted the 12 experimental levels to the theoretical levels with the same assignments as in AEL. The 4 electrostatic parameters A, F_2, G_1, and G_3 were used to determine the 6 terms. The rms error obtained was 162. Furthermore, all the 12 levels fitted very nicely in the GLS. This result is significant and indicates that the interaction with the configuration sp is not strong here.

V III – $3d^24p$. In the configuration d^2p, there are 19 terms splitting into 45 levels. In the paper by Iglesias [16], 18 observed terms splitting into 43 levels are given – the only term missing is $(^1S)^2P$.

The only change in assignment was

$$(^3F)z^2D_{\frac{5}{2}} \longleftrightarrow (^3F)z^4D_{\frac{5}{2}}$$

Without the exchange, the deviations of these two levels were -680 for $z^2D_{\frac{5}{2}}$ and 410 for $z^4D_{\frac{5}{2}}$. With the exchange the deviations were reduced to -152 and -128 respectively. In addition, the eigenfunctions of the two levels are strongly mixed.

Since there are no levels based on the core $d^2\,^1S$, we can only have a maximum of 4 electrostatic parameters of d^2 to satisfy the 4 terms ^3P, ^1D, ^3F, and ^1G. These 4 parameters are A, B, C, and α. If we give either T or β freedom then the problem is overdefined. In the individual least squares the mean error in fitting 43 levels with β and T eliminated was 135.

Cr III – $3d^34p$. In the configuration d^3p there are 48 theoretical terms splitting into 110 levels. In AEL, there are 27 observed terms splitting into 74 levels. We found it necessary to reject 7 experimental levels.

The following is a list of the 7 levels neglected with their approximate deviations had they been inserted into the last GLS

Name	Value	Deviation
$(^4F)z^5D_0$	95779	−810
$(^2G)z^1G_4$	114355	1160
$(^2H)y^1G_4$	117099	−2090
$(^2G)z^1H_5$	117187	3840
$(^2F)v^3D_2$	138362	5740
$(^2F)v^3D_3$	138976	6710
$(b^2D)v^3F_3$	150972	1680

In the individual least squares, the deviation obtained for the level $(^4F)z^5D_0$ was -625, whereas the other levels of z^5D fitted with deviations of less than 50. Thus we felt justified in neglecting the level z^5D_0. The levels $(^2G)z^1G_4$, $(^2H)y^1G_4$, $(^2G)z^1H_5$ and $(^2F)v^3D_2$ had deviations higher than 1000 in the individual least squares, and were thus rejected. In the individual least squares we considered the variation of assigning the level $(b^2D)v^3F_3$ to $(b^2D)^1F_3$. However, this required that β have a value of -590, whereas the value of β from the GLS is -195. With the latter value of β, the deviation obtained on assigning v^3F_3 to $(b^2F)^1F$ is -1056, and thus too high to be considered.

The following changes in assignment were performed

$$(a^4F)z^5D_1 \longleftrightarrow (a^4F)z^5F_1$$

$$\text{AEL } (a^4P)z^3P_2 \longrightarrow (^4P)y^5D_2$$

$$\text{AEL } (a^4P)y^5D_{0,2} \longrightarrow (^4P)z^3P_{0,2}$$

$$\text{AEL } (a^4P)y^3D_{1,2,3} \longrightarrow (^2P)z^3D_{1,2,3}.$$

In the first three cases the eigenfunctions of all the levels concerned are mixed considerably. The term $(^4P)^3D$ is definitely higher than the term $(^2P)^3D$.

By neglecting the level $(^2D)v^3F_3$ at 150972, it was found that β and T did not suffer any appreciable change. Thus, the best result in the individual least squares was obtained on fitting 22 terms splitting into 67 levels with 7 electrostatic and 2 spin-orbit parameters, to yield a mean error of 136.

Mn III $-3d^4 4p$. The configuration d^4p comprises 68 terms splitting into 180 levels. In AEL there are only 6 observed terms, all based on $d^4\,{}^5D$, which split into 25 levels. No individual least squares were performed as then we would have to keep the parameters α, B, and C fixed. The 25 observed levels fit very well in the GLS with the same assignments as in AEL.

Fe III $-3d^5 4p$. In the configuration d^5p there are 88 terms splitting into 214 levels, of which 75 terms splitting into 189 levels are known experimentally for Fe III. All the observed levels fit well with the following changes in assignment:

$$(a^4P)z^5D_3 \longleftrightarrow (a^4G)z^5F_3$$

$$(a^2I)z^3I_{6,7} \longleftrightarrow (a^2I)z^3K_{6,7}$$

$$(a^4F)y^5G_5 \longleftrightarrow (a^2F)y^3G_5$$

$$\text{AEL } (b^2F)t^3F_4 \longrightarrow (b^2F)w^1G_4$$

$$\text{AEL } (a^2H)x^1G_4 \longrightarrow (b^2F)t^3F_4$$

It should be emphasized that in each of the changed levels the composition is never pure, but contains a contribution of that level which has the same assignment as that given in AEL. In general the mixing in this configuration is very strong. Racah [17] has shown that for d^5, or equivalently for d^5p, all diagonal second-order effects are well represented by two-body interactions. Thus, the parameter T has little if any significance here. In the individual least squares the mean error was 186 with β eliminated, and 144 when β was allowed to vary freely. Then β assumed a value of -292 ± 23.

Co III $-3d^6 4p$. From 68 theoretical terms splitting into 180 levels there are 33 experimental terms splitting into 95 levels.

The two levels $(^3P)y^4P_{\frac{5}{2}}$ and $(^3P)z^2D_{\frac{5}{2}}$ are given with question marks in AEL. As they would yield deviations of around -800 and -600 respectively, if inserted into the GLS, they were neglected.

The following changes in assignment were performed:

$$(^3H)z^4H_{\frac{9}{2},\frac{11}{2},\frac{13}{2}} \longleftrightarrow (^3H)z^4I_{\frac{9}{2},\frac{11}{2},\frac{13}{2}}$$

$$(^3G)x^4G_{\frac{9}{2}} \longleftrightarrow (^3G)x^4F_{\frac{9}{2}}$$

$$(^1I)x^2H_{\frac{9}{2},\frac{11}{2}} \longleftrightarrow (A^1G)w^2H_{\frac{9}{2},\frac{11}{2}}$$

$$\text{AEL } (^3P')z^4S_{\frac{3}{2}} \longrightarrow (B^3P)^4D_{\frac{3}{2}}$$

$$\text{AEL } (^3P')x^4P_{\frac{5}{2}} \longrightarrow (B^3P)^4D_{\frac{5}{2}}$$

In each of the first three exchanges there was considerable mixing of the eigenfunctions involved.

The calculated values of the levels $(B^3P)^4S_{\frac{3}{2}}$ and $(B^3P)^4P_{\frac{5}{2}}$ are 161611 and 164334, respectively. Thus, the two levels $z^4S_{\frac{3}{2}}$ and $x^4P_{\frac{5}{2}}$ cannot be fitted to the theoretical levels with the same assignments. The only possible assignment for the level $(^3P')z^4S$ is the theoretical level consisting of a mixture of $(B^3P)^4D_{\frac{3}{2}}$ and $(B^3F)^4D_{\frac{3}{2}}$. In the GLS the deviation for this level is -282. Similarly the level $(^3P')x^4P_{\frac{5}{2}}$ was assigned to the same theoretical term as z^4S with J equal to $\frac{5}{2}$ giving a deviation of 120 in the GLS.

In the individual least squares β and T have a marked effect. On fitting 93 levels using 7 electrostatic parameters and 2 spin-orbit parameters (β and T eliminated) the mean error was 176. When β and T were allowed to vary freely, the mean error was reduced to 130. The values of β and T in that variation were

$$\beta = -424 \pm 86$$

$$T = -4.8 \pm 0.6$$

Ni III $-3d^7 4p$. From 48 predicted terms splitting into 110 levels, Shenstone [18] gives 43 experimental terms which split into 95 levels. The following 3 levels were rejected:

$(^2P)^3P_2$ at 141112.5?

$(b^2D)u^3D_2$ at 173062.0?

$(b^2D)u^3D_3$ at 172916.9?

The calculated level $(^2P)^3P_2$ is at 133902, and since for J equal to 2 all the theoretical levels in the vicinity of 141000 have corresponding experimental levels, the level $(^2P)^3P_2$ was rejected. Similarly the calculated levels $(b^2D)u^3D_{2,3}$ are at 183976 and 184740, respectively, and since there are no theoretical levels in the vicinity of 173000, the levels $u^3D_{2,3}$ could not be inserted into the least-squares calculations.

Shenstone [18] mentions that two strong lines should be due to transitions between the odd levels z^3I_7, z^3H_6 and the even levels a^3H_6, a^3G_5. Shenstone then attributes these two lines as being due to $a^3G_5 - z^3H_6$ (56304.2 cm^{-1}) and $a^3H_6 - z^3I_7$ (57044.7 cm^{-1}). Thus, he obtains the levels $(^2G)z^3H_6$ at 131428 and $(^2H)z^3I_7$ at 138731. However, from our initial diagonalization the level $(^2H)z^3I_7$ was at 137842 and the level $(^2G)z^3H_6$ was at 131901. This shows that the transitions to which Shenstone attributes these two lines should

be interchanged. Then one obtains the experimental levels $(^2H)z^3I_7$ at 137990.6 and $(^2G)z^3H_6$ at 132168.9. In the GLS these fitted with deviations of 154 and 263, respectively.

As suggested by Professor Racah the two strong lines given by Shenstone at 147723 cm^{-1} and 145094 cm^{-1} correspond to the transitions $(^2F)^1F_3 - a^1D_2$ and $(^2F)^1F_3 - a^3P_{2'}$, respectively. Then it follows that the experimental level $(^2F)^1F$ should have a value of 161755. In the GLS this level fitted with a deviation of only 20. The following changes in assignment were performed:

1. $(^4P)y^3D_{2,3} \longleftrightarrow (^4P)z^5P_{2,3}$
2. Shen. $(^4P)z^3P_0 \longrightarrow (^2P)^1S_0$
3. Shen. $(^2P)z^1P_1 \longrightarrow (^2P)^3S_1$
4. Shen. $(^2P)y^3P_1 \longrightarrow (^2P)^1P_1$
5. $(^2F)w^3F_2 \longleftrightarrow (^2F)w^1D_2$
6. $(^2F)w^3F_3 \longleftrightarrow (^2F)y^3D_3$
7. Shen. $(^2F)w^3F_4 \longrightarrow (^2F)^3G_4$

In the first case there is considerable mixing between the eigenfunctions of $(^4P)y^3D$ and $(^4P)z^5P$. The predicted level $(^4P)^3P_0$ is at 135695 cm^{-1}, and thus the experimental level z^3P_0 at 138147 cm^{-1} cannot be assigned to the theoretical level with the same term designation. This level fits quite well to the theoretical level $(^2P)^1S$ as indicated by change 2. It should be noted that the eigenfunction of $(^2P)^1S$ contains 39 percent of $(^4P)^3P$.

A variation was considered to fit the level $(^2P)z^1P$ to the theoretical level with the same term designation and perform the change $(^2P)y^3P_1 \rightarrow (^2P)^3S_1$. However, the deviations for both levels were much larger than the deviations with changes 3 and 4 (−167 for the level $(^2P)^3S$ and 22 for the level $(^2P)z^1P$).

When the levels of the term $(^2F)w^3F$ were assigned to the theoretical levels of the same term designation, the deviations were almost 1000. Since such high deviations are completely incompatible with the other results obtained, we performed the changes 5, 6, and 7, thus completely splitting the term $(^2F)w^3F$. It should be noted, however, that in all these changes the parent, ^2F, remains the same.

In the individual least squares, on inserting 93 experimental levels with β and T eliminated, the mean error was 169. When β and T were allowed to vary freely the mean error was reduced to 136. In that variation the values of β and T were

$$\beta = -413 \pm 63$$
$$T = -4.9 \pm 0.6.$$

Cu III $-3d^84p$. Of the 19 predicted terms of d^8p, the only experimental term missing in Cu III is $(^1S)^2P$. The only change in assignment was

$$(^3P)x^2D_{\frac{3}{2}} \leftrightarrow (^3P)y^2P_{\frac{3}{2}}.$$

The eigenfunctions of these two levels are strongly mixed.

As for d^2p, since there are no levels based on the parent $(d^2)^1S$, it is not possible to let either β or T change freely.

In the individual least squares, the mean error on fitting 43 levels with β and T eliminated was 126. For the values of β and T fixed at −427 and −4.9 respectively (the values obtained for those parameters in the first GLS) the mean error dropped only to 125.

This result is as expected since the inclusion of β affects only the term $d^8(^1S)$, which is not known experimentally, and T reduces in this case to a two-body interaction, the effect of which is absorbed by the other d^8 parameters.

Zn III $-3d^94p$. In this configuration all 12 predicted levels are known. The following changes in assignment were performed:

1. $^3D_2 \leftrightarrow {}^1D_2$
2. $^3D_3 \leftrightarrow {}^1F_3$.

In both cases there was mixing between the eigenfunctions of the levels involved.

In the individual least squares using the 4 electrostatic parameters A, F_2, G_1, and G_3 as well as the 2 spin-orbit parameters ζ_d and ζ_p, the mean error was 105.

Ga III $-3d^{10}4p$. Like Sc III $-p$ this configuration consists of only 1 term splitting into 2 levels, and is useful in providing a value for ζ_p.

4. Table Entries

The numerical values of all levels and parameters given in the following tables are in units of cm^{-1}

1. *Parameters:* Tables 1–10

In the general diagonalization all the parameters with the exception of ζ_d had approximate expressions of the form

$$P(d^np) = P + (n-5)\Delta P.$$

In the general least squares then only P and ΔP were the independent parameters.

For ζ_d we had

$$\zeta_d(d^np) = \zeta_d + (n-5)\Delta_1\zeta_d + [(n-5)^2 - 10]\Delta_2\zeta_d.$$

Here ζ_d, $\Delta_1\zeta_d$ and $\Delta_2\zeta_d$ were the independent parameters in the general least squares.

The numerical values of the parameters for the initial general diagonalization are given in the column GDIAG 1.

The columns ILS1 and GLS1 give the values of

the parameters of the initial iteration with β and T eliminated, in the individual and general least squares, respectively. The columns ILS'1 and GLS'1 give the values of the parameters of the initial iteration with β and T free to change in the individual and general least squares respectively.

The parameters as given in GLS'1 were taken for the general diagonalization of the final iteration. The column GLS'2 gives the values of the parameters in the general least squares of the final iteration.

TABLE 1. *Parameters of* Ti III – 3d4p

Parameter	GDIAG 1	ILS 1	GLS 1	GLS' 1	GLS' 2
A	79440	78917 ± 52	78938	79016	78999
F_2	460	437 ± 10	443	442	441
G_1	410	423 ± 13	409	408	407
G_3	50	48 ± 4	48	49	50
α	84	Fix 84	78	66	68
ζ_d	115	154 ± 58	136	135	139
ζ_p	359	379 ± 206	334	336	328
Δ		162			

TABLE 2. *Parameters of* V III – $3d^24p$

Parameter	GDIAG 1	ILS 1	GLS 1	GLS' 1	GLS' 2
A	95958	95900 ± 43	95992	96387	96313
B	911	880 ± 4	903	918	915
C	3062	3183 ± 33	3060	3091	3078
F_2	466	454 ± 4	452	451	450
G_1	410	416 ± 5	408	407	405
G_3	52	49 ± 2	51	51	51
α	84	72 ± 5	79	63	62
β	0	Fix 0	Fix 0	−220	−150
T	0	Fix 0	Fix 0	−1.7	−1.3
ζ_d	177	220 ± 24	206	207	208
ζ_p	442	371 ± 64	420	414	406
Δ		135			

TABLE 3. *Parameters of* Cr III – $3d^34p$

Parameter	GDIAG 1	ILS 1	GLS 1	GLS' 1	GLS' 2
A	113164	113160 ± 70	113142	113633	113559
B	966	962 ± 4	960	969	966
C	3350	3354 ± 21	3347	3417	3406
F_2	472	458 ± 7	461	460	459
G_1	410	403 ± 6	407	406	405
G_3	54	57 ± 2	53	53	53
α	84	81 ± 3	80	61	63
β	0	Fix 0	Fix 0	−254	−195
T	0	Fix 0	Fix 0	−2.2	−1.9
ζ_d	257	272 ± 28	290	292	291
ζ_p	525	496 ± 58	496	492	486
Δ		136			

TABLE 4. *Parameters of* Mn III – $3d^44p$

Parameter	GDIAG 1	GLS 1	GLS' 1	GLS' 2
A	138047	137848	138256	138187
B	1021	1015	1019	1017
C	3638	3634	3743	3734
F_2	478	470	469	468
G_1	410	406	405	404
G_3	56	54	54	54
α	84	81	58	60
β	0	Fix 0	−289	−240
T	0	Fix 0	−2.8	−2.5
ζ_d	355	385	389	387
ζ_p	608	572	570	562

TABLE 5. *Parameters of* Fe III – $3d^54p$

Parameter	GDIAG 1	ILS 1	ILS' 1	GLS 1	GLS' 1	GLS' 2
A	126350	125832 ± 91	125710 ± 74	125843	125781	125725
B	1076	1071 ± 2	1068 ± 2	1071	1070	1068
C	3926	3920 ± 9	4071 ± 9	3921	4069	4062
F_2	484	477 ± 4	474 ± 3	479	478	477
G_1	410	404 ± 4	397 ± 3	405	403	403
G_3	58	55 ± 1	57 ± 1	56	56	56
α	84	82 ± 1	55 ± 1	82	56	57
β	0	Fix 0	−292 ± 23	Fix 0	−323	−285
T	0	Fix 0	Fix 0	Fix 0	−3.3	−3.2
ζ_d	471	484 ± 30	521 ± 23	494	498	494
ζ_p	691	730 ± 43	692 ± 34	648	648	640
Δ		186	144			

TABLE 6. *Parameters of* Co III – $3d^64p$

Parameter	GDIAG 1	ILS 1	ILS' 1	GLS 1	GLS' 1	GLS' 2
A	131330	131748 ± 131	131593 ± 106	131512	131544	131507
B	1131	1139 ± 6	1120 ± 5	1127	1121	1119
C	4214	4177 ± 15	4426 ± 32	4208	4395	4390
F_2	490	506 ± 5	497 ± 4	488	486	486
G_1	410	412 ± 6	403 ± 5	403	402	402
G_3	60	55 ± 2	57 ± 1	57	58	58
α	84	88 ± 3	47 ± 6	83	53	55
β	0	Fix 0	−424 ± 86	Fix 0	−358	−330
T	0	Fix 0	−4.8 ± 0.6	Fix 0	−3.8	−3.8
ζ_d	605	641 ± 30	672 ± 30	615	621	617
ζ_p	774	662 ± 56	672 ± 43	724	727	718
Δ		176	130			

TABLE 7. *Parameters of* Ni III – $3d^74p$

Parameter	GDIAG 1	ILS 1	ILS' 1	GLS 1	GLS' 1	GLS' 2
A	129516	129509 ± 52	129715 ± 47	129556	129751	129733
B	1186	1176 ± 4	1166 ± 3	1182	1171	1170
C	4502	4530 ± 18	4762 ± 32	4495	4721	4718
F_2	496	499 ± 5	499 ± 4	497	495	495
G_1	410	395 ± 5	398 ± 4	403	401	401
G_3	62	59 ± 2	58 ± 2	59	59	59
α	84	83 ± 3	49 ± 5	84	51	52
β	0	Fix 0	−413 ± 63	Fix 0	−393	−375
T	0	Fix 0	−4.9 ± 0.6	Fix 0	−4.4	−4.2
ζ_d	757	703 ± 26	726 ± 18	750	755	751
ζ_p	857	772 ± 54	755 ± 38	800	805	796
Δ		169	136			

TABLE 8. *Parameters of* Cu III – $3d^84p$

Parameter	GDIAG 1	ILS 1	GLS 1	GLS' 1	GLS' 2
A	131863	131864 ± 45	131847	132122	132123
B	1241	1247 ± 5	1238	1222	1221
C	4790	4764 ± 35	4782	5047	5046
F_2	502	498 ± 4	507	504	503
G_1	410	402 ± 5	402	400	401
G_3	64	64 ± 3	60	61	61
α	84	84 ± 5	86	48	49
β	0	Fix 0	Fix 0	−427	−420
T	0	Fix 0	Fix 0	−4.9	−5.0
ζ_d	927	890 ± 5	897	902	898
ζ_p	940	862 ± 49	877	883	874
Δ		126			

TABLE 9. *Parameters of* Zn III – $3d^94p$

Parameter	GDIAG 1	ILS 1	GLS 1	GLS' 1	GLS' 2
A	142734	142277 ± 39	142285	142529	142531
F_2	508	504 ± 6	516	513	512
G_1	410	408 ± 6	401	398	399
G_3	66	60 ± 6	62	63	62
α	84	Fix 84	87	46	46
ζ_d	1215	1095 ± 39	1056	1062	1059
ζ_p	1023	1013 ± 72	953	961	952
Δ		105			

TABLE 10. *General parameters of the third spectra of the iron group*

Parameter	GDIAG 1	GLS 1	GLS' 1	GLS' 2
B	1076	1071.4± 1.5	1070.0± 1.3	1068.5± 1.3
ΔB	55	55.8± 1.1	50.6± 0.9	50.9± 0.9
C	3926	3920.8± 6.3	4068.8±10.0	4062.2± 9.9
ΔC	288	287.1± 5.5	326.0± 8.5	327.8± 8.6
F_2	484	479.3± 2.2	477.5± 1.8	477.0± 1.8
ΔF_2	6	9.3± 1.1	8.8± 0.9	8.9± 0.9
G_1	410	404.8± 2.1	403.4± 1.7	402.7± 1.7
ΔG_1	0	−0.9± 1.1	−1.3± 0.9	−1.0± 0.9
G_3	58	55.6± 0.7	56.0± 0.6	56.0± 0.6
ΔG_3	2	1.5± 0.5	1.6± 0.4	1.6± 0.4
α	84	82.2± 1.1	55.9± 1.8	57.4± 1.7
$\Delta\alpha$	0	1.2± 0.9	−2.5± 1.4	−2.9± 1.4
β	0	Fix 0	−323.5±23.6	−285.0±21.7
$\Delta\beta$	0	Fix 0	−34.5±20.2	−45.1±20.5
T	0	Fix 0	−3.3± 0.2	−3.2± 0.2
ΔT	0	Fix 0	−0.5± 0.2	−0.6± 0.2
ζ_d	561	558.0±17.5	560.9±13.8	560.3±13.5
$\Delta_1\zeta_d$	125	115.2± 5.1	115.9± 4.1	115.4± 4.0
$\Delta_2\zeta_d$	9	6.4± 2.5	6.3± 2.0	6.5± 2.0
ζ_p	691	648.2±22.6	648.4±17.9	639.5±17.7
$\Delta\zeta_p$	83	76.3±11.0	78.1± 8.7	78.1± 8.6
Δ		180.3	140.1	138.4

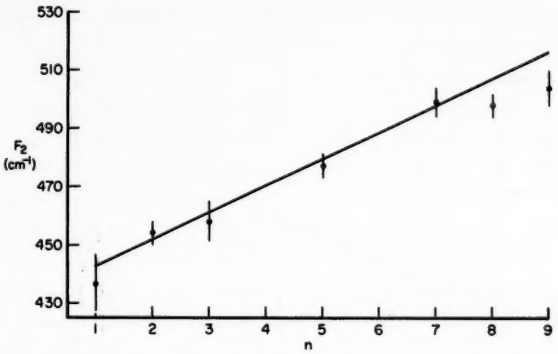

FIGURE 3. *Parameter* F_2(dp) *versus* n *for* $3d^n4p$ *configurations* (Ti III to Zn III).

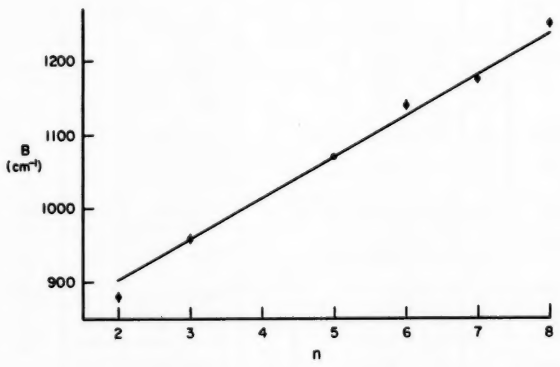

FIGURE 1. *Parameter* B(dd) *versus* n *for* $3d^n4p$ *configurations* (V III to Cu III).

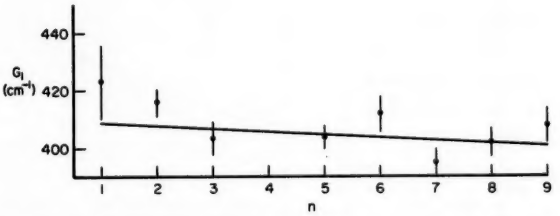

FIGURE 4. *Parameter* G_1(dp) *versus* n *for* $3d^n4p$ *configurations* (Ti III to Zn III).

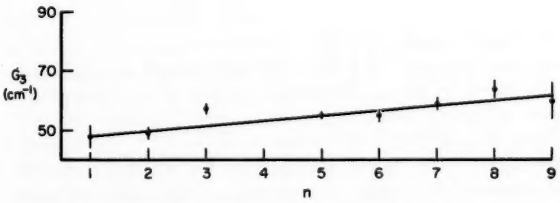

FIGURE 5. *Parameter* G_3(dp) *versus* n *for* $3d^n4p$ *configu-rations* (Ti III to Zn III).

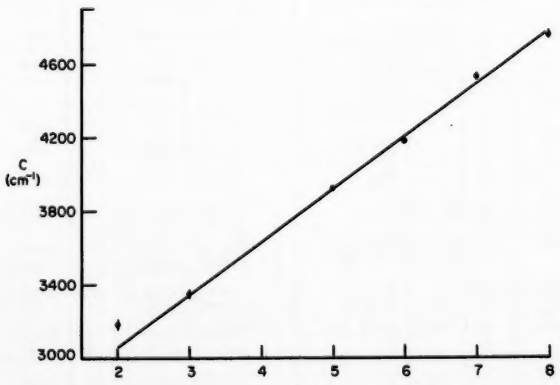

FIGURE 2. *Parameter* C(dd) *versus* n *for* $3d^n4p$ *configurations* (V III to Cu III).

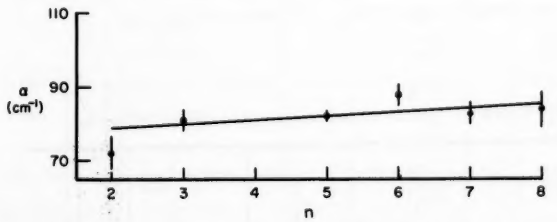

FIGURE 6. *Parameter* α *versus* n *for* $3d^n4p$ *configurations* (V III to Cu III).

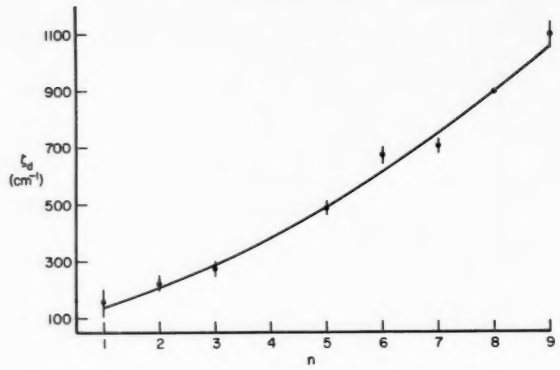

FIGURE 7. *Parameter* ζ_d *versus* n *for* $3d^n4p$ *configurations* (Ti III to Zn III).

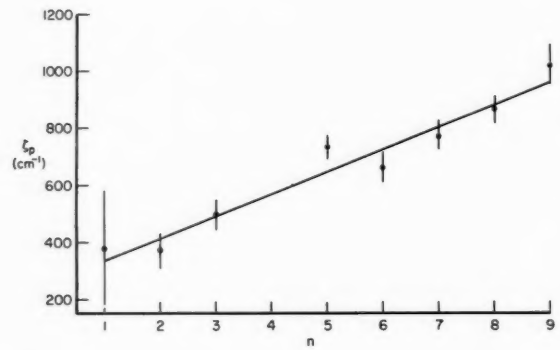

FIGURE 8. *Parameter* ζ_p *versus* n *for* $3d^n4p$ *configurations* (Ti III to Zn III).

2. *Levels:* Tables 11–21

In the column "NAME" the calculated designation of the term is given. Whenever terms of the parent d^n have different seniorities these are denoted by the letters A and B (for d^5 ^{2}D by A, B, and C), the higher calculated term being designated by A. Whenever a calculated term has a corresponding experimental term, the small letters *z*, *y*, *x* . . . are used as in AEL [13].

The entries in the columns "*J*", "OBSERVED", and "CALCULATED" are self-evident. In the column "PERCENTAGE", for each calculated level either the three highest contributions or all those contributions exceeding 7 percent are given.

TABLE 11. *Observed and calculated levels of* SC III 4p

Name	*J*	Percentage	AEL	Observed	Calculated	O−C	Lande C.
4p	1/2	100		62102	62152	−50	0.667
	3/2	100		62576	62526	50	1.333

TABLE 12. *Observed and calculated levels of* Ti III 3d4p

Name	*J*	Percentage	AEL	Observed	Calculated	O−C	Lande C.
$(^2D)z^1D$	2	98		75197	75413	−216	0.997
$(^2D)z^3D$	1	100		77000	76926	74	0.501
	2	95 + 4(^{2}D)^{3}F		77167	77096	71	1.144
	3	93 + 6(^{2}D)^{3}F		77424	77334	90	1.317
$(^2D)z^3F$	2	94 + 5(^{2}D)^{3}D		77421	77444	−23	0.693
	3	94 + 6(^{2}D)^{3}D		77746	77728	18	1.100
	4	100		78159	78107	52	1.250
$(^2D)_z{}^3P$	0	100		80944	81010	−66	
	1	99		80938	81011	−73	1.496
	2	100		81024	81086	−62	1.499
$(^2D)z^1F$	3	100		83117	82791	326	1.000
$(^2D)z^1P$	1	99		83796	83987	−191	1.003

TABLE 13. *Observed and calculated levels of* V III $3d^24p$

Name	*J*	Percentage	AEL	Observed	Calculated	O−C	Lande C.
$(^3F)z^4G$	5/2	98		85524	85539	−15	0.579
	7/2	99		85876	85871	5	0.986
	9/2	100		86306	86279	27	1.172
	11/2	100		86809	86753	56	1.273
$(^3F)z^4F$	3/2	98		86717	86651	66	0.407
	5/2	99		86938	86866	72	1.028
	7/2	99		87219	87147	72	1.236
	9/2	99		87544	87490	54	1.332
$(^3F)z^2F$	5/2	85 + 6(^{1}D)^{2}F + 4(^{3}F)^{2}D		87881	87952	−71	0.878
	7/2	88 + 5(^{1}D)^{2}F + 5(^{3}F)^{4}D		88328	88424	−96	1.156
$(^3F)z^2D$	3/2	59 + 29(^{3}F)^{4}D + 9(^{3}P)^{2}D		88559	88720	−161	0.913
	5/2	52 + 35(^{3}F)^{4}D + 9(^{3}P)^{2}D	(^{3}F)z^{4}D	89458	89610	−152	1.260
$(^3F)z^4D$	1/2	96 + 4(^{3}F)^{4}D		89006	89026	−20	0.001
	3/2	67 + 25(^{3}F)^{2}D + 4(^{3}P)^{2}D		89193	89264	−71	1.080
	5/2	59 + 28(^{3}F)^{2}D + 5(^{3}F)^{2}F	(^{3}F)z^{2}D	88944	89072	−128	1.285
	7/2	91 + 4(^{3}F)^{2}F + 4(^{3}F)^{4}D		89418	89520	−102	1.414
$(^3F)z^2G$	7/2	96		91710	91483	227	0.890
	9/2	96		92053	91871	182	1.112
$(^3P)z^2S$	1/2	99		94714	94906	−192	1.992
$(^3P)z^4S$	3/2	74 + 25(^{1}D)^{2}P		97512	97509	5	1.826
$(^1D)z^2P$	1/2	97		98399	98300	99	0.674
	3/2	70 + 26(^{3}P)^{2}S		98062	98063	−1	1.490
$(^1D)_y{}^2F$	5/2	88 + 7(^{3}F)^{2}F		98384	98240	144	0.872
	7/2	86 + 6(^{3}F)^{2}F + 5(^{3}P)^{4}D		98825	98598	227	1.157
$(^3P)_y{}^4D$	1/2	95 + 4(^{3}F)^{4}D		99073	99044	29	0.004
	3/2	91 + 4(^{3}F)^{4}D + 4(^{1}D)^{2}D		99182	99170	12	1.184
	5/2	88 + 5(^{1}D)^{2}D		99440	99421	19	1.349
	7/2	91 + 5(^{1}D)^{2}F		99941	99846	95	1.413
$(^1D)_y{}^2D$	3/2	81 + 6(^{3}P)^{2}D + 6(^{3}F)^{2}D		99508	99765	−257	0.836
	5/2	80 + 7(^{3}P)^{4}D + 6(^{3}F)^{2}D		99805	100046	−241	1.217
$(^3P)z^4P$	1/2	99		101646	101618	28	2.662
	3/2	99		101786	101757	29	1.729
	5/2	98		102075	102040	35	1.590
$(^1G)_y{}^2G$	7/2	96 + 4(^{3}F)^{2}G		102961	102970	−9	0.890
	9/2	96 + 4(^{3}F)^{2}G		103035	103032	3	1.110
$(^3P)_x{}^2D$	3/2	80 + 10(^{1}D)^{2}D + 9(^{3}F)^{2}D		105320	105269	51	0.807
	5/2	82 + 10(^{3}F)^{2}D + 8(^{1}D)^{2}D		105283	105267	16	1.200
$(^1G)z^2H$	9/2	99		106441	106288	153	0.910
	11/2	100		106903	106682	221	1.091
$(^3P)_y{}^2P$	1/2	99		107060	107049	11	0.667
	3/2	97		107166	107184	−18	1.327
$(^1G)_x{}^2F$	5/2	97		110181	110364	−183	0.857
	7/2	97		109855	110075	−220	1.143
$(^1S)^2P$	1/2	98			129512		0.667
	3/2	98			130003		1.333

Whenever the experimental and calculated term designations differ, the experimental designation is entered in the column "AEL" using the notation of C. Moore [13]. In many instances the exchanges involve complete terms rather than isolated levels. Unless specified otherwise the entries in the column "AEL" pertain to exchanges in terms. The column "O—C" gives the difference between the observed and calculated values of the levels. The column "LANDE C", gives the calculated Lande g-values.

The entries are in ascending order of magnitude of the calculated terms.

TABLE 14. *Observed and calculated levels of* Cr III $3d^34p$

Name	J	Percentage	AEL	Observed	Calculated	O−C	Lande C.
$(^1F)z^3G$	2	100		93766	93780	−14	0.335
	3	100		94029	94045	−16	0.917
	4	100		94375	94394	−19	1.150
	5	100		94800	94823	−23	1.267
	6	100		95304	95330	−26	1.333
$(^1F)z^3D$	0	97			96592		
	1	$78+19(^1F)^3P$	$(a^4F)z^5F$	96774	96686	88	1.207
	2	$35+37(^1F)^3F+26(^1F)^3D$	$(a^4F)z^5D$	96386	96451	−65	1.224
	3	$60+26(^1F)^3F+12(^1F)^3D$		96713	96750	−37	1.413
	4	$83+15(^1F)^3F$		97097	97124	−27	1.476
$(^1F)z^5F$	1	$46+38(^1F)^3D+13(^1F)^5D$	$(a^4F)z^5D$	96148	96244	−96	0.404
	2	$47+51(^1F)^3D$	$(a^4F)z^5F$	96921	96857	64	1.263
	3	$70+29(^1F)^3D$		97120	97083	37	1.323
	4	$84+14(^1F)^3D$		97359	97357	2	1.369
	5	98		97618	97670	−52	1.395
$(^1F)z^3D$	1	$53+35(^1F)^3F+6(^1F)^3D$		97077	97150	−73	0.389
	2	$65+16(^1F)^3F+11(^1F)^3D$		97306	97431	−125	1.178
	3	$79+9(^1F)^3D+6(^1P)^3D$		97683	97885	−202	1.344
$(^1F)z^3G$	3	$93+5(^2G)^3G$		99841	99697	144	0.753
	4	$93+5(^2G)^3G$		100100	99981	119	1.053
	5	$92+5(^2G)^3G$		100421	100344	77	1.204
$(^1F)z^3F$	2	96		101444	101476	−32	0.668
	3	95		101745	101801	−56	1.083
	4	96		102100	102187	−87	1.250
$(^1P)z^5P$	1	99		108248	108192	56	2.488
	2	98		108459	108404	55	1.826
	3	99		108793	108708	85	1.665
$(^1P)z^3P$	0	$45+44(^1P)^3D+5(A^2D)^3P$	$(a^4P)y^5P$	109146	108985	161	
	1	$46+46(^1P)^3D+6(A^2D)^3P$			109807		1.505
	2	$61+28(^1P)^3D+6(A^2D)^3P$		109434	109250	184	1.500
$(^2G)z^3H$	4	$85+14(^2H)^3H$		109534	109614	−80	0.804
	5	$83+14(^2H)^3H$		109944	110017	−73	1.036
	6	$84+15(^2H)^3H$		110505	110560	−55	1.166
$(^1P)y^5D$	0	$52+36(^1P)^3P+4(^3P)^1S$			109686		
	1	$45+42(^1P)^3P$		109237	109147	90	1.497
	2	$69+25(^1P)^3P$	$(a^4P)z^5P$	109570	109806	−236	1.502
	3	96		109721	109936	−215	1.499
	4	97		110154	110350	−196	1.500
$(^3G)y^3G$	3	$86+5(^1F)^3G$		111375	111399	−24	0.770
	4	$89+5(^1F)^3G$		111643	111663	−20	1.051
	5	$87+5(^1F)^3G$		111854	111877	−23	1.189
$(^3P)z^1S$	0	$90+8(^1P)^3P$			111843		
$(^2G)y^3F$	2	$70+22(A^2D)^3F$		112398	112522	−124	0.688
	3	$71+14(A^2D)^3F+6(^2G)^1F$		112466	112599	−133	1.061
	4	$52+37(^2G)^1G+8(A^2D)^3F$		112371	112492	−121	1.151
$(^2G)^1G$	4	$59+30(^2G)^3F+5(A^2D)^3F$			113199		1.086
$(^2G)^1H$	5	$77+18(^2H)^1H$			113346		1.005
$(^3P)^3P$	0	$64+32(A^2D)^3P$			113292		
	1	$59+33(A^2D)^3P$			113380		1.489
	2	$40+25(A^2D)^3P+18(^1P)^3S$			114207		1.521

TABLE 14. *Observed and calculated levels of* Cr III $3d^34p$—Con.

Name	J	Percentage	AEL	Observed	Calculated	O−C	Lande C.
$(^2G)z^1F$	3	$74+15(A^2D)^1F+7(^2G)^3F$			113539		1.005
$(^3P)^1D$	2	$32+17(^3P)^3P+17(A^2D)^1D$			113602		1.225
$(^4P)z^5S$	2	$71+12(^3P)^1D+10(A^2D)^1D$		113356	113768	−412	1.728
$(^3P)y^3D$	1	$80+12(^3P)^3D+5(^4F)^5D$	$(a^4P)y^3D$	114716	114441	275	0.515
	2	$73+10(^3P)^3D+5(^3P)^1D$		115182	114927	255	1.145
	3	$70+12(^3P)^3D+5(^4F)^3D$		115553	115315	238	1.312
$(^2H)y^3H$	4	$82+14(^2G)^3H$		115570	115362	208	0.809
	5	$85+14(^2G)^3H$		115669	115460	209	1.034
	6	$84+15(^2G)^3H$		115844	115643	201	1.165
$(^3P)^3S$	1	$50+32(A^2D)^3P+8(^3P)^1P$			116127		1.534
$(A^2D)^1P$	1	$36+42(^3P)^3S+15(^3P)^1P$			116202		1.385
$(A^2D)z^3F$	2	$63+16(^2G)^3F+13(^1P)^3D$		116392	116348	44	0.759
	3	$51+20(^3P)^3D+17(^1P)^3D$		116532	116724	−192	1.176
	4	$84+12(^2G)^3F$		116967	117017	−50	1.250
$(^1P)^3D$	1	$59+16(^3P)^3D+9(A^2D)^3D$			116665		0.583
	2	$57+19(^3P)^3D+10(A^2D)^3F$			116625		1.105
	3	$55+23(A^2D)^3F+7(A^2D)^1D$			116490		1.259
$(^2H)z^3I$	5	98		117145	116957	188	0.837
	6	99		117488	117297	191	1.025
	7	100		117922	117727	195	1.143
$(A^2D)z^3D$	1	$85+9(^1P)^3D$		118055	118006	49	0.520
	2	$88+9(^1P)^3D$		118423	118322	101	1.169
	3	$84+6(^1P)^3D$		118598	118580	18	1.313
$(^2H)^1G$	4	$81+15(^2F)^1G$			119191		1.002
$(^2H)y^1H$	5	$79+19(^2G)^1H$		119040	119224	184	1.005
$(A^2D)^3P$	0	$57+33(^3P)^3P+10(^1P)^3P$			119575		
	1	$53+31(^3P)^3P+10(^1P)^3P$			119457		1.495
	2	$52+36(^3P)^3P+11(^1P)^3P$			119334		1.494
$(A^2D)^1F$	3	$79+11(^2G)^1F+5(A^2D)^3D$			119682		1.017
$(^2H)^1I$	6	99			120120		1.001
$(^2H)z^3G$	3	$90+5(^2F)^3G$		120765	120795	−30	0.756
	4	$89+5(^2F)^3G$		120748	120808	−60	1.048
	5	$90+4(^2F)^3G$		120700	120755	−55	1.194
$(^1P)^1S$	1	$63+22(^3P)^1P+7(A^2D)^1P$			121744		1.676
$(^3P)^1P$	1	$50+32(^1P)^3S+17(A^2D)^1P$			122192		1.312
$(A^2D)^1D$	2	$59+39(^3P)^1D$			122689		1.003
$(^2F)w^3F$	2	95		128754	128943	−189	0.671
	3	94		128782	128981	−199	1.080
	4	94		128849	129055	−206	1.246
$(^2F)w^3G$	3	$92+6(^2H)^3G$		131118	131009	109	0.756
	4	$92+5(^2H)^3G$		131267	131160	107	1.054
	5	$95+5(^2H)^3G$		131449	131337	112	1.200
$(^2F)^1D$	2	$79+19(B^2D)^1D$			132294		0.998
$(^2F)^3D$	1	$93+6(B^2D)^3D$			132846		0.500
	2	$92+6(B^2D)^3D$			132624		1.164
	3	$91+7(B^2D)^3D$			132261		1.329
$(^2F)^1G$	4	$83+16(^2H)^1G$			133967		1.001
$(^2F)^1F$	3	94			134899		1.002
$(B^2D)^3D$	1	$95+4(^2F)^3D$			146918		0.504
	2	$94+4(^2F)^3D$			146939		1.166
	3	$94+4(^2F)^3D$			147030		1.330
$(B^2D)^1D$	2	$74+12(^2F)^1D+12(B^2D)^1F$			148648		0.955
$(B^2D)^1F$	2	$84+12(B^2D)^1D$			149279		0.714
	3	94			149289		1.084
	4	98			149495		1.250
$(B^2D)^3P$	0	99			151996		
	1	99			151828		1.496
	2	99			151493		1.497
$(B^2D)^1F$	3	97			152028		1.002
$(B^2D)^1P$	1	100			156958		1.000

TABLE 15. *Observed and calculated levels of* Mn III $3d^4 4p$

Name	J	Percentage	AEL	Observed	Calculated	O–C	Lande C.
$(^5D)z^6F$	1/2	100		110037	109996	41	−0.664
	3/2	100		110174	110136	38	1.067
	5/2	100		110400	110366	34	1.314
	7/2	100		110713	110684	29	1.397
	9/2	100		111113	111090	23	1.434
	11/2	100		111603	111583	20	1.454
$(^5D)z^4P$	3/2	98		111778	111553	225	2.388
	5/2	98		111885	111700	185	1.881
	7/2	100		112060	111926	134	1.713
$(^5D)z^4D$	1/2	73 + 24(^5D)^4D		112816	112716	100	2.828
	3/2	66 + 30(^5D)^4D		113080	113150	−70	1.784
	5/2	51 + 48(^5D)^4D		113678	113772	−94	1.626
$(^5D)z^4D$	1/2	75 + 24(^5D)^4P		113993	114055	−62	3.169
	3/2	69 + 30(^5D)^4P		114097	114169	−72	1.825
	5/2	52 + 46(^5D)^4P		114290	114382	−92	1.632
	7/2	99		114211	114337	−126	1.583
	9/2	97		114503	114661	−158	1.548
$(^5D)z^4F$	3/2	96		116582	116438	144	0.403
	5/2	96		116694	116567	127	1.032
	7/2	95		116853	116754	99	1.243
	9/2	94		117064	117007	57	1.340
$(^5D)z^4D$	1/2	98		120977	121090	−113	0.002
	3/2	98		121094	121223	−129	1.200
	5/2	98		121270	121425	−155	1.371
	7/2	98		121484	121669	−185	1.428
$(^5H)z^4H$	7/2	80 + 18(^5G)^4H			130903		0.672
	9/2	79 + 17(^5G)^4H			131077		0.967
	11/2	79 + 16(^5G)^4H			131322		1.128
	13/2	82 + 14(^5G)^4H			131645		1.226
$(A^3P)^4D$	1/2	83 + 14(A^3F)^4D			130981		0.025
	3/2	82 + 16(A^3F)^4D			131401		1.202
	5/2	78 + 20(A^3F)^4D			132018		1.370
	7/2	69 + 29(A^3F)^4D			132746		1.424
$(^5H)^4I$	9/2	94			132880		0.743
	11/2	95			133244		0.973
	13/2	96			133604		1.112
	15/2	100			133950		1.200
$(A^3F)^4G$	5/2	72 + 18(^5G)^4G + 9(^5H)^4G			133037		0.577
	7/2	59 + 15(^5G)^4G + 11(^5H)^4G			133207		0.974
	9/2	45 + 13(^5G)^4G + 12(^5H)^4G			133423		1.152
	11/2	55 + 22(^5H)^4G + 20(^5G)^4G			133918		1.267
$(A^3P)^2S$	1/2	50 + 42(A^3P)^4P			133423		2.205
$(^5H)^2G$	7/2	49 + 28(A^3F)^2G + 7(^5G)^2G			133868		0.903
	9/2	39 + 27(A^3F)^2G + 18(A^3F)^2G			134085		1.124
$(A^3P)^4P$	1/2	52 + 32(A^3P)^2S + 13(A^3P)^2P			134548		2.180
	3/2	91			134369		1.724
	5/2	90			135057		1.570
$(A^3F)^4F$	3/2	50 + 30(A^3F)^2D + 6(^5D)^2D			135191		0.620
	5/2	50 + 25(^5H)^4G + 6(^5G)^4G			135572		0.889
	7/2	84 + 8(^5H)^4G			135754		1.215
	9/2	86 + 4(^5H)^4G			135853		1.322
$(^5H)^4G$	5/2	34 + 24(A^2F)^4F + 19(A^3F)^4G			135382		0.763
	7/2	52 + 28(A^3F)^4G + 12(^5G)^4G			135466		1.004
	9/2	54 + 31(A^3F)^4G + 10(^5G)^4G			135517		1.175
	11/2	51 + 40(A^3F)^4G + 8(^5G)^4G			135570		1.268
$(A^3P)^2P$	1/2	71 + 17(A^3P)^2S + 7(A^3F)^4D			136005		0.870
	3/2	44 + 28(A^3P)^2S + 15(A^3F)^4F			135666		1.352
$(A^3F)^2D$	3/2	33 + 26(A^3F)^4F + 25(A^3P)^2S			136101		1.001
	5/2	54 + 18(A^3F)^4F + 12(^5D)^2D			136199		1.170
$(^5H)^2I$	11/2	92 + 4(^3I)^2I			136218		0.932
	13/2	93			136350		1.082
$(A^3P)^2S$	3/2	39 + 30(A^3P)^2P + 16(A^3F)^4D			136593		1.508
$(A^3F)^4D$	1/2	78 + 15(A^3P)^4D			136897		0.051
	3/2	61 + 15(A^3P)^4D + 13(A^3P)^2P			136927		1.217
	5/2	62 + 18(A^3P)^4D			136823		1.301

TABLE 15. *Observed and calculated levels of* Mn III $3d^4 4p$ — Con.

Name	J	Percentage	AEL	Observed	Calculated	O–C	Lande C.
	7/2	51 + 27(A^3P)^4D + 7(A^3F)^2F			136851		1.372
$(^3H)^2H$	9/2	71 + 14(A^1G)^2H + 6(^3G)^2H			137452		0.915
	11/2	72 + 11(A^1G)^2H + 9(^3G)^4H			137936		1.096
$(A^3F)^2F$	5/2	35 + 28(^3G)^2F + 15(^3D)^2F			137521		0.918
	7/2	38 + 23(^3G)^2F + 14(^3D)^2F			137828		1.175
$(^3G)^4H$	7/2	80 + 17(^3H)^4H			137669		0.674
	9/2	76 + 15(^3H)^4H + 5(^3H)^2H			137961		0.970
	11/2	73 + 13(^3H)^4H + 12(^3H)^2H			138285		1.127
	13/2	83 + 14(^3H)^4H			138650		1.226
$(A^3P)^2D$	3/2	70 + 13(A^3F)^2D + 7(^3G)^4F			137890		0.780
	5/2	55 + 21(^3G)^4F + 9(A^3F)^2D			138811		1.146
$(^3G)^4F$	3/2	68 + 14(^3D)^4F + 8(A^3P)^2D			138607		0.462
	5/2	50 + 25(A^3P)^2D + 11(^3D)^4F			138435		1.074
	7/2	69 + 14(^3D)^4F + 10(A^3F)^4F			138540		1.227
	9/2	71 + 13(^3D)^4F + 6(A^3F)^4F			138501		1.312
$(A^3F)^2G$	7/2	53 + 24(^3H)^2G + 9(A^1G)^2G			139649		0.903
	9/2	44 + 24(^3H)^2G + 12(^3G)^2H			139893		1.096
$(^3G)^2F$	5/2	42 + 41(A^3F)^2F + 7(^3G)^4G			139903		0.835
	7/2	48 + 40(A^3F)^2F			140385		1.138
$(^3G)^2H$	9/2	48 + 18(^3G)^4G + 9(^3H)^2H			140092		0.999
	11/2	53 + 23(^3G)^4G + 10(^3H)^4G			140069		1.149
$(^3G)^4G$	5/2	57 + 25(^3H)^4G + 8(A^3F)^2F			140169		0.616
	7/2	62 + 24(^3H)^4G			140310		0.996
	9/2	46 + 17(^3G)^2H + 17(^3H)^4G			140611		1.113
	11/2	47 + 27(^3G)^2H + 16(^3H)^4G			140880		1.212
$(^3G)^2G$	7/2	74 + 15(^3H)^2G + 6(A^1G)^2G			143210		0.897
	9/2	67 + 17(^3H)^2G + 12(A^1G)^2G			143338		1.111
$(^3D)^4D$	1/2	92			143618		0.047
	3/2	87			143625		1.198
	5/2	79 + 12(^3D)^4P			143659		1.383
	7/2	88			143821		1.413
$(^3I)^2I$	11/2	90 + 7(A^1G)^2H			144109		0.935
	13/2	74 + 23(^3I)^2K			144067		1.045
$(A^1G)^2H_4$	9/2	80 + 10(^3H)^2H			144414		0.914
	11/2	76 + 10(^3H)^2H			144756		1.082
$(^3I)^2K$	13/2	77 + 23(^3I)^2I			144789		0.966
	15/2	100			145221		1.067
$(^3D)^4F$	3/2	70 + 16(^3G)^4F + 8(^3D)^4P			144791		0.552
	5/2	72 + 16(^3G)^4F + 6(^3D)^4D			144912		1.050
	7/2	77 + 16(^3G)^4F + 6(^3D)^4D			145044		1.248
	9/2	83 + 16(^3G)^4F			145161		1.332
$(^3D)^4P$	1/2	93			144897		2.630
	3/2	82 + 8(^3D)^4F			144635		1.584
	5/2	81 + 10(^3D)^4D			144220		1.557
$(A^1G)^2F$	5/2	81 + 5(^3G)^2F			144986		0.864
	7/2	82 + 4(^3G)^2F			144427		1.138
$(^3D)^2P$	1/2	45 + 47(A^1S)^2P			145317		0.658
	3/2	56 + 38(A^1S)^2P			145564		1.333
$(A^1G)^2G$	7/2	80 + 10(^3G)^2G			146744		0.895
	9/2	78 + 15(^3G)^2G			146939		1.111
$(^1I)^2H$	9/2	87 + 9(^3G)^2H			148625		0.910
	11/2	85 + 9(^3G)^2H + 6(A^1G)^2H			148261		1.089
$(^3D)^2F$	5/2	73 + 11(^3G)^2F + 5(^1F)^2F			148837		0.858
	7/2	73 + 9(^3G)^2F			148611		1.142
$(A^1S)^2P$	1/2	41 + 42(^3D)^2P + 12(A^1D)^2P			148942		0.666
	3/2	43 + 24(^3D)^2P + 13(A^1D)^2P			148779		1.264
$(^3D)^2D$	3/2	64 + 15(A^1D)^2D + 9(B^3F)^2D			149769		0.859
	5/2	58 + 30(A^1D)^2D			149334		1.200
$(A^1D)^2D$	3/2	67 + 15(^3D)^2D			151050		0.815
	5/2	58 + 23(^3D)^2D			151384		1.187
$(A^1D)^2F$	5/2	81 + 5(^1F)^2F			152281		0.872
	7/2	83 + 10(^1F)^2F			152678		1.143
$(A^1D)^2P$	1/2	86 + 6(^3D)^2P			155354		0.668
	3/2	81 + 8(^3D)^2P			155436		1.331

TABLE 15. *Observed and calculated levels of* Mn III $3d^4 4p - Con.$

Name	J	Percentage	AEL	Observed	Calculated	O−C	Lande C.
$(^1F)^2F$	5/2	$81+7(A^1D)^2F+6(A^1G)^2F$			156247		0.860
	7/2	$78+10(A^1D)^2F+6(A^1G)^2F$			156404		1.139
$(^1F)^2G$	7/2	94			158193		0.894
	9/2	95			158795		1.112
$(^1F)^2D$	3/2	$70+16(B^3P)^2D+10(B^3F)^2D$			160897		0.797
	5/2	$66+18(B^3P)^2D+11(B^3F)^2D$			160156		1.199
$(B^3F)^4F$	3/2	96			163001		0.422
	5/2	92			163010		1.048
	7/2	92			163054		1.247
	9/2	98			163169		1.331
$(B^3P)^4P$	1/2	$82+11(B^3P)^4D$			163878		2.268
	3/2	$69+18(B^3P)^4D$			163655		1.592
	5/2	$49+30(B^3P)^4D+10(B^3F)^4D$			163647		1.469
$(B^3P)^4D$	1/2	$58+26(B^3F)^4D+14(B^3P)^4P$			164305		0.394
	3/2	$47+22(B^3F)^4D+22(B^3P)^4P$			164266		1.311
	5/2	$34+45(B^3P)^4P+15(B^3F)^4D$			164249		1.461
	7/2	$63+28(B^3F)^4D$			163950		1.412
$(B^3F)^4G$	5/2	$79+16(B^3F)^4F$			165162		0.636
	7/2	$80+15(B^3F)^4F$			165369		1.015
	9/2	97			165617		1.172
	11/2	99			165794		1.272
$(B^3F)^4F$	5/2	$73+16(B^3F)^4G$			166018		0.823
	7/2	$73+17(B^3F)^4G$			165864		1.118
$(B^3P)^2D$	3/2	$47+23(^1F)^2D+22(B^3F)^2D$			165686		0.819
	5/2	$45+24(^1F)^2D+16(B^3F)^2D$			165463		1.191
$(B^3P)^4S$	3/2	97			168114		1.991
$(B^3F)^2G$	7/2	97			169691		0.890
	9/2	97			169375		1.111
$(B^3F)^4D$	1/2	$70+29(B^3P)^4D$			170024		0.007
	3/2	$69+30(B^3P)^4D$			169959		1.201
	5/2	$69+30(B^3P)^4D$			169810		1.370
	7/2	$68+31(B^3P)^4D$			169537		1.426
$(B^3P)^2P$	1/2	90			170434		0.688
	3/2	93			170053		1.333
$(B^3P)^2S$	1/2	98			172395		1.975
$(B^1G)^2H$	9/2	$68+29(B^1G)^2G$			173087		0.970
	11/2	98			173889		1.091
$(B^1G)^2G$	7/2	95			173425		0.896
	9/2	$68+29(B^1G)^2H$			173870		1.051
$(B^3F)^2D$	3/2	$66+33(B^3P)^2D$			175759		0.801
	5/2	$41+36(B^1G)^2F+17(B^3P)^2D$			175377		1.038
$(B^1G)^2F$	5/2	$50+30(B^3F)^2D+11(B^3P)^2D$			175850		0.999
	7/2	$83+6(B^3F)^2F$			175345		1.137
$(B^1D)^2P$	1/2	94			190177		0.667
	3/2	94			189762		1.331
$(B^1D)^2F$	5/2	93			192652		0.860
	7/2	94			193245		1.143
$(B^1D)^2D$	3/2	98			196243		0.802
	5/2	99			196498		1.197
$(B^1S)^2P$	1/2	95			216022		0.667
	3/2	96			216787		1.333

TABLE 16. *Observed and calculated levels of* Fe III $3d^5 4p$

Name	J	Percentage	AEL	Observed	Calculated	O−C	Lande C.
$(^6S)z^7P$	2	100		82002	81854	148	2.331
	3	99		82334	82159	175	1.915
	4	100		82847	82626	221	1.750
$(^6S)z^5P$	1	98		89491	89343	148	2.499
	2	98		89335	89177	158	1.835
	3	98		89085	88916	169	1.668
$(^4G)z^5G$	2	96		113584	113807	−223	0.341
	3	$91+5(^4G)^2G$		113605	113832	−227	0.897
	4	$89+8(^4G)^2H$		113635	113873	−238	1.130
	5	$88+9(^4G)^2H$		113677	113932	−255	1.251
	6	$90+7(^4G)^2H$		113740	114020	−280	1.323
$(^4G)z^3H$	3	$94+5(^4G)^2G$		114949	114731	218	0.525
	4	$90+8(^4G)^2G$		115111	114913	198	0.923

TABLE 16. *Observed and calculated levels of* Fe III $3d^5 4p - Con.$

Name	J	Percentage	AEL	Observed	Calculated	O−C	Lande C.
	3	$90+9(^4G)^2G$		115290	115106	184	1.116
	6	$92+7(^4G)^2G$		115474	115295	179	1.223
	7	100		115642	115455	187	1.286
$(^4G)z^5F$	1	$76+12(^4P)^2D+6(^4D)^2F$		116938	116890	48	0.222
	2	$57+28(^4P)^2D+6(^4D)^2D$		116975	116960	15	1.197
	3	$55+22(^4P)^2D+9(^4D)^2F$	$(a^4P)z^5D$	116475	116467	8	1.326
	4	$81+7(^4D)^2F$	$(a^4G)z^5F$	116467	116451	16	1.355
	5	$90+5(^4D)^2F$		116317	116328	−11	1.397
$(^4P)z^5D$	0	$80+16(^4D)^2D$		116365	116485	−120	
	1	$67+16(^4D)^2D+11(^4G)^2F$		116380	116466	−86	1.279
	2	$46+29(^4G)^2F+11(^4D)^2D$		116419	116458	−39	1.310
	3	$49+32(^4G)^2F+10(^4D)^2D$	$(a^4G)z^5F$	117069	117110	−41	1.425
	4	$75+14(^4D)^2D+8(^4G)^2F$	$(a^4P)z^5D$	117522	117597	−75	1.484
$(^4P)z^5S$	2	92		116898	117246	−348	1.961
$(^4G)z^3F$	2	90		118164	118310	−146	0.671
	3	$75+10(^4P)^2P$		118247	118433	−186	1.174
	4	89		118350	118543	−193	1.242
$(^4G)z^3H$	4	95		118686	118562	124	0.810
	5	97		118557	118469	88	1.035
	6	96		118355	118310	45	1.168
$(^4P)y^5P$	1	$78+14(^4D)^2P$		118868	118825	43	2.433
	2	$69+19(^4D)^2P$		118722	118678	44	1.801
	3	$53+22(^4D)^2P+14(^4G)^2F$		118443	118385	58	1.559
$(^4P)z^3P$	0	$76+17(^4D)^2P$		120180	120299	−119	
	1	$71+18(^4D)^2P$		119982	120089	−107	1.534
	2	$66+18(^4D)^2P+5(^4P)^2P$		119698	119801	−103	1.528
$(^4D)y^5F$	1	$85+11(^4G)^2F$		120697	120731	−34	0.025
	2	$84+10(^4G)^2F$		120826	120867	−41	1.012
	3	$84+8(^4G)^2F$		121009	121055	−46	1.258
	4	$87+7(^4G)^2F$		121242	121285	−43	1.353
	5	$92+6(^4G)^2F$		121469	121480	−11	1.399
$(^4G)z^3G$	3	94		121920	121931	−11	0.751
	4	95		121941	121986	−45	1.051
	5	95		121950	122030	−80	1.201
$(^4D)y^5D$	0	$75+19(^4P)^2D$		123456	123106	350	
	1	$35+46(^4P)^2D+8(^4P)^2D$	$(a^4P)z^5D$	122843	122812	31	1.044
	2	$36+46(^4P)^2D+7(^4P)^2D$		122628	122571	57	1.330
	3	$36+31(^4P)^2D+14(^4D)^2P$	$(a^4D)y^5D$	122830	122761	69	1.459
	4	$78+16(^4P)^2D$		122944	122552	392	1.495
$(^4P)z^3D$	1	$41+22(^4D)^2P+21(^4D)^2D$	$(a^4D)y^5D$	122921	123066	−145	1.303
	2	$40+25(^4D)^2D+18(^4D)^2P$		122899	122953	−54	1.410
	3	$53+29(^4D)^2D+5(^4P)^2D$	$(a^4P)z^3D$	122347	122310	37	1.389
$(^4D)z^5P$	1	$56+20(^4D)^2D+12(^4P)^2P$		123553	123473	80	2.141
	2	$55+18(^4P)^2P+16(^4D)^2D$		123697	123749	−52	1.728
	3	$45+23(^4P)^2P+13(^4D)^2D$		123750	123857	−107	1.583
$(^4D)y^3D$	1	$84+8(^4F)^2D$		124955	124817	138	0.515
	2	$84+7(^4F)^2D$		124904	124747	157	1.183
	3	$71+12(^4D)^2P$		124854	124704	150	1.380
$(^4D)y^3F$	2	$88+6(A^2G)^2F$		125673	125735	−62	0.687
	3	$86+6(A^2G)^2F$		125638	125714	−76	1.100
	4	$90+6(A^2G)^2F$		125444	125510	−66	1.254
$(^4P)z^2S$	1	95		126391	126437	−46	1.981
$(^4D)y^3P$	0	$77+18(^4P)^2P$		128372	128649	−277	
	1	$74+19(^4P)^2P$		128606	128904	−298	1.513
	2	$72+21(^4P)^2P$		128918	129237	−319	1.499
$(^2I)z^2K$	6	$83+15(^2I)^2I$	$(a^2I)z^2I$	129855	129757	98	0.886
	7	$76+17(^2I)^2I+6(^2I)^1K$		130041	130111	−70	1.038
	8	100		130852	130705	147	1.125
$(^2I)z^2I$	5	$82+9(^2I)^1H$		130256	130362	−106	0.859
	6	$78+16(^2I)^2K$	$(a^2I)z^2K$	130757	130793	−36	1.003
	7	$71+21(^2I)^2K$		131035	130791	244	1.110
$(A^2D)z^1D$	2	$32+26(A^2F)^2F+24(A^2D)^2F$		131445	131665	−220	0.858
$(^2I)z^1H$	5	$69+13(^2I)^2I+9(A^2G)^1H$		131711	131986	−275	0.982
$(^2I)z^1K$	7	$89+9(^2I)^2I$		131992	131987	5	1.013
$(A^2D)z^2F$	2	$42+26(A^2D)^1D+17(A^2F)^1D$		132105	132331	−226	0.832
	3	$58+25(A^2F)^2F$		132080	132183	−103	1.058
	4	$58+22(A^2F)^2F+10(A^2F)^2G$		132785	132847	−62	1.198
$(^2I)y^2H$	4	84		132659	132797	−138	0.832
	5	$86+6(^2I)^1H$		132565	132743	−178	1.031
	6	90		132263	132442	−179	1.160
$(A^2F)z^1G$	4	$57+17(A^2F)^2G+10(^2F)^1G$		134360	134247	113	1.014

TABLE 16. *Observed and calculated levels of* Fe III $3d^5 4p - Con.$

Name	J	Percentage	AEL	Observed	Calculated	O−C	Lande C.
$(^2F)y^3G$	3	$53+25(A^2D)^1F+13(A^2F)^3F$		134549	134476	73	0.881
	4	$54+36(A^2F)^3F+5(^4F)^5G$		135554	135461	93	1.127
	5	$55+35(^4F)^5G$	$(a^4F)y^5G$	135316	135120	196	1.225
$(A^2D)x^3P$	0	$90+6(^4F)^1D$		135088	134978	110	
	1	$59+20(A^2D)^3D+11(A^2F)^3D$		134549	134467	82	1.130
	2	$67+25(A^2F)^3D$		134265	134149	116	1.385
$(A^2D)x^3D$	1	$60+22(A^2D)^3P+8(^4F)^5F$		135217	135197	20	0.708
	2	$62+12(^4F)^5G+9(^4F)^3F$		135279	135283	−4	1.040
	3	$32+25(A^2F)^3D+24(^4F)^5G$		134976	135047	−71	1.182
$(^4F)y^5G$	2	$75+10(A^2F)^3F+7(A^2D)^3D$		134938	134888	50	0.477
	3	$54+27(A^2D)^3D$		135097	134996	101	1.065
	4	$81+8(A^2F)^1G$		135240	135158	82	1.134
	5	$58+39(A^2F)^3G$	$(a^2F)y^3G$	135735	135548	187	1.239
	6	$50+44(^2I)^4I$	$(a^2I)z^4I$	135582	135552	30	1.176
$(^2I)z^4I$	6	$50+46(^4F)^5G$	$(a^4F)y^5G$	135739	135635	104	1.159
$(A^2F)w^3D$	1	$66+19(A^2D)^1P$		136465	136194	271	0.687
	2	$36+37(^4F)^3F+10(A^2D)^3D$		136794	136487	307	1.097
	3	$65+11(A^2D)^3D$		135706	135411	295	1.264
$(A^2D)z^4F$	3	$31+24(A^2F)^3G+10(^4F)^3F$		136200	136174	26	0.994
$(^4F)x^5F$	1	$76+10(A^2D)^3D$		136236	136305	−69	0.155
	2	$38+36(A^2F)^3D+13(^4F)^3D$		136118	136172	−54	1.103
	3	$65+13(^4F)^3D+6(A^2F)^5G$		136009	136150	−141	1.229
	4	$74+17(^4F)^3D$		135991	136121	−130	1.368
	5	88		136185	136310	−125	1.386
$(A^2F)w^5F$	2	$46+19(A^2D)^3F+10(A^2F)^3D$		136532	136675	−143	0.790
	3	$41+14(A^2D)^3F+14(A^2D)^1F$		136797	136846	−49	1.105
	4	$42+28(A^2D)^3F+15(A^2F)^5G$		136613	136555	58	1.194
$(^2H)x^3H$	4	$46+44(A^2G)^3H$	$(a^2G)x^3H$	137528	137500	28	0.821
	5	$43+42(A^2G)^3H+6(^2H)^3I$		137764	137731	33	1.035
	6	$46+41(A^2G)^3H+6(^2H)^3I$		138264	138248	16	1.154
$(^4F)x^5D$	0	$91+6(A^2D)^3P$		137573	137608	−35	
	1	$85+6(A^2D)^3P$		137561	137605	−44	1.404
	2	$77+9(^4F)^3F$		137545	137610	−65	1.425
	3	$74+14(^4F)^3F$		137423	137509	−86	1.443
	4	$75+16(^4F)^3F$		137210	137297	−87	1.464
$(^2H)x^3G$	3	$41+28(^4F)^5G+16(A^2F)^5G$		138188	138313	−125	0.768
	4	$43+30(^4F)^5G+13(A^2F)^5G$		138103	138228	−125	1.051
	5	$47+29(^4F)^5G+10(A^2F)^5G$		138055	138214	−159	1.141
$(A^2D)z^4P$	1	$71+17(A^2F)^3D$		138692	138498	194	0.905
$(^4F)w^5G$	3	$42+41(A^2G)^5G+7(^2H)^5G$		139680	139539	141	0.767
	4	$42+36(A^2G)^5G+10(^2H)^5G$		139625	139477	148	1.044
	5	$43+25(A^2G)^5G+16(^2H)^5I$		139461	139350	113	1.141
$(^2H)y^5I$	5	$79+8(^2H)^5H+7(^4F)^5G$		139509	139410	99	0.904
	6	$87+5(^2H)^5H$		139846	139762	84	1.033
	7	96		140196	140165	31	1.142
$(A^2G)y^1G$	4	$40+19(A^2F)^1G+17(^2H)^1G$		139827	139749	78	1.037
$(A^2F)y^1D$	2	$56+38(A^2D)^1D$		139764	139779	−15	0.991
$(A^2F)y^1F$	3	$72+8(A^2D)^1F+6(A^2G)^1F$		140453	140468	−15	1.001
$(A^2G)x^3F$	2	$42+31(^4F)^3F+13(^4F)^3D$		140751	140998	−247	0.749
	3	$42+26(^4F)^3F+15(^4F)^3D$		140693	140901	−208	1.120
	4	$45+26(^4F)^3F+9(A^2G)^1G$		141003	141195	−192	1.205
$(^2H)y^1I$	6	$88+5(^2H)^3H$		141540	141442	98	1.013
$(^4F)x^3D$	1	$84+6(^4D)^3D$		141469	141576	−107	0.512
	2	$68+8(A^2G)^3F+6(^4D)^3D$		141399	141571	−172	1.081
	3	$64+7(A^2G)^3F+7(^4D)^3D$		141467	141663	−196	1.278
$(^4F)w^5F$	2	$48+24(A^2G)^3F+22(A^2F)^3F$		142535	142682	−147	0.679
	3	$50+24(A^2G)^3F+20(A^2F)^3F$		142313	142460	−147	1.080
	4	$50+25(A^2G)^3F+21(A^2F)^3F$		142047	142197	−150	1.246
$(A^2G)w^5H$	4	$45+47(^2H)^3H$	$(a^2H)w^3H$	142856	142754	102	0.819
	5	$46+38(^2H)^3H+9(A^2G)^3G$		142908	142783	125	1.052
	6	$50+40(^2H)^3H+7(^2H)^1I$		143321	143253	68	1.155
$(A^2G)x^3G$	3	$43+24(A^2F)^3G+18(^4F)^5G$		144117	143854	263	0.766
	4	$42+23(A^2F)^3G+14(^4F)^5G$		144086	143844	242	1.048
	5	$40+20(A^2F)^3G+12(^2H)^5G$		143884	143657	227	1.172
$(B^2F)x^1G$	4	$35+30(A^2F)^3F+14(A^2G)^1G$	$(b^2F)z^3F$	144332	144445	−113	1.090
$(A^2G)y^1H$	5	$66+18(^2H)^1H+12(^2I)^1H$		144587	144462	125	1.005
$(B^2F)x^3F$	2	$66+19(A^2G)^3F+7(^4F)^3F$		144502	144598	−96	0.694
	3	$73+11(A^2G)^3F+6(^4F)^3F$		144571	144697	−126	1.076
	4	$48+20(B^2F)^1G+8(^2H)^1G$	$(a^2H)x^1G$	144968	145120	−152	1.156

TABLE 16. *Observed and calculated levels of* Fe III $3d^5 4p - Con.$

Name	J	Percentage	AEL	Observed	Calculated	O−C	Lande C.
$(^2H)x^1H$	5	$70+23(A^2G)^1H$		144843	144729	114	1.007
$(A^2G)x^1F$	3	$76+5(B^2F)^1F+5(B^2D)^1F$		145039	145227	−188	1.006
$(B^2F)x^1D$	2	$82+7(B^2F)^3F+7(B^2D)^1D$		145618	145658	−40	0.979
$(B^2F)w^5G$	3	$55+36(^2H)^5G+6(A^2G)^5G$		146891	146938	−47	0.759
	4	$59+32(^2H)^5G+6(A^2G)^5G$		147161	147217	−56	1.052
	5	$66+28(^2H)^5G+5(A^2G)^5G$		147406	147490	−84	1.200
$(B^2F)w^3D$	1	90		147556	147602	−46	0.533
	2	89		147615	147700	−85	1.171
	3	$86+7(^4F)^3D$		147636	147761	−125	1.326
$(^2S)w^3P$	0	$85+12(B^2D)^3P$		148655	148596	59	
	1	$82+13(B^2D)^3P$		148915	148854	61	1.466
	2	$82+14(B^2D)^3P$		149526	149441	85	1.492
$(^2H)w^1G$	4	$34+44(B^2F)^1G+21(A^2G)^1G$	$(b^2F)w^1G$	149013	149063	−50	1.001
$(B^2F)w^1F$	3	93		150655	150566	89	1.005
$(^2S)y^1P$	1	$78+19(B^2D)^1P$		151637	151652	−15	1.004
$(B^2D)x^3F$	2	$75+18(B^2D)^3D$		157684	157737	−53	0.765
	3	$61+27(B^2D)^3D+6(B^2D)^1F$		157982	157940	42	1.149
	4	94		158563	158559	4	1.249
$(B^2D)x^3D$	1	95		158257	157919	338	0.520
	2	$76+18(B^2D)^3F$		158417	158123	294	1.080
	3	$67+29(B^2D)^3F$		158729	158447	282	1.256
$(B^2D)w^1F$	3	$82+12(B^2G)^1F$		159493	159453	40	1.010
$(B^2D)w^3P$	0	$87+13(^2S)^3P$			160319		
	1	$82+13(^2S)^3P$			160307		1.468
	2	$81+14(^2S)^3P$		160038	160291	−253	1.483
$(B^2D)^1P$	1	$80+15(^2S)^1P$			161258		1.010
$(B^2D)w^1D$	2	$92+6(B^2F)^1D$		162085?	161749	336	1.003
$(B^2G)x^3H$	4	$93+5(B^2G)^5G$		165719	165640	79	0.814
	5	$90+6(B^2G)^5G$		165940	165834	106	1.043
	6	98		166187?	166287	−100	1.167
$(B^2G)x^3F$	2	$93+5(C^2D)^3F$		167002	167059	−57	0.667
	3	$50+46(B^2G)^5G$		166498	166531	−33	0.928
	4	$81+11(B^2G)^3F$		166222	166268	−46	1.220
$(B^2G)x^5G$	3	$53+44(B^2G)^3F$		167085	167065	20	0.907
	4	$85+11(B^2G)^3F$		167207	167154	53	1.064
	5	$91+7(B^2G)^3H$		167299	167242	57	1.185
$(B^2G)w^1H$	5	95		168780	168674	106	1.006
$(B^2G)w^1G$	4	96		169278?	169202	76	1.003
$(B^2G)w^1F$	3	$87+12(C^2D)^1F$		170311?	170439	−128	0.998
$(^2P)^3P$	0	$77+22(C^2D)^3P$			178674		
	1	$76+23(C^2D)^3P$			178823		1.502
	2	$76+24(C^2D)^3P$			179241		1.497
$(^2P)^1S$	0	99			181398		
$(^2P)^3D$	1	93			182519		0.504
	2	$66+22(^2P)^1D+5(C^2D)^1D$			182490		1.121
	3	$92+7(C^2D)^3D$			183099		1.333
$(^2P)^1D$	2	$57+26(^2P)^3D+14(C^2D)^1D$			183519		1.047
$(^2P)^3S$	1	98			184869		1.979
$(^2P)^1P$	1	$78+19(C^2D)^1P$			185970		1.013
$(C^2D)^3F$	2	$91+5(B^2G)^3F$			191071		0.690
	3	$89+5(C^2D)^3D$			191235		1.096
	4	96			191700		1.250
$(C^2D)^3D$	1	94			192255		0.505
	2	$89+6(^2P)^3D$			192579		1.147
	3	$89+7(^2P)^3D$			192934		1.318
$(C^2D)^1D$	2	$69+16(^2P)^1D+11(C^2D)^3P$			193395		1.067
$(C^2D)^1F$	3	94			194617		1.003
$(C^2D)^3P$	0	$77+22(^2P)^3P$			194973		
	1	$77+23(^2P)^3P$			194703		1.498
	2	$66+20(^2P)^3P+12(C^2D)^1D$			194332		1.430
$(C^2D)^1P$	1	$81+18(^2P)^1P$			198959		0.999

TABLE 17. *Observed and calculated levels of* Co III $3d^64p$

Name	J	Percentage	AEL	Observed	Calculated	O−C	Lande C.
$(^5D)z^6D$	1/2	99		99182	99357	−175	3.324
	3/2	99		99044	99207	−163	1.863
	5/2	98		98823	98971	−148	1.654
	7/2	97		98546	98671	−125	1.585
	9/2	99		98290	98386	−96	1.553
$(^5D)z^6F$	1/2	98		103691	103488	203	−0.650
	3/2	98		103656	103446	210	1.069
	5/2	97		103594	103372	222	1.315
	7/2	96		103502	103264	238	1.397
	9/2	96		103387	103124	263	1.433
	11/2	100		103245	102950	295	1.454
$(^5D)z^6P$	3/2	98		106592	106534	58	2.380
	5/2	94		105965	105912	53	1.860
	7/2	$91+7(^5D)^4D$		105009	104964	45	1.691
$(^5D)z^4D$	1/2	95		107508	107468	40	−0.006
	3/2	94		107297	107250	47	1.213
	5/2	$91+5(^5D)^6P$		106955	106897	58	1.392
	7/2	$89+7(^5D)^6P$		106489	106415	74	1.447
$(^5D)z^4F$	3/2	98		108403	108435	−32	0.407
	5/2	97		108053	108073	−20	1.035
	7/2	96		107530	107536	−6	1.244
	9/2	96		106765	106760	5	1.336
$(^5D)z^4P$	1/2	98		111283	111318	−35	2.665
	3/2	98		110962	110993	−31	1.733
	5/2	98		110371	110401	−30	1.599
$(A^3P)z^4S$	3/2	$61+36(A^3P)^4P$			124189		1.881
$(^3H)z^4G$	5/2	$44+44(A^3F)^4G+6(^3G)^4G$		125369	125406	−37	0.608
	7/2	$46+40(A^3F)^4G+7(^3G)^4G$		125227	125264	−37	0.987
	9/2	$47+33(A^3F)^4G+7(^3G)^4G$		125012	125053	−41	1.151
	11/2	$64+27(A^3F)^4G+7(^3G)^4G$		124766	124861	−95	1.269
$(^3H)z^4I$	9/2	$57+26(^3H)^4H+7(^3H)^4G$	$(^3H)z^4H$	125422	125418	4	0.852
	11/2	$59+30(^3H)^4H+7(^3G)^4H$		125296	125286	10	1.030
	13/2	$58+31(^3H)^4H+6(^3H)^6I$		125276	125308	−32	1.150
	15/2	100		126119	125945	174	1.199
$(^3H)z^4H$	7/2	$60+14(^3H)^2G+8(^3G)^4H$		125690	125839	−149	0.761
	9/2	$41+35(^3H)^4I+10(^3H)^2G$	$(^3H)z^4I$	126239	126246	−7	0.921
	11/2	$55+36(^3H)^4I+6(^3G)^4H$		126501	126505	−4	1.073
	13/2	$59+34(^3H)^4I+5(^3G)^4H$		126475	126507	−32	1.185
$(A^3P)y^4P$	1/2	$90+6(A^3P)^4D$			126373		2.465
	3/2	$30+29(A^3P)^4S+28(A^3P)^4D$			126631		1.562
	5/2	$60+25(A^3P)^4D+9(A^3P)^2D$			125343		1.472
$(A^3F)y^4F$	3/2	$86+7(^3D)^4F$		126987	127217	−230	0.425
	5/2	$78+6(^3D)^4F$		126871	127096	−225	1.034
	7/2	$48+16(A^3P)^4D+9(^3H)^4H$		126892	127048	−156	1.192
	9/2	82		126998	127160	−162	1.305
$(^3H)z^2G$	7/2	$43+18(A^3F)^4F+11(^3G)^2G$		127318	127499	−181	0.953
	9/2	$59+15(^3G)^2G+12(^3H)^4H$		127051	127272	−221	1.086
$(A^3P)z^2D$	3/2	$32+23(A^3P)^4P+23(A^3P)^4D$			127793		1.251
	5/2	$58+25(A^3P)^4P+8(A^3F)^2D$			126336		1.309
$(A^3P)y^4D$	1/2	$90+6(A^3P)^4P$		128536	128152	384	0.168
	3/2	$42+31(A^3P)^2D+12(A^3F)^2D$		128423	128681	−258	1.034
	5/2	$60+15(A^3P)^2D+10(A^3P)^4P$		128085	128242	−157	1.345
	7/2	$80+7(A^3F)^4F$		126549	126588	−39	1.388
$(^3H)z^2I$	11/2	92		128259	128200	59	0.935
	13/2	$90+7(^3H)^4I$		127673	127650	23	1.082
$(A^3F)x^4D$	1/2	$84+11(^3D)^4D$		128937	129158	−221	0.015
	3/2	$80+10(^3D)^4D$		128805	129036	−231	1.179
	5/2	$73+9(^3D)^4D$		128525	128755	−230	1.343
	7/2	$69+8(^3D)^4D$		128018	128257	−239	1.353
$(A^3F)y^4G$	5/2	$35+27(^3H)^4G+24(A^3F)^2F$		129747	129740	7	0.672
	7/2	$44+26(^3H)^4G+12(A^3F)^2F$		129707	129680	27	1.009
	9/2	$52+25(^3H)^4G+9(A^3F)^4G$		129592	129534	58	1.162
	11/2	$68+22(^3H)^4G$		129556	129505	51	1.261
$(A^3F)z^2F$	5/2	$41+19(^3H)^4G+9(^3G)^2F$		130407	130400	7	0.752
	7/2	$49+12(^3G)^2F+8(^3H)^4G$		130184	130233	−49	1.095
$(A^3P)y^2P$	1/2	$55+34(A^3P)^2S$			130940		1.149
	3/2	$87+6(A^1D)^2P$			131328		1.322
$(A^3F)y^2G$	7/2	$62+17(^3G)^4G$		131279	131283	−4	0.941
	9/2	$60+13(^3G)^2H+9(A^3F)^4G$		130802	130782	20	1.073
$(^3H)z^2H$	9/2	$37+23(^3G)^2H+21(A^3F)^2G$		131538	131606	−68	0.978
	11/2	$23+34(^3G)^2H+22(^3G)^4G$		131054	131109	−55	1.137
$(^3G)x^4G$	5/2	$63+17(^3G)^4F+8(A^3F)^2F$		131884	131773	111	0.709
	7/2	$38+24(^3G)^4F+20(A^3F)^4G$		131582	131491	91	1.040
	9/2	$49+24(^3G)^4F+8(^3G)^4G$	$(^3G)x^4F$	131887	131857	30	1.194
	11/2	$59+19(^3H)^2H+10(^3H)^4G$		131098	131311	−213	1.218

TABLE 17. *Observed and calculated levels of* Co III $3d^64p$—Con.

Name	J	Percentage	AEL	Observed	Calculated	O−C	Lande C.
$(A^3P)^2S$	1/2	$65+29(A^3P)^2P$			132300		1.540
$(^3G)y^4H$	7/2	$74+11(^3H)^4H+6(A^3F)^2G$		132624	132433	191	0.715
	9/2	$76+9(^3H)^4H$		132587	132392	195	0.987
	11/2	$74+10(^3H)^2H+7(^3H)^4H$		132507	132322	185	1.135
	13/2	$88+10(^3H)^4H$		132377	132144	233	1.228
$(^3G)x^4F$	3/2	$71+14(^3D)^4F$		132592	132454	138	0.437
	5/2	$56+18(^3G)^4G+11(^3D)^4F$		132489	132392	97	0.934
	7/2	$44+28(^3G)^4G+9(^3D)^4F$		132277	132219	58	1.108
	9/2	$52+32(^3G)^4G+5(^3D)^4F$	$(^3G)x^4G$	131098	131011	87	1.268
$(A^3F)^2D$	3/2	$72+19(A^3P)^2D$			134195		0.776
	5/2	$78+13(A^3P)^2D$			133837		1.183
$(^3G)y^2H$	9/2	$50+39(^3H)^2H$		135404	135521	−117	0.922
	11/2	$47+45(^3H)^2H$		134696	134850	−154	1.094
$(^3G)y^2F$	5/2	$54+18(^3D)^2F+10(A^3F)^2F$		136129	136217	−88	0.869
	7/2	$57+14(A^3F)^2F+13(^3D)^2F$		136290	136361	−71	1.128
$(^3G)x^2G$	7/2	$72+14(^3H)^2G$		137812	137684	128	0.912
	9/2	$74+18(^3H)^2G$		137661	137565	96	1.103
$(^1I)^2K$	13/2	98			137375		0.936
	15/2	100			138185		1.067
$(A^1G)x^2H$	9/2	$69+17(^1I)^2H$	$(^1I)x^2H$	138921	138722	199	0.927
	11/2	$49+44(^1I)^2H$		139138	139035	103	1.090
$(^3D)^4P$	1/2	$82+8(^3D)^4D$			139158		2.333
	3/2	$82+5(^3D)^4D$			138832		1.668
	5/2	90			138618		1.584
$(^3D)^4F$	3/2	$72+19(^3G)^4F$			139436		0.443
	5/2	$68+16(^3G)^4F+6(^3D)^4D$			139585		1.050
	7/2	$46+14(^3D)^4D+10(^3G)^4F$			139727		1.231
	9/2	$54+30(A^1G)^2G$			140141		1.246
$(^3D)^4D$	1/2	$53+20(^3D)^2P+12(^3D)^4P$			139616		0.510
	3/2	$55+18(^3D)^2P+10(^3D)^4P$			139831		1.252
	5/2	$77+9(A^3F)^4D+8(^3D)^4F$			140109		1.337
	7/2	$27+22(^3D)^4F+17(A^1G)^2F$			140090		1.202
$(A^1G)x^2G$	7/2	$61+13(^3D)^4F$		140383	140214	169	0.966
	9/2	$54+29(^3D)^4F$		140358	140308	50	1.177
$(^3D)^2P$	1/2	$54+25(^3D)^4D+12(A^1S)^2P$			140568		0.479
	3/2	$60+23(^3D)^4D+10(A^1S)^2P$			140444		1.296
$(A^1G)x^2F$	5/2	$48+21(^3D)^2F+10(A^3F)^2F$		140787	140734	53	0.875
	7/2	$30+44(^3D)^4D+7(A^3F)^4D$		140646	140582	64	1.285
$(^1D)x^2H$	9/2	$68+21(A^1G)^2H$	$(^1G)x^2H$	141347	141443	−96	0.912
	11/2	$33+50(A^1G)^2H$		141191	141140	51	1.072
$(^1D)y^2I$	11/2	$87+9(^1I)^2H$		141874	141926	−52	0.945
	13/2	99		141869	141925	−56	1.076
$(^3D)^2D$	3/2	88			142052		0.820
	5/2	90			142664		1.200
$(^3D)^2F$	5/2	$56+23(A^1G)^2F$ $+13(A^1D)^2F$			143970		0.865
	7/2	$61+17(A^1G)^2F$ $+14(A^1D)^2F$			143377		1.145
$(A^1S)^2P$	1/2	$51+28(A^1D)^2P$ $+12(^3D)^2P$			144469		0.673
	3/2	$43+43(A^1D)^2P$ $+10(^3D)^2P$			143865		1.319
$(A^1D)^2F$	5/2	$53+18(A^1D)^2D+15(A^1G)^2F$			146196		0.935
	7/2	$72+15(A^1G)^2F$			147106		1.144
$(A^1D)^2D$	3/2	$78+11(^1F)^2D$			146760		0.838
	5/2	$62+17(A^1D)^2F+14(^1F)^2D$			147093		1.125
$(A^1D)^2P$	1/2	$65+27(A^1S)^2P$			147373		0.671
	3/2	$43+38(A^1S)^2P$			147994		1.299
$(^1F)^2G$	7/2	92			151919		0.892
	9/2	95			152806		1.112
$(^1F)^2D$	3/2	$79+11(A^1D)^2D$			154134		0.813
	5/2	$71+15(A^1D)^2D$			153438		1.198
$(B^3P)^4D$	1/2	$54+44(B^3F)^4D$			155753		0.004
	3/2	$50+45(B^3F)^4D$	$(^3P^1)z^4S$	155702	155984	−282	1.188
	5/2	$38+45(B^3F)^4D+14(^1F)^2F$	$(^3P^1)x^4P$	156291	156171	120	1.290
	7/2	$29+35(B^3F)^4D+35(^1F)^2F$			156215		1.313
$(^1F)^2F$	5/2	$75+7(B^3F)^4D+7(B^3P)^4D$			156526		0.941
	7/2	$54+23(B^3F)^4D$ $+17(B^3P)^4D$			156628		1.256
$(B^3P)^2S$	1/2	93			159796		2.024

TABLE 17. *Observed and calculated levels of* Co III $3d^64p$ – Con.

Name	J	Percentage	AEL	Observed	Calculated	O – C	Lande C.
$(B^3F)^4G$	5/2	97			160338		0.575
	7/2	96			160581		0.984
	9/2	95			160820		1.171
	11/2	98			161090		1.272
$(B^3P)^4S$	3/2	98			161611		1.989
$(B^3F)^2D$	3/2	51 + 37$(B^3P)^2D$			163340		0.844
	5/2	49 + 35$(B^3P)^2D$ + 8$(B^3P)^4P$			163896		1.229
$(B^3P)^4P$	1/2	91			163229		2.611
	3/2	88			163563		1.667
	5/2	71 + 8$(B^3F)^4D$ + 8$(B^3P)^4D$			164334		1.510
$(B^3F)^2G$	7/2	89			164268		0.907
	9/2	88			163773		1.125
$(B^3F)^4D$	1/2	54 + 42$(B^3P)^4D$			164541		0.042
	3/2	40 + 37$(B^3P)^4D$ + 15$(B^3F)^4F$			164765		1.091
	5/2	39 + 42$(B^3F)^4F$ + 14$(B^3P)^4P$			165040		1.251
	7/2	32 + 38$(B^3P)^4D$ + 29$(B^3F)^4F$			165903		1.360
$(B^3F)^4F$	3/2	78 + 9$(B^3F)^4D$			165215		0.557
	5/2	51 + 23$(B^3P)^4D$ + 22$(B^3F)^4D$			165546		1.194
	7/2	62 + 22$(B^3P)^4D$ + 11$(B^3F)^4D$			165234		1.286
	9/2	93 + 6$(B^3F)^4G$			165624		1.318
$(B^3P)^2D$	3/2	41 + 36$(B^3F)^2D$ + 16$(B^3P)^2P$			166507		0.877
	5/2	60 + 34$(B^3F)^2D$			167276		1.210
$(B^3P)^2P$	1/2	92			167203		0.652
	3/2	77 + 12$(B^3P)^2D$			167968		1.240
$(B^3F)^2F$	5/2	94			168299		0.858
	7/2	87 + 12$(B^1G)^2F$			168167		1.142
$(B^1G)^2H$	9/2	95			170204		0.915
	11/2	98			171002		1.091
$(B^1G)^2F$	5/2	86 + 6$(^1F)^2F$			172252		0.858
	7/2	57 + 27$(B^1G)^2G$ + 6$(B^3F)^2F$			171679		1.072
$(B^1G)^2G$	7/2	68 + 21$(B^1G)^2F$			173022		0.962
	9/2	94			172850		1.108
$(B^1D)^2D$	3/2	98			190563		0.805
	5/2	98			190826		1.195
$(B^1D)^2F$	5/2	95			194508		0.862
	7/2	96			195232		1.143
$(B^1D)^2P$	1/2	93 + 6$(B^1S)^2P$			196236		0.667
	3/2	93 + 5$(B^1S)^2P$			195859		1.328
$(B^1S)^2P$	1/2	94 + 6$(B^1D)^2P$			219596		0.667
	3/2	95 + 5$(B^1D)^2P$			220550		1.333

TABLE 18. *Observed and calculated levels of* Ni III $3d^74p$

Name	J	Percentage	AEL	Observed	Calculated	O – C	Lande C.
$(^4F)z^5F$	1	96		112402	112376	26	0.054
	2	88 + 9$(^4F)^5D$		111914	111907	7	1.031
	3	78 + 17$(^4F)^5D$		111221	111241	−20	1.281
	4	65 + 29$(^4F)^5D$		110371	110431	−60	1.387
	5	94 + 5$(^4F)^5G$		110212	110157	55	1.391
$(^4F)z^5G$	2	88 + 5$(^4F)^5D$ + 5$(^4F)^5F$		114371	114162	209	0.436
	3	86 + 7$(^4F)^5F$		114110	113895	215	0.959
	4	84 + 8$(^4F)^5F$ + 6$(^4F)^5G$		113705	113482	223	1.165
	5	82 + 12$(^4F)^5G$ + 6$(^4F)^5F$		113141	112921	220	1.266
	6	100		112787	112489	298	1.333
$(^4F)z^5D$	0	91 + 8$(^4P)^5D$		114295	114441	−146	
	1	88 + 8$(^4P)^5D$		114095	114226	−131	1.450
	2	78 + 8$(^4F)^5G$ + 7$(^4P)^5D$		113651	113746	−95	1.369
	3	73 + 13$(^4F)^5F$ + 8$(^4F)^5G$		112935	113002	−67	1.420
	4	63 + 26$(^4F)^5F$ + 6$(^4F)^5G$		111898	111939	−41	1.437
$(^4F)z^5G$	3	88 + 7$(^4F)^5F$		117606	117660	−54	0.786
	4	83 + 9$(^4F)^5F$ + 7$(^4F)^5G$		116674	116706	−32	1.076
	5	87 + 13$(^4F)^5G$		115272	115292	−20	1.208

TABLE 18. *Observed and calculated levels of* Ni III $3d^74p$ – Con.

Name	J	Percentage	AEL	Observed	Calculated	O – C	Lande C.
$(^4F)z^3F$	2	92		118115	118082	33	0.678
	3	83 + 8$(^4F)^3G$		117251	117232	19	1.068
	4	85 + 10$(^4F)^3G$		116192	116167	25	1.232
$(^4F)z^3D$	1	93		120273	120304	−31	0.500
	2	92		119670	119694	−24	1.155
	3	90 + 5$(^4F)^3F$		118746	118754	−8	1.318
$(^4P)z^3S$	2	99		122282	122739	−457	1.994
$(^4P)y^5D$	0	86 + 8$(^4F)^5D$ + 5$(^2P)^3P$		130190	130242	−52	
	1	75 + 7$(^4F)^5D$ + 7$(^2P)^3P$		129958	130022	−64	1.531
	2	82 + 7$(^4F)^5D$		129913	129937	−24	1.484
	3	84 + 7$(^4F)^5D$		129954	129944	10	1.490
	4	93 + 6$(^4F)^5D$		130312	130224	88	1.497
$(^4P)z^3S$	1	53 + 12$(^2P)^3S$ + 11$(^4P)^3D$		130863	131111	−248	1.908
$(^2G)z^3H$	4	61 + 28$(^2G)^3F$ + 6$(^2G)^1G$		132157	132057	100	0.953
	5	74 + 15$(^2G)^1H$ + 7$(^2G)^3G$		131500	131367	133	1.035
	6	96		132169	131906	263	1.163
$(^4P)z^3P$	1	73 + 20$(^4P)^3S$		133340	133446	−106	2.279
	2	45 + 21$(^2P)^3P$ + 20$(^4P)^3D$	$(^4P)y^3D$	132818	132919	−101	1.549
	3	71 + 19$(^4P)^3D$		133095	133060	35	1.576
$(^4G)y^5F$	2	94		134233	134198	35	0.676
	3	78 + 11$(^2G)^3G$		133158	133174	−16	1.055
	4	41 + 33$(^2G)^3H$ + 13$(^2G)^3G$		131792	131814	−22	1.051
$(^2G)z^1G$	4	47 + 24$(^2G)^3F$ + 14$(^2H)^1G$		133325	133415	−90	1.064
$(^2P)^3P$	0	69 + 19$(A^2D)^3P$ + 6$(^4P)^3P$			133134		
	1	45 + 19$(^4P)^3D$ + 12$(^4P)^3P$			133556		1.399
	2	49 + 10$(^2P)^3D$ + 9$(^4P)^3P$			133902		1.417
$(^4P)y^3D$	1	54 + 15$(^2P)^3D$ + 13$(^2P)^3P$		133840	134055	−215	0.806
	2	42 + 37$(^4P)^3P$ + 6$(^4P)^3D$	$(^4P)z^3P$	133500	133406	94	1.432
	3	65 + 20$(^4P)^3P$		133391	133434	−43	1.384
$(^2G)z^1H$	5	62 + 23$(^2G)^3H$ + 14$(^2G)^3G$		134218	134119	99	1.034
$(^2G)y^3G$	3	70 + 16$(^2G)^1F$ + 8$(^2G)^3F$		134335	134375	−40	0.832
	4	73 + 14$(^2G)^1G$ + 6$(^2H)^1G$		134415	134523	−108	1.028
	5	78 + 19$(^2G)^1H$		133692	133722	−30	1.156
$(^2G)z^1F$	3	57 + 15$(^2G)^3G$ + 14$(A^2D)^1F$		135024	135062	−38	0.965
$(^4P)z^3P$	0	52 + 35$(^2P)^1S$ + 11$(^2P)^3P$			135695		
	1	78 + 11$(^2P)^3D$		136099	136192	−93	1.371
	2	75 + 10$(A^2D)^3P$		135351	135455	−104	1.470
$(^2P)x^3D$	1	54 + 15$(A^2D)^3D$ + 12$(^4P)^3P$		137364	137395	−31	0.682
	2	41 + 29$(^2P)^1D$ + 12$(A^2D)^3D$		136813	136950	−137	1.113
	3	77 + 8$(A^2D)^3F$		136965	136964	1	1.322
$(^2P)^1D$	2	20 + 24$(^2P)^3D$ + 20$(^4P)^3D$			137768		1.137
$(^2H)^3I$	5	95		138061	137997	64	0.843
	6	74 + 25$(^2H)^1I$		137392	137357	35	1.020
	7	100		137991	137837	154	1.143
$(^2H)x^3G$	3	85 + 6$(^2F)^3G$		138852	138891	−39	0.771
	4	90 + 5$(^2F)^3G$		138031	138118	−87	1.052
	5	94 + 5$(^2F)^3G$		137020	137161	−141	1.198
$(^2P)^1S$	0	61 + 39$(^4P)^3P$	$(^4P)z^3P$	138147	138618	−471	
$(A^2D)w^3D$	1	50 + 27$(^2P)^1P$ + 12$(^2P)^3D$		138979	138889	90	0.669
	2	63 + 10$(^2P)^3D$ + 7$(^2P)^1D$		139254	139172	82	1.121
	3	79 + 11$(A^2D)^3F$		138487	138359	128	1.307
$(^2H)z^1I$	6	74 + 24$(^2H)^3I$		139634	139600	34	1.010
$(A^2D)x^3F$	2	73 + 10$(A^2D)^3D$ + 8$(A^2D)^1D$		140916	140871	45	0.782
	3	71 + 8$(^2P)^3D$ + 6$(^2G)^1F$		140545	140503	42	1.117
	4	98		140184	140117	67	1.250
$(^2P)^3S$	1	67 + 8$(^2P)^1P$ + 8$(^4P)^3S$	$(^2P)z^1P$	140885	141052	−167	1.780
$(^2P)z^1P$	1	49 + 17$(A^2D)^3D$ + 13$(^2P)^3S$	$(^2P)y^3P$	141415	141393	22	1.077
$(A^2D)z^1D$	2	46 + 29$(A^2D)^3P$ + 15$(^2P)^1D$		142434	142323	111	1.155
$(^2H)y^3H$	4	95		143004	143062	−58	0.810
	5	95		142576	142642	−66	1.034
	6	98		142188	142259	−71	1.165
$(A^2D)y^1F$	3	73 + 16$(^2G)^1F$ + 7$(A^2D)^3F$		143865	143944	−79	1.014
$(^2H)y^1G$	4	70 + 27$(^2G)^1G$		144154	144162	−8	0.997
$(A^2D)x^3P$	0	80 + 15$(^2P)^3P$			145110		
	1	67 + 11$(^2P)^3P$ + 9$(^4P)^1P$		144624	144667	−43	1.431
	2	48 + 24$(A^2D)^3D$ + 11$(^2P)^3P$		143560	143476	84	1.334
$(A^2D)y^1P$	1	88		145950	146006	−56	1.062

TABLE 18. *Observed and calculated levels of* Ni III $3d^74p-Con.$

Name	J	Percentage	AEL	Observed	Calculated	O−C	Lande C.
$(^2H)y^1H$	5	96		146326	146504	−178	1.001
$(^2F)y^1D$	2	$60+32(^2F)^3F$	$(^2F)w^3F$	155444	155123	321	0.897
$(^2F)^3G$	3	$82+10(^2F)^3F+6(^2H)^3G$			155392		0.787
	4	$73+15(^2F)^3F+6(^2F)^1G$	$(^2F)w^3F$	155842	155842	0	1.078
	5	$94+5(^2H)^3G$			156734		1.200
$(^2F)w^3F$	2	$64+29(^2F)^1D$	$(^2F)y^1D$	156524?	156518	6	0.786
	3	$68+19(^2F)^3D+8(^2F)^3G$	$(^2F)v^3D$	156853	156444	409	1.107
	4	$50+28(^2F)^1G+20(^2F)^3G$			156906		1.138
$(^2F)v^3D$	1	$93+5(B^2D)^3D$		157235	157142	93	0.502
	2	$85+8(^2F)^1D$		157155	157121	34	1.152
	3	$72+18(^2F)^3F$	$(^2F)w^3F$	156972	156833	139	1.270
$(^2F)x^1G$	4	$65+32(^2F)^3F$		157376	157317	59	1.084
$(^2F)^1F$	3	97		161755	161735	20	1.003
$(B^2D)w^3P$	0	99		176738	176727	11	
	1	98		176583	176601	−18	1.491
	2	99		176488	176513	−25	1.497
$(B^2D)v^3F$	2	96			177858		0.670
	3	96		178452?	178440	12	1.083
	4	97			179196		1.250
$(B^2D)^1P$	1	95			181237		0.991
$(B^2D)^1F$	3	97			181516		1.007
$(B^2D)^3D$	1	95			183763		0.518
	2	$73+25(B^2D)^1D$			183976		1.123
	3	96			184740		1.327
$(B^2D)^1D$	2	$72+25(B^2D)^3D$			184456		1.042

TABLE 19. *Observed and calculated levels of* Cu III $3d^84p$

Name	J	Percentage	AEL	Observed	Calculated	O−C	Lande C.
$(^3F)z^4D$	1/2	$94+6(^3P)^4D$		122637	122764	−127	0.004
	3/2	$93+5(^3P)^4D$		121864	122012	−148	1.185
	5/2	$91+5(^3P)^4D$		120578	120765	−187	1.357
	7/2	$93+4(^3P)^4D$		118864	119113	−249	1.421
$(^3F)z^4G$	5/2	$93+6(^3F)^4F$		123440	123316	124	0.604
	7/2	$81+10(^3F)^4F+8(^3F)^2G$		122504	122416	88	1.008
	9/2	$66+22(^3F)^2G+12(^3F)^4F$		121337	121318	19	1.178
	11/2	100		121698	121488	210	1.273
$(^3F)z^4F$	3/2	$90+5(^3F)^2D$		125745	125721	24	0.445
	5/2	$84+6(^3F)^4G$		125382	125324	58	1.011
	7/2	$73+13(^3F)^4F+10(^3F)^4G$		124558	124506	52	1.202
	9/2	$82+14(^3F)^2G$		123550	123516	34	1.296
$(^3F)z^2G$	7/2	$82+10(^3F)^2F+6(^3F)^4G$		126094	126175	−81	0.926
	9/2	$64+31(^3F)^4G+5(^3F)^4F$		124442	124432	10	1.141
$(^3F)z^2D$	3/2	$82+8(^1D)^2D+7(^3F)^4F$		128435	128465	−30	0.781
	5/2	$77+14(^3F)^2F+5(^1D)^2D$		126892	126934	−42	1.149
$(^3F)z^2F$	5/2	$79+14(^3F)^2D+5(^3F)^4F$		128679	128736	−57	0.912
	7/2	$75+12(^3F)^4F+9(^3F)^2G$		126829	126902	−73	1.127
$(^3P)z^4P$	1/2	$90+7(^1D)^2P$		137041	137012	29	2.468
	3/2	$76+10(^1D)^2P+5(^1D)^2D$		136483	136500	−17	1.607
	5/2	$76+15(^1D)^2D$		136607	136605	2	1.497
$(^1D)y^2F$	5/2	$81+8(^3P)^4P$		138084	138009	75	0.939
	7/2	$83+10(^3P)^4D+6(^1G)^2F$		138982	139819	163	1.170
$(^1D)y^2D$	3/2	$57+17(^3P)^2P+9(^1D)^2P$		138988	139077	−89	1.044
	5/2	$77+14(^3P)^4P$		139757	139823	−66	1.240
$(^1D)z^2P$	1/2	$62+26(^3P)^2P+9(^3P)^4P$		139261	139189	72	0.865
	3/2	$59+23(^1D)^2D+10(^3P)^2P$		140201	140177	24	1.220
$(^3P)y^4D$	1/2	93		142550	142492	58	0.019
	3/2	$87+5(^3F)^4D+4(^3P)^2D$		142512	142443	69	1.186
	5/2	$77+13(^3P)^2D+4(^1D)^2F$		142426	142397	29	1.326
	7/2	$86+8(^1D)^2F$		142820	142737	83	1.397
$(^3P)x^2D$	3/2	$60+26(^3P)^2P+7(^1D)^2P$	$(^3P)y^2P$	145353	145214	139	1.005
	5/2	$81+15(^3P)^4D$		144194	144262	−68	1.219
$(^3P)y^2P$	1/2	$68+26(^1D)^2P+5(^3P)^2S$		146676	146409	267	0.721
	3/2	$52+34(^3P)^2D+11(^1D)^2P$	$(^3P)x^2D$	144875	144764	111	1.139
$(^1G)z^2H$	9/2	99		146534	146430	104	0.911
	11/2	100		147647	147437	210	1.091
$(^3P)z^2S$	1/2	94		147652	147970	−318	1.922
$(^3P)z^4S$	3/2	98		147816	147975	−159	1.988
$(^1G)x^2F$	5/2	$92+6(^1D)^2F$		148663	148649	14	0.860
	7/2	$88+9(^1D)^2F$		147806	147893	−87	1.144
$(^1G)y^2G$	7/2	99		153609	153743	−134	0.891
	9/2	99		153808	153942	−134	1.110
$(^1S)^2P$	1/2	99			183398		0.667
	3/2	99			184608		1.333

TABLE 20. *Observed and calculated levels of* Zn III $3d^94p$

Name	J	Percentage	AEL	Observed	Calculated	O−C	Lande C.
$(^2D)z^2P$	0	100		141401	141285	116	
	1	97		140080	140060	20	1.480
	2	98		137876	138023	−147	1.493
$(^2D)z^2F$	2	96		142491	142405	86	0.688
	3	$71+26(^2D)^1F$		140664	140726	−62	1.068
	4	100		141335	141195	140	1.250
$(^2D)z^1F$	3	$67+18(^2D)^3F+12(^2D)^3D$	$(^2D)^3D$	144511	144544	−33	1.066
$(^2D)z^1D$	2	$62+34(^2D)^3D$	$(^2D)^3D$	145252	145451	−199	1.051
$(^2D)z^1P$	1	98		147505	147279	226	0.998
$(^2D)z^2D$	1	97		147577	147587	−10	0.521
	2	$61+37(^2D)^1D$	$(^2D)^1D$	147928	148015	−87	1.101
	3	$82+11(^2D)^3F+7(^2D)^1F$	$(^2D)^1F$	145974	146023	−49	1.283

TABLE 21. *Observed and calculated levels of* Ga III $3d^{10}4p$

Name	J	Percentage	AEL	Observed	Calculated	O−C	Lande C.
$(^1S)^2P$	1/2	100		65167	65254	−87	0.667
	3/2	100		66885	66798	87	1.333

This paper was supported in part by the National Bureau of Standards, Washington, D.C.

The author wishes to acknowledge with everlasting gratitude and appreciation the unremitting kind interest in this work by the late Professor Giulio Racah.

5. References

[1] Shadmi, Y., Bull. Res. Counc. of Israel, **10F**, No. 3, 109 (1962).

[2] Shimoni, E., M.Sc. Thesis, The Hebrew University of Jerusalem (1959).

[3] Hollander, S., M.Sc. Thesis, The Hebrew University of Jerusalem (1960).

312-248 O-68—6

[4] Abraham, B. Z., M.Sc. Thesis, The Hebrew University of Jerusalem (1961).
[5] Trees, R. E., Phys. Rev. **83,** 756 (1951); ibid., **84,** 1089 (1951).
[6] Racah, G., Phys. Rev. **85,** 381 (1952).
[7] Racah, G., Rydberg Centennial Conference, Lunds Univ. Arsskr. **50,** 31 (1955).
[8] Racah, G., Phys. Rev. **63,** 367 (1943).
[9] Racah, G., and Shadmi, Y., Phys. Rev. **119,** 156 (1960).
[10] Trees, R. E., and Jorgensen, C. K., Phys. Rev. **123,** 1278 (1961).
[11] Trees, R. E., Phys. Rev. **129,** 1220 (1963).
[12] Rajnak, K., and Wybourne, B. G., Phys. Rev. **132,** 280 (1963).
[13] Racah, G., and Stein, J., Phys. Rev. **156,** 58 (1967).
[14. Racah, G., Bull. Res. Counc. of Israel **8F,** No. 1, 1 (1959).
[15] Moore, C. E., "Atomic Energy Levels", NBS Circular 467, Vol. **I** (1949), ibid., Vol. **II** (1952).
[16] Iglesias, L., An. Real. Soc. Espan. Fis. Quim. (Spain), **58** (A), No. 7–8, 191 (1962).
[17] Racah, G., J. Quant. Spectrosc. Radiat. Transfer **4,** 617 (1964). Pergamon Press Ltd.
[18] Shenstone, A. G., J. Opt. Soc. Am. **44,** 749 (1954).

(Paper 72A5–518)

JOURNAL OF RESEARCH of the National Bureau of Standards—A. Physics and Chemistry
Vol. 72A, No. 5, September–October 1968

Electron Impact Excitation of Hydrogen Lyman-α Radiation

Robert L. Long, Jr.,*† Donald M. Cox,* and Stephen J. Smith**

Joint Institute for Laboratory Astrophysics††

(May 8, 1968)

An experimental investigation of electron impact excitation of the $2p$ state of atomic hydrogen is described. A beam of electrons was passed through a chopped beam of hydrogen atoms in a high vacuum apparatus. The modulated flux of Lyman-α photons emitted in the radiative decay of the $2p$ state was taken as a measurement of the excitation probability resulting from direct excitation plus indirect excitation resulting from cascading. The region surrounding the intersection of the two beams was electrically and magnetically shielded to prevent quenching of metastable $2s$ atoms and thereby to ensure that the observed Lyman-α flux resulted from decay of the short-lived $2p$ state. The experimental results are consistent with those obtained by Fite, Stebbings, and Brackmann [1959], and confirm the existence of a large discrepancy between theoretical and experimental results in the electron energy range below 50 eV.

Key Words: Atomic hydrogen; beams; electron impact excitation; experimental; high vacuum; Lyman-α.

1. Introduction

The scattering of electrons by hydrogen atoms is the simplest atomic scattering process and therefore a convenient prototype of scattering problems for light atoms. In addition, it is an important astrophysical process, particularly in stellar atmospheres. For these reasons it has earned much theoretical and some experimental attention [Moiseiwitsch and Smith, 1968; Burke and Smith, 1962]. The number of experimental investigations has been restricted primarily due to the difficulty of producing atomic hydrogen but these investigations are necessary for critical evaluation of the theoretical calculations.

Inelastic collisions of electrons with ground state hydrogen atoms can produce excited atoms in the $2p$ state which quickly decay to the ground state with the emission of Lyman-α (1216 Å, 10.2 eV) radiation:

$$\mathrm{H}(2p) \rightarrow \mathrm{H}(1s) + \text{Ly-}\alpha. \tag{1}$$

The primary process for production of H($2p$) is direct excitation:

$$e^- + \mathrm{H}(1s) \rightarrow e^- + \mathrm{H}(2p). \tag{2}$$

A significant number of atoms in the $2p$ state can also be produced by cascade processes:

$$e^- + \mathrm{H}(1s) \rightarrow e^- + \mathrm{H}(nl), \tag{3}$$

$$\mathrm{H}(nl) \rightarrow \mathrm{H}(2p) + h\nu, \tag{4}$$

where H(nl) represents any excited state that can spontaneously decay to the $2p$ state, by a direct or indirect route. The radiation $h\nu$ in eq (4), shown as a direct process, will be in a line of the Balmer series. An appreciable number of metastable $2s$ state hydrogen atoms are also produced by processes similar to those given in eqs (2), (3), and (4). The shape of the cross section for metastable production has been measured [Lichten and Schultz, 1959; Stebbings, Fite, Hummer and Brackmann, 1961; Hils, Kleinpoppen and Koschmieder, 1966]. Born approximation calculations suggest that the peak value of the $2s$ state excitation cross section is about one-fifth of that for the $2p$ state.

Measurements of the relative amount of Lyman-α radiation emitted in the decay of the H($2p$) atoms produced by electron collisions have been made [Fite and Brackmann, 1958; Fite, Stebbings and Brackmann, 1959; Chamberlain, Smith and Heddle, 1964; Williams, Curley and McGowan, 1968] primarily in order to obtain information about the cross section for the direct excitation of H($2p$), as given in eq (2). A difficulty arises in the interpretation of the measure-

*Supported by NSF Grant No. 5959.
†Current Address: Sandia Laboratory, Albuquerque, N.M. 87115.
**Staff Member, Laboratory Astrophysics Division, National Bureau of Standards, and the University of Colorado Campus, Boulder, Colorado 80302.
††Of the National Bureau of Standards and University of Colorado.

ments because of the cascade processes (eqs (3)-(4)) that also yield H($2p$) atoms. However, the situation is fairly simple in two energy regions:

1. At energies below the threshold for excitation of the $n=3$ states of hydrogen (12.1 eV), no cascade processes can occur and the excitation of the H($2p$) state can be observed directly.

2. At electron energies greater than 100 eV, Born approximation calculations of electron-hydrogen atom excitation are believed [Silverman and Lassettre, 1966] to be reasonably accurate and cascade corrections can be estimated. Furthermore, the calculated cascade contribution [Moiseiwitsch and Smith, 1968] is only about 2 percent of the total Lyman-α radiation for electron energies in the neighborhood of 200 eV. The intermediate range of 12.1 to 100 eV is complicated by larger cascade components.

The first measurements of the electron impact excitation of Lyman-α photons emitted from the $2p$ state of atomic hydrogen were carried out by Fite and his collaborators [Fite and Brackmann, 1958; Fite et al., 1959]. Using a modulated crossed beam technique and observing the Lyman-α photons resulting from excitation in a field free region, to avoid quenching of $2s$ atoms, they obtained a relative cross section, including cascading, with confidence limits stated as being about ± 12 percent. These measurements, even with the relatively large assigned errors, have played a very important role because they depart quite significantly from theoretical results for direct $2p$ state excitation in the energy range below about 70 eV. It is not possible to explain the departures in terms of cascading.

A series of elaborate close coupling calculations was undertaken [Burke, 1963; Burke, Schey, and Smith, 1963] by P. G. Burke and his associates with limited success at narrowing the gap between theory and experiment. The difference remains very large in the first 20 v above threshold.

This paper describes a program undertaken with the objectives of verifying and improving on the H($2p$) excitation measurements of Fite et al. The work described here is the development of measurement technology and the effort to improve that technology to the point that results accurate to within a few percent might be made available for a critical test of the ability of theory to accurately predict properties of the simplest atom.

A detailed description of the apparatus is presented in section 2. This is followed by an outline of the procedures for data acquisition and reduction in section 3. Some results and a discussion of accuracy are given in section 4. Discussion of the current experimental data and some of the theoretical calculations appear in section 5.

2. Experimental Apparatus

The measurement used the high-vacuum crossed beam method, shown schematically in figure 1, involving a chopped atomic beam (D) of hydrogen

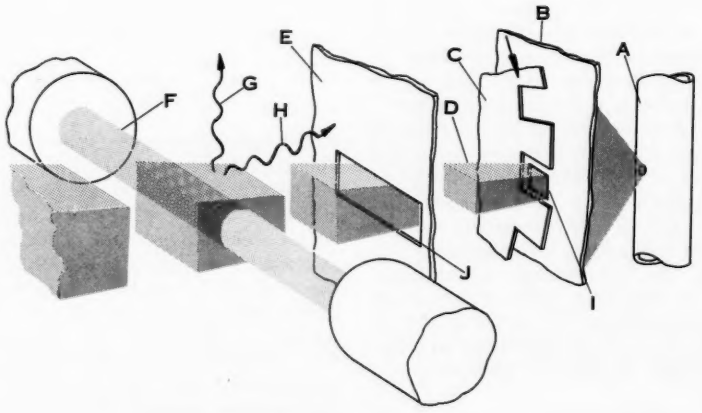

FIGURE 1. *Schematic diagram of the crossed beam configuration.*

A—the 4.8 *mm* I.D. tungsten dissociator with a 0.8 *mm* hole to permit the emission of gas; B—the bulkhead to the source chamber, which mounts the 2.5 *mm* × 2.5 *mm* field aperature (I) at a distance of 4.6 *cm* from the source, to define the atom beam (D); C—the chopping wheel consisting of twenty teeth on a wheel rotated at 5 revolutions per second; E—the bulkhead to the buffer chamber, with a differential pumping aperature (J) which plays no part in defining the atom beam; F—the electron beam which intersects the chopped atom beam at a point 9.5 *cm* from the source, to excite photons which are detected by means of ionization chambers placed to intercept emission in particular directions (G and H) perpendicular to the atom beam axis.

gas which was intersected at right angles by an electron beam (F). A fraction of the Lyman-α photons which were emitted in a particular direction, such as perpendicular (G) to the plane containing the electron and hydrogen beams was detected in an ionization chamber. The relative Lyman-α production cross section, $Q_\perp$, was given by

$$Q_\perp = (S - S_0)/IP, \tag{5}$$

where S is proportional to the ion chamber current during Lyman-α production, S_0 is proportional to the apparent ion chamber current without Lyman-α production, I is the total electron current, and P is a pressure proportional to the hydrogen atom beam intensity.

2.1. Vacuum System

The apparatus was a fairly conventional atomic beams machine (see fig. 2). The vacuum chamber was divided into three compartments (by bulkheads as shown in fig. 1 and fig. 2b): a source chamber, which was pumped by a 70 liter/sec (l/s) diffusion pump and by a titanium sublimator; a buffer chamber, also pumped by a 70 l/s diffusion pump; and an interaction chamber, which was pumped by a 600 l/s diffusion pump. Mercury, instead of oil, diffusion pumps were chosen to minimize potential sources of background hydrogen gas and to avoid possible deposition of undesirable insulating films on the electron gun structure. A water-cooled baffle and a liquid nitrogen-cooled trap were used above each diffusion pump to prevent mercury vapor from entering the system. A sorbent trap was installed in the foreline to catch organic vapors from the forepump. Welded stainless steel construction was used wherever feasible and connections were made with metal gaskets. These measures enabled low pressure, less than 4×10^{-8} torr (nitrogen equivalent), to be maintained in the interaction chamber with pressures of about 1×10^{-7} and 1×10^{-6} torr in the intermediate and source chambers, respectively, while hydrogen gas was flowing into the system. The base pressure in the interaction region was as low as 1 or 2×10^{-8} torr. No baking of the chamber was employed except for mild outgassing of the titanium deposition surface.

2.2. Atomic Beam

The hydrogen atoms were produced by thermal dissociation of molecular hydrogen gas. This method is preferable to some others, e.g., radio frequency discharge dissociation, because no excited atoms are produced. Also under the assumption of thermal

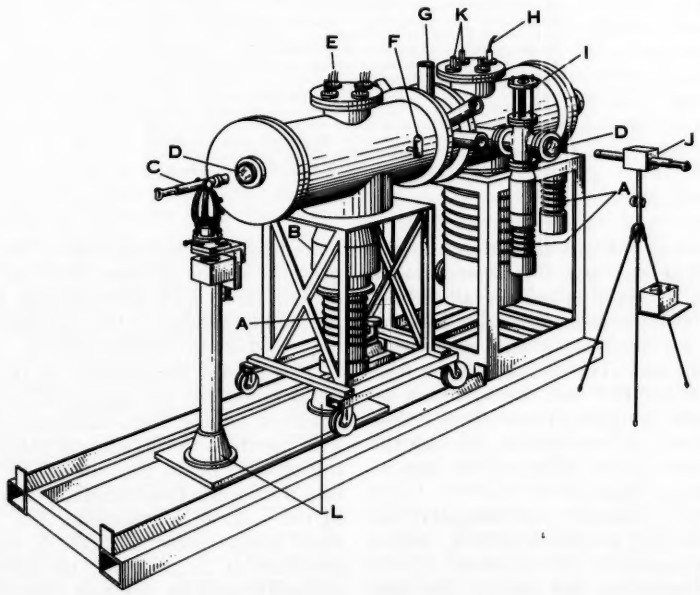

FIGURE 2a. *Hydrogen beam apparatus.*

A—mercury vapor diffusion pumps; B—liquid nitrogen cooled trap; C—alignment telescope (on the hydrogen beam axis); D—windows; E—electrical feed throughs; F—ionization type vacuum gauge (three vacuum gauges are utilized: one as shown, one for the hydrogen source chamber and one for the chopper chamber); G—shielded electrical feedthroughs for the Lyman-α detectors and electron gun current measurement; H—hydrogen gas inlet; I—valve for mercury diffusion pump; J—optical pyrometer (views the furnace); K—heavy copper feedthroughs for furnace power; L—fixed base for alignment telescope.

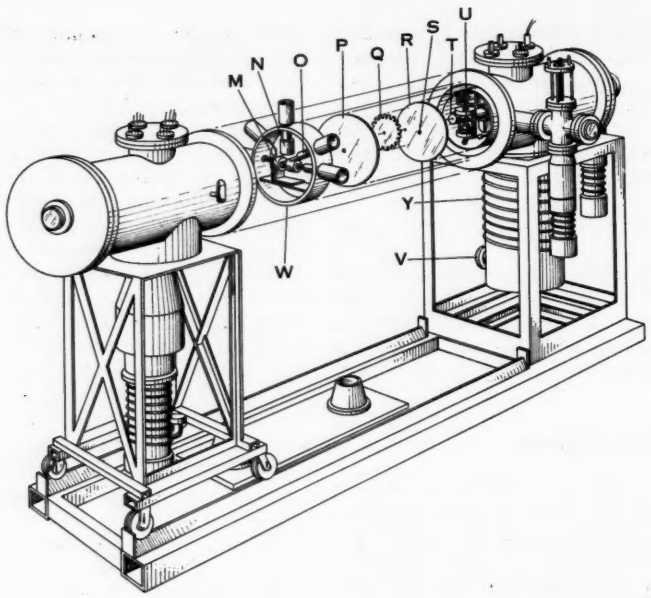

FIGURE 2b. *Hydrogen beam apparatus (expanded view).*

M—electron gun; N—Lyman-α photon detector positioned at ninety degrees with respect to the electron beam; O—Lyman-α photon detector positioned at thirty degrees with respect to the electron beam; P—partition to separate chopper (buffer) chamber and interaction chamber ("second partition"); Q—Chopper wheel; R—partition to separate chopper chamber and hydrogen source chamber ("first partition"); S—collimating slit for hydrogen beam ("field aperture"); T—chopper wheel driveshaft (a synchronous motor and gear train mounted outside the vacuum chamber is magnetically coupled through the rear flange to drive the chopper); U—tungsten furnace and support structure; V—header for titanium sublimation pump; W—removable stainless steel ring which supports the Lyman-α detectors and electron gun (the mechanism for positioning the ring is not shown; soft aluminum gaskets cut from sheet stock are used between knife edges machined on the ring and the main system to effect a vacuum seal); Y—casing for titanium sublimation pump.

equilibrium, an estimate of the absolute atomic beam intensity is possible. The gas was introduced into a glass plenum through a silver-palladium alloy leak [Hunter, 1960; Young, 1963] in order to purify the ordidary tank hydrogen gas used and was piped into a tubular tungsten furnace. The furnace tube was made from tungsten foil, 0.013 mm thick, rolled up on a mandrel, 4.8 mm in diam, four layers thick. A hole, 0.8 mm in diameter, was drilled through the wall of the tube at its center, allowing the gas to flow out into the source chamber.

In order to dissociate hydrogen, the tungsten furnace was resistance heated to about 2500 K with a direct current of approximately 125 A (about 425 W of power was required including line losses). The temperature was measured with an estimated accuracy of ± 15 K by means of an optical pyrometer which viewed the side of the furnace near the exit hole. Corrections for the emissivity of tungsten [Kohl, 1960; Poland, Green and Margrave, 1961] and window transmission [Foote, Fairchild and Harrison, 1921] were applied. The furnace pressure was estimated from measurements of the molecular hydrogen pressure at the plenum near the silver-palladium leak (a calibrated high pressure ion gauge was used) and the conductances of the tubulation leading to the furnace and of the furnace exit.

The lateral dimensions of the atomic beam were determined by the square (2.5 mm × 2.5 mm) field aperture in the first bulkhead (see figs. 1 and 2b). The aperture in the second partition did not collimate the atomic beam but served to reduce the gas flow into the interaction chamber from the background gas in the volume surrounding the furnace. With a furnace temperature of 2500 K and a typical furnace pressure of 25 millitorr, the calculated atomic beam intensity passing through the field aperture, assuming effusive molecular flow from the furnace, was 9.85×10^{13} atoms sec^{-1}. The atomic beam cross section of uniform density at 9.5 cm from the furnace exit, where the electron beam axis intersects the atomic beam axis, was 4.6 mm × 4.6 mm; and the average atom density there in a fully dissociated beam would be 2.2×10^{8} atoms cm^{-3}.

2.3. Chopper

The atomic beam chopper was located in the intermediate chamber of the vacuum system. The chopper was a toothed wheel which was rotated by a synchronous electric motor so that the teeth interrupted the beam 100 times per second with a duty cycle of 0.5. This enabled the use of a narrow band, a-c amplifier for the photon signal. The detection bandwidth was further reduced by using synchronous demodulation of the a-c signal. The reference signal was derived from a photocell that viewed a beam of light which also was interrupted by the atomic beam chopper. Such a-c techniques have the advantage of greater gain stability than would be possible with a d-c amplifier: lower electronic noise than a wide band amplifier, and elimination of the undesired, unmodulated photon signals produced in collisions of electrons with the hydrogen background gas or the electron gun electrodes.

2.4. Electron Gun Structure

A cross sectional diagram of the electron gun, Faraday cage, and retarding potential analyzer is shown in figure 3. The source of electrons was an indirectly heated, impregnated cathode (Phillips type BP-1B),[1] electrode W. It acted as the first element of a Soa-type acceleration stage [Simpson, 1961] which also included the grid, electrode F, and the anode, electrode G. This stage was followed by a lens consisting of a second plate at anode potential, electrode H, and the grounded electrode I which focused the electrons into the Faraday cage (electrodes L and M). This lens was operated as a decelerating lens for cathode potentials $\leqq 90$ V, where the anode-cathode potential difference was not inconveniently large, and as an accelerating lens for cathode potentials $\geqq 70$ V. The overlap at 70 to 90 V in these two modes was used to test whether results were independent of focusing mode; gross disagreement occasionally observed between the two modes could be eliminated by cleaning the gun electrodes and was evidently due to surface charging effects. The cathode holder was made of stainless steel, electrodes F and G were molybdenum, and the remaining electrodes were gold plated Advance or stainless steel.

The electron beam axis intersected the atomic beam axis in the interaction region between electrodes J and K. The interaction region was enclosed by gold plated nickel mesh, approximately 85 percent transparent, supported by a rectangular framework fastened to the grounded electrode J. The mesh provided shielding against electric fields from the high voltage leads to the ion chamber and the electron gun, thereby preventing disturbance of the electron beam and electric quenching of the metastable hydrogen atoms in the $2s$ state. The quenching, which can be significant for fields as low as 1 V cm^{-1} [Luders, 1950], would result in Lyman-α photons indistinguishable from those produced by excitation of the $2p$ state. Maximum space charge fields were a few tenths of a volt per centimeter at threshold for currents used (see fig. 4) assuming a 1 mm beam radius at the interaction region. These fields would reduce the mean life from 1/7 s in field free space to about 10^{-2} s. The atoms spend less than 10^{-4} s in the interaction region. Magnetic field quenching of the metastable atoms was prevented by a magnetic shield installed around the electron gun structure, which gave a residual field of less than 10 mG. Thus the metastable atoms drifted out of sight of the photon detector before decaying.

The apertures in electrodes H through J were 2.4 mm in diameter to ensure that all of the electron beam passed through the umbra of the larger atomic beam and that it then entered the Faraday cage. A guard electrode (K) with an aperture 4 mm in diameter was mounted in front of the Faraday cage (aperture 5 mm) to detect any excessive spread in the electron beam diameter. The electron beam focus, controlled by the potential difference between the anode and cathode of the electron gun for each cathode potential, was selected by obtaining near minimum guard electrode current and near maximum Faraday cage current. The potential of the grid controlled the magnitude of the total current and was 1–3 V positive with respect to the cathode, depending on the amount of current desired. For currents less than 10 μA, the guard current was less than 0.3 percent of the Faraday cage current at cathode potentials greater than 14 V. It was at most one or two percent of the Faraday cage current at 9 eV, but was critically dependent on the primary current. Evidently the effect at low energy is a space charge limitation. All currents were measured with low impedance meters, so that the electrodes were less than 8 mV from ground potential, in order to minimize stray electric fields.

Approximate calculations of the focusing properties of the electron gun showed that the focus of the electron beam occurred inside the Faraday cage for both focusing modes. These calculations also indicated that the electron path length through the hydrogen beam for the extreme electron trajectories differed by no more than 1/4 percent from a path parallel to the axis for the two focusing modes. Any larger disagreement between signals from the two different focusing modes for the same electron energy should therefore be caused by some other effect.

The Faraday cage which was used to collect the electron current was composed of electrodes L and M and the electrodes immediately beyond them. No magnetic field was used to collimate the electron beam so the reflection of the incident electrons from the rear of the cage is assumed to be approximately diffuse. The probability of reflected and secondary electrons escaping from the cage was small because the solid angle subtended by the entrance aperture at the rear of the cage was only about 0.01 sr. There-

[1] Certain commercial materials are identified in this paper in order to adequately specify the experimental procedure. In no case does such identification imply recommendation or endorsement by the National Bureau of Standards, nor does it imply that the material identified is necessarily the best available for the purpose.

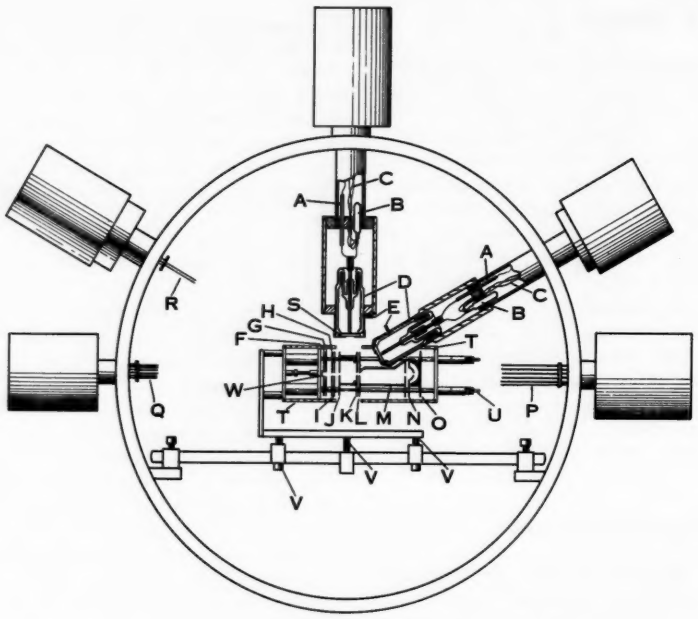

FIGURE 3. *Cross-sectional view in the plane of the electron beam axis and perpendicular to the atom beam axis.*

The inside diameter of the ring is 16 in. A, B, and C show elements of the input stages of the low noise preamplifiers sealed into bulkheads near the ionization chambers (D) for minimum stray input capacitance. The grid of the input tube (B) is operated near ground potential with d-c feedback through a 10^{10} Ω resistor (A). The ion chamber voltage (~ -550 *V*) is applied to a cylindrical electrode consisting of a platinized layer on the inside of the glass shell connecting to leads E. The electron gun, consisting of cathode W and electrodes F through O, is discussed in the text (Section 2.4). Leads in the multiple feed-through P are connected to electrodes K, L–M–N, and O for current measurements using high impedance electrometers. Feedthrough Q is used for applying electron gun and ionization chamber voltages. Feedthrough R is used for the gun cathode heater, S identifies a MgF_2 window which provides the short wavelength cut-off of the detector. T identifies magnetic shields, U the steel rods on which the gun is assembled using glass tubing as insulators and spacers, and V the leveling screws used to align the gun.

fore the current collection efficiency of the cage was high for all electron energies used.

The eccentric shape of the cylindrical part of the Faraday cage was provided to allow mounting of an ion chamber at an angle of 30° from the axis of the electron beam. This detector, installed in addition to the one at 90°, is intended for use in measurements of the angular distribution of Lyman-α photons. Sectors were cut out of both electrodes K and L to allow this chamber to view the interaction region. In order to prevent consequent stray electric fields in that region, wire mesh was fastened across the aperture in electrode L.

The rear electrode of the Faraday cage had a hole 1 mm in diameter at its center which allowed a small percentage of the electron current to pass into the hemispherical retarding potential analyzer [Simpson, 1961]. This analyzer was composed of electrodes N and O (see fig. 3) and had a design resolution, $\Delta E/E$, of 0.25 percent. The energy distribution could be measured at any cathode voltage by a modulated retarding potential technique [Leder and Simpson, 1958]. The full energy width at half maximum of the distribution was 0.3 to 0.5 eV, depending on the state of the cathode. The energy of the peak of the measured distribution (i.e., the most probable electron energy) was taken to be the effective electron beam energy in the interaction region. This assumption led to values for the threshold energy for production of Lyman-α photons within 0.15 eV of the spectroscopic value (10.2 eV). The retarding potential at which the peak occurred was about 1.5 V lower than the applied cathode potential; this difference was attributed to contact potentials. The instantaneous value of the contact potential depended upon the previous history of the system and whether or not hydrogen gas was flowing but it varied less than 50 mV during a day, after equilibrium with flowing hydrogen was achieved. Data taken on different days, with identical applied voltages, may have had somewhat different

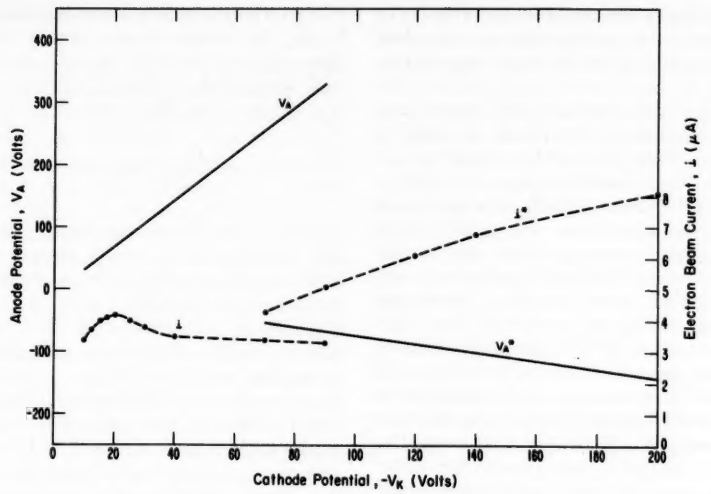

FIGURE 4. *Typical values of anode potentials (V_A), relative to laboratory ground, as a function of negative cathode potential ($-V_K$).*

The electron gun anode was programmed to these voltages in order to maintain desired focal properties as the electron beam energy was changed. Corresponding electron currents were those observed in taking the data summarized in table 2. The unstarred values are in the decelerating lens mode and starred values are in the accelerating lens mode (see text, sec. 2.4).

average contact potentials. The energy scale accuracy is estimated to be about ± 0.2 eV. The calibration of the cathode voltage power supply was checked by a digital voltmeter and did not change more than 0.15 percent. The electron energies for the data presented in section 4.2. were corrected both for the average contact potential and for deviation of the cathode power supply from the nominal, programed voltage.

All measurements of the total electron beam current were made with the two retarding potential electrodes connected to the Faraday cage current meter. The best gun operation was obtained for electron beam currents less than 10 μA but currents larger than 30 μA could be obtained, especially at the higher cathode potentials. In figure 4 are shown electron gun operating voltages and current yields typically used in a measurement.

2.5. Lyman-α Detector

Photons produced at the junction of the electron and hydrogen atom beams were detected by an ion chamber located on an axis perpendicular to the plane containing the crossed beams. The entrance aperture to the ion chamber was limited by a metal cap with an opening 6.9 mm $\times$ 19 mm, the longer dimension being perpendicular to the electron beam axis. Wire mesh about 85 percent transparent was stretched across this opening for electric shielding. Since this cap was 32 mm from the electron beam axis and its opening was centered on the intersection of the beams, photons from the center of the interaction volume could enter the ion chamber if they came off at 84° to 96° away from the electron beam axis within an azimuthal range of 33°. (The threshold data presented in sec. 4.1. were taken with the face of the detector mounted 16 mm from the interaction volume center. Therefore, the angles were larger in that experiment.) Metal strips were fastened to the top of the interaction region enclosure to leave an opening there of the same size as, and centered on, the opening in the ion chamber. These shields reduced the possibility of detecting photons emanating from regions other than the junction of the atom and electron beams, especially reflected photons, thereby preserving the angular resolution of the measurement and minimizing the background.

The front window of the ion chamber was required to transmit the 1216 Å Lyman-α radiation. Originally cleaved LiF (1.5 mm thick) was used but later (see sec. 4.2) polished MgF_2 (1 mm thick) was used. Both materials were obtained from the Harshaw Chemical Company. Care was taken to select pieces expected to have transmissions least dependent on light polarization, since the polarization of the Lyman-α radiation changes with electron energy [Percival and Seaton, 1958; Ott, Kauppila, and Fite, 1967]. The window had a clear diameter of about 16 mm and was cemented to the glass body of the ion chamber with low vapor pressure epoxy cement. The inner surface of the body was platinized to provide the negative electrode. The central tube (see fig. 3) was the electron current collector. A grounded Kovar ring was installed interrupt-

ing the glass envelope between the two electrodes in order to reduce leakage current to the center electrode, which was operated at very high impedence near ground potential.

The ionizing gas used in the ion chamber was nitric oxide, which has an ionization threshold of 1340 Å [Carver and Mitchell, 1964]. Since the cutoff wavelength of the LiF (or MgF_2) window was at 1050 Å (or 1130 Å), [Heath and Sacher, 1966], this provided a detector which was sensitive over only a 290 Å (or 210 Å) band approximately centered on the wavelength of interest. Therefore, the ion chamber was insensitive to the radiation of all atomic hydrogen lines except Lyman-α. However, some of the radiation produced by excitation of the small fraction of H_2 molecules in the atomic beam was within the bandwidth of the detector; the amount of this contribution was calculated from data taken with a pure molecular beam, as described in section 3, and could be subtracted from the atomic plus molecular data.

In order to fill the ion chamber with pure nitric oxide gas, it was connected to a gas handling system through its central tube and pumped out by an oil diffusion pump having a liquid nitrogen-cooled trap. Prior to filling the chamber, a pressure of less than 8×10^{-8} torr was indicated by an ion gage in the gas handling system. Then the diffusion pump was valved off and nitric oxide gas was introduced into the chamber to a pressure of 15 ± 1 torr, as indicated by a mercury manometer trapped by a slush of ethyl alcohol and liquid nitrogen. After initial testing of the ion chamber with ultraviolet light from a hydrogen rf discharge lamp, the copper filling tube was pinched off to seal and disconnect it from the gas handling system. Further testing was done after it was installed in the apparatus.

The ion chamber was operated in the proportional counter mode. The gas gain, given by the ratio of the ion current with the body electrode at -550 V to that at -50 to -150 V (the latter range was roughly a plateau, cf. Carver and Mitchell [1964] fig. 5), was about 65. The photon intensity was measured relatively by monitoring the ion current in the chamber with an electrometer tube preamplifier [Smith and Branscomb, 1960] having an effective input impedance of 10^8 Ω and a voltage gain of about 30. The first stage tube and the grid resistor of the preamplifier were mounted inside the vacuum system in order to minimize the input capacitance so that the gain at 100 Hz, the frequency at which the atomic beam was chopped, would be maximized. The a-c output of the preamplifier was further amplified and then synchronously demodulated (cf. sec. 2.3).

Typical operating parameters for the ion chamber are indicated in the following estimate of the magnitude of the output current. Earlier measurements [Fite and Brackmann 1958; Fite et al., 1959] of the Lyman-α production cross-section shape gave $Q_\perp = 0.8\pi a_0^2$ near the peak, when normalized to the Born approximation at high energy. From dimensions given above, the entrance aperture of the ion chamber subtends a solid angle (Ω) of 0.13 sr and the effective electron path length (d) in the atomic beam is 0.54 cm. Using the atomic beam density (n_a) of 2.2×10^8 cm^{-3} given in section 2.2., an electron current (I) of 5μA, and assuming isotropic radiation, the photon intensity incident on the detector is

$$S = n_a d \frac{I}{e} Q_\perp \Omega/4\pi = 2.6\times10^3 \text{ photons sec}^{-1}$$

where e is the electronic charge. The transmission of the LiF window for Lyman-α photons [Heath and Sacher, 1966] is about 0.69 (about 0.65 for the MgF_2 window) and of the wire mesh in front of it is 0.85. The fraction of transmitted photons absorbed in the 2 cm active length of nitric oxide gas at 15 torr is 0.91, using the measured value of 65.4 cm^{-1} for the absorption coefficient [Watanabe, Matsunaga, and Sakai, 1967]. Taking the photoionization yield of nitric oxide at Lyman-α to be 0.81 [Watanabe, et al., 1967] and the gas gain of 65, the ion chamber current for the above photon intensity would be 1.1×10^{-14} A. The output of the preamplifier for this input current would be 34 μV, which could be readily amplified to the level required for measurement.

2.6. Alinement

In order to obtain a well defined atomic beam and ensure that the electron beam axis crossed it at the proper location, careful alinement of the apparatus was necessary. A jig transit was positioned with its optical alinement axis centered on the field aperture in the first partition (see fig. 2) and approximately parallel to the axis of the vacuum chamber. This partition was then removed and the furnace tube was installed with the exit hole centered on the alinement axis. The furnace position could be maintained by means of a vertical screw drive to within 0.25 mm in order to compensate for thermal motions. The first partition was then replaced, the transit alinement was readjusted if necessary, the atomic beam chopper and the second partition were installed, and the second aperture was centered on the alinement axis. The ion chamber was alined with machinist's gages to an axis through the mechanical center of the ring assembly. The ring was then positioned and clamped on the fixed part of the vacuum chamber with the ion chamber axis vertical so that the center of the ring coincided with the alinement axis. The electron gun axis was alined by means of its support screws to be level, and to intersect the alinement (i.e., atomic beam) axis and the center line of the ion chamber. The accuracy of the intersection of these three axes is estimated to be within 0.25 mm. The accuracy of the 90° angle between the electron beam and the ion chamber axis is estimated to be within 0.5°. Some movement of the electron gun was noticed when the gun cathode was heated but this was minimized by a clamp on the end of the gun structure and could be compensated by moving the furnace tube in the opposite direction.

3. Data Acquisition and Reduction

A demodulated photon signal, obtained as described in sections 2.3 and 2.5, is noisy due to statistical fluctuations (shot-noise) in the small photon flux and due to electrical noise from the amplifiers. The electrical noise is predominately due to sources in the preamplifier grid circuit [see Smith and Branscomb, 1960]. The most important of these are thermal noise in the 10^{10} Ω input resistor, shunted by 5 to 10 pF of stray and grid capacitance, and shot noise in the grid current of the first preamplifier tube. These two sources are comparable and are roughly equivalent to a noise current of a few times 10^{-16} A in a 1/10 Hz bandwidth. As a first step in reducing the effects of noise, the photon signal (S) was integrated for 10 s by an operational amplifier with a capacitor feedback element and the integrated voltage, $\int S dt$, was recorded. The Faraday cage current (I) was integrated simultaneously, although drift was usually negligible during a measurement. After recording these data at one cathode potential, the automatic programer which was used to set the electron gun voltages advanced to its next position. Following a delay of about 10 s to ensure electron beam equilibrium, the next integration was started. The sequence of preselected cathode voltages could be repeated as many times (typically 60 in 1 day) as desired. This frequent repetition of short observations was used to eliminate the effects of any possible long term drifts.

The integrated data, together with elapsed time, furnace temperature, cathode potential, and other information, were recorded automatically by a data acquisition system on punched paper tape. The punched paper tape was later used to generate punched cards which were convenient for manual editing of the data before reducing them with a digital computer.

In order to determine the baseline for the relative photon intensity measurements, data were taken during each cathode voltage sequence at an electron energy of about 8.5 eV, which was too low to produce photons with energy sufficient to ionize the nitric oxide in the ion chamber. Scatter in the baseline data, from electronic noise, was comparable to that which occurred in the Lyman-α signals at the higher energies. The average of all the integrated signals taken at 8.5 eV, $\int S_0 dt$, was designated the zero signal level and was subtracted from all the integrated photon signals to give values which were directly proportional to the Lyman-α photon intensity. If the 8.5 eV data appeared to have a significant time dependence, such as may arise from drift in the demodulator bias, they could be fitted to a straight line by the least squares method and a time dependent zero correction could then be made. The magnitude of the signal integral was checked periodically with the low level a-c preamplifier disconnected. This essentially noise-free signal always agreed with the average obtained for $\int S_o dt$ within statistical errors.

The linearity of the current meter was checked using a Keithley model 261 picoampere source and corrections to the integrated current values were made, if necessary, by adding (or subtracting) a value (which always corresponded to the integral of less than 0.03 μA) to each current integral. Since this correction was effectively a zero correction, it could be represented by the term $\int I_0 dt$ which was defined above. This gave integrated current values which were linear within 0.5 percent over the range of measurements.

The data acquisition system was zeroed and calibrated before taking data each day; when checked after taking data, no significant changes were detected. Parameters that were monitored periodically during the day were the feedback voltage of the battery powered ion chamber preamplifier, the zero setting and emission current of the hydrogen gas plenum pressure gage circuit, the electron beam energy distribution, the electron gun contact potential, the zero level of the electron current integral, the photon signal demodulator output bias, the furnace temperature, and the positions of the furnace and electron gun.

The relative cross section, $Q_\perp$, for production of Lyman-α photons (including possible radiation from the small H_2 molecular component of the atomic beam) emitted perpendicular to the electron beam was given by the formula

$$Q_\perp(H+H_2) = \{\int S dt - \int S_0 dt\}/P_p\{\int I dt - \int I_0 dt\}$$
$$= \int S dt/P_p\{\int I dt - \int I_0 dt\} - \int S_0 dt/P_p\{\int I dt - \int I_0 dt\}. \quad (6)$$

Here P_p is the average plenum pressure (in millitorr) indicated by the gas manifold gage (held constant to within ±1 percent by adjusting the temperature of the silver-palladium leak). The other symbols were defined above. The ratios in eq (6) were computed from the data of each ten second integration and the individual relative values of $Q_\perp$ were calculated. All those values of $Q_\perp$ for the same electron energy (i.e., gun cathode potential) taken in one day then were averaged together. The standard deviation of each resulting average $Q_\perp$ was given by the square root of the sum of the squares of the statistical standard deviations of the two averaged ratios in eq (6), which were computed in the usual manner [Beers, 1957].

The contribution of the molecular component of the atomic beam was estimated from data taken with the furnace at several temperatures too low to produce dissociation, i.e., with a 100 percent molecular beam. Data were taken above 1000 K for comparison with those taken at room temperature. The two results were consistent in shape and magnitude when corrections for the pressure and temperature differences were made. The molecular contribution correction to be applied for each electron energy was calculated by use of the formula

$$\int S_M(T) dt = \left\{\int S_M(T_r) dt - \int S_M(T_r)_0 dt\right\}$$
$$\{(1-\gamma) n_F(T)/n_F(T_r)\}$$
$$\cdot \{\overline{v_M(T)}/\overline{v_M(T_r)}\} \cdot \{\overline{v'_M(T_r)}/\overline{v'_M(T)}\}. \quad (7)$$

Here T is the temperature of the furnace used in the measuring of the quantities in eq (7), $S_M(T)$ is the estimated photon signal due to H_2 molecules with the furnace at absolute temperature T, $S_M(T_r)$ is the average photon signal measured at a given electron energy with the furnace at room temperature $T_r(\cong 295$ K), $S_M(T_r)_0$ is the corresponding zero correction, $n_F(T)(1-\gamma)$ is the molecular density inside the furnace at temperature T and with the gas plenum pressure P_p used in measuring $Q_\perp(H+H_2)$, $n_F(T_r)$ is the molecular density in the furnace at room temperature, $\overline{v_M(T)}$ and $\overline{v_M(T_r)}$ refer to mean molecular velocities inside the furnace, $\overline{v'_M(T)}$ and $\overline{v'_M(T_r)}$ refer to the mean molecular velocities in the atom beam, and γ is the estimated fractional dissociation of hydrogen at the temperature T and pressure $P_F(T)$. The factors

$$\{(1-\gamma)n_F(T)/n_F(T_r)\}\cdot\{\overline{v_M(T)}/\overline{v_M(T_r)}\}$$

allow for the temperature dependence of the effusion rate of the molecules from the furnace and the factor $\{\overline{v'_M(T_r)}/\overline{v'_M(T)}\}$ allows for the dependence of the excitation probability on molecular velocity. Since the molecular mean velocities are proportional to the square root of the furnace temperature T, the velocity ratios cancel. Defining pressure in terms of density through the ideal gas law $P_F(T)=(1+\gamma)n_F(T)kT$, eq (7) can be simplified to

$$\int S_M(T)dt=\left\{\int S_M(T_r)dt-\int S_M(T_r)_0dt\right\}\cdot\{(1-\gamma)P_F(T)T_r\}/\{(1+\gamma)P_F(T_r)T\} \quad (8)$$

where $P_F(T)$ is the total pressure due to atoms and molecules in the furnace at temperature T.

The estimation of $P_F(T)$ from the pressure P_p in the plenum is based on a measurement of the total conductance from the rate of decay of pressure in the plenum, at the operating pressure, and calculation of the conductance of the furnace orifice from the geometry and the assumptions of ideal gas behavior. This permits a determination of the conductance of the tubulation leading to the furnace.

The estimation of γ is described in the appendix. It is based on the assumption of thermal equilibrium. It is not possible to make a conclusive statement as to the validity of the assumption, but the evidence indicates that it is useful as the basis for approximate calculations. The mean-free-path of molecular hydrogen [Dushmann, 1962] at 25 millitorr is comparable with the 2.4 mm radius of the furnace, but short compared to its length, so that an atom or molecule should be contained within the central hot section of the furnace but should make frequent wall collisions. Investigations of the interaction of hydrogen with tungsten surfaces [e.g., Hickmott, 1960] indicate that there is a substantial molecular sticking probability (~ 0.05) not very dependent on temperature, and that atomic hydrogen is evaporated from the surface at a rate consistent with equilibrium thermodynamics.

The velocity of gas flow is negligible compared to the atom velocities and therefore would not interfere with the effectiveness of wall collisions in establishing equilibrium.

Indirect evidence of approach to thermal equilibrium lies in the observation that the Lyman-α signal saturates rapidly as the temperature rises above 2000 K. Similar observations were noted by Lockwood and Everhart [1962] in connection with charge exchange between protons and hydrogen in a tungsten furnace.

The correction $C(H_2)$ to $Q_\perp(H+H_2)$ as given by eq (6) is

$$C(H_2)=\int S_M(T)dt/P'_p\left\{\int I'dt-\int I'_0dt\right\} \quad (9)$$

where the values of the current I' and I'_0, are those registered during the measurement of

$$\left\{\int S_M(T_r)dt-\int S_M(T_r)_0dt\right\},$$

and P'_p is the average value of the plenum pressure. As in the application of eq (6) the ratios of the photon signal to electron current and plenum pressure were computed for each integration and the average of all the ratios for the same electron energy was used to calculate $C(H_2)$ for each electron energy. The cross section for production of Lyman-α radiation from hydrogen atoms alone is then

$$Q_\perp(H)=Q_\perp(H+H_2)-C(H_2). \quad (10)$$

This procedure of subtracting two sets of relative data is only convenient if the apparatus used for the two measurements is identical (including the gains of the amplifiers), as was the case in the present work.

Since the calculation of $C(H_2)$ is not very accurate due to the uncertainties in P_F and γ and the possible effect of thermal excitation of the molecules on the cross section, the data used in calculating $Q_\perp(H+H_2)$ were taken under conditions of furnace temperature and pressure where the molecular concentration in the atomic beam was estimated to be less than 5 percent. This resulted in $C(H_2)$ being only a few percent of $Q_\perp(H+H_2)$. Since $Q_\perp(H)\cong Q_\perp(H+H_2)$, even a 100 percent error in $C(H_2)$ could not alter the value of $Q_\perp(H)$ more than 2 percent.

The energy dependence of $C(H_2)$ is, of course, the same as for a relative cross section $Q_\perp(H_2)$. From the relative values of $C(H_2)$ as given by eq (9) and of $Q_\perp(H)$ as given by eq (10), it is possible to determine the ratio of the atomic to the molecular cross sections by taking account of the relative densities of atoms and molecules in the beam at the temperature T used in eq (7). Since, as stated above, the effects of relative velocities on the relative effusion rates and on the relative beam densities of the two components cancel, the ratio of densities in the beam is the same as in the furnace and may be stated in terms of the dissociation fraction γ at temperature T, assuming thermal equilibrium as in all this discussion. The significance of the molecular cross section is rather arbitrary since it is determined by the band pass of the Lyman-α detectors.

4. Results

4.1. Threshold Data

The first investigation conducted with the apparatus described was of the threshold behavior of the Lyman-α production cross section. The results have been published [Chamberlain et al., 1964; Moiseiwitsch and Smith, 1968] and are included here in figure 5 for completeness.

Since the electron energies used in that work were less than the threshold for production of radiation in the band of sensitivity of the photon detector (1050 to 1340 Å) from H_2 molecules, which was about 1.4 eV above the Lyman-α energy of 10.2 eV, several advantages ensued:

(1) The results were independent of the degree of dissociation of the hydrogen beam. Of course, high dissociation was desired to obtain appreciable photon intensities.

(2) Over the small electron energy and consequent gun voltage ranges, there were no significant changes in the following parameters:

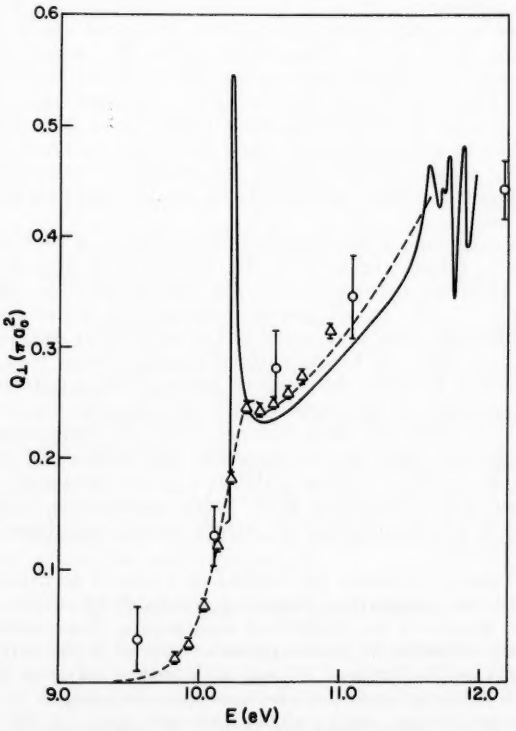

FIGURE 5. *The relative cross section for excitation of the* 2p *state of atomic hydrogen is shown as measured in this laboratory by Chamberlain, Smith and Heddle [1964],* △; *by Fite, Stebbings, and Brackmann [1959],* ○; *and as calculated by Burke, Taylor, and Ormonde [1967], solid curve.*

The dashed line results from folding the electron energy distribution used by Chamberlain *et al.* into the solid curve from Burke *et al.* This permits a valid comparison of theory and experiment. The error bars on the triangles represent the standard deviations of the mean values; those on the circles are confidence limits.

(a) Electron beam focus, and
(b) x-ray production (believed important in later work, see below).

The price for these advantages included the necessity for a narrow, well-measured electron beam energy distribution and careful measurement of any changes in the contact potential, neither being restrictive in later work. It was also necessary to use low electron current ($\sim 1.5\ \mu$A) so that space charge effects on current collection efficiency were negligible.

The most interesting feature of the threshold work was the plateau in $Q_\perp$ near the threshold, which is consistent with a finite value of $Q_\perp$ at threshold. In addition to the agreement with theory previously noted [Chamberlain et al., 1964] these results have been found to be in good agreement with recent calculations by Burke, Ormonde, and Whitaker [1966] and by Burke, Taylor, and Ormonde [1967], as can be seen in figure 5.

4.2. Results From Threshold to 200 eV

After completion of the threshold investigation, the emphasis was shifted to the shape of the excitation cross section at higher energies. Measurements there would permit additional comparisons with theory and previous experiments and normalization of the relative measurements to Born approximation calculations of the cross section. However, this work has been complicated by additional instrumental problems, primarily due to differing electron gun characteristics over the larger electron energy range, which have proved difficult to solve.

For electron energies greater than 90 eV, the electron gun was operated in an accelerating lens mode rather than the decelerating mode used at lower energies, as was described in section 2.4. A necessary condition for a successful measurement is that possible differences in the geometry of the electron beam in these two modes must not affect the results. Data were taken in both modes for cathode potentials of 70 to 90 V. On occasion the two sets of data were found to be quite different. After considerable investigation, the difficulty was removed by a thorough cleaning of the electron gun electrodes.

Another check on the operation of the apparatus was made by taking data with cathode potentials of 10 V (zero Lyman-α signal) and 40 V (near the peak of the excitation cross section) two or more times in the sequence of programed gun voltages. The purpose of this was to check for spurious voltage dependences of the data. The two different 10 V data points were always in agreement within their standard deviations, showing that the determination of the zero signal baseline was valid. However the 40 V data were not at first reproducible. This is illustrated in table 1, in which are listed photon signal data at 40 V taken after successively larger cathode potentials. The observed systematic decrease in the data implied that the high voltage data points were probably spuriously depressed. Additional studies showed that the magnitude of this effect decreased with time after exposure at the high voltage

data point. These effects were attributed to a short term change in the sensitivity of the ion chamber.

TABLE 1. *Effect of preceding gun voltages on the apparent relative photon intensity at 40 eV electron energy, using a LiF covered detector*

Voltage sequence	Mean value of 40 V measurements	Standard deviation of the mean value
30→40 V	0.0548	±0.0006
90→40 V	.0517	±.0004
120→40 V	.0507	±.0005
150→40 V	.0498	±.0004
200→40 V	.0489	±.0004

One possible cause of this phenomenon was a buildup of charge on the LiF window of the ion chamber from scattered electrons, which might change the electric field inside the ion chamber and thus the detection efficiency. Since the differential electron scattering cross section and the electron beam trajectory change with energy, this would be an energy dependent effect which would also be time dependent, owing to the finite surface resistance of the LiF window. This hypothesis was tested in two ways: a second LiF window was placed in front of the ion chamber with a grounded wire mesh in front of it (the grounded mesh on the surface of the ion chamber window itself was retained), so that scattered electrons deposited on the extra window could not make as large a change in the sensitivity of the detector, and a magnetic field of about 7 G was established parallel to the electron beam axis, in order to reduce the number of electrons that traveled perpendicular to the electron beam axis. These measures did not improve the agreement among the 40 V data, so another solution was sought.

Heath and Sacher [1966] have shown that LiF is particularly sensitive to irradiation by 1 and 2 MeV electrons, the transmittance at the Lyman-α wavelength of the sample tested decreasing from 60 percent before to 2 percent after irradiation. On the other hand the transmittance of a MgF_2 sample decreased only from 52 percent to 36 percent under the same conditions. To test the behavior of MgF_2 in the present situation an extra window of that material was placed in front of the ion chamber window (still LiF). The results were favorable: the 40 V data were in much better agreement. Therefore, the LiF window was removed from the ion chamber and a MgF_2 window installed, with the recognition of further possible advantages in the longer wavelength cutoff (1130 versus 1050 Å) and lower water absorbency of this material. Due to the need for insensitivity to the polarization of the Lyman-α radiation, a polished crystal of MgF_2 with its optical axis perpendicular to the faces of the window was used. With the window alone, all 40 V data were in agreement within their standard deviations, as expected. Therefore, although Heath and Sacher's work [1966] showed that MgF_2 was not impervious to radiation damage, it was much less affected than LiF in this application.

Since the possibility of electrons hitting the window of the detector had been discounted, we suggest that the trouble with LiF may have been caused by soft x-rays coming from parts of the electron gun electrodes exposed to the electron beam, e.g., the edges of the electron beam apertures. Although it is well known that hard x-rays affect the optical properties of LiF by production of *f*-centers, etc., no mention of sensitivity to soft x-rays was found in a brief search of the literature, so this explanation is only tentative. Due to the dependence on specific apparatus geometry that this effect would have, it is not possible to estimate its importance in other experiments. However, it may possibly have contributed to the anomalous results noted by Fite and his co-workers [Ott et al., 1967].

During the course of taking data, exceptionally large noise pulses in the photon signal occurred rather regularly. The pulses originated in the ion chamber since they did not occur when the ion chamber voltage was reduced. They were readily detected as large discontinuities in the continuously recorded output of the integrating circuit. Some may have been caused by cosmic rays (an early ion chamber design incorporated uranium glass whose radioactivity was readily detectable) but most were believed due to voltage breakdown inside the ion chamber. These events were orders of magnitude larger than the usual noise. In order to overcome these large errors, the output was monitored visually and spoiled data replaced with immediate repetitions. Spoiled data that were missed during visual monitoring were replaced by good data taken at another time the same day. These corrections were made with the aid of the graphic record of the integrator output during editing of the punched data cards.

Correction of the data by interpretation of the integrator output records has the disadvantage that bias in choosing data points for rejection is possible. The pulses occur in all phases, presumably with equal probability, and may make either positive or negative contributions to the integrated signals. Some bias is possible because the positive pulses have a different appearance in the recorded integral than do negative pulses. (Recently data rejection based on oscilloscope triggering with the discriminator set well above the random noise level has exhibited significant improvement over the edited data. Pulse rejection is phase independent. Statistical errors were significantly reduced.)

Table 2 presents the results of a run of 38 cycles. With the results are listed the standard deviations of the means of the individual data points. The consistency of the 40 V points is noteworthy, as is the agreement within pairs of 70 and 90 V points taken in the two different modes of electron beam focusing.

Table 2 also shows the results of measurements of the molecular excitation cross section required to correct $Q_\perp(H+H_2)$ using equations (9) and (10). The relative cross section $Q_\perp(H)$ corrected for molecular excitation is given in table 2, column 5. In column 6 $Q_\perp(H)$ is presented, normalized to the Born approximation [Moiseiwitsch and Smith, 1968], with an allowance of 2 percent for cascading.

TABLE 2. *Measured values of the relative cross section for electron impact excitation of hydrogen*

Nominal [a] cathode potential	Electron [b] energy	$Q_\perp(H+H_2)$ from eq (6) in text	$C(H_2)$ from eq (9)	$Q_\perp(H)$ from eq (10)	$Q_\perp(H)$ [c]
V	*eV*				(πa_0^2)
10	8.4	-0.0008 ± 0.0013			
12.5	11.0	$+.0263 \pm .0016$		0.0263	0.259 ± 0.016
15.0	13.4	$.0546 \pm .0010$	0.0001	.0545	$.537 \pm .010$
17.5	16.0	$.0655 \pm .0009$	.0004	.0651	$.642 + .009$
20.0	18.5	$.0715 \pm .0010$	.0007	.0708	$.698 \pm .010$
25.0	23.5	$.0818 \pm .0010$	.0009	.0809	$.796 \pm .010$
30	28.5	$.0872 \pm .0010$	.0010	.0862	$.850 \pm .010$
40	38.6	$.0887 \pm .0010$	.0012	.0875	$.863 \pm .010$
50	48.6	$.0865 \pm .0011$	.0013	.0852	$.840 \pm .011$
10	8.4	$+.0008 \pm .0013$			
70	68.6	$.0807 \pm .0012$	0.0013	0.0794	0.783 ± 0.012
*70	68.6	$.0801 \pm .0014$	.0013	.0788	$.777 \pm .014$
90	88.7	$.0736 \pm .0013$	.0012	.0724	$.714 \pm .013$
*90	88.7	$.0749 \pm .0013$	.0012	.0737	$.727 \pm .013$
40	38.6	$.0878 \pm .0014$	.0012	.0866	$.854 \pm .014$
*120	118.8	$.0640 \pm .0012$	.0011	.0629	$.620 \pm .012$
40	38.6	$.0886 \pm .0013$	.0012	.0874	$.862 \pm .013$
*150	148.9	$.0585 \pm .0008$	.0010	.0575	$.567 \pm .008$
40	38.6	$.0884 \pm .0012$	.0012	.0872	$.860 \pm .012$
*200	199.1	$.0501 \pm .0007$	.0008	.0493	$.486 \pm .007$
40	38.6	$.0870 \pm .0010$	.0012	.0858	$.846 \pm .010$

[a] Starred values signify the accelerating focusing mode; unstarred values the decelerating focusing mode.
[b] Corrected for contact potential and power supply nonlinearity.
[c] Normalized to the Born approximation at 200 eV.

The statistical errors in the results listed in table 2 are about 1.5 percent of the peak value at 40 eV. The significance of systematic errors is difficult to estimate. The errors associated with the electronic measurement instrumentation, consisting of carefully calibrated high quality systems, may be of the same order as the statistical error. Of more concern is the possibility of small residual errors of the type which appeared on a larger scale requiring corrective measures as has been described above: sensitivity of windows to low energy radiation, apparent charging up of surfaces, stray fields, etc. The evidence that such effects as these are not serious is largely circumstantial:

(1) The statistics show that the measurement with the automatic rejection system is very stable. Such effects as surface charging should lead to erratic performance of the apparatus.

(2) The signal at 40 V was completely independent of its position in the cycle.

(3) The 70 V and 90 V points were consistent when measured in the two focusing modes. This suggests insensitivity of the result to electron beam geometry and demonstrates that there is no serious field penetration from the anode potentials.

5. Discussion and Conclusion

In order to facilitate comparison of our relative data with data from other experiments and with theoretical calculations, they were normalized to a value for $Q_\perp(H)$ at 200 eV that was interpolated from values calculated using the Born approximation: $Q(H)=0.486\ \pi a_0^2$. This value includes a cascade contribution to the population of the $H(2p)$ state of about 2 percent. The normalized data are shown in figure 6 along with the earlier experimental data of Fite and Brackmann [1958] and Fite et al. [1959] and some theoretical cross sections. Our data are in agreement with those of Fite and his co-workers within the quoted experimental error estimates, except very near to threshold where uncertainty in absolute electron energy makes comparison difficult. The two sets of measurements were made with somewhat independent techniques since Fite and his co-workers used an iodine vapor ion chamber with a molecular oxygen filter and LiF windows whereas we used a nitric oxide ion chamber with a MgF_2 window and no filter. The smaller limits of error on our data are probably due to the lower background gas pressure in our apparatus and the automated data acquisition system that we used, which facilitated the collection of more data.

Two of the several theoretical calculations [Burke and Smith, 1962; Moiseiwitsch and Smith, 1968] of the $H(2p)$ excitation cross section are included in figure 6. The Born approximation curves [Moiseiwitsch and Smith, 1968] are included to demonstrate the validity of the normalization of the data to a value deduced from that theory at 200 eV. Note that the experimental data fall on the curve down to about 125 eV. However the Born approximation values are considerably larger than the experimental values at lower energies where the former are not expected to be valid.

The second theoretical curve plotted in figure 6 is the result of a close coupling calculation including the 1*s*, 2*s*, and 2*p* states of hydrogen [Burke et al., 1963]. Note that it, too, is quite different from the experimental curve, both in the size and the energy of the maximum value of the cross section. The disagreement in size seems even more striking when it is remembered that the experimental values include a cascade contribution and so ought to be larger than the theoretical values, which do not include cascade in that energy region.

The good agreement between the experimental measurements of the relative cross section for production of Lyman-α radiation suggests that there are no serious errors in them and that the lack of agreement with theory appears to be a fault of the latter. Thus a need for further theoretical work is indicated. Additional experimental investigations are also underway in our laboratory and elsewhere with the emphasis on measuring the angular distribution of the photons [Ott et al., 1967] and microscopic details of the cross section [Burke et al., 1966, 1967].

We acknowledge the cooperation of members of the technical staff of the Joint Institute for Laboratory Astrophysics in the design and construction of much of the apparatus and the work of G. Chamberlain and D. Heddle in obtaining the threshold data. We appreciate the assistance of John Vornhagen at Harshaw Chemical Company on our problem with the ion chamber windows.

6. Appendix: Estimation of the Dissociation Fraction, γ

Assuming thermal equilibrium applies, the degree of thermal dissociation, γ, of molecular hydrogen in the

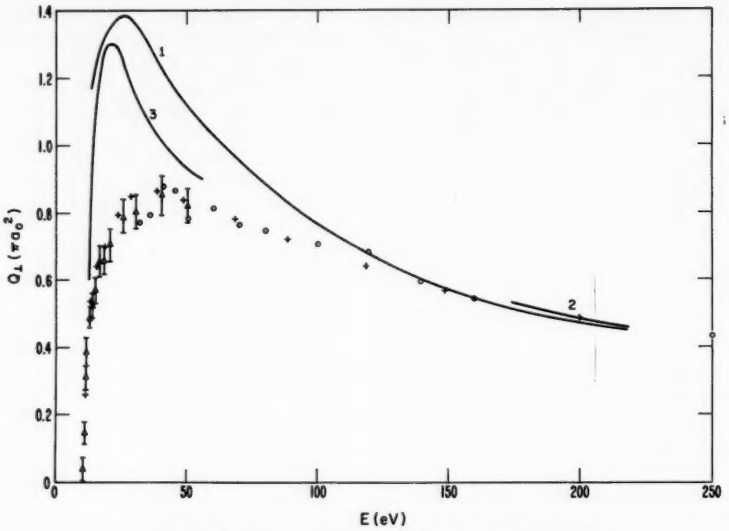

FIGURE 6. *The results of relative measurements of electron impact excitation of the* 2p *state of atomic hydrogen, from Table 2, shown as crosses* (+), *are compared with the experimental results obtained by Fite and Brackmann (1958), circles* (○); *and with the threshold results of Fite, Stebbings, and Brackmann (1959), triangles* (△).

The error bars shown on the triangles are confidence limits as are the ± 12% errors assigned to the points represented as circles. Statistical probable errors associated with the present work are about 1%, but the accuracy may be limited by systematic errors two or three times larger. Curve 1 shows the Born approximation result (see Moiseiwitsch and Smith, 1968) and the experimental results are normalized to curve 2 which allows for cascading. Curve 3 is a 1s-2s-2p close coupling calculation (Burke, Schey and Smith, 1963).

tungsten furnace depends on the furnace temperature T and pressure P_F inside it according to the following relation [Wooley, 1955; Liepmann and Roshko, 1957]:

$$\gamma^2 = \frac{K(T)}{4P_F + K(T)},$$

where $K(T)$ is the dissociation constant for the reaction $H_2 \leftrightarrows 2H$ at the temperature T. Values of $K(T)$ are tabulated by Wooley [1955] and by Stull and Sinke [1956]. Wooley [1955] also presents a useful chart relating P_F, γ, and T, whereby any of the three quantities can be found from the other two.

Of the three quantities above only the furnace temperature T was measured directly. The gas pressure P_p was measured upstream from the furnace at the plenum in the gas manifold. The pressure in the furnace is related to the plenum pressure in a complicated manner depending on the conductances of various elements of the gas handling system, on the furnace and manifold temperatures, and on the degree of dissociation of the gas. If thermal equilibrium is assumed in the furnace this relation can be derived.

The following symbols will be used:

P_p = gas plenum pressure
T_r = room temperature
n_F = (number of H_2 molecules per cm^3) + (one-half the number of H atoms per cm^3)
$C_1^m(T_r)$ = conductance (cm^3/s) of the gas handling elements leading from the plenum to the furnace and assumed to be at room temperature
$C_2^m(T)$ = conductance (cm^3/s) of the furnace orifice for molecules at the temperature of the furnace
$C_2^a(T)$ = conductance (cm^3/s) of the furnace orifice for atoms at the temperature of the furnace
n_p = number of molecules in the gas plenum per cm^3.

The flow equations for molecular and atomic hydrogen are:

number of molecules per second flowing into the furnace $= C_1^m(T_r)[n_p - n_F]$;
number of molecules per second flowing out of the furnace $= C_2^m(T)[(1-\gamma)n_F]$;
number of atoms per second flowing out of the furnace $= C_2^a(T)[2\gamma n_F]$.

Conservation of mass flow is now applied by equating the mass flow rate into the furnace to the mass flow rate out of the furnace, where m_{H_2} is the mass of molecular hydrogen and m_H is the mass of atomic hydrogen.

$$m_{H_2}C_1^m(T_r)[n_p - n_F] = m_{H_2}C_2^m(T)[1-\gamma]n_F + m_H C_2^g(T)[2\gamma n_F]. \quad \text{(A1)}$$

Using the fact that $m_{H_2} = 2m_H$ and solving for n_F, eq (A1) becomes

$$n_F = n_p \left[\frac{1+[1-\gamma]C_2^m(T)+\gamma C_2^g(T)}{C_1^m(T_r)}\right]^{-1} \quad \text{(A2)}$$

If molecular flow is assumed then the conductance of the furnace orifice is proportional to $(T/M)^{1/2}$ [Dushmann, 1962] where M is the mass number. Hence

$$\sqrt{2}C_2^m(T) = C_2^g(T) \quad \text{(A3)}$$

and

$$\frac{C_2^m(T)}{C_2^m(T_r)} = \sqrt{\frac{T}{T_r}}. \quad \text{(A4)}$$

n_p and n_F are related to the pressures P_p and P_F respectively by the following relations:

$$P_p = n_p k T_r \quad \text{(A5)}$$

and

$$P_F = (1+\gamma)n_F k T, \quad \text{(A6)}$$

where the $(1+\gamma)$ appears in eq (A6) because dissociation occurs in the furnace. Substituting eqs (A3), (A4), (A5), and (A6) into eq (A2) gives

$$P_F = \frac{P_p(1+\gamma)T}{T_r + \sqrt{T_r T}[1+(\sqrt{2}-1)\gamma]C_2^m(T_r)/C_1^m(T_r)}. \quad \text{(A7)}$$

The dissociation fraction is not known initially and therefore the furnace pressure cannot be determined directly from this equation. However, an iteration procedure may be employed: An approximate value of γ is used in eq (A7) along with appropriate values of C_1 and C_2 and values of T, T_r, and P_p to obtain an approximate value of the furnace pressure. Using this value together with the known value of the furnace temperature T, the graph of Wooley [1955] may be used to obtain a more accurate value of γ. This procedure is continued until a set of values of γ, P_F, and T are obtained which are consistent with the input data for T and P_p through eq (A7).

It should be noted that the pressure versus temperature curve for a given dissociation [see Wooley, 1955] has a very steep slope such that a relatively large pressure change yields a small dissociation fraction change while a temperature change of the same relative amount as the pressure change would yield a very large dissociation fraction change. Therefore the dissociation fraction depends much more critically upon the temperature than upon the pressure in the furnace. Values of the total conductance, measured at different temperatures, varied over a range of approximately 20 percent. Therefore the furnace pressure P_F has a corresponding uncertainty, but the resulting uncertainty in γ is very much smaller.

As a typical example, let the gas manifold pressure be 100 torr, the furnace temperature be 2500 K, $C_1^m(T_r) = 16$ cm³/s, and $C_2^m(T_r) = 231$ cm³/s. Using the procedure described above, the furnace pressure was found to be 27 torr and the dissociation fraction to be 0.90. For the data reported in table 2, with a pressure P_p of 87 torr and temperature of 2570 K, the dissociation fraction was estimated to be 0.95 ± 0.01.

7. References

Beers, Y., Introduction to the Theory of Error, 2d ed., p. 30 (Addison-Wesley, Reading, 1957).

Burke, P. G., Proc. Phys. Soc. (London) **82,** 443 (1963).

Burke, P. G., Ormonde, S., and Whitaker, W., Phys. Rev. Letters **17,** 800 (1966).

Burke, P. G., Schey, H. M., and Smith, K., Phys. Rev. **129,** 1258 (1963).

Burke, P. G., and Smith, K., Rev. Mod. Phys. **34,** 458 (1962).

Burke, P. G., Taylor, A. J., and Ormonde, S., Proc. Phys. Soc. (London) **92,** 345 (1967); Erratum, J. Phys. B (Proc. Phys. Soc.), [2], (Proc. Phys. Soc.) Ser. [2], **1,** 325 (1968).

Carver, J. H., and Mitchell, P., J. Sci. Instr. **41,** 555 (1964).

Chamberlain, G. E., Smith, S. J., and Heddle, D. W. O., Phys. Rev. Letters **12,** 647 (1964).

Dushmann, S., Scientific Foundations of Vacuum Technique, 2d ed. (John Wiley & Sons, New York, 1962).

Fite, W. L., and Brackmann, R. T., Phys. Rev. **112,** 1151 (1958).

Fite, W. L., Stebbings, R. F., and Brackmann, R. T., Phys. Rev. **116,** 356 (1959).

Foote, P. D., Fairchild, C. O., and Harrison, T. R., Pyrometric Practice, National Bureau of Standards Technical Paper No. 170 (1921).

rieath, D. F., and Sacher, P. A., Appl. Optics **5,** 937 (1966).

Hickmott, T. W., J. Chem. Phys. **32,** 810 (1960).

Hils, D., Kleinpoppen, H., and Koschmieder, H., Proc. Phys. Soc. (London) **89,** 35 (1966).

Hunter, J. B., Platinum Metals Rev. **4,** 130 (1960).

Kohl, W. H., Materials and Techniques for Electron Tubes, p. 272 (Reinhold, New York, 1960).

Leder, L. B., and Simpson, J. A., Rev. Sci. Instr. **29,** 571 (1958).

Lichten, W., and Schultz, S., Phys. Rev. **116,** 1132 (1959).

Liepmann, H. W., and Roshko, A., Elements of Gasdynamics (John Wiley & Sons, New York, 1957).

Lockwood, G. J., and Everhart, E., Phys. Rev. **125,** 567 (1962).

Luders, G., Z. Naturforsch **5a,** 608 (1950).

Moiseiwitsch, B. L., and Smith, S. J., Rev. Mod. Phys. **40,** 238 (1968).

Ott, W. R., Kauppila, W. E., and Fite, W. L., Phys. Rev. Letters **19,** 1361 (1967).

Percival, I. C., and Seaton, M. J., Phil. Trans. Roy. Soc. **251,** A990 (1958).

Poland, D. E., Green, J. W., and Margrave, J. L., Corrected Optical Pyrometer Readings, National Bureau of Standards Monograph 30 (1961).

Silverman, S. M., and Lassettre, E. N., J. Chem. Phys. **44,** 2219 (1966).

Simpson, J. A., Rev. Sci. Instr. **32,** 1283 (1961).

Smith, S. J., and Branscomb, L. M., Rev. Sci. Instr. **31,** 733 (1960).

Stebbings, R. F., Fite, W. L., Hummer, D. G., and Brackmann, R. T., Phys. Rev. **124,** 2051 (1961).

Stull, D. R., and Sinke, G. C., Thermodynamic properties of the elements, in Advances in Chemistry, volume 18, 104 (American Chemical Society, Washington, D.C., 1956).

Watanabe, K., Matsunaga, F. M., and Sakai, H., Appl. Optics **6,** 391 (1967).

Williams, J. F., Curley, E. K., and McGowan, J. W., Bull. Am. Phys. Soc. **13,** 214 (1968).

Wooley, H. W., Effect of dissociation on thermodynamic properties of pure diatomic gases, National Advisory Committee for Aeronautics, Technical Note 3270 (1955).

Young, J. R., Rev. Sci. Instr. **34,** 891 (1963).

(Paper 72A5–519)

JOURNAL OF RESEARCH of the National Bureau of Standards—A. Physics and Chemistry
Vol. 72A, No. 5, September–October 1968

Publications of the National Bureau of Standards*

Selected Abstracts

Blaine, R. L., Arni, H., and DeFore, M. R., **Interrelations between cement and concrete properties. Part 3, compressive strengths of portland cement test mortars and steam-cured mortars,** *Bldg. Sci. Series 8 (Apr. 1968), 55 cents.*
The relationships between cement characteristics and compressive strength of 1:2.75 (cement to graded Ottawa sand) mortars of standard consistency at ages of 24 hours to 10 years, and made with 199 cements of different types, were studied by fitting multivariable regression equations with the aid of a digital computer. The dominant variables associated with the differences of compressive strength, strength gain, and strength ratios were different at the various test ages, and after different curing conditions. The additional use of certain trace elements with commonly determined independent variables resulted in a significantly better fit between the equations and the observed data. Interactions between the fineness values and other independent variables were noted. Certain parallelisms and differences were noted with respect to variables associated with compressive strength differences at various ages and the heat of hydration of the cements at these ages.

Key Words: Chemical composition; fineness; heat of hydration; strength gain of portland cements; trace elements.

Corliss, C. H., and Tech, J. L., **Oscillator strengths and transition probabilities for 3288 lines of Fe I,** *Mono. 108 (Mar. 1968), 45 cents.*
A homogeneous set of intensity-related data has been calculated for 3288 spectral lines of Fe I in the region from 2100 to 9900 angstroms. The quantities tabulated in the present monograph include log $(gf\lambda)$, log (gf), gf, f, gA, and A. The data are presented on the absolute scale established in a previous work by Corliss and Bozman. In that work and the later extensions of it by Corliss and Warner, the calculation of gf-values included the application of an empirically determined normalization correction to the level populations, the normalization being given as a function of upper energy level for the transition. Since recent investigations do not support these excitations corrections in the case of Fe I and certain other spectra, the present tabulation incorporates a removal of that normalization function. This recalculation affects the values for all lines whose upper energy levels lie above 46000 cm^{-1} and should significantly improve the internal consistency of the present data.

Key Words: Fe I; iron; oscillator strengths; spectrum; spectrum of neutral iron; transition probabilities in Fe I.

Furukawa, G. T., Saba, W. G., and Reilly, M. L., **Critical analysis of the heat-capacity data of the literature and evaluation of thermodynamic properties of copper, silver, and gold from 0 to 300 °K,** *Natl. Std. Ref. Data Series 18 (Apr. 1968), 40 cents.*
The literature sources of heat-capacity data on copper, silver, and gold between 0 and 300 °K have been compiled and the data critically analyzed. Tables of heat capacity (C_p), enthalpy $(H-H_0^\circ)$, entropy (S°), Gibbs energy $(G-H_0^\circ)$, enthalpy function $\left(\frac{H-H_0^\circ}{T}\right)$, and Gibbs energy function $\left(\frac{G-H_0^\circ}{T}\right)$ have been obtained from the analyses. The literature values of the heat capacity, the electronic coefficient of heat capacity (γ), and the 0 °K limiting Debye characteristic temperature $(\theta_D(0))$ are compared with the selected values. The sources of the data are tabulated chronologically along with the temperature range of measurements, purity of sample, and the pertinent experimental procedures used. A bibliography of the references is listed. A brief appraisal of low-temperature calorimetry is given.

Key Words: Calorimetry; copper; Debye theta (θ); electronic coefficient of heat capacity; enthalpy; entropy; Gibbs energy; gold; heat capacity; silver; temperature scales; thermodynamic properties.

Glennon, B. M., and Wiese, W. L., **Bibliography on atomic transition probabilities, May 1966 through December 1967,** *Misc. Publ. 278 Supplement (Apr. 1968), 30 cents.*
A supplement to NBS Miscellaneous Publication 278, Bibliography on Atomic Transition Probabilities is presented, which covers the most recent literature on this subject from May 1966 through December 1967. The papers are arranged according to elements and stages of ionization, and the method employed and class of transitions are indicated behind each reference. Only articles on discrete transitions, both allowed and forbidden, are listed. Papers containing data for more than 20 individual elements or stages of ionization are collected separately in front of the list in order to keep this bibliography at a reasonable size. Also included is a selected list of papers dealing with the subject of transition probabilities from a general point of view.

Key Words: Allowed; atomic; discrete; forbidden; transition probability.

Hanley, H. J. M., and Klein, M., **On the selection of the intermolecular potential function: application of statistical mechanical theory to experiment,** *Tech. Note 360 (Nov. 20, 1967), 50 cents.*
We have developed a method here to evaluate quantitatively the relationship between model intermolecular potential functions and macroscopic experimental properties. Specifically, we have studied the function families: m-6, Kihara, exp:6, and Morse, and the properties: viscosity coefficient, diffusion coefficient, second virial, and Joule-Thomson coefficient. Our method is not restricted to these functions and properties; it is valid for any function and any property provided the appropriate theoretical expressions are available. The principal conclusions from this work are: 1. A temperature range exists (around room temperature for most substances) in which data are completely insensitive to the potential function. This range makes it possible to quantitatively define what is meant by "high" or "low" temperatures. These definitions are most important when extrapolation of data arises. 2. The function families studied are essentially equivalent. 3. More than one function is required to represent data over a range of about 1000 °K. 4. We have estimated the experimental error which can be tolerated if experimental data are to be used to select a potential function. The conclusions are experimentally verified for both transport and equilibrium properties.

Key Words: Intermolecular potential function; experimental data; theory; correlation; transport properties; equilibrium properties.

Ho, C. Y., Powell, R. W., and Liley, P. E., **Thermal conductivity of selected materials, Part 2,** *Natl. Std. Reference Data Series 16 (Feb. 1968), $2.00.*
The work presented in this report comprises the critical evaluation, analysis, and synthesis of the available thermal conductivity data and the generation of recommended values for twelve metallic elements, mainly for the solid state, for a range of graphites, and for

312-248 O-68—7

three fluids in the gaseous state. These are cadmium, chromium, lead, magnesium, molybdenum, nickel, niobium, tantalum, tin, titanium, zinc, zirconium, Acheson graphite, ATJ graphite, pyrolytic graphite, 875S graphite, 890S graphite, acetone, ammonia, and methane. For each of the materials recommended values are given over a wide range of temperature.

Key Words: Thermal conductivity; metallic elements; metals; graphites; gases; critical evaluation; recommended values; standard reference data.

Lee, R. W., and Worral, R. W., Ed., **Electronic composition in printing. Proceedings of a Symposium held at the National Bureau of Standards June 15–16, 1967,** *Spec. Publ. 295 (Feb. 1968), 70 cents.* (This series was formerly known as the Miscellaneous Publication Series.)
A Symposium on Electronic Composition in Printing was held at the Gaithersburg Laboratories of the National Bureau of Standards June 15 and 16, 1967. Sponsored by the NBS Center for Computer Sciences and Technology, the symposium was a state-of-the-art review of a rapidly advancing field of computer application with great potentialities for increased efficiency and savings in the Federal Government.
Twenty-nine papers were presented and are published in this Proceedings. They include a diverse group by industry representatives reporting recent technological advancements in the field. Several papers define government policy and describe the new Linotron system of photocomposition at the Government Printing Office; another series is devoted to nongovernment applications and research; and a final group details specific applications within several Government agencies.

Key Words: Character generation; composition language; computer technology; computerized text processing; electronic composition; electronic computer; electronic printing; GRACE; Linotron; MACRO coding; MEDLARS; microfilm; photocomposition; Photon; programming; text editing.

Petersen, P. H., and Watstein, D., **Shrinkage and creep in prestressed concrete,** *Bldg. Sci. Series 13 (Mar. 22, 1968), 15 cents.*
The loss of prestress resulting from creep and shrinkage in concrete was investigated for concrete specimens made with Type I portland cement and with Type III portland cement. The primary variables in this study were:
1. Relative humidity at which the concrete was maintained while under observation.
2. Age of the concrete at the time it was prestressed.
3. Ratio of prestress to strength; variation of this parameter required that the ratio of reinforcement be a variable.
4. Mass ratio factor defined as the ratio of the cross-section area of concrete specimen to its surface area per unit length.
Forty-nine sets of specimens were fabricated and tested; each set consisted of a prestressed specimen and an otherwise identical companion specimen without reinforcement.
The length changes with time were observed at intervals up to an age of 500 days. These observations were made for concretes subjected to different levels of prestress, and for concretes prestressed at different ages. Length changes in nonreinforced companion specimens were also obtained. Thus this study is concerned with elastic deformation occurring at time of stress transfer, shrinkage or swelling, and creep.

Key Words: Creep; relaxation; prestressed concrete; shrinkage; loss of prestress; variable prestress.

Radebaugh, R., **Thermodynamic properties of He^3-He^4 solutions with applications to the He^3-He^4 dilution refrigerator,** *Tech. Note 362 (Dec. 29, 1967), 70 cents.*
The thermodynamic properties of liquid He^3-He^4 solutions between 0 and 1.5 °K are calculated by using the weakly interacting Fermi-Dirac gas model for He^3 in He^4. Certain experimental data below about 0.4 °K are used to evaluate some of the parameters in the model. The properties of both He^3 in He^4 and the total solution are calculated for concentrations of He^3 up to 30 percent. All experimental data agree very well with the calculated results, although little data exist below 0.4 °K. The calculated properties are used to analyze the behavior of the He^3-He^4 dilution refrigerator in both the continuous and single-cycle processes. The maximum heat absorption below about 0.04 °K is found to be 82 T^2 joules per mole of He^3 circulated. The effect of an imperfect heat exchanger and He^4 circulation on the refrigeration capacity is discussed. An analysis of two new types of single-cycle processes is also given.

Key Words: Cryogenics; dilution refrigerator; enthalpy; entropy; Fermi-Dirac gas; helium-3; helium-4; liquid; mixtures; osmotic pressure; quantum fluid; specific heat; thermodynamic properties.

Roberts, A. G., **Organic coatings. Properties, selection, and use,** *Bldg. Sci. Series 7 (Feb. 1968), $2.50.*
This publication was prepared to fill the need for a comprehensive, unifying treatise in the field of organic coatings. Besides presenting practical information on the properties, selection, and use of organic coatings (and certain inorganic coatings), it provides basic principles in a number of important areas such as polymer structure, coatings formulation, pigment function, use of thinners, coating system compatibility, and theory of corrosion. Each chapter deals with a major area of the coatings field, including types of coatings, properties of synthetic resins, selection of coating systems, storage and safety, application methods, and surface preparation and pretreatment. There is also a consolidating chapter with illustrative examples of solutions to typical coatings problems. Interrelationships among the various areas of information are indicated through appropriate cross-referencing in the text. Specific references to Federal, Military, and other specifications are given where pertinent, and an entire chapter is devoted to a quick guide and summary of Federal specifications for organic coating materials. Finally, a selected bibliography and a comprehensive index are provided. While written primarily to meet the informational needs of the engineer, architect, maintenance superintendent, and responsible coatings procurement officer, the treatise is sufficiently broad in scope to serve as a general manual, a concise text, or a convenient reference source in the field of organic coatings.

Key Words: Application; coatings; coating systems; corrosion-inhibiting; Federal specifications; fire-retardant; lacquer; latex; multicolor; organic coatings; paint; pigments; polymers; properties; resins; selection; substrates; surface preparation; varnish; water-thinned.

Robbins, D., Ed., **Disclosures on: Autoeditor—a semi-automatic copy-editing apparatus,** *Tech. Note 440 (Apr. 1968), 40 cents.*
This note is a disclosure on a semi-automatic apparatus for incorporating editorial revisions in narrative text using punched paper tape combined with mark-sensing techniques. Pencil marks placed on the original draft by the editor are sensed and arranged to automatically capitalize the first letter of a word, to capitalize an entire word, or stop the apparatus at the point where a change is to be made. Addition of text is entered manually with an electric typewriter; deletion of text is accomplished by activating a "mark skip" key which advances the tape without typing until the next control mark is sensed.

Key Words: Narrative text editing; editorial mark sensing; automatic capitalization; automatic stop for revision; manual additions; automatic deletions; punched paper tape typewriter.

Shelton, C. F., **Spectral emission properties of NBS standard phosphor samples under photo-excitation,** *Tech. Note 417 (Mar. 1968), 25 cents.*
The photo-excitation spectral emission properties of 10 of the 14 NBS standard phosphor samples have been determined. Pressed tablets of the phosphors were excited by radiation from a mercury arc lamp, passing through a narrow band-pass filter to obtain either 2537 Å or 3650 Å excitation. The measurement system is described, correction of the data is discussed, and the spectral emission data are presented. Relative quantum efficiencies were calculated. The results are compared with measurements reported by two other laboratories.

Key Words: Phosphors; photo-excitation; photoluminescence; spectral emission; spectral radiometry; standard phosphor samples.

Shimanouchi, T., **Tables of molecular vibrational frequencies, Part 3,** *Natl. Std. Reference Data Series 17 (Mar. 1968), 30 cents.*
A compilation of vibrational frequency data for selected molecules is being conducted at the University of Tokyo in cooperation with the National Standard Reference Data Program of the National Bureau of Standards as a part of an international effort to compile and evaluate physical and chemical data. This report, as a continuation of Part 1 published as NSRDS–NBS–6, and Part 2, published as NSRDS–NBS–11, contains fundamental vibrational frequencies of 54 molecules together with vibrational assignments, sources of data, brief comments, and citations of references. The procedures used for the preparation of tables are the same as given in Part 1. The fundamental frequencies are obtained mainly from the infrared and Raman spectra. When these are not available, other experimental data such as microwave results are taken into account. The selection of vibrational fundamentals from observed data is based upon careful studies of the spectral data and comprehensive mathematical analyses. The tables were designed to provide a concise summary needed for the computation of ideal gas thermodynamic properties. They may also provide a convenient source of information to those who require vibrational energy levels and related properties in molecular spectroscopy, analytical chemistry, and other fields of physics and chemistry.

Key Words: Molecular; vibrational; frequencies; data; tables; spectral.

Standard reference materials: catalog and price list of standard materials issued by the National Bureau of Standards, *Misc. Publ. 260, 1968 Edition (Jan. 31, 1968), 45 cents. (Supersedes NBS Misc. Publ. 260, 1967 Edition.)*
This catalog describes the various Standard Reference Materials issued by the National Bureau of Standards. These materials are used to calibrate measurement systems and provide scientific information that can be referred to a common base. A schedule of prices and quantities is included for each material, as well as directions for ordering. Listed are the types and compositions of those chemical standards that are presently available. Announcements of new standard reference materials are made in the Federal Register, in scientific and trade journals, and in the Technical News Bulletin of the National Bureau of Standards. Changes affecting the current status of the various standards will be indicated by an insert sheet available quarterly from the Bureau.

Key Words: Analysis; catalog; certificate; characterization; composition; price list; property of material; purity; standard reference materials; standards.

Wegstein, J. H., **A computer oriented single-fingerprint identification system,** *Tech. Note 443 (Mar. 1968), 25 cents.*
A procedure is described for computing a set of numerical descriptors that identify a single fingerprint. The procedure starts with the X and Y coordinates and the individual directions of the minutiae (ridge endings and bifurcations) of a fingerprint impression. Sets of descriptors are computed corresponding to groups or constellations of these minutiae. Descriptors corresponding to various fingerprint impressions are stored on magnetic tape. A fragment of a fingerprint impression such as occurs in a latent fingerprint may also be used.
A second computer program reads the descriptors corresponding to two different fingerprint impressions from magnetic tape. A score is computed that indicates how well the two impressions match. Preliminary experimental results suggest that this procedure might be suitable as a basis for a single-fingerprint classification system.

Key Words: Classification; computer; descriptor; file; fingerprint; identification; pattern-recognition.

Berger, M. J., **Energy deposition in water by photons from point isotropic sources,** *J. Nucl. Med. Suppl.* **1,** *15–25 (Feb. 1968).*
This pamphlet contains tabulations of energy absorption buildup factors for point isotropic gamma ray sources for use in nineteen source energies between 3 MeV and 15 keV. An analytical representation of the buildup factors in the form of a polynomial in the source-detector distance is also given.

Key Words: Energy absorption; buildup factor; photons; absorbed fraction; gamma rays; point-isotropic source.

Dibeler, V. H., and Liston, S. K., **Mass-spectrometric study of photoionization. VIII. Dicyanogen and the cyanogen halides,** *J. Chem. Phys.* **47,** *No. 11, 4548–4555 (Dec. 1, 1967).*
Photoion-yield curves are obtained for the molecule and selected radical ions of C_2N_2, FCN, ClCN, BrCN, and ICN from threshold to 600 Å. Vibrationally excited states of ions and autoionization of Rydberg levels in the molecules are observed and discussed briefly. The X^+ ion thresholds in the heavier cyanogen halides are used to obtain the following results with estimated uncertainties: $\Delta Hf_0^\circ(CN) = 101.5 \pm 1.0$ kcal-mol^{-1}, $\Delta Hf_0^\circ(CN^+) = 430.0 \pm 1.0$ kcal-mol^{-1}, and $I(CN) = 14.2_5$ eV. These are applied to compute $\Delta Hf_0^\circ(FCN) < 5.6$ kcal-mol^{-1}, $I(C_2) = 12.15$ eV and other thermochemical properties. The formation of CN^+ from dicyanogen apparently includes about 0.6 eV excess energy near threshold.

Key Words: Photoionization; mass spectrometer; vacuum uv monochromator; Rydberg levels; autoionization; heats of formation; C_2N_2; FCN; ClCN; BrCN; ICN.

Johannesen, R. B., Brinckman, F. E., and Coyle, T. D., **Nuclear magnetic resonance studies of inorganic fluorides. V. Fluorosilanes,** *J. Phys. Chem.* **72,** *660–667* (1968).
Nuclear magnetic resonance (n.m.r.) chemical shifts of ^{19}F nuclei and ^{29}Si-^{19}F coupling constants have been measured for a number of compounds containing silicon-fluorine bonds. For most of these, ^{29}Si chemical shifts were also determined by (heteronuclear) (^{19}F-{^{29}Si}) double resonance.
With few exceptions, ^{19}F and ^{29}Si resonances in substituted fluorosilanes are on the low-field side of the corresponding resonances in SiF_4. The ^{29}Si shift in the $SiF_6^=$ ion is about 75 ppm to high field of SiF_4 and is well outside the range of previously reported silicon shift values. Magnitudes of ^{29}Si-^{19}F coupling constants range from 167.6 Hz in Si_2OF_6 to 384.9 Hz in Si_2Cl_5F. The variation of these parameters with the nature and extent of substitution on silicon is discussed.

Key Words: Nuclear magnetic resonance; double resonance; silicon; fluorine; chemical shift; coupling constant; spin-coupling; fluorosilanes; solvent effects.

Krause, R. F., Jr. and Douglas, T. B., **The vapor pressure, vapor dimerization, and heat of sublimation of aluminum flouride, using the entrainment method,** *J. Phys. Chem.* **72,** *No. 2, 475–481 (Feb. 1968).*
The vapor pressure P of anhydrous aluminum fluoride was measured at eight temperatures between 1194 and 1258 °K by an entrainment method. The standard deviation of P from a least squares fit was 0.15%, and systematic uncertainties of 0.4% in P and 1 deg in T were estimated. If the vapor were assumed to be completely monomeric and ideal, this fit would yield Second Law values and their standard deviations at 1000 °K of $\Delta H^\circ = 69.64 \pm 0.06$ kcal and $\Delta S^\circ = 45.48 \pm 0.06$ eu for

$$AlF_3(c) = AlF_3(g) \qquad (1)$$

However, corresponding Third Law values were found sufficiently lower as to indicate that the saturated vapor could be treated as ideal only by taking into account the occurrence of some dimerization,

$$2AlF_3(g) = Al_2F_6(g) \qquad (2)$$

P was considered as the sum of the monomeric and twice the dimeric vapor pressure, and smooth values of P and dP/dT at 1225 °K were determined. The other two independent thermodynamic quantities necessary to define reactions 1 and 2 were taken as (a) the standard entropy of reaction 1 derived from published spectroscopic and crystalline heat capacity data, and (b) the mol fraction of dimer as newly evaluated from two published mass spectrometric studies. The final interconsistent results at 1000 °K along with their uncertainties were the Third Law, $\Delta H^\circ = 68.94$ kcal using $\Delta S^\circ = 48.80 \pm 0.4$ eu for reaction 1, and $\Delta H^\circ = -56 \pm 5$ kcal and $\Delta S^\circ = -41 \pm 5$ eu for reaction 2. Owing to the precision and accuracy of this entrainment data, these values are believed to be more reliable than those previously recommended.

Key Words: Vapor pressure; temperature; entrainment method; vapor dimerization; heat of sublimation; aluminum fluoride.

Landgrebe, A. R., McShrarry, W. O., and Cefola, M., **The radiometric titration of trace amounts of zinc,** *Intern. J. Appl. Radiation Isotopes* **19,** *1, 23–26 (1968).*
A method of radiometric titration for the determination of trace amounts of metals has been developed. The EDTA complex of the metal to be determined is formed, and the excess, uncomplexed metal ions are removed by means of a cationic exchanger. A titration curve is then constructed by plotting the activity of the liquid phase, versus the amount of EDTA added. Both the batch and column method were tried in this laboratory, and it is our opinion that the batch method is easier from a manipulative point of view. A new method of determining the end point was developed. If both the resin and solution are counted, this is a simple way of determining the half equivalent point. Methods are underway to maximize the sensitivity for zinc by chelating radiometric titration.

Key Words; Radiometric; titrations; zinc; EDTA; batch; column; cationic; exchanger.

Landgrebe, A. R., Rodriguez-Pasques, R. H., and Schima, F. J., **The rapid radiochemical separation of radioactive praseodymium from radioactive cerium,** *Intern. J. Appl. Radiation Isotopes* **19,** *No. 2, 147–149 (1968).*
A method of rapid radiochemical separation was developed to separate the cerium and praseodymium radioactivities produced after a praseodymium target was irradiated at the NBS Linac. The praseodymium metal is dissolved in nitric acid and the solution is divided into at least two portions. One fraction is used to precipitate cerium (IV) iodate, giving an aqueous phase free of cerium radioactivity. A second fraction is extracted with hydrogen di-(2 ethylhexyl) orthophosphoric acid (HDEHP). The organic phase is free from any praseodymium radioactivities.

Key Words; Rapid separation; praseodymium; cerium; radioactive; Linac; solvent extraction; precipitation.

Milligan, D. E., and Jacox, M. E., **Infrared and ultraviolet spectroscopic study of the products of the vacuum-ultraviolet photolysis of methane in Ar and N_2 matrices. The infrared spectrum of the free radical CH_3,** *J. Chem. Phys.* **47,** *No. 12, 5146–5156 (Dec. 15, 1967).*
The vacuum ultraviolet photolysis of methane in an argon or a nitrogen matrix at 14 °K leads to the formation of a sufficient concentration of the methyl radical for observation both of its 1500 Å electronic transitions and of its out-of-plane deformation fundamental, which appears at 611 cm^{-1} for CH_3 trapped in a nitrogen matrix. The value observed for this fundamental of CD_3 is in reasonable agreement with the value previously derived from analysis of the 2160 Å band system. Isotopic substitution studies support the assignment of the 611 cm^{-1} feature to ν_2 of CH_3. Data are consistent with the previous report of a planar structure. Evidence is presented suggesting that CH_3 may rotate in an argon matrix. Although CH_2 has not been directly observed, an appreciable concentration of CH_2N_2 appears in the N_2 matrix experiments. Three electronic transitions of CH are observed in the argon matrix experiments, and there is evidence for the production of a small concentration of C atoms.

Key Words: Free radical; infrared; matrix isolation; methyl; methylene; photolysis; rotation; spectrum; ultraviolet; vacuum ultraviolet.

Milligan, D. E., and Jacox, M. E., **Matrix-isolation study of the infrared and ultraviolet spectra of the free radical NCO,** *J. Chem. Phys.* **47,** *No. 12, 5157–5168 (Dec. 15, 1967).*
The free radical NCO is stabilized in sufficient concentration for direct infrared and ultraviolet spectroscopic identification upon vacuum ultraviolet photolysis of HNCO suspended in various matrix materials at 4° and at 14 °K. Observations on the $B(^2H)$-$X(^2H)$ electronic transition of NCO have been extended to shorter wavelengths than those previously reported. Isotopically substituted NCO has been prepared in supplementary experiments involving the vacuum ultraviolet photolysis of $CO:HN_3$ and $Ar:HCN:N_2O$ samples, as well as by the mercury arc photolysis of matrix-isolated samples of $NO + N_3CN$. The three vibrational fundamentals of ground-state NCO appear at 487, 1275, and 1922 cm^{-1} in an Ar matrix. The values obtained for the stretching force constants suggest that the carbon-oxygen bond may be somewhat stronger than the carbon-nitrogen bond. There is an appreciable positive stretching-interaction force constant. NCO is found to photolyze when subjected to radiation of wavelength near 2537 Å, leading to the production of N + CO. Reactions occurring in the various systems investigated are discussed.

Key Words: C atom reaction; CN reaction; HN_3 photolysis; infrared spectrum; matrix isolation; NCO free radical; NO reaction; O atom reaction; ultraviolet spectrum; vacuum ultraviolet photolysis.

Okabe, H., and Lenzi, M., **Photodissociation of NH_3 in the vacuum ultraviolet,** *J. Chem. Phys.* **47,** *No. 12, 5241–5246 (Dec. 15, 1967).*
Two photodissociation processes of NH_3 producing electronically excited radicals have been studied in the vacuum ultraviolet. $NH_3 \rightarrow NH_2A^2A_1 + H$ (1) $- NH_3 \rightarrow NHc^1\Pi + H_2$ (2). The intensity of the fluorescence from these radicals, lying in the spectral regions 4000 A to 6000 A and at 3240 A respectively, has been measured as a function of wavelength of incident light with a resolution of 7A. The fluorescence curves thus obtained were compared with the absorption spectrum of NH_3. It is shown that the process (1) may be correlated with the $^1E''$ (1665 A bands), $^1A_2''$ (1434 A bands), $^1A_2''$ (1330 A bands), 1286 A bands, and the continuum (1250 to 1600 A). On the other hand, the process (2) may be associated with the continua (1250 A to 1600 A and below 1250 A). The threshold wavelength of process (2) is 1325 ± 7A. The electronic energy 'a' of the first singlet state $NHa^1\Delta$ with respect to the ground triplet state $X^3\Sigma^-$ is $a \leq 1.6 + 0.1$ eV which is obtained from the threshold wavelength together with the heat of reaction (3.9 ± 0.1 eV) $NH_2 \rightarrow NHX^3\Sigma^- + H_2$ and the electronic energy of the $NHc^1\Pi$ (3.813 eV) with respect to the $a^1\Delta$. Various other primary processes are discussed in conjunction with the absorption spectrum. For incident light of wavelength below 1200 A the ionization process $NH_3 \rightarrow NH_3^+ + e$ (3) and the process (2) both of which may arise from the continuum become predominant. Dissociation processes appear to be dictated by the spin conservation rule.

Key Words: Photodissociation; NH_3; vacuum ultraviolet; adsorption; fluorescence; excited NH_2; excited NH.

Pella, P. A., Landgrebe, A. R., DeVoe, J. R., and Purdy, W. C., **Differential controlled-potential coulometry utilizing substoichiometric radioisotope dilution,** *Anal. Chem.* **39,** *1781–1785 (Dec. 1967).*
A controlled-potential coulometric procedure is described which permits the utilization of the principle of substoichiometric radioisotope dilution. This technique employs two identical cells connected in series. Under prescribed conditions, the same amount of the element to be analyzed is deposited in each cell. The procedure involves the addition of a known amount of the element to the control cell, which is held at a constant potential, and an unknown amount to the sample cell. An equal, known amount of a radioisotope of that element is then added to each cell. The difference in the amount is determined by measuring the radioactivity remaining in each of the cells after a finite electrolysis time. This method was applied to the determination of cadmium in an NBS Standard Reference Material, zinc spelter, with a result of 0.0928% with a standard deviation of the mean of 0.0005%.

Key Words: Coulometry; radioactive tracers; trace analysis; electrolysis; substoichiometric; radioisotope dilution; cadmium; zinc spelter.

Taylor, L. S., **Responsibilities of the physician in his use of radiation,** *Rev. Mex. Radiol.* **XVIII,** *No. 69, 22–31 Jan.–Feb. 1964).*
After comparing various sources of radiation exposure to which the public is subjected, suggestions are given with regard to the responsibility of the medical profession in the protection of patients during medical procedures.
Attention is directed to the substantial differences in practice between the radiologist and the general practitioner. Practically all of the conditions under which the general practitioner has to operate militate against maximizing the protection of the patient

as well as the staff. Public concern over radiation hazards in medical procedures has reached such proportions that better doctor-patient relationships in the administration of radiation are clearly called for.

Key Words: Radiation exposure; radiation hazards.

Whittaker, J. K., **Instability and decoupling in nuclear electronics,** *Nucl. Instr. Methods* **57,** *No. 1, 156 (Dec. 1967).*
The instabilities which can occur in semiconductor electronics and the necessary decoupling to remove these instabilities and their effects are discussed, with particular reference to the present concept of modular electronic systems.

Key Words: Instability; decoupling; f_T; high frequency; low frequency; NIM System.

Mielenz, K. D., Nefflen, K. F., Rowley, W. R. C., Wilson, D. C., and Englehard, E., **Reproducibility of helium-neon laser wavelengths at 633 nm,** *Appl. Opt.* **7,** *No. 2, 289–293 (Feb. 1968).*
Measurements on helium-neon lasers stabilized on the Lamb dip, performed at NBS, NPL, and PTB, have shown that the wavelengths of such lasers are reproducible within approximately 1 part in 10^7. Beyond this limit, different lasers were found to emit different wavelengths. In addition, the wavelength of a given laser may vary during the life of its discharge tube. Pressure shifts appear to be a major cause of such variations.

Key Words: Frequency-stabilized; helium-neon; krypton 86 lamp; Lamb dip; laser; wavelength.

Allan, D. W., Fey, L., Machlan, H. E., and Barnes, J. A., **An ultraprecise time synchronization system designed by computer simulation,** *Frequency* **6,** *No. 1, 11–14 (Jan. 1968).*
Any two independent time scales will exhibit time departure due to two main causes, i.e., systematic differences in the frequency standards and inherent random noise processes. For time synchronization, some theoretical considerations indicate the plausibility of a third-order feedback system which will automatically remove the systematic difficulties of typical frequency standards used in time scale work. Because of the random nature of the second difficulty, the whole system is simulated with a computer to determine the systems feasibility and operating parameters. Two basic assumptions are that time comparisons for synchronization would be intermittent and that the model for the frequency standard is represented by a systematic linear frequency drift with a random flicker noise spectrum $\left(\frac{1}{|\omega|}\right)$ of the frequency fluctuations.
On the basis of the computer results an electromechanical system was designed and built. When the input to the system is the frequency from a high quality quartz crystal oscillator, the output frequency has no frequency drift. If synchronization is performed every 12 hours, the rms time error predicted by the system at the time of the next synchronization is 70 nanoseconds, which is near optimum.

Key Words: Time scales; time synchronization; computer simulation; flicker noise; optimum prediction; frequency drift; third order feedback system.

Arenhovel, H., and Hayward, E., **Scattering of plane-polarized photons by the giant resonances of nuclei,** *Phys. Rev.* **165,** *No. 4, 1170–1174 (Jan. 20, 1968).*
The cross sections for the electric dipole scattering of plane polarized photons are expressed in terms of the angular momentum transferred to the nucleus in the two-step scattering process. These scattering cross sections have been evaluated in the dynamic collective model for a number of vibrational nuclei at 15.1 MeV and for a number of deformed nuclei at 11.4 and 15.1 MeV. A sum rule is derived that relates the total scattering cross section for an odd-A nucleus to that of its even-even neighbor.

Key Words: Photon scattering; giant resonance; polarized photons; sum rule.

Bennet, L. H., Swartzendruber, Watson, R. E., **Hyperfine fields and electronic structure of CsCl-type ternary alloys of the first transition series,** *Phys. Rev.* **165,** *No. 2, 500–505 (Jan. 10, 1968).*
The ^{59}Co Knight shift (K) and the ^{57}Fe isomer shift have been measured in $TiFe_{1-x}Co_x$ alloys over most of the composition range $0 \leqslant x \leqslant 1$. At room temperature, K varies from a maximum of 2.7 $\pm 0.2\%$ at $x \approx 0.8$, and roughly follows the electronic specific heat as the composition is varied, with a minimum of $K = 0.3 \pm 0.2\%$ near $x = 0$. K increases substantially as the temperature is lowered for x near 1, and decreases somewhat for x near 0. The maximum K measured is $4.2 \pm 0.2\%$ for $x \approx 0.8$ at 120 °K. The maximum positive slope of K vs. susceptibility occurs near $x \approx 0.8$. The isomer shift variation from -0.15 ± 0.01 (mm/sec relative to pure Fe) at TiFe to -0.19 ± 0.02 at TiCo, is similar to Fe in Cr-Mn. The ^{47,49}Ti Knight shift in TiFe is $0.26 \pm 0.04\%$ at room and at liquid nitrogen temperatures. The experimental results are discussed in terms of correlations with electron concentration and s-admixture in the d-bands.

Key Words: Hyperfine fields; electronic structure; alloys; Knight shift; isomer shift; electronic specific heat; Ti; Fe Co; s-admixture.

Brown, R. L. and Dittmann, S., **Vibrational relaxation and quenching in the yellow nitrogen afterglow,** *Chem. Commun.* **21,** *1144–1146 (Nov. 8, 1967).*
The vibrational distribution in the $B^3\Pi_g$ state of molecular nitrogen populated by recombination of nitrogen atoms has been found to depend on pressure and on the nitrogen atom concentration. These effects can be explained by a mechanism involving quenchinf of the $B^3\Pi_g$ state by nitrogen atoms and by carrier gas molecules and collision induced vibrational relaxation.

Key Words: Active nitrogen, nitrogen atoms; afterglow; vibrational relaxation; quenching; atom recombination.

Christ, B. W. and Giles, P. M., **Metallurgical uses of the Fe^{57} Mössbauer effect in metallic iron and plain carbon steels,** *Book, Advances in Mössbauer Methodology 3, 37–65 (Plenum Press, Inc., New York, N.Y., Jan. 1967).*
Literature describing the Fe^{57} Mössbauer effect in metallic iron, steels and ferrous compounds occurring in steels is reviewed and compared with new, computer-analyzed data obtained in 298 °K measurements on metallic iron and carbon steels. Characteristics of Mössbauer patterns are sensitive to carbon content and thermomechanical history. Relative to standard sodium nitroprusside, the average effective magnetic field (EMF) for three grades of recrystallized iron is 339 ± 3 kilo-oersteds.
Patterns reveal several superimposed hyperfine interactions between 0.02 and 1 w/o C. The most intense magnetic hyperfine pattern (MHP) is attributable to iron atoms remote from interstitials. The EMF of this pattern increases with increasing C in solution, e.g., 355 ± 3 kilo-oersteds at 1 w/o C. In quenched 0.3, 0.7, and 1 w/o C alloys, irregularities in peak shape arise from sets of iron atoms with various C near-neighbor configurations. A weak, resolvable MHP exhibiting a small quadrupole effect and an EMF 20% smaller than that of the intense pattern originates at iron atoms with one carbon nearest neighbor.
Phases identifiable by their patterns include ferrite, martensite, austenite, cementite, and ϵ-carbide. Dislocations produce no detectable effect. Application of Mössbauer spectroscopy to the study of martensite tempering and quantitative analysis for retained austenite is discussed.

Key Words: Fe^{57} iron; carbon steels; tempering; retained austenite hyperfine interactions.

deWit, R., **Thermodynamic force on a dislocation,** *J. Appl. Phys.* **39,** *No. 1, 137–141 (Jan. 1968).*
The thermodynamic force on a dislocation is defined as the negative gradient of the Gibbs free energy of the crystal with respect to dislocation motion. This is shown to lead to a consistent force expression which contains two terms: the Peach-Koehler force due to the stress and the Bardeen-Herring force due to the vacancy concentration. The precise definition of these two terms is arbitrary, though their sum is unique. Various forms of the force expression are derived in terms of different reference vacancy concentrations, including the original forms of Weertman and Lothe and Hirth.

Key Words: Concentration; crystal; defect; dislocation; energy; equilibrium; force; hydrostatic; pressure; vacancy.

Hafner, H., Simpson, J. A., and Kuyatt, C. E., **Comparison of the spherical deflector and the cylindrical mirror analyzers,** *Rev. Sci. Instr.* **39,** *No. 1, 33–35 (Jan. 1968).*
The calculated performance of the cylindrical mirror deflection energy analyzer for charged particles is compared with that of the spherical analyzer. It is shown that through terms through the 3rd order the cylindrical device is significantly superior.

Key Words: Cylindrical mirror; electron energy analyzer; electron optics; spherical deflector.

Holt, H. K., **Observation of the effect of frequency correlations on a cascade transition,** *Phys. Rev. Letters* **20,** *No. 9, 410–412 (Feb. 26, 1968).*
The effect of frequency correlations on a cascade transition has been observed.

Key Words: Laser; line profile; neon.

Hummer, D. G., **Non-coherent scattering-III. The effect of continuous absorption on the formation of spectral lines,** *Monthly Notices Roy. Astron. Soc.* **138,** *No. 1, 73–108 (1968).*
The formation of spectral lines by completely redistributed non-coherent scattering is systematically investigated for situations in which photo-ionization or extinction by dust grains occurs at the line frequencies. Particular attention is given to cases for which the source function associated with the continuous opacity differs from the Planck function at the local electron temperature. Very large effects are found to occur, even when the ratio of continuous opacity to line opacity is very small. Extensive numerical results are presented, and the relevant scaling laws and the generalized thermalization length are discussed.

Key Words: Non-coherent scattering; continuous absorption; spectral lines; Planck function; source function.

Kamper, R. A., **Millidegree noise thermometry,** *Proc. Symp. Physics of Superconducting Devices, University of Virginia, Apr. 28–29, 1967, pp. M–1–M–5 (Office of Naval Research, Wash., D.C., 1968).*
Assuming that the linewidth of the A. C. Josephson radiation is caused entirely by thermal fluctuations in the bias voltage, we show that it can be used with quite simple instrumentation to measure absolute temperatures down to one millidegree or lower.

Key Words: Millidegree; noise; thermometry; Josephson effect; linewidth; superconductivity.

Klein, R., and Scheer, M. D., **Mechanism of O(^{3}P) addition to condensed films. II. Propene, 1-butene, and their mixtures,** *J. Phys. Chem.* **72,** *No. 2, 616–622 (Feb. 1968).*
The kinetics of O(^{3}P) addition to condensed films of propene and 1-butene has been investigated at 90 °K. The reaction rate was found to be independent of olefin concentration for both propene and 1-butene using propane as an inert diluent. Films containing mixtures of propene and 1-butene yielded mostly C_3 products at high olefin concentration and approached a limiting value of about 1.6 for the C_3-C_4 product ratio at infinite dilution in propane. When C_3D_6 films were used, the ratio of carbonyl to epoxide was measurably less than that obtained with C_3H_6.
The results are interpreted in terms of a model which depicts the olefin film to be a nearly perfect sink for O(^{3}P) atoms. The primary process is assumed to be the formation of a triplet adduct which undergoes either ring closure to form the epoxide or an intramolecular migration of a hydrogen atom to produce a carbonyl compound. The latter exhibits the expected isotope effect when D is substituted for H in the olefin reactant. The behavior of propene, 1-butene mixtures can be accounted for qualitatively by assuming that propene not only reacts more rapidly but diffuses more easily than does the 1-butene.

Key Words: Oxygen atom; oxidation; low temperature chemistry; olefins; propylene; 1-butene.

LeLevier, R. E., and Branscomb, L. M., **Ion chemistry governing mesospheric electron concentrations,** *J. Geophys. Res., Space Physics* **73,** *No. 1, 27–41 (Jan. 1, 1968).*
A theory and methodology for investigating the ion chemistry governing mesospheric electron concentrations is presented. In this theory, macroscopic reaction coefficients are defined in terms of the microscopic chemical reactions that take place between positive ions, electrons, and negative ions. The role of minor constituents of the atmosphere, O, O_3, CO_2, NO, and NO_2, is discussed using reaction rates measured in the laboratory. One reaction, the associative detachment of O_2^- by atomic oxygen, is so fast that mechanisms for inhibiting or suppressing this reaction are required. The need for such mechanisms is dictated by field data on riometer absorption induced by the nuclear explosions of the 1962 Christmas Island air drops. The importance of terminating negative ions, i.e., negative ions that withstand the attack of atomic oxygen, is emphasized. Also emphasized is the influence of the ion-ion mutual neutralization coefficient of terminating negative ions. Four illustrative models of the ion chemistry are presented ranging from the simplest O_2^- model, which is certainly unrealistic, to a more complex model involving six species of negative ions. This model, which is suggested by recent measurements of reaction rates in the laboratory, does not include the effect of water vapor in the reaction scheme since little laboratory data exist on the reaction of negative ions with water.

Key Words: Ion chemistry; mesospheric electron concentrations; microscopic chemical reactions; negative ions.

Manson, S. T., and Cooper, J. W., **Photo-ionization in the soft x-ray range: Z dependence in a central-potential model,** *Phys. Rev.* **165,** *No. 1, 126–138 (Jan. 5, 1968).*
Using a one electron model with a realistic central potential, photoionization calculations have been performed which emphasize the soft X-ray spectral range (~ 100 eV to ~ 2 keV). The $M_{II,III}(3p)$ subshell was studied in Ar, Cu and Ge, as well as the $M_{IV,V}(3d)$ and $M_{II,III}$ in Kr, Rh, Xe, Eu, Au and Fm in an effort to explain the combined Z and energy dependence of the photoionization cross sections for these subshells. In addition, calculations have been performed for 3*s*, 4*s*, 5*s*, 4*p*, 5*p*, 5*d*, 5*d* and 4*f* subshells in certain elements. The results, which are considerably different from the predictions of the hydrogen-like model, show certain regularities which are explained in terms of the potentials. Comparisons with experiment show that the model correctly predicts the gross spectral shape of photoionization cross sections but the results are somewhat numerically inaccurate in the vicinity of large absorption peaks. This calculation is considered to be a first approximation which can be improved by taking exchange into account more exactly and by including electron-electron correlation.

Key Words: Central potential model; photoabsorption cross section; photoionization cross section; soft X-rays.

Maximon, L. C., and Tzara, C., **Influence of the radiative background on muon and electron scattering from nuclei,** *Physics Letters* **26B,** *No. 4, 201–203 (Jan. 22, 1968).*
The influence of radiative tails and radiative corrections to inelastic scattering on nuclei at low excitation is compared for muons and electrons. It is found that only for low momentum transfers $Q \lesssim 50$ MeV/*c* is the radiative background substantially less for muons than for electrons.

Key Words: Muon scattering; electron scattering; inelastic scattering; radiative tail; radiative corrections.

O'Connell, J. S., and Prats, F., **Photodisintegration of the tri-nucleon system in a separable potential model,** *Physics Letters* **26B,** *No. 4, 197–200 (Jan. 22, 1968).*
Two- and three-body photodisintegration cross sections of ^{3}H and ^{3}He are calculated. The ground state wave function used is an exact solution of the three-body Schrödinger equation with separable potentials of the Yamaguchi type. The final states contain the interactions between nucleon pairs. Results are shown both for the Yamaguchi-Sitenko-Kharchenko set and for the Tabakin set of interaction parameters.

Key Words: Cross sections; electric dipole; helium-3; photodisintegration; separable potential; tritium.

Pfeiffer, E. R., and Schooley, J. F., **Effect of stress on the superconductive transition temperature of strontium titanate,** *Phys. Rev. Letters* **19,** *No. 14, 783–785 (Oct. 2, 1967).*
The superconductive transition temperatures T_c of single crystal specimens of reduced strontium titanate have been measured as functions of hydrostatic and uniaxial compressional stresses up to 1.5 kbar. The prominent features of the experimental results are a large non-linear hydrostatic pressure effect and an anisotropic uniaxial stress effect. The relative decrease of transition temperature with pressure $d \ln T_c/dp$ is about an order of magnitude larger than that seen in metallic superconductors.

Key Words: Anisotropic uniaxial stress effect; hydrostatic pressure; reduced strontium titanate; single crystal; stresses; superconductive transition temperatures; uniaxial stresses.

Swanson, N., **Characteristic energy-loss spectra and $-\mathrm{Im}(1/\epsilon)$ for amorphous and polycrystalline Al_2O_3,** *Phys. Rev.* **165,** *No. 3, 1067–1070 (Jan. 15, 1968).*
Characteristic energy loss spectra of 20 keV electrons in amorphous and polycrystalline Al_2O_3 have been measured in transmission at zero scattering angle. The dominant loss peak, due to plasmon excitation, occurred at 22.6+0.2* eV and 24.3+0.2 eV for the amorphous and polycrystalline films, respectively. Lower lying weaker losses were observed at about 8.7 eV and 13.5 eV in both films, with an additional loss at 17.7 eV in the polycrystalline film. Using a previously developed technique, values of $-\mathrm{Im}\epsilon^{-1}$ and electron energy loss oscillator strength were derived from the loss spectra. The results for anodized Al_2O_3 are in excellent agreement with existing optical measurements.

*(estimated uncertainty).

Key Words: Characteristic energy loss; aluminum oxide; dielectric constant; oscillator strength; cross section; plasmon.

Swartzendruber, L. J., and Bennett, L. H., **The effect of Fe on the corrosion rate of copper rich Cu-Ni alloys,** *Scripta Metallurgica* **2,** *93–98 (1968).*
The occurrence of a minimum in the reduction of the corrosion rate in hot sea water upon the addition of small quantities of Fe to copper rich Cu-Ni alloys is studied in relation to the Mössbauer spectra of ^{57}Fe in these alloys. It is proposed that as long as Fe remains in solid solution it reduces the corrosion rate due to the formation of local magnetic moments, but when Fe rich precipitates are formed the corrosion rate increases.

Key Words: Corrosion; iron; copper; nickel; Mössbauer effect; magnetic moment; d-electron.

Vriens, L., Simpson, J. A., and Mielczarek, S. R., **Tests of Born approximations: differential and total $2\,^3S$, $2\,^1P$, and $2\,^1S$ cross sections for excitation of He by 100- to 400-eV electrons,** *Phys. Rev.* **165,** *No. 1, 7–15 (Jan. 5, 1968).*
The angular dependence of $2\,^3S$, $2\,^1P$ and $2\,^1S$ excitation of He for incident electron energies from 100 to 225 eV ($2\,^3S$) and 400 eV ($2\,^1P$ and $2\,^1S$) has been measured. Apparent generalized oscillator strengths $f(K)$ and differential cross sections for the transition $1\,^1S \rightarrow 2\,^1P$ are obtained by normalizing on the optical oscillator strength of Schiff and Pekeris. From the experimental intensity ratios $2\,^3S/2\,^1P$ and $2\,^1S/2\,^1P$ we then calculate differential $1\,^1S \rightarrow 2\,^3S$ and $1\,^1S \rightarrow 2\,^1S$ cross sections. The differential cross sections are integrated to get total cross sections. The $f(K)$ found here for $2\,^1P$ and $2\,^1S$ excitation decrease faster with increasing K than in earlier studies. Departures from the Born approximation appear only below 200 eV for $2\,^1P$ excitation, but occur at higher energy for $2\,^1S$ excitation and are larger for large momentum transfers. The angular dependence found for $2\,^3S$ excitation disagrees strongly with the Ochkur approximation. Our total $2\,^3S$ cross sections are much lower than all other existing theoretical and experimental data.

Key Words: Born approximation; cross sections; electrons; excitation cross sections; helium; Ochkur approximation.

Weiss, A. W., **Theoretical multiplet strengths for Mg I, Al II, and Si III,** *J. Chem. Phys.* **47,** *No. 9, 3573–3578 (Nov. 1, 1967).*
Superposition of configurations wavefunctions have been computed for the ground state and some lower excited states of the first three members of the magnesium isoelectronic sequence. The excited states are all those with configurations involving the low-lying orbitals, 3*s*, 3*p*, 3*d* and 4*s*. Multiplet strengths were also computed for all the allowed electric dipole transitions among these states. Only excitations of the outer two valence electrons were included in the multi-configuration expansion, with the virtual orbitals being derived from a pseudo-natural orbital transformation. Comparisons are made with predictions of the *Z*-expansion method.

Key Words: Superposition of configurations; wavefunctions; multiplet strengths.

Yakowitz, H, and Heinrich, K. F. J., **Quantitative electron probe microanalysis: Absorption correction uncertainty,** *Mikrochim. Acta* **1,** *182–200 (1968).*
The accuracy of the x-ray absorption correction for quantitative microprobe analysis is affected by errors in the input parameters (mass attenuation coefficients, x-ray emergence angle, and operating voltage), as well as by inaccuracies in the proposed absorption correction models. If the mass attenuation coefficient is known within 5%, then to keep the error of this correction below 1%, the absorption function, $f(x)$, must be equal to or higher than 0.8. Experimental conditions leading to small absorption corrections are discussed, and the advantages of high x-ray emergence angles are demonstrated. As an illustration, the analysis (theoretical and experimental) of aluminum-magnesium alloys is discussed.

Key Words: Absorption of x-rays; Al-Mg analysis; electron microprobe; errors in microanalysis; quantitative microanalysis; microprobe absorption correction comparisons; microprobe experimental conditions.

Ausloos, P., and Lias, S. G., **Gas-phase photolysis of hydrocarbons in the photoionization region,** *Rad. Res. Rev.* **1,** *No. 1, 75–107 (Mar. 1967).*
When a molecule is irradiated with photons whose energy is higher than the threshold for ionization, not only ions but also neutral excited molecules, similar in lifetime and behaviour to those formed at lower energies, will be produced. Until very recently, most studies of molecules irradiated in the photoionization region have been concerned only with ionization phenomena. Such studies ranged from simple measurements of ion currents during photolysis to actual identification and quantitative measurement of the ions formed, by means of a light source linked with a mass spectrometer. In these studies, which have been reviewed recently, the fate of the excited molecules was generally not considered since the light sources used were of such low intensity that the steady state concentration of neutral intermediates was necessarily well below the limits of detection for uncharged species.
The study of the behaviour of neutral excited molecules is of concern to the photochemist and radiation chemistry who usually deduce information about primary and secondary processes from a chemical analysis of the final products formed when a compound is irradiated in a closed vessel. The recent development of high intensity monochromatic light sources in the vacuum ultraviolet wavelength range made possible the use of traditional photochemical methods in the investigation of events following absorption of radiation in the photoionization region. This review is primarily concerned with presenting information derived from such studies; the emphasis will be on information obtained from analysis of end products formed upon photolysis in a closed system. Information from studies concerned with physical measurement of ionization phenomena will be presented here whenever pertinent, but a complete survey of these studies is not within the scope of this review. It is evident that, in addition to permitting the study of the excitation events which accompany photoionization phenomena, the use of a closed system also allows the investigator a certain flexibility in the design of his experiments denied him by the nature of the instrumentation in alternate approaches such as mass spectrometry. For example, pressure and temperature can easily be varied over wide ranges permitting him to determine the effect of these parameters on ionic and neutral fragmentation mechanisms.

Key Words: Hydrocarbons; gas phase photolysis; excitation; ionization; absorption.

Ausloos, P., and Lias, S. G., **Gas-phase radiolysis of hydrocarbons,** *Book, Actions Chimique et Biologiques des Radiations, Ed. M. Haissinsky, 10, 1 (Masson and Company, Paris, France, 1967).*
This manuscript is a critical review of the gas phase radiolysis of hydrocarbons covering the literature up to September 1, 1966.

Key Words: Hydrocarbon; radiolysis; ion molecule reactions; neutral excited molecules; free radicals.

Ausloos, P., and Lias, S. G., **Photoionization of cycloalkanes in the gas phase. A study of charge transfer-processes,** *Book, The Chemistry of Ionization and Excitation, Ed. G. Johnson and G. Schales, pp. 77–89 (Taylor and Francis, Ltd., London, England, 1967).*
The photoionization of cyclopentane (I.P. 10.5 eV), cyclohexane (I.P. 9.9 eV), and cycloheptane (I.P. 10 eV) has been investigated at 11.6–11.8 eV using an argon resonance lamp as light source. It is shown that, because of the limited degree of fragmentation of the parent cycloalkane ion at these energies, the importance of charge transfer between the different cycloalkanes can be evaluated. The yield of the parent cyclohexane ion is estimated by measuring the products CD_3CDHCD_2H and C_3D_8 formed by the H_2 and D_2 transfer reactions

$$C_nH_{2n}^+ + C_3D_6 \rightarrow C_nH_{2n-2}^+ + CD_3CDHCD_2H$$

$$C_nD_{2n}^+ + C_3D_6 \rightarrow C_nD_{2n-2}^+ + C_3D_8$$

On the basis of these reactions, charge transfer can readily be established in mixtures such as $C_6H_{12}-C_6D_{12}$, $C_6D_{12}-C_5H_{10}$, $C_5D_{10}-C_7H_{14}$, and $C_6D_{12}-C_7H_{14}$ to which small amounts of propylene-d_6 have been added. It is, for instance, noted that charge transfer occurs from $C_6D_{12}^+$ to C_6H_{12} as well as from $C_6H_{12}^+$ to C_6D_{12}. In addition, the cyclohexane parent ions can transfer their charge to propylene. Taking this process into account, a value of 0.38 is obtained for the equilibrium ratio $C_6D_{12}^+/C_6H_{12}^+$, independent of the composition of the mixture. In the mixtures of cycloalkanes of different chemical identity, charge transfer from the parent ion with the higher ionization potential to that with the lower ionization potential occurs efficiently. It is shown that charge transfer occurs in all cases with a rate which is comparable to that of the H_2 and D_2 transfer reactions, whose rate is probably close to the collision rate.

Key Words: Charge transfer; cycloalkanes; photochemistry.

Ausloos, P., Scala, A. A., and Lias, S. G., **Ion-molecule reactions in the condensed-phase radiolysis of hydrocarbon mixtures II. Cyclopentane and cyclohexane,** *J. Am. Chem. Soc.* **89,** *3677–3683 (1967).*
The radiolysis of *c*-C_5H_{10} and *c*-C_6H_{12}, as well as of equimolar *c*-$C_5H_{10}-c$-C_5D_{10} and *c*-$C_5H_{12}-c$-C_6D_{12} mixtures has been investigated in the presence of 0.5 to 5 mole percent $(CD_2)_3$, C_2D_2, C_2D_4, or CD_3CDCD_2. Isotopic analysis of the products formed in the radiolysis of cycloalkane-$(CD_2)_3$ mixtures points to the occurrence of the following ion-molecule reactions: (a) $C_nH_{2n}^+ + (CD_2)_3 \rightarrow C_nH_{2n-2}^+ + CD_2HCD_2CD_2H$ and (b) $C_nH_{2n}^+ + (CD_2)_3 \rightarrow C_nH_{2n-1}^+ + CD_2HCD_2CD_2$. The formation of *n*-propyl radicals in reaction (b) is confirmed by the production of $CD_3CD_2CD_2H$ as in major species in the radiolysis of $C_nD_{2n}-(CD_2)_3-H_2S$ mixtures. The ion molecule character of the reactions is further confirmed by the facts that addition of a known parent ion interceptor such as H_2S reduces *G* (propane) while addition of an electron scavenger such as CCl_4 raises *G* (propane). When cyclopentane is the solvent, the H_2-transfer reaction (a) is of major importance. The most efficient H_2-acceptor molecule for the cyclopentane parent ion is C_2D_4, and the least efficient is C_2D_2. When *c*-$C_5H_{10}-c$-C_5D_{10} (1:1) mixtures are irradiated in the presence of deuterated H_2-acceptor molecules such as C_2D_4 or C_2D_2, the ratio of products of reaction (a) $C_2D_4H_2/C_2D_6$ or $C_2D_2H_2/C_2D_4$ is greater than unity, indicating the occurrence of charge transfer processes favoring the formation of *c*-$C_5H_{10}^+$: (c) $c\text{-}C_5D_{10}^+ + c\text{-}C_5H_{10} \rightarrow c\text{-}C_5H_{10}^+ + c\text{-}C_5D_{10}$. A decrease in the mole percent of the C_2D_4 or C_2D_2 from 6% to 2% raises $C_2D_4H_2/C_2D_6$ or $C_2D_2H_2/C_2D_4$ from 1.7 to 2.6, demonstrating that relatively high concentrations of H_2-acceptor molecules can interfere with the charge transfer mechanism. When cyclohexane is the solvent, reaction (b) predominates over reaction (a). A plot of the square root of the $(CD_2)_3$ concentration versus *G* (propane) yields a straight line which goes through the origin, demonstrating the difficulty of obtaining chemical evidence for the presence of free ions.

Key Words: Ion-molecule reactions; H_2-transfer reactions; cyclopentane; cyclohexane; free radical.

Bates, R. G., and Covington, A. K., **Behavior of the glass electrode and other pH-responsive electrodes in biological media,** *Ann. N.Y. Acad. Sci.* **148,** *67–80 (Feb. 1, 1968).*
The theory and experimental techniques underlying the use of hydrogen-ion-responsive electrodes in biological systems are reviewed. Particular attention is given to the development of special forms of electrodes for bio-medical purposes and to applications reported during the past 15 years.

Key Words: Electrodes; bioelectrodes; pH measurement; biological systems; glass electrode; antimony electrode; quinhydrone electrode; membrane electrodes.

Currie, L. A., **Limits for qualitative detection and quantitative determination, application to radiochemistry,** *Anal. Chem.* **40,** *No. 3, 586–593 (Mar. 1968).*
The occurrence in the literature of numerous, inconsistent and limited definitions of a "detection limit" has led to a re-examination of the questions of signal detection and signal extraction in analytical chemistry and nuclear chemistry. Three limiting levels have been defined: L_C – the net signal level (instrument response) above which an *observed* signal may be reliably recognized as "detected"; L_D – the "true" net signal level which may be *a-priori* expected to lead to detection; L_Q – the level at which the measurement precision will be satisfactory for quantitative determination. Exact defining equations as well as series of working formulae are presented both for the general analytical case and for radioactivity. The latter, assumed to be governed by the Poisson distribution, is treated in such a manner that accurate limits may be derived for both short- and long-lived radionuclides either in the presence or absence of interference. The principles are illustrated by simple examples of spectrophotometry and radioactivity, and by a more complicated example of activation analysis in which a choice must be made between alternative nuclear reactions.

Key Words: Detection limit; determination limit; decision level; analytical chemistry; activation analysis; interference; radioactivity; Poisson distribution; hypothesis testing.

Fatiadi, A. J., **Stable radicals obtained by treatment of azulene with periodic acid and other oxidants,** *Chem. Commun.* **8,** *456–458 (Apr. 24, 1968).*
Treatment of the non-benzenoid, aromatic hydrocarbon azulene with periodic acid gives a free radical which is extremely stable to air and heat; the product has been found to be polymeric. Treatment of azulene with iodic acid of antimony pentachloride also gives stable free radicals.

Key Words: Azulene; periodic acid; polymeric product; stable free radical.

Haller, W., **Correlation between chromatographic and diffusional behaviour of substances in beds of pore controlled glass. Contribution to the mechanism of steric chromatography,** *J. Chromatog.* **32,** *676–684 (1968).*
Chromatography and diffusion experiments were performed with columns and suspensions of grains of pore-controlled glass of 620 Å pore diameter. The elution positions of tobacco mosaic virus and of benzyl alcohol coincide with the actual void volume and the total fluid volume of the column. A spherical virus (MS2) of 260 Å diameter eluted at a normalized elution volume of $k_e = 0.44$, and its peak position shifted only very slightly over a wide range of elution rates.
The diffusional uptake of virus (MS2) by the porous glass grains from a well stirred suspension indicated that the total pore volume of the glass was accessible to the virus. It took approximately 30 seconds for one half of the ultimate amount of virus to penetrate

the glass. In the light of these results it is very unlikely that a volume exclusion mechanism determines the elution position of the virus. Since porous glass columns of uniform and controlled pore size display elution spectra similar to those of gel columns, it is also unlikely that volume exclusion governs the elution spectrum in steric chromatography on gels.

Key Words: Chromatography; diffusion; gel chromatography; gel filtration; gel-permeation chromatography; glass; chromatography; GPC; pore-controlled glass; restricted diffusion; steric-exclusion chromatography.

Hetzer, H. B., Robinson, R. A., and Bates, R. G., **Conventional pa_H values for buffer solutions of piperazine phosphate from 0° to 50° C**, *Anal. Chem.* **40**, *634–636 (Mar. 1968).*
Values of $pa_H(=-\log a_H^+)$ have been determined for solutions of piperazine phosphate (molality 0.02 and 0.05 mol kg^{-1}) from 0 to 50 °C by means of emf measurements of cells without liquid junction.

Key Words: Piperazine phosphate; buffer solutions; *p*H.

Ito, J., **A new yttrium magnesium silicate garnet, $Y_6Mg_2Si_3O_{24}$ and its rare earth and nickel analogues,** *Mater. Res. Bull.* **2**, *1093–1098 (1967).*
A new magnesium yttrium silicate garnet and its rare-earth analogues with 4 and 6 coordinated magnesium and nickel ions have been synthesized hydrothermally. Its solid solubility with yttrium aluminum garnet was investigated.

Key Words: Hydrothermal synthesis; rare-earth garnet; crystal chemistry; X-ray powder analysis.

Lafferty, W. J., **Direct l-type doubling transitions in some axially symmetric molecules,** *J. Mol. Spectry.* **25**, *No. 8, 359–364 (Mar. 1968).*
Direct l-type doubling transitions have been observed in the states v_5^1 in FCN, v_7^1 and $3v_7^1$ in cyanoacetylene and ν_8(E) in methyl cyanide. Precise values for q and the higher order term μ have been obtained for each of these vibrations. The effect of the l-type resonance between the π and Φ levels of $3\nu_7$ of cyanoacetylene is discussed.

Key Words: Direct l-type doubling transitions; microwave spectroscopy; l-type resonance; l-type doubling constants; fluorocyanogen; cyanocetylene; methyl cyanide.

Marantz, S., and Armstrong, G. T., **Heats of combustion of trans-stilbene and trans-2,2′,4,4′,6,6′-hexanitrostilbene (HNS),** *J. Chem. Eng. Data* **13**, *No. 1, 118–121 (Jan. 1968).*
The standard heats of combustion, ΔH_{c298}°, of trans-stilbene(c) and trans-2,2′,4,4′,6,6′-hexanitrostilbene(c) were measured in an oxygen bomb calorimeter to be -1759.28 kcal mol^{-1} and -1535.54 kcal mol^{-1}, respectively. Estimated uncertainties of these results were 0.93 kcal mol^{-1} and 1.08 kcal mol^{-1} including contribution of errors from both random and systematic sources. With these results, the standard heats of formation, ΔH_{f298}°, of trans-stilbene(c) and trans-2,2′,4,4′,6,6′-hexanitrostilbene(c) were calculated to be -32.68 kcal mol^{-1} and -13.89 kcal mol^{-1}, respectively. The standard heats of formation of the gas phases were calculated to be -12.0 and $+29.2$ kcal mol^{-1}, respectively.
In the light of these results, and analogous data for toluene(g) and trinitrotoluene(g), the addition of six nitro groups to trans-stilbene may be interpreted as weakening the central C=C bond by 34.1 kcal mol^{-1}.

Key Words: Stilbene, heat of combustion; hexanitrostilbene, heat of combustion; bond energy; (C=C) bond.

May, L., Spijkerman, J. J., **Mössbauer spectroscopy,** *Chemistry* **40**, *14–17 (Dec. 1967).*
A review of Mössbauer spectroscopy is presented for the high school senior and college freshmen chemistry students. The fundamental concepts of nuclear resonance fluorescence are described in particular for its application to Chemistry. Specific examples are given of how Mössbauer spectroscopy solved analytical and structural problems. A list of selected references are included for further study by the readers.

Key Words: Review; Mössbauer spectroscopy; chemistry.

Scala, A. A., and Ausloos, P., **Condensed-phase photolysis and radiolysis of 2-methylbutane,** *J. Chem. Phys.* **47**, *No. 12, 5129–5139 (Dec. 15, 1967).*
The condensed phase photolysis of i-$C_5H_{12}-i$-C_5D_{12} mixtures, and of $CH_3CD(CH_3)CH_2CH_3$ has been investigated at photon energies above and below the ionization energy of 2-methylbutane (10.32 eV), that is, at 1470 Å (8.4 eV), 1236 Å (10.0 eV) and 1048–67 Å (11.6–11.8 eV). The electronically excited 2-methylbutane molecule undergoes essentially the same decomposition processes in the condensed phase as in the gas phase. The internally excited fragments formed in primary processes are entirely deactivated. In the krypton and argon sensitized radiolysis at 77 and 20 °K, respectively, energy transfer from the rare gas matrix to 2-methylbutane occurs with high efficiency. In these experiments, all products can be accounted for by decomposition of neutral excited 2-methylbutane, formed by excitation transfer and/or neutralization of ions formed in charge transfer reactions with rare gas ions.
In the radiolysis of pure 2-methylbutane in the presence of oxygen at 77 °K or at 195 °K, ethane and propane are almost entirely formed through molecular elimination and geminate radical disproportionation processes. Addition of an electron scavenger such as CCl_4 lowers the yields of these products, as well as those of the corresponding olefins (e.g. C_6H_6 and C_2H_4 indicating that in the pure alkane, these products are mainly formed as a result of neutralization of the parent ion. Apparently fragmentation of the parent ion is unimportant. The product butane ($G \sim 0.1$) can, however, with some degree of certainty be related to the reaction of the fragment $C_4H_8^+$ ion. The modes of formation of other products, such as the pentenes and the hydrogen remain unexplained.

Key Words: Condensed phase radiolysis; photolysis; 2-methylbutane; ionization.

Spijkerman, J. J., **The Mössbauer chemical shift in tin chemistry,** *Advan. Chem. Ser.* **68**, *105–112 (1968).*
The Mössbauer spectra of a large number of organic and inorganic tin compounds have been published. From these spectra, the oxidation state of tin in most compounds can be determined.
To interpret the Mössbauer spectra properly, the relationship between the chemical shift and the electron density at the Sn nucleus must be established. This requires that the magnitude and sign of $\Delta R/R$ (a factor that relates the change in the effective charge radius of the tin nucleus on passing from the excited to the ground state) must be known in most instances, this factor can be determined from nuclear shell model calculation, but, for tin, it must be evaluated experimentally. The discussion includes the results of the various experiments that were designed to obtain this factor so that the chemical shift observed for tin compounds could be interpreted correctly.

Key Words: Mössbauer spectroscopy; chemical shift; tin chemistry.

Astin, A. V., **A time for action in international standardization,** *Mater. Res. Std.* **8**, *No. 5, 18–24 (May 1968).*
Technology and economics find a common challenge in the field of international standardization. How well or poorly America faces this challenge will have a great influence on the stature of the United States in the world markets. Since the resources for standards used in U.S. trade are in the private sector, it behooves private industry and groups such as ASTM in the private sector to fulfill the urgent need for sound standards.

Key Words: Standards; evaluation; consumers; purchasing.

Eberhard, J. P., **Systems and design—an extrapolation to 2000 A.D.,** *Mater Res. Std.* **8**, *No. 5, 12–17 (May 1968).*
Systems analysis is necessary for a thorough rethinking of major hardware problems of the city. One of the problems concerns itself with performance standards in this context and their need to include an understanding of how they interact with man. A need for an ideal model of the highest concept of civilization must be defined in order to build a practical approach to urban systems design and construction. It is hoped that new mass production techniques may provide practical solutions to the problem of low cost urban living units that will be both attractive as well as providing inspiration. This paper

was originally presented at the Third Annual Meeting of the National Academy of Engineering, 20–24 September, 1967, University of Michigan, Ann Arbor, Mich.

Key Words: Systems engineering; city planning; standards; human factors.

Schofer, R. E., and Levin, B. M., **The urban transportation planning process,** *Socio-Econ. Plan. Sci.* **1,** *185–197 (Pergamon Press Ltd., London, England, 1967).*
The goal of urban transportation planning is to develop a plan for efficient, balanced transportation system for an urban area—one which will promote a desirable pattern of human activities. While the process has been standardized to some extent, each study must nevertheless acquire and manage a massive amount of information about the specific region with which it is concerned. This information, together with computer representations of transportation networks and travel patterns, is used to produce estimates of future travel demand and utilization of facilities. Thus computers play an inportant role in providing transportation planners with the capability for evaluating a variety of proposed transportation systems in order to recommend allocation of government resources and to guide transportation policy. This paper describes specific computer applications to the process of urban transportation planning.

Key Words: Transportation planning; urban transportation; systems analysis; travel forecasting; modal choice.

Jespersen, J. L., Kamas, G., and Morgan, A. H., **A proposed ranging system with application to VLF timing,** *IEEE Trans. Instr. Meas.* **IM-16,** *No. 4, 282–285 (Dec. 1967).*
In general, it is not possible to determine the range between a radio transmitting and receiving site by making only passive observations at the receiving site. However, if the medium is dispersive, signals transmitted simultaneously from the same site, at different carrier frequencies, will not arrive simultaneously at some distant point. Thus, the difference in arrival time is related to the observer's distance from the transmitter. This effect is considered in conjunction with the VLF two-frequency timing system.

Key Words: VLF; Range; Time; Dispersion.

Damburg, R. J., and Geltman, S., **Excitation of $n=2$ states in hydrogen by electron impact,** *Phys. Rev. Letters* **20,** *No. 10, 485–487 (Mar. 4, 1968).*
A possible source of incompleteness in the most recent close coupling calculations for the excitation cross sections of the $n=2$ levels in hydrogen, some of the results of which disagree with experiment, is pointed out. We present a method which removes this difficulty by the implicit inclusion of all important effective polarization potential terms of order α/r^4.

Key Words: Hydrogen; excitation; polarization; close-coupling; Lyman α, electron impact.

Hanley, H. J. M., and Childs, G. E., **Discrepancies between viscosity data for simple gases,** *Science* **159,** *No. 3819, 1114–1117 (Mar. 8, 1968).*
It has been known for some time that Kestin and his co-workers have reported dilute gas viscosity coefficients which differ from the usually accepted values. Recent work supplements Kestin's results. We show that there is no evidence for not accepting this different data. We feel that the whole subject of dilute gas viscosity measurements above room temperature should be reexamined both from the experimenter's and correlater's viewpoint. There is evidence that published tables may be incorrect by as much as 10% above about 600 °K.

Key Words: Dilute gas; high temperature viscosity; discrepancies; argon; potential function; correlation.

Marshak, H., Langsford, A., Wong, C. Y., and Tamura, T., **Total neutron cross section of oriented ^{165}Ho from 2 to 135 MeV,** *Phys. Rev. Letters* **20,** *No. 11, 554–558 (Mar. 11, 1968).*
The effect of nuclear orientation on the total neutron cross section of the highly deformed ^{165}Ho nucleus has been measured from 2 to 135 MeV. The data are successfully fitted by adiabatic coupled-channel calculations. The origin of this effect can also be understood by a semi-empirical model which makes use of both the black-nucleus model and the nuclear Ramsauer effect.

Key Words: Black nucleus; coupled-channel calculations; nuclear deformation effect; nuclear orientation; nuclear Ramsauer effect; ^{165}Ho nucleus; optical model; total neutron cross section.

Weiss, A. W., **Theoretical electron affinities for some of the alkali and alkaline-earth elements,** *Phys. Rev.* **166,** *No. 1, 70–74 (Feb. 5, 1968).*
The $(ns)^2$ correlation energies for the negative ions, Li^-, Na^- and K^-, have been calculated by the method of superposition of configurations. Comparisons with Hartree-Fock calculations of the neutral species yield electron affinities of .62, .54, and .47 eV respectively. A study of the computed ionization potentials of the neighboring iso-electronic atoms and ions suggests a maximum uncertainty of .1 eV. Similar calculations on the $ns(np)^2\ ^4P$ states of Be^- and Mg^- indicate they are metastable with electron affinities, relative to the $nsnp\ ^3P$ of the neutral, of .24 and .32 eV respectively.

Key Words: Electron affinity; superposition of configurations; atomic wavefunction; correlation energy.

Wells, J. S., Matarrese, L. M., and Sukle, D. J., **Electron spin resonance in single crystals of anhydrous copper sulfate,** *J. Chem. Phys.* **47,** *No. 7, 2259–2262 (Oct. 1, 1967).*
The magnetic resonance of synthetic anhydrous copper sulfate has been investigated at 23.3 GHz at temperatures between 77 °K and 4.1 °K. In the paramagnetic region, the observed resonance consists of two lines. One of these is relatively narrow and remains essentially fixed even down to 4.1 °K. The second line is unusually broad and its behavior indicates that it is due to the copper ions in the anhydrous crystal. The g values and corresponding linewidths have been measured for the broad line at 77 °K. As the temperature drops to the Neel point, this broad line increases in width, shifts, and disappears rather rapidly, indicating that it is associated with the antiferromagnetic phase.

Key Words: Electron spin resonance; antiferromagnetic resonance; anhydrous copper sulfate.

Beckett, C. W., **Status of properties research in the kilodegree range,** *Book, The Characterization of High-Temperature Vapors, Ed. J. L. Margrave, Chapt. 1, pp. 3–15 (John Wiley and Sons, Inc., New York, N.Y., 1967).*
This paper is an informal discussion of the status of thermodynamic and other properties at high temperatures in relation to current technical needs. It contains comment on a few noteworthy achievements, some unexplored areas, and on the lag between basic research on properties and well-known technical needs. It is to be included in the transactions of an ACS symposium on high temperature chemistry at the request of the publisher.

Key Words: High temperature chemistry; high temperatures; kilodegree range; thermodynamic properties; vapors.

Bozman, W. R., **The application of computers in printing scientific manuscripts,** *Book, New Techniques in Office Operations, Chapt. 13, pp. 120–124 (The Business Press, Elmhurst, Ill., Mar. 1968).*
A description is given of the use of computers to help prepare a file of information on 30,000 organic and inorganic crystals. Some of the problems of input keyboarding, and data corrections are discussed, as well as cross-checking the data for internal consistency and preparation of the final output magnetic tape for operation of a phototypesetting machine.

Key Words: Data processing; phototypesetting; photocomposing; computer typesetting.

Brady, G., McIntyre, D., Myers, M. E., Jr., and Wims, A. M., **Critical scattering of perfluoroheptane-isooctane system** *(Proc. Cong. Small-angle X-ray Scattering, Syracuse Univ., Syracuse, N.Y., June 1965), Book, Small-Angle X-ray Scattering, Ed. H. Brumberger, pp. 425–448 (Gordon and Breach, Science Publ. Inc., New York, N.Y., 1967).*

The critical opalescence of mixtures of perfluoroheptane-isooctane near and at the critical concentration has been examined by x-ray scattering measurements over a large angular range.
The measurements are discussed and shown to agree well with the assumed correlation function proportional to $e^{-kr/r^{1.1}}$ near the critical temperature. The evidence for the persistence of large molecular clusters away from the critical point is reviewed.

Key Words: Critical opalescence; critical phenomena; low angle x-ray scattering; perfluoroheptane; isooctane; correlation function.

Braun, W., and Lenzi, M., **Resonance fluoroescence method for kinetics of atomic reactions. Reactions of atomic hydrogen with olefins,** *Disc. Far. Soc.* **44,** *252–261 (1967).*
Using the technique of flash photolysis, absorption of Lyman-α radiation by H atoms and measurement of the subsequent Lyman alpha emission, the absolute rate constants for the reaction of hydrogen atoms with several olefins have been measured at room temperature. The method distinguishes hydrogen from deuterium atoms and can be used to measure either.
The absolute limiting high pressure rate constants at room temperature for the reactions $H + C_2H_4$, C_2D_4, and trans-2-butene, have been found to be approximately the same, $k \doteq 1.0 \pm (15\%) \times 10^{-12}$ cc molecule^{-1} sec^{-1}. The absolute rate constant for the reaction H + isobutene was found to be $k = 3.8 \pm (15\%) \times 10^{-12}$ cc molecule^{-1} sec^{-1}. For the reaction $H + C_2H_4$ a pressure effect on the bimolecular rate constant has been observed and this effect is discussed. The experimental method is described in detail since it appears to be the first of its kind and in principle generally applicable to the study of reactions of atoms other than hydrogen or deuterium.

Key Words: Apparatus; hydrogen atom reactions; olefins; absolute rate constants; flash photolysis-emission spectroscopy; Lyman-α–fluoroescence.

Campbell, P. G., and Wright, J. R., **Asphalt hardening by gaseous oxidants: the relationship between softening point and chemical change as measured by infrared spectroscopy,** *J. Mater.* **2,** *No. 3, 581–596 (Sept. 1967).*
The use of oxidized asphalts has been increasing steadily and much work had been reported on the process of blowing asphalt fluxes to produce a coating grade asphalt. Previous work was reviewed in which asphalt fluxes were treated with various oxidants (oxygen, ozone, air, nitrogen oxides) at relatively mild temperatures and the complex changes taking place during the hardening process were studied by infrared spectroscopy. This work was extended to include other gaseous mixtures (sulfur dioxide, sulfur dioxide-air, nitrogen dioxide-air).
The study of the effects of the gaseous oxidants on the softening points of the asphalt fluxes with time of blowing indicated that, in every case, the rate of softening point increase was greater than that obtained when air alone was used to harden the flux. Infrared spectral analysis, in which changes in functionality are detected, was found to be a convenient method to follow the asphalt hardening process.

Key Words: Asphalt flux; carbonyl absorbance; coating-grade asphalt; infrared analysis; nitrogen oxides; oxidation; softening point; sulfur dioxide.

Catanzaro, E. J., **Absolute isotopic abundance ratios of three common lead reference samples,** *Earth and Planetary Sci. Letters* **3,** *No. 4, 343–346 (1968).*
The absolute isotopic abundance ratios have been determined for three common lead reference samples, using solid-sample mass spectrometry. Samples of known isotopic composition, prepared from nearly pure separated ^{206}Pb and ^{208}Pb isotopes, were used to calibrate the mass spectrometers. The resulting absolute values are as follows. GS 4: $^{204}Pb/^{206}Pb = 0.061888 \pm 0.000065$, $^{207}Pb/^{206}Pb = 0.95342 \pm 0.00036$, $^{208}Pb/^{206}Pb = 2.2181 + 0.0010$; NBS 200: $^{204}Pb/^{206}Pb = 0.068353 \pm 0.000072$, $^{207}Pb/^{206}Pb = 1.00538 \pm 0.00038$, $^{208}Pb/^{206}Pb = 2.3675 \pm 0.0011$; C.I.T. Pb Std.: $^{204}Pb/^{206}Pb = 0.060151 \pm 0.000063$, $^{207}Pb/^{206}Pb = 0.93081 \pm 0.00035$, $^{208}Pb/^{206}Pb = 2.1835 \pm 0.0010$. The indicated uncertainties are overall limits of error based on 95 percent confidence limits for the mean and allowances for effects of known sources of possible systematic error.

Key Words: Lead; isotopic abundances; absolute ratios; reference samples.

Clark, J. E., and Harrison, C. W., **Accelerated weathering of polymers: radiation,** *Appl. Polymer Symp.* **4,** *97–110 (1967).*
The objective of this work was to study the radiation characteristics in three artificial weathering devices and to do a preliminary survey of the effects of high-intensity irradiation on plastics.
An absolute radiometer was used to measure radiation characteristics in the xenon arc and sunshine carbon and enclosed carbon arc Weather-Ometers. The irradiance from the xenon arc was stable over one hour, but the irradiance from the carbon arcs fluctuated. Irradiance received in one hour at the sample drum for sunshine and enclosed carbon arcs ranged from 315 to 1020 W/m^2 and 297 to 679 W/m^2, respectively, while the xenon arc showed a relatively constant irradiance of 910 W/m^2. All three devices had a maximum irradiance near the center of the sample drum with intensities at top and bottom being 15–40% less.
Seven plastic films were exposed to a xenon arc over a 200-fold intensity range by decreasing the arc-to-sample distance.
At up to 6.1 times earth-level sunlight, no significant changes resulted within 100 hours. At 81 times earth-level sunlight, white-pigmented film decomposed within 30 hours and clear film showed changes in ultraviolet and infrared spectra within 69 hours. At 379 times earth-level sunlight, five clear plastics decomposed within 12 hours or less.

Key Words: Carbon arc; degradation; irradiance; photodegradation; plastics; polymers; radiation; radiometry; sun; weathering; xenon arc.

Cook, R. L., and Kirchhoff, W. H., **Further investigations on the microwave spectrum of NSF; evaluation of the molecular force field, centrifugal distortion constants, and the dipole moment,** *J. Chem. Phys.* **47,** *No. 11, 4521–4527 (Dec. 1. 1967).*
The measurements of the microwave spectrum of NSF has been extended to include transitions involving J as high as 40 and the centrifugal distortion effects have been accounted for. By combining the analysis of the vibrational and rotational spectra, the molecular force field for NSF has been calculated and the following quadratic potential constants, in mdynes/Å, were obtained: $f_1 = 10.703$, $f_2 = 2.872$, $F_\alpha/d^2 = 0.411$ and $f_{2\alpha}/d = 0.014$. Here 1 refers to the SN bond, 2 to the SF bond, α to the NSF bond angle and d is the geometric mean of the SN and SF bond distances. It was found that the data were too insensitive to calculate $f_{1\alpha}$ and f_{12} and these contants were assumed to be zero.
The dipole moment was calculated from the Stark effect of the $5_{1,4}$–$4_{2,3}$ transition and was found to be $1.902 \pm 0.012D$, where the uncertainty represents the spread in the value of the dipole moment obtained from different methods of treating the data.

Key Words: Dipole moment; microwave spectrum; pyrazole; Stark effect; structure; tautomerism.

Covington, A. K., Paabo, M., Robinson, R. A., and Bates, R. G., **Use of the glass electrode in deuterium oxide and the relation between the standardized $pD(pa_D)$ scale and the operational pH in heavy water,** *Anal. Chem.* **40,** *No. 4, 700–706 (Apr. 1968).*
Commercial glass electrodes have been compared both directly and indirectly with the deuterium gas electrode at 25° C in buffered solutions of pD from 1 to 13. It is confirmed that the glass electrode functions as well in heavy water as in ordinary water. The relation between the operational pH of a buffer solution in heavy water (obtained with a glass electrode standardized in an ordinary light buffer solution) and its pD or pa_D value obtained from measurements on cells without liquid junction has been examined and correction factors determined for both glass and gas electrodes. The operational pH of buffer solutions in heavy water at 25° C, measured with the glass electrode, can be converted into a pD value by adding 0.41 (molar scale) or 0.45 (molal scale) for $2 < pD < 9$.

Key Words: Glass electrode; deuterium oxide; heavy water; deuterium electrode; acidity; pD measurement.

Hughes, E. E., and Dorko, W. D., **Accurate mass spectrometric determination of low concentrations of carbon dioxide in nitrogen,** *Anal. Chem.* **40,** *No. 4, 750–755 (Apr. 1968).*
A method for the rapid and accurate determination of low concentrations of carbon dioxide in nitrogen has been developed. The method is based on high-pressure mass spectrometry in which the mass 44 to mass 28 ratio is compared to the same ratio in a carefully calibrated standard. Concentrations from 180 to 380 parts per million were determined with an accuracy of better than 1 percent.

Key Words: Mass spectrometric analysis; carbon dioxide; gas analysis; air analysis.

Kasuya, T., Lafferty, W. J., and Lide, D. R., Jr., **Microwave spectrum, structure, boron quadrupole coupling constants, and dipole moment of difluoroborane,** *J. Chem. Phys.* **48,** *No. 1, 1–4 (Jan. 1, 1968).*
The microwave spectra of $HB^{10}F_2$, $HB^{11}F_2$, $DB^{10}F_2$, and $DB^{11}F_2$ have been assigned. Rotational constants are 74494.82, 10496.74, and 9181.67 MHz for $HB^{11}F_2$; 77244.25, 10495.35, and 9221.49 MHz for $HB^{10}F_2$; 52896.09, 10498.29, and 8740.56 MHz for $DB^{11}F_2$; and 54081.82, 10496.89, and 8771.57 MHz for $DB^{10}F_2$. The structural parameters obtained from these constants and their estimated uncertainties are $r_{BF} = 1.311 \pm 0.005$ Å, $r_{BH} = 1.189 \pm 0.010$ Å and $<FBF = 118.3° \pm 1°$. The quadrupole coupling constants have been obtained. The dipole moment is 0.971 ± 0.010 *D*.

Key Words: Difluoroborane; microwave spectra; rotational constants; quadrupole coupling constants; dipole moment; molecular structure.

Lias, S. G., and Ausloo, P., **Gas-phase photolysis and radiolysis of isobutane,** *J. Chem. Phys.* **48,** *No. 1, 392–400 (Jan. 1, 1968).*
The photolysis of $(CH_3)_3CH$, $(CH_3)_3CD$, and of $(CH_3)_3CH-(CD_3)_3CD$ and $(CD_3)_3CD-H_2S$ mixtures has been investigated at 1470 Å (8.4 eV), 1236 Å (10.0 eV), and 1048–67 Å (11.6–11.8 eV). Since the irradiating photons in these experiments have energies both higher and lower than the ionization energy of isobutane (10.6 eV), the modes of decomposition of the "superexcited" molecule can be compared with those of the molecule excited to states below the ionization potential. On the basis of isotopic analyses of the major products, it was determined that the following primary modes of decomposition of the excited isobutane molecule occur in the photolysis at all three energies: $i\text{-}C_4H_{10}^* \rightarrow CH_4 + C_3H_6$; $i\text{-}C_4H_{10}^* \rightarrow C_2H_8 + CH_2$; $i\text{-}C_4H_{10}^* \rightarrow CH_3 + \text{sec-}C_3H_7$; $C_4H_{10}^* \rightarrow H_2 + i\text{-}C_4H_8$. Most of the propyl radicals decompose further: $C_3H_7\text{-}H + C_3H_6$; $C_3H_7 \rightarrow CH_3 + C_2H_4$. An increase in photon energy increases the relative importance of C–C cleavage processes. The parent ions formed in the photolysis with 11.6–11.8 eV photons decompose to form $C_3H_6^+$ and sec-$C_3H_7^+$. The $C_3H_6^+$ ions react with isobutane to form sec-C_3H_7 radicals or propane: $C_3H_6^+ + i\text{-}C_4H_{10} \rightarrow CH_3CHCH_3 + C_4H_9^+$; $C_3H_6^+ + i\text{-}C_4H_{10} \rightarrow C_3H_8 + C_4H_9^+$. The probability of the former reaction is 1.5 times that of the latter, in agreement with a value for this ratio derived from the radiolysis of $C_4D_{10}-H_2S$ and $C_4H_{10}-C_4D_{10}$ mixtures. The role of superexcited molecules in the radiolysis is discussed and it is estimated that the number of dissociating neutral excited molecules per ion pair is no greater than 0.46.

Key Words: Photolysis; photoionization; isobutane; ion-molecule reactions; free radical reactions; primary processes.

Maienthal, E. J., and Taylor, J. K., **Polarographic methods in determination of trace inorganics in water,** *Book, Trace Inorganics in Water, Chapt. 10, Advances in Chemistry Series 73, 172–182 (American Chemical Society, Wash., D.C., Apr. 1968).*
Polarography is a particularly suitable method for the determination of trace inorganic material in water. Owing to the selectivity of electrode processes, interferences and hence prior chemical separations are minimized. Often several elements may be determined concurrently in the same supporting electrolyte. Anodic stripping and linear sweep voltammetry give an increased sensitivity which permits determinations in the ppb range to be made. Polarographic methodology is reviewed. A survey of the literature concerned with determination of trace inorganic material in water is given. Procedures used in this laboratory for the determination of such elements as aluminum, arsenic, cadmium, copper, indium, iodine, iron, lead, tellurium, and zinc are discussed. The matrices include laboratory distilled water, river water, and reactor cooling water. In addition a comparative technique is described whereby precisions of better than 1% can be obtained at the 0.1 ppm level.

Key Words: Trace analysis; water analysis; polarographic analysis.

Mies, F. H., **Quantum oscillations in the shape of pressure-broadened atomic lines,** *J. Chem. Phys.* **48,** *No. 1, 482–494 (Jan. 1, 1968).*
Oscillatory or bandlike structure is predicted to occur in the wings of pressure-broadened atomic lines when the interaction potential between the emitting atom M* and the perturbing atom A is deeply attractive compared to kT and the interaction is the final state is repulsive. The oscillations in intensity arise from quantum effects and are associated with the nodal structure of the continuum wavefunction which describes the dissociated state of the diatomic molecule (A + M*). The number of maxima in the line shape is a measure of the number of bound states which can be supported in the potential while the amplitude and resolution of the oscillations depends on the long range behavior of the potential. The bandlike structure, which may extend over thousands of cm^{-1} on the long wavelength side of the atomic emission line, is resolvable as long as $kT <$ approx. $1/10$ the vibrational quantum $\hbar\omega_e$ of the AM* molecule. This is a generalization of similar bandlike structure which has been calculated *and observed* to occur in the collision induced radiation of helium metastable atoms and which is merely a special case of pressure broadening involving forbidden lines. Specific calculations are presented for the broadening of the hydrogen Lyman α line by H(1*s*), and the visible absorption spectra of H(1*s*) in the presence of free protons.
The quantum theory of line shape which is employed here was first developed by Jablonski but then neglected due to difficulties involved in evaluating essentially the bandstrength for continuum-continuum transitions of diatomic molecules. Jablonski introduced the W.K.B. and other approximations into his theory which reduced it to the classical statistical theory. These approximations are compared to exact quantum mechanical calculations. The W.K.B. approximation is shown to be quite valid in the special case of attractive-repulsive transitions, but Jablonski then improperly averaged over these very quantum oscillations of interest here. This structure offers a unique and extremely sensitive method of studying interaction potentials involving excited states of atoms.

Keywords: Pressure broadening; atomic lines; broadening; quantum mechanics; interaction potential; emission absorption; wavefunctions; W.K.B.; diatomic molecules; continuum-continuum transitions; band strengths.

Miller, K. J., and Krauss, M., **Born inelastic differential cross sections in H_2,** *J. Chem. Phys.* **47,** *No. 10, 3754–3762 (Nov. 15, 1967).*
First Born differential cross-sections are calculated for inelastic electron scattering of 300 eV electrons from the ground electronic-vibrational state of H_2 into the vibrational levels of the B, B′, C, D, and D′ Rydberg states. The initial and final state electronic wavefunctions were approximated by Hartree-Fock functions. In order to facilitate the calculation, the molecular orbitals were expanded in a linear combination of Gaussian-type atomic orbitals.
The variation of the electronic scattering amplitude was examined as a function of the molecular orientation, internuclear separation, and scattering angle (or electron momentum transfer). Use of the Franck-Condon factors to determine relative intensities for scattering into different vibrational levels yields errors less than 20 percent, and hence these factors are a good approximation to the relative intensities.
The theoretical differential cross-section for zero-angle scattering is in good agreement with the most recent experimental data. However, it is shown that transition moments extracted from electron scattering data are overestimated and in poor agreement with the theoretical values.

Key Words: Born cross-sections; hydrogen; Rydberg states; Hartree-Fock; differential cross-sections.

Rebbert, R. E., and Ausloos, P., **Photolysis of methyl iodide in matrices of organic compounds at 20 and 77 °K. Reactions of hot methyl radicals,** *J. Chem. Phys.* **48,** *No. 1, 306–311 (Jan. 1, 1968).*

Methyl iodide–hydrocarbon and methyl iodide–alcohol matrices have been photolyzed with 2537 Å radiation both at 20 and 77 °K. The probability of abstraction of an H atom by the hot CH_3 radical formed upon photodissociation CH_3I is at least a factor of 10 larger in the solid phase than in the gas phase. However, the relative probabilities of abstracting an H atom from various organic compounds are about the same in both phases. Also hot CH_3 radicals are more reactive than CD_3 radicals in both phases.
Photolysis of CH_3I or CD_3I in the presence of (a) equimolar mixtures of perprotonated and perdeuterated hydrocarbons and (b) partially deuterium labelled hydrocarbons, shows that the hot methyl radicals abstracts an H atom and D atom with equal probability. The hot methyl radical does, however, exhibit a certain selectivity as to the position in the molecule from where it abstracts an H atom. For instance, an H atom is abstracted more readily when attached to a secondary carbon atom than to a primary carbon atom. This nonstatistical behavior is, however, less accentuated in the solid phase than in the gas phase. When the matrix consists of an unsaturated hydrocarbon, the hot methyl radical can add to the double bond as well as abstract an H atom. It is shown that hot methyl radicals add to ethylene to form n-C_3H_7 radicals which subsequently react with the I atom with which they are in juxtaposition. At 20 °K about one-fourth of the hot methyl radicals add to C_2H_4.

Key Words: Methyl iodide; photolysis; hot methyl radicals; H atom; D atom.

van Reuth, E. C., and Waterstrat, R. M., **Atomic ordering in binary A15-type phases,** *Acta. Cryst.* **B24,** *Part 2, 186–196 (Feb. 1968).*
The degree of long-range order has been determined for 18 binary A15-type phases containing only transition elements. A tendency toward a lower degree of order was noted as the component elements were chosen successively from columns in the periodic table approaching the Mn column. A comparison of the ordering in the A15-type phases with the ordering previously reported for various binary sigma phases suggests that the remarkable stability of these phases may result from an interdependence between the electronic structure and the ability of the atoms to undergo deformations in conforming to geometrical packing requirements.

Key Words: A15-type phases; Beta-tungsten phases; ordering of atoms; transition metals; sigma phases; phase stability; electronic structure; atomic packing; order-disorder transformation.

Woelfel, J. B., and Paffenbarger, G. C., **Evaluation of complete dentures lined with resilient silicone rubber,** *J. Am. Dent. Assoc.* **76,** *582–590 (Mar. 1968).*
Twenty-four complete dentures, which had been in use for at least seven years, were lined with a soft resilient silicone rubber. The dentures did not warp or change dimensions significantly during or after the lining. The liner was tasteless, odorless, was well tolerated by the tissues, did not bond well to the periphery of the hard denture base, could not be easily removed for the relief of inflammed mucosa, nor were the stability and retention of the dentures improved over that expected from rebasing or relining a denture with a hard resin. On half of the lined dentures colonies of Candida albicans developed on the silicone rubber. Many of the colonies could not be brushed or scraped off and attacked the lining. The liner is not a cure all for denture problems as has been reported in the literature and its routine use is not recommended, but it has some limited applications in special cases.

Key Words: Dentures; resilient reliners; silicone rubber; retention; stability; Candida albicans; dimensional changes in dentures; oral tissues.

Coleman, J. A., **Germanium for gamma-ray detectors. A review of current problems,** *Book, Lithium-Drifted Germanium Detectors, STI/Publ./132, pp. 37–41 (International Atomic Energy Agency, Vienna, Austria, 1966).*
The performance of germanium gamma radiation detectors depends, to a large extent, on the quality of the germanium used to produce the devices. Presently, the demand for better resolution, faster response times, and larger volume detectors imposes severe requirements on the germanium for detectors in terms of crystal purity and perfection. The specifications commonly used to describe germanium for detectors, such as resistivity, carrier lifetime, and etch pit density, were originally derived from those used by the semiconductor device industry. The relevance of these specifications for material to produce a detector with good performance, including long-term stability, is not well-understood. A semiconductor detector requires extreme perfection throughout a large volume single crystal. Common transistors and diodes have much smaller volumes and often operate at much higher currents and noise levels than a radiation detector; therefore, material requirements are usually not as stringent as those for detectors.

The Electron Devices Section of the NBS is engaged in studies of the correlations between the properties of semiconductor materials and the performance of semiconductor devices fabricated from such material. Presently, the effects of carrier lifetimes and mobility and impurities such as oxygen, copper and gold in germanium, on the performance and stability of gamma ray detectors are being investigated. The use of germanium gamma ray detectors at NBS for such applications as activation analysis, photonuclear reaction studies, decay scheme investigations and Mossbauer spectroscopy is limited at the present time, but it is expected to be greatly expanded in the very near future.

Key Words: Germanium; gamma ray detectors; semiconductor detectors.

Coleman, J. A., Love, D. P., Trainor, J. H., and Williams, D. J., **Low-energy proton damage effects in silicon surface-barrier detectors,** *IEEE Trans. Nucl. Sci.* **NS–15,** *No. 1. 482–490 (Feb. 1968).*
In order to predict the useful lifetime of semiconductor detectors which operate in the Earth's trapped radiation belts, the effects of damage by 50 keV, 200 keV, 600 keV and 1 MeV protons on silicon, surface-barrier, transmission detectors have been studied for fluences from 10^{10} to 10^{14} protons/cm^2. Detector current, noise and capacitance increased with fluence, with significant increases occurring after 10^{13} protons/cm^2. Bias-voltage-dependent multiple peaking was observed with Am-241 alpha particles. The effect of damage by protons with these low energies is significantly reduced in transmission detectors if the protons enter the rear, aluminum contact rather than the front, gold contact.

Key Words: Proton; radiation effect; semiconductor; detector; silicon.

Foster, B. E., **Attenuation of x-rays and gamma rays in concrete,** *Mater. Res. Std.* **8,** *No. 3, 19–24 (Mar. 1968).*
Concrete is widely used as a shielding material against X-ray and gamma-ray sources. The purpose of the paper is to furnish a brief elementary background for the concrete technologist on the physics of X-ray shielding. A brief description is given of the characteristics of X-ray and gamma rays. This is followed by a short discussion of attenuation by the photoelectric, pair-production, and Compton effect mechanisms, as a function of X-ray or gamma-ray energy and barrier material. Performances of various shielding materials in various energy ranges are compared, and the problems in shield design brought about by the scattering processes are discussed.

Key Words: X-ray attenuation; gamma-ray attenuation; concrete shields.

Motz, J. W., and Sparrow, J. H., **A simple device for the energy and current measurement of an accelerator electron beam,** *Record of the IEEE 9th Ann. Symp. Electron, Ion, and Laser Beam Technology, Berkeley, Calif., May 9–11, 1967, pp. 34–41 (San Francisco Press Inc., San Francisco, Calif., May 1967).*
A simple apparatus has been developed which permits the simultaneous measurement of the electron energy and current of an accelerator electron beam. This measurement is accomplished with negligible interference of the beam during the continuous operation of the accelerator and applies to electron energies greater than approximately 50 keV. The apparatus consists of a thin aluminum foil which intercepts the beam with a negligible energy loss (less than 1 kilovolt), and two cylindrical aluminum electrodes which are positioned respectively on the incident and exit sides of the foil with axes normal to the foil surface and coincident with the beam direction. With a suitable distribution of electric potentials in this system,

the incident electrode current, I_i, is inversely proportional to the square of the electron velocity and the exit electrode current, I_e, is inversely proportional to the square of the product of the electron velocity and momentum. Therefore, when an electron beam passes through this system, the electron energy can be determined from the current ratio, I_i/I_e, and the incident electron current can be determined from the current, I_i, as shown in previous measurements with secondary emission monitors. The energy dependences described above for each electrode has been confirmed over a wide range of electron velocities by measurements carried out with a constant potential electron accelerator in the energy region from 50 to 500 keV.

Key Words: Electron beam; energy current; secondary electron; Møller scattering; Mott scattering; thin foils.

Berendt, R. D., Winzer, G. E., and Burroughs, C. B., **A guide to airborne, impact, and structure borne noise control in multifamily dwellings,** *FT/TS-24, (U.S. Dept. Housing and Urban Development, Supt. Doc's., Government Printing Office, Wash., D.C., Jan. 1968, $2.50).*
The guide analyzes the basic causes of the airborne, impact and structure-borne noise problems in multifamily dwellings and recommends corrective measures, building structures and construction techniques to alleviate and control such problems.
Airborne and impact sound insulation criteria for three grades of multifamily dwellings are presented and recommended for use by the FHA in its Minimum Property Standards. Sound insulation data, fire ratings, descriptions and architectural illustrations are presented for 137 wall constructions and 111 ceiling-floor structures. The guide is illustrated with 345 detailed architectural drawings which show the proper construction and installation of wall and floor assemblies, building equipment, appliances, heating, airconditioning, plumbing and electrical systems, services or utilities required for adequate sound insulation, noise control and privacy in multifamily dwellings.
In addition, the guide summarizes the sound insulation criteria of various foreign countries and contains three appendices which discuss fire ratings, the relationship between laboratory and field measurements of sound insulation and common noise sources.
Highly technical and mathematical discussions were purposely avoided in the writing of this guide, so that it could be widely used and readily understood by architects, builders, craftsmen, laymen and others engaged in the design and construction of multifamily residences.

Key Words: Airborne; multifamily; noise control; structure-borne noise control.

Bowman, H. A., Gallagher, W., and Schoonover, M. R., **The development of a working density standard** *(Proc. 20th Annual ISA Conf., Oct. 4–7, 1965, Los Angeles, Calif.) ISA Preprint No. 14, 8–4–65 (1965).*
Inasmuch as density is the ratio between two well standardized quantities, any working standard of density must be consistent with them. The establishment of fixed reference points on the density scale presents several unique problems which demand techniques and apparatus of interest to instrumentation scientists. NBS has gone far down the road toward a working standard. Progress to date and goals believed achievable at the present state of the art will be discussed.

Key Words: Density; density standard; volume; volumetric measurement; hydrostatic weighing.

Bullis, W. M., and Coleman, J. A., **Characterization of germanium and silicon for nuclear radiation detectors,** *Book, Nucleonics in Aerospace, Ed. P. Polishuk, pp. 166–175 (Plenum Press Inc., New York, N.Y., 1968).*
Semiconductor detectors have been extensively used for about eight years. Uncontrolled variations in the quality of germanium and silicon intended for this application have occurred during this period for reasons which, even now, are not well understood. Crystals are presently selected on the basis of room temperature resistivity, photoconductive decay lifetime and etch pit density. Use of these parameters does not always enable one to discriminate between material suitable for detector fabrication and material which is not. This paper describes a research program now in progress at the National Bureau of Standards which has the objective of identifying those parameters which will be the most useful in specifying detector-grade material. Because of the immediacy of the problem, study of results of this program should also be applicable in the characterization of detector-grade silicon.

Key Words: Carrier; drift mobility; carrier trapping; charge collection efficiency; energy resolution; gamma ray detectors; Hall mobility; infrared absorption; lithium drift mobility; lithium precipitation; oxygen; photoconductive decay lifetime; reverse recovery time.

Bur, A. J., and Roberts, D. E., **High polymeric materials,** *Digest of Literature on Dielectrics* **28,** *231–260 (1964).*
The literature on polymer dielectrics published in 1964 is reviewed. The following subjects are covered: theory; relaxation phenomena; dipole moments; semiconducting polymers; biopolymers; effects of radiation; and technology. This paper contains 229 references.

Key Words: Dielectrics; electrical insulation; polymeric materials; polymer dielectrics.

Cassidy, E. C., **Time-resolved studies of spectra produced by electrically exploded wires,** *Naturwissenschaften* **55,** *No. 3, 125–128 (1968).*
Time-resolved spectroscopic studies of electrically exploded wires are described. The spectral distribution of the radiation emitted by aluminum and titanium wires exploded in various controlled atmospheres are given. Atomic and molecular species produced by the explosion are identified. The effects of environment, pressure, and electrical energy input on the explosion spectrum are discussed, and conditions which were found to be conducive to the production of several selected spectral features by the exploding wire method are indicated. This paper summarizes the results of spectroscopic exploding wire studies at the U.S. National Bureau of Standards over the past few years.

Key Words: Exploding wire; time-resolved spectroscopy; electrical discharge; molecular spectra; atomic spectra; AlO.

Goldman, D. T., **Suggested procedures for utilizing MUFT resonance parameters to include Doppler broadening,** *Nucl. Sci. Engr.* **31,** *346–349 (1968).*
Keeping within the MUFT framework a method is proposed for including the effect of Doppler (temperature) broadening of resonances on the calculation of resonance integrals. This method is seen to be simple in its application. Some attempt has been made to determine its range of validity especially in comparison with the technique presently in use in MUFT. Finally an additional proposal is made to replace the Narrow Resonance Infinite Mass approximation presently in use in MUFT with the Narrow Resonance approximation for all nuclei.

Key Words: Neutron; resonances; Doppler broadening; and slowing down.

Hall, J. L., and Siegel, M. W., **Angular dependence of the laser photodetachment of the negative ions of carbon, oxygen, and hydrogen,** *J. Chem. Phys.* **48,** *No. 2, 943–945 (Jan. 15, 1968).*
The angular distribution of electrons photodetached by polarized (laser) light from (a beam of) negative ions is dependent on the type of initial and final angular momentum states available. In O^- and C^-, a *p*-type electron is photodetached into either *s*-wave or *d*-wave continuum states. The experimental angular distributions are consistent with the predicted 1) strong destructive interference between the *s*-wave and *d*-wave channels.
For H^-, only *s-p* transitions are expected, which is consistent with the experimental observation of pure $\cos^2\theta$ behavior in this case.

Key Words: Negative ion; photodetachment; angular distribution; photoelectron spectroscopy; O^-; C^-; H^-.

McKinley, J. D., **Effects of the reaction with bromine on nickel surface morphology,** *Surface Sci.* **10,** *No. 2, 287–290 (May 1968).*
Electron micrographs of single crystal nickel specimens show that exposure of nickel to bromine at 800 °K produces etch pits bounded by {100} crystallographic planes. The surface reaction product is

volatile $NiBr_2$; reaction proceeds by recession of the {100} planes into the metal.

Key Words: Nickel; bromine; surface reaction; surface morphology; single crystal; electron micrograph.

Tauke, J., Litovitz, T. A., and Macedo, P. B., **Viscous relaxation and non-Arrhenius behavior in B_2O_3,** *J. Am. Ceramic Soc.* **51,** *No. 3, 158–163 (Mar. 1968).*
Ultrasonic shear and longitudinal relaxation measurements were made in B_2O_3 over a large temperature range (650°–1000° C). From this data both the shear and volume relaxation time spectra were determined. Both spectra had the same temperature dependence, although the volume spectrum was always broader than the shear. The shear relaxation process can be represented by a single relaxation time above 800 °C in the region where the shear viscosity is Arrhenius. Both processes exhibit an increasingly broad distribution of relaxation times in the non-Arrhenius region. The temperature dependence of the shear spectrum was analyzed in terms of a distribution of activation energies. A surprising conclusion of this study is that activation energies smaller than the activation energy present in the Arrhenius region appear at low temperatures.

Key Words: Viscous relaxation; ultrasonic relaxation; B_2O_3; shear spectra of relaxation times.

Other NBS Publications

J. Res. NBS 72B (Math. Sci.), No. 2 (Apr.–June 1968), 75 cents.
The probability of an equilibrium point. K. Goldberg, A. J. Goldman, and M. Newman.
Differentiable generalized inverses. J. Z. Hearon and J. W. Evans.
On spaces and maps of generalized inverses. J. Z. Hearon and J. W. Evans.
Principal submatrices V: Some results concerning principal submatrices of arbitrary matrices. R. C. Thompson.
Mathematical basis for the plasma kinetic equations (BBGKY). J. J. Sopka.
On the diffusion of an ion sheet in Poiseuille flow. S. Jarvis, Jr.
A class of thickness-minimal graphs. A. M. Hobbs and J. W. Grossman.

J. Res. NBS 72C (Engr. and Instr.), No. 3 (July–Sept. 1968), 75 cents.
Gas density balance design considerations. E. C. Creitz.
Standard mismatch—the production of controlled small reflections in waveguides. L. Lewin.
Viscoelastic behavior of dental amalgam. P. L. Oglesby, G. Dickson, M. L. Rodriquez, R. M. Davenport, and W. T. Sweeney.
The steady-state creep behavior of dental amalgam. G. Dickson, P. Oglesby, and R. Davenport.
Koeser, R. L., Editor, **Report of the 52nd National Conference on Weights and Measures 1967,** *Spec. Publ.* **297** *(May 1968), $1.25* (This series was formerly known as the Miscellaneous Publication Series).

Safety rules for the installation and maintenance of electric supply and communication lines, Handb. 81, Supplement 2 (Mar. 1968), 5 cents.

Armstrong, R. W., NBS dynamic seat belt tester, Proc. 10th Stapp Car Crash Conf., 6571st Aeromedical Research Laboratory, Alamogordo, N. Mex., Nov. 8–9, 1966, pp. 38–45 (Society of Automotive Engineers, New York, N.Y., 1966).
Astin, A. V., Welcoming remarks (Proc. Fifth Transducer Workshop, National Bureau of Standards, Gaithersburg, Md., Oct. 3–4, 1967), Telemetry Working Group Document 112–68, 3–4 (Secretariat, Range Commanders Council, White Sands Missile Range, N. Mex., 1968).
Barnes, J. A., and Allan, D. W., An approach to the prediction of coordinated universal time, Frequency **5,** No. 6, 15–20 (Nov.–Dec. 1967).
Blandford, J. M., A progress report on the NBS–ARF apparel materials evaluation project, First Annual Conf. Apparel Research Foundation, Nov. 29–Dec. 1, 1967, Washington, D.C. (Apparel Research Foundation, Washington, D.C. 20036, 1967).
Bloss, R. L., The measurement of Strain (Proc. 22nd Annual ISA Conf., Sept. 11–14, 1967, Chicago, Ill.) ISA Preprint No. P1–1–PHYMMID–67 (1967).
Bowman, R. R., Remarks on the paper "Field strength above 1 GHz: Measurement procedures for standard antennas," Proc. IEEE **56,** No. 2, 216 (Feb. 1968).
Bridges, J. M., and Wiese, W. L., Comparison of the Stark widths of the Balmer lines H_β and H_α, Proc. Seventh Intern. Conf. Phenomena in Ionized Gases, Ed. B. Perovic and D. Tosic, III, No. 165, 165–167 (Gradevinska Knjiga Publ. Co., Beograd, Yugoslavia, 1966).
Brown, W. E., A mechanism for growth of apotitic crystals (Proc. Intern. Symp. Composition, Properties and Fundamental Structure of Tooth Enamel, London, England, Apr. 1964), Book, Tooth Enamel, pp. 11–14 (John Wright & Sons, Ltd., Bristol, England, 1965).
Butterfield, M. A., Care and preservation of the new media-equipment needs, Proc. A Pioneer Presentation of a National Symposium on the Impact of Automation on Documentation, Denver, Colo., Apr. 27–29, 1967, pp. 60–64 (1968).
Canfield, L. R., Johnson, R. G., Codling, K., and Madden, R. P., Comparison of an ionization chamber and a thermopile as absolute detectors in the extreme ultraviolet, Appl. Opt. **6,** No. 11, 1886–1888 (Nov. 1967).
Cuthill, J. R., McAlister, A. J., Williams, M. L., Watson, T. W., Density of states of Ni: Soft-x-ray spectrum and comparison with photoemission and ion neutralization studies, Phys. Rev. **164,** No. 3, 1006–1007 (Dec. 15, 1967).
Deslattes, R. D., Photoionization of the M shell of xenon, Phys. Rev. Letters **20,** No. 10, 483–484 (Mar. 4, 1968).
Deslattes, R. D., X-ray monochromators and resonators from single crystals, Appl. Phys. Letters **12,** No. 4, 133–135 (Feb. 15, 1968).
Domsitz, M. G., Transducer activities at NBS (Proc. Fifth Transducer Workshop, National Bureau of Standards, Gaithersburg, Md., Oct. 3–4, 1967), Telemetry Working Group Document 112–68, 11–12 (Secretariat, Range Commanders Council, White Sands Missile Range, New Mexico, 1968).
Hamer, W. J., A Joule centennial, J. Chem. Educ. **45,** No. 2, 123–125 (Feb. 1968).
Hughes, E. E., A simple technique for the absolute determination of atmospheric oxygen, Environ. Sci. Technol. **2,** No. 3, 201–203 (Mar. 1968).
Hilten, J. S., The National Bureau of Standards inter-agency transducer project—a progress report (Proc. Fifth Transducer Workshop, National Bureau of Standards, Gaithersburg, Md., Oct. 3–4, 1967), Telemetry Working Group Document 112–68, 17–36 (Secretariat, Range Commanders Council, White Sands Missile Range, New Mexico, 1968).
Jensen, M. W., Milk meters, farm milk tank testing, and plastic containers for milk, Proc. 31st Annual Meeting International Association of Milk Control Agencies, Biloxi, Mississippi, Oct. 23–25, 1967, pp. 26–31 (1968).
Kushner, L. M., The role of the Institute for Applied Technology (Proc. Fifth Transducer Workshop, National Bureau of Standards, Gaithersburg, Md., Oct. 3–4, 1967), Telemetry Working Group Document 112–68, 5–10 (Secretariat, Range Commanders Council, White Sands Missile Range, New Mexico, 1968).
Maki, A. G., Assignment of some DCN and HCN laser lines, Appl. Phys. Letters **12,** No. 4, 122–124 (Feb. 15, 1968).
Marzetta, L. A., Incorrect usage of exact closed-loop voltage gain formula in operational amplifiers, Analog Dialogue Letter **2,** No. 1. 6 (Mar. 1968).
Moore, C. E., Necrology: Carl C. Kiess, J. Opt. Soc. Am. **58,** No. 2, 292–293 (Feb. 1968).
Rasberry, S. D., Caul, H. J., and Yezer, A., X-ray fluoroescence analysis of silver dental alloys with correction for a line interference, Spectrochim. Acta **23B,** 345–351 (Mar. 1968).
Schima, F. J., and Hutchinson, J. M. R., Energy of the isomeric transition in ^{109}Ag, Nucl. Phys. **A102,** 667–672 (1967).
Simpson, J. A., Special sources of monoenergetic electrons, Book, Methods of Experimental Physics, Volume 4, Atomic and Electron Physics, Chapter, Sources of Atomic Particles, Section 1.1.7, pp. 124–135 (Academic Press Inc., New York, N.Y., 1967).

Stern, J., Activities of the Basic Instrumentation Section (Proc. Fifth Transducer Workshop, National Bureau of Standards, Gaithersburg, Md., Oct. 3–4, 1967), Telemetry Working Group Document 112–68, 13–15 (Secretariat, Range Commanders Council, White Sands Missile Range, N. Mex., 1968).

**Publications for which a price is indicated are available by purchase from the Superintendent of Documents, U.S. Government Printing Office, Washington, D.C. 20402 (foreign postage, one-fourth additional). The NBS nonperiodical series are also available from the Clearinghouse for Federal Scientific and Technical Information, Springfield, Va. 22151. Reprints from outside journals and the NBS Journal of Research may often be obtained directly from the authors.*

U.S. GOVERNMENT PRINTING OFFICE : 1968 OL—312-249

JRRA OCT 46129
UNIVERSITY MICROFILMS INC
ATTN SERIALS SECTION
300 NORTH ZEEB RD
ANN ARBOR MICH 48106

UNITED STATES
GOVERNMENT PRINTING OFFICE
DIVISION OF PUBLIC DOCUMENTS
WASHINGTON, D.C. 20402

OFFICIAL BUSINESS

POSTAGE AND FEES PAID
U.S. GOVERNMENT PRINTING OFFICE

JOURNAL OF RESEARCH of the National Bureau of Standards Vol. 72A, No. 5 September–October 1968
A. Physics and Chemistry

Contents

Page

Studies in bomb calorimetry. A new determination of the energy of combustion of benzoic acid in terms of electrical units. K. L. Churney and G. T. Armstrong. 453

Effect of low pressures on the room temperature transitions of polytetrafluoroethylene. G. M. Martin and R. K. Eby. 467

Electrostatic potentials and their spatial derivatives about point defects in ionic crystals. Herbert S. Bennett. 471

Electric fields produced by a charge density in ionic crystals. Herbert S. Bennett. 475

Mass spectrometric study of the photoionization of some fluorocarbons and trifluoromethyl halides. Clemente Juan Noutary. 479

Infrared matrix spectra of lithium fluoride. Stanley Abramowitz, Nicolo Acquista, and Ira W. Levin. 487

Electronic transition moment integrals for first ionization of CO and the A–X transition in CO^+. Some limitations on the use of the r-centroid approximation. Paul H. Krupenie and William Benesch. 495

The configurations $3d^n4p$ in doubly ionized atoms of the iron group. C. Roth. 505

Electron impact excitation of hydrogen Lyman-α radiation. Robert L. Long, Jr., Donald M. Cox, and Stephen J. Smith. 521

Publications of the National Bureau of Standards. 537

Library of Congress Catalog Card Number: 62–37059

For sale by the Superintendent of Documents, U.S. Government Printing Office, Washington, D.C. 20402. Price $1.00 (single copy). Subscription price: $6 a year; $1.25 additional for foreign mailing.
UNITED STATES GOVERNMENT PRINTING OFFICE, WASHINGTON : 1968